



# Kent Academic Repository

Young, P. R. (1998) *A study of coupled dielectric waveguides and their application to millimetre-wave components*. Doctor of Philosophy (PhD) thesis, University of Kent.

## Downloaded from

<https://kar.kent.ac.uk/94744/> The University of Kent's Academic Repository KAR

## The version of record is available from

<https://doi.org/10.22024/UniKent/01.02.94744>

## This document version

UNSPECIFIED

## DOI for this version

## Licence for this version

CC BY-NC-ND (Attribution-NonCommercial-NoDerivatives)

## Additional information

This thesis has been digitised by EThOS, the British Library digitisation service, for purposes of preservation and dissemination. It was uploaded to KAR on 25 April 2022 in order to hold its content and record within University of Kent systems. It is available Open Access using a Creative Commons Attribution, Non-commercial, No Derivatives (<https://creativecommons.org/licenses/by-nc-nd/4.0/>) licence so that the thesis and its author, can benefit from opportunities for increased readership and citation. This was done in line with University of Kent policies (<https://www.kent.ac.uk/is/strategy/docs/Kent%20Open%20Access%20policy.pdf>). If you ...

## Versions of research works

### Versions of Record

If this version is the version of record, it is the same as the published version available on the publisher's web site. Cite as the published version.

### Author Accepted Manuscripts

If this document is identified as the Author Accepted Manuscript it is the version after peer review but before type setting, copy editing or publisher branding. Cite as Surname, Initial. (Year) 'Title of article'. To be published in *Title of Journal*, Volume and issue numbers [peer-reviewed accepted version]. Available at: DOI or URL (Accessed: date).

## Enquiries

If you have questions about this document contact [ResearchSupport@kent.ac.uk](mailto:ResearchSupport@kent.ac.uk). Please include the URL of the record in KAR. If you believe that your, or a third party's rights have been compromised through this document please see our [Take Down policy](https://www.kent.ac.uk/guides/kar-the-kent-academic-repository#policies) (available from <https://www.kent.ac.uk/guides/kar-the-kent-academic-repository#policies>).



**A STUDY OF COUPLED DIELECTRIC WAVEGUIDES**

**AND**

**THEIR APPLICATION TO MILLIMETRE-WAVE COMPONENTS**



**A Study of Coupled Dielectric Waveguides**  
**and**  
**Their Application to Millimetre-Wave Components**

P. R. YOUNG

A thesis submitted for the degree of Doctor of Philosophy

Electronic Engineering Laboratories

University of Kent at Canterbury

---

# ABSTRACT

---

This thesis studies the propagation characteristics of coupled dielectric waveguides and their application to millimetre-wave components. Firstly, by applying the transverse boundary conditions, exact characteristic equations for single and coupled dielectric slab waveguides are obtained. By assuming that the loss tangent of the guiding and surrounding region is small, approximate expressions for the attenuation constant are then derived. These expressions relate the attenuation constant directly to the lossless propagation constant and the waveguide parameters; their evaluation is then straightforward. Secondly, by defining an effective loss tangent, the slab guide solutions are used in the effective dielectric constant (EDC) method and the dual effective-index method (DEIM) to yield a simple, yet accurate method for the evaluation of the complex propagation constant of single and coupled dielectric waveguides with rectangular cross-sections. Furthermore, it is shown that the presented results are in good agreement with both finite element values and experimental data obtained using the open resonant cavity technique.

By considering transitions between single and coupled dielectric slab guides, and the resulting coupling effects, several dielectric waveguide components are described. Each device relies on a short length of coupled waveguide formed by placing a movable block of dielectric parallel to a dielectric guide. It is shown that if the block is of the same material, and has identical cross-sectional dimensions to the waveguide, the effects of coupling can be exploited to achieve a variable attenuation. It is further shown that the separation at which maximum attenuation arises is dependent on the operating frequency; the structure can therefore be used as a wavemeter. By introducing large asymmetries into the device, the effects of coupling are prevented. Under these conditions, the device operates as a low-loss phase-shifter.

---

# ACKNOWLEDGEMENTS

---

I would like to express my appreciation to all the people who have contributed, in one way or another, to my work. In particular, Peter Bianconi and David Morales for their assistance with the phase-shifter and resonant cavity measurements. Ingo Boese for his help with the HFSS simulations. Finally, Richard Collier for many enjoyable discussions on my work and other matters. Thank you.

## CONTENTS

<b>1. INTRODUCTION</b>	<b>1</b>
1.1 ADVANTAGES OF DIELECTRIC WAVEGUIDE ABOVE 110 GHZ	2
1.2 OUTLINE OF THESIS	4
REFERENCES	6
<b>2. PROPAGATION CHARACTERISTICS OF DIELECTRIC WAVEGUIDES</b>	<b>8</b>
2.1 MAXWELL'S EQUATIONS	9
2.2 THE DIELECTRIC SLAB WAVEGUIDE	11
2.2.1 TE Mode Solutions	14
2.2.2 TM Mode Solutions	21
2.2.3 Field Profiles	25
2.2.4 Complex Propagation Constant	28
2.3 THE EFFECTIVE DIELECTRIC CONSTANT METHOD	32
2.3.1 The EDC Method	33
2.3.2 The EDC Method with Dielectric Losses	35
2.3.3 The Dual Effective-Index Method (DEIM)	38
2.3.4 The DEIM with Losses	41
2.4 SUMMARY	44
REFERENCES	45
<b>3. PROPAGATION CHARACTERISTICS OF COUPLED DIELECTRIC WAVEGUIDES</b>	<b>48</b>
3.1 ASYMMETRICAL COUPLED SLAB WAVEGUIDES	49
3.1.1 TE Mode Solutions	50
3.1.2 Symmetrical Coupled Slab Waveguides	53
3.1.3 Asymmetrical Coupled Slab Waveguides	55
3.1.4 Limiting Cases ( $2D=0$ and $2D\rightarrow\infty$ )	58
3.1.5 TM Mode Solutions	62
3.2 FIELD PROFILES	66
3.3 SYNCHRONOUS SOLUTIONS	72
3.4 LOSSES IN COUPLED SLAB GUIDES	73
3.5 THE EDC METHOD FOR COUPLED GUIDES	81
3.6 SUMMARY	96
REFERENCES	97

<b>4. DIELECTRIC WAVEGUIDE MEASUREMENTS</b>	<b>100</b>
4.1 THE INSERTION LOSS TECHNIQUE	100
4.2 THE OPEN RESONANT CAVITY TECHNIQUE	101
4.2.1 Dielectric Waveguides	105
4.2.2 Coupled Dielectric Waveguides	114
4.3 SUMMARY	127
REFERENCES	128
<b>5. DISCONTINUITIES IN DIELECTRIC WAVEGUIDES</b>	<b>129</b>
5.1 RADIATION MODES	129
5.2 WAVEGUIDE DISCONTINUITIES	131
5.3 SUMMARY	149
REFERENCES	150
<b>6. DIELECTRIC WAVEGUIDE COMPONENTS</b>	<b>151</b>
6.1 DIELECTRIC WAVEGUIDE ATTENUATOR	151
6.2 DIELECTRIC WAVEGUIDE WAVEMETER	157
6.3 LOW-LOSS PHASE-SHIFTER	161
6.4 SUMMARY	165
REFERENCES	166
<b>7. CONCLUSIONS</b>	<b>168</b>
7.1 SUMMARY	168
7.2 FUTURE WORK	172
<b>APPENDIX A - COUPLED MODE THEORY</b>	<b>174</b>
<b>APPENDIX B - COUPLED DIELECTRIC WAVEGUIDE RESULTS</b>	<b>182</b>
<b>APPENDIX C - LIST OF PUBLICATIONS</b>	<b>190</b>

*'One cannot escape the feeling that these mathematical formulas have an independent existence and an intelligence of their own, that they are wiser than we are, wiser even than their discoverers, that we get more out of them than was originally put into them.'*

–Heinrich Hertz on Maxwell's equations.

---

# 1. INTRODUCTION

---

In recent years there has been a great deal of interest in the millimetre-wave frequency spectrum above 110 GHz. Applications at these frequencies range from intelligent vehicle guidance systems, collision avoidance and space debris tracking to radio astronomy and high speed LANs. Circuits for millimetre-wave frequencies are available using monolithic microstrip or coplanar waveguide technology. Furthermore, it has been shown that the guiding structures on integrated circuits can be implemented in hybrid dielectric waveguides. These include insulated image guide [1], dielectric ridge guide [2], inverted strip dielectric waveguide [3] and more recently layered ridge dielectric waveguide [4]. Unfortunately, complete systems cannot in general be realised completely on-wafer. Connections to source oscillators, antenna feeds and test equipment are just some examples where guiding structures are required to connect to and from integrated circuits.

Although microstrip and coplanar waveguides are well suited for on-wafer connections, they suffer from very high losses at millimetre-wave frequencies due to surface roughness and the skin effect. They are therefore of little use for propagation over distances much greater than a few millimetres. Coaxial cables are widely used at microwave frequencies, however, above 110 GHz the high attenuation and the small sizes required for monomode propagation make them impractical. The new classes of integrated circuits, using hybrid dielectric waveguides, have low losses but are not well suited for propagation over large distances due to their complicated geometries. Therefore, due to its compatibility with sources and test equipment, conventional metallic waveguide is usually the chosen structure. Unfortunately, as we shall see, rectangular metallic waveguide is far from ideal above 110 GHz and thus a different class of waveguide is required.

Optical fibres have been used for many years as a means of ultra-low-loss propagation. The principle of total internal reflection is exploited to reflect a beam of

light off the boundary between the fibre and the cladding and thus guide the energy down the fibre. This principle is equally valid at microwave and millimetre-wave frequencies. Indeed, much work was done in the seventies and eighties on dielectric waveguides for millimetre-wave frequencies. It is therefore surprising that dielectric waveguides, of the type shown in Figure 1.1, are not more widely used in industry.

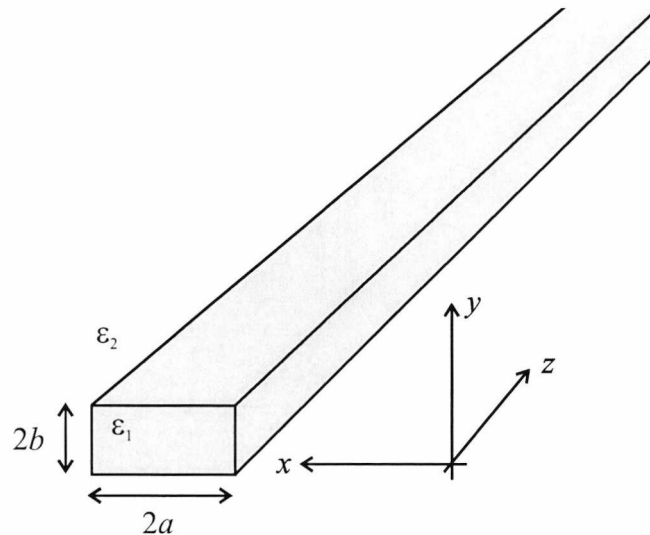


Figure 1.1. Rectangular dielectric waveguide.

The main reason for the neglect of dielectric waveguides is that below 110 GHz the advantages they have over conventional metallic waveguides are less apparent. In addition, the fear of external fields and the increased complexity of the problem has persuaded many engineers to use metallic guides where possible. However, above 110 GHz the advantages that dielectric waveguides have over conventional waveguide far outweigh their disadvantages, making them better suited to millimetre-wave propagation. Accordingly, we start with a summary of the main advantages that dielectric waveguides have above 110 GHz.

## 1.1 ADVANTAGES OF DIELECTRIC WAVEGUIDE ABOVE 110 GHz

The attenuation constant in metallic waveguide increases with at least  $f^{1.5}$  [5] due to the skin effect. In comparison, losses in dielectric waveguide increase with approximately  $f$ . We find that for silver rectangular waveguide the losses are greater

than  $6 \text{ dB m}^{-1}$  at 140 GHz, whereas dielectric guides with losses of just  $1 \text{ dB m}^{-1}$  are readily constructed at the same frequency [6]. Since the attenuation in dielectric waveguides is dependent on the geometry, the dimensions of the structure can usually be adjusted to achieve the required attenuation constant. For example, Yeh [7] has shown that dielectric waveguides with large aspect ratios and high dielectric constants can achieve losses of just  $20 \text{ dB km}^{-1}$  using commercially available material.

In conventional waveguide, the phase velocity varies from infinity to that of free space. In contrast, the phase velocity in dielectric waveguides varies from the plane wave velocity in the surrounding region to that of the guiding medium. Accordingly, the variation of velocity with frequency is much less for dielectric waveguide and consequently the dispersion is less. The bandwidth in conventional waveguides is usually limited to about half an octave to achieve monomode transmission with tolerable dispersion. In dielectric waveguides, the fundamental mode has, in theory, no lower cut-off frequency resulting in much larger bandwidths. However, for sufficient confinement of the field energy, a bandwidth of about an octave is chosen [8].

Conventional waveguide junctions are extremely sensitive to alignment errors in the transverse direction. Moreover, if there is an air gap in the longitudinal direction, the structure works as a good open circuit, reflecting most of the incident wave. Dielectric waveguide junctions, however, are far less sensitive to alignment discontinuities, even in the longitudinal direction [9]. As a result, the insertion loss in dielectric waveguide junctions is far less than conventional guides. Furthermore, transitions from dielectric waveguide to both metallic and coplanar waveguide are possible using waveguide horns and dielectric probing heads [10], respectively. It is further envisaged that transitions between dielectric waveguide and integrated circuits using hybrid dielectric guiding structures could be realised since both structures use the same technology.

At 35 GHz the internal dimensions of rectangular metallic waveguide are 7.112 mm by 3.556 mm; at 140 GHz they are 1.651 mm by 0.8255 mm. Clearly the manufacture of hollow metallic tubes at these dimensions is no trivial task, particularly over large lengths. In contrast, dielectric waveguides of similar dimensions can be manufactured far easier since they are solid, rather than hollow structures. As a result, the cost of dielectric waveguide is much less than metallic

guide at millimetre-wave frequencies. In addition, it is often convenient to have some flexibility in the guiding structure. For example, in mechanically scanning antennas or movable probe stations. Metallic waveguide can be made flexible, but at millimetre frequencies, this is extremely difficult. In comparison, dielectric waveguides made from low-loss materials such as PTFE are inherently flexible and are ideally suited for systems where movement is required. It should be noted that dielectric waveguides suffer from radiation loss if the radius of curvature is small. However, with careful design, sharp bends can be avoided.

Many components are available for metallic waveguide such as phase shifters and attenuators. Components of this nature can be very useful, particularly in measurement systems. If dielectric guides were to replace conventional guides at millimetre-wave frequencies, it would be advantageous if passive components were also available. The main aim of this thesis is, therefore, the design of passive components using dielectric waveguides. However, to achieve this goal, several additional subjects must first be examined. These include the propagation characteristics of both single and coupled dielectric waveguides and the transitions that exist between the two types of structure. All of these topics are studied in the following chapters, an outline of which is given below.

## **1.2 OUTLINE OF THESIS**

In order to use dielectric waveguides their propagation characteristics must be known. Therefore, in Chapter 2 the complex propagation constants of dielectric waveguides are considered. Firstly, the general slab waveguide with dielectric losses in both the guiding and surrounding region is defined. From this, an exact set of coupled transcendental equations for the complex propagation constants are derived. Then, by assuming that the losses are small, approximate expressions for both the real and imaginary parts of the propagation constant are obtained. Secondly, the approximate solutions are used in the effective dielectric constant method (EDC) and the dual effective-index method (DEIM) by introducing an effective loss tangent. Solutions are then compared with finite element results.

The dielectric waveguide components studied in Chapter 6 rely on coupled guides. Accordingly, Chapter 3 looks at the general asymmetrical coupled dielectric waveguide. As in Chapter 2, we firstly consider slab waveguides. Exact

transcendental equations for lossless coupled slab waveguides with asymmetry in width and permittivity are derived and the various limiting values are examined. Field profiles for both forms of asymmetry are displayed giving some insight into the coupling phenomena. Next, approximate solutions for symmetrical coupled slab waveguides with dielectric losses are derived. Finally, by using the solutions for coupled slab waveguides together with the expressions derived in Chapter 2, we obtain approximate solutions for coupled dielectric waveguides using the EDC method. Again, solutions are compared with finite element results.

In order to verify the theoretical models, experimental results for dielectric waveguides are given in Chapter 4. For the single waveguide both the real and imaginary parts of the complex propagation constant are measured and compared with finite element results and the technique in Chapter 2. For coupled structures, results are compared with the technique of Chapter 3 and finite element results.

Chapter 5 studies the discontinuities arising from single to coupled waveguide transitions using the mode matching technique. Firstly, the complete set of modes on dielectric waveguides are introduced. The field continuity equations for single to coupled waveguide transitions are then given. By using the bounded approach, it is shown that very little energy is reflected or radiated from the discontinuity. This leads to a simple approximate value for the transmitted mode amplitudes. Secondly, using the approximate expressions, the effects of separation and asymmetry on the coupling of energy between the two guides is studied.

In Chapter 6, the work of chapters 2, 3, 4 and 5 is combined to demonstrate several dielectric waveguide components, namely wavemeters, attenuators and low-loss phase-shifters. For simplicity, experimental results at 10 GHz are given to verify the theoretical models of the components. Finally, in Chapter 7, several conclusions are made and suggestions for future work.

---

**REFERENCES**

- 1 W. V. McLevige, T. Itoh and R. Mittra, "New waveguide structures for millimeter-wave and optical integrated circuits," *IEEE Trans. Microwave Theory Tech.*, vol. MTT-23, October 1975, pp. 788-794.
- 2 T. Wang and S. E. Schwarz, "Design of dielectric ridge waveguides for millimetre-wave integrated circuits," *IEEE Trans. Microwave Theory Tech.*, vol. MTT-31, February 1983, pp. 128-134.
- 3 T. Itoh, "Inverted strip dielectric waveguide for millimeter-wave integrated circuits," *IEEE Trans. Microwave Theory Tech.*, vol. MTT-24, November 1980, pp. 821-827.
- 4 A. G. Engel and L. P. B. Katehi, "Low-loss monolithic transmission lines for submillimeter and terahertz frequency applications," *IEEE Trans. Microwave Theory Tech.*, vol. 39, no. 11, November 1991, pp. 1847-1854.
- 5 S. Ramo, J. R. Whinnery and T. Van Duzer, "Fields and waves in communication electronics," *John Wiley & Sons*, 1984.
- 6 F. I. Shimabukuro and C. Yeh, "Attenuation measurements of very low loss dielectric waveguides by the cavity resonator method applicable in the millimeter/submillimeter wavelength range," *IEEE Trans. Microwave Theory Tech.*, vol. 36, no. 7, July 1988, pp. 1160-1166.
- 7 C. Yeh, F. I. Shimabukuro and J. Chu, "Dielectric ribbon waveguide: An optimum configuration for ultra-low-loss millimeter/submillimeter dielectric waveguide," *IEEE Trans. Microwave Theory Tech.*, pp. 691-701, June 1990.

- 
- 8 R. J. Collier and R. D. Birch, "The bandwidth of image guide," *IEEE Trans. Microwave Theory Tech.*, vol. MTT-28, no. 8, August 1980, pp. 932-935.
  - 9 R. J. Collier and M. F. D'Souza, "Comparison of junctions in both dielectric guides and metallic guides above 75 GHz," *IEE Proceedings A*, vol. 139, no. 5, September 1992, pp. 226-228.
  - 10 I. M. Boese, R. J. Collier, A. K. Jastrzebski, H. Ahmed, J. R. Cleaver and D. Hasko, "An on wafer probe for measurement at 140 GHz," *IEE colloquium on terahertz technology and its applications*, 10 April 1997.

---

## 2. PROPAGATION CHARACTERISTICS OF DIELECTRIC WAVEGUIDES

---

Many techniques for the solution of rectangular dielectric waveguides have been presented. One of the first of these techniques was given by Marcatili [1]. By assuming that very little energy flowed in the four corner regions he matched the fields along the guide boundaries producing a set of characteristic equations that could be solved for weakly guiding structures. Goel [2] provided a more accurate mode matching technique by expanding the fields in terms of circular harmonics. By analysing several slab waveguide structures Knox and Toullos [3] provided a simple technique that gave results comparable to Marcatili's method but was easier to implement than Goel's technique. Since then, many techniques have been presented, such as finite difference and finite element approaches, a review of which can be found in [4]. These techniques can be extremely accurate, however in general they are numerically intensive. Consequently, the effective dielectric constant method of Knox and Toullos is still widely used for dielectric waveguide design. Furthermore, the accuracy of the technique has been improved in recent years to form the dual effective-index method [5].

Although the losses in dielectric waveguides are usually far less than metallic waveguides at millimetre-wave frequencies, they can still be significant. The majority of work on dielectric waveguides has been at optical wavelengths where the dielectric losses are negligible. As a result many of the techniques have dealt with simply the imaginary part of the complex propagation constant. The numerical techniques such as the finite element or finite difference methods have been applied to lossy structures; however, their complexity and large computational times limit their use for general design purposes. In contrast, the widely used effective dielectric constant method is accurate and extremely simple to implement. Accordingly, in this chapter an extension to the effective dielectric constant and dual effective-index methods is presented to allow for dielectric losses.

## 2.1 MAXWELL'S EQUATIONS

We begin this section with Maxwell's well-known equations in differential form:

$$\nabla \times \tilde{\mathbf{E}}(\mathbf{r}, t) = -\frac{\partial \tilde{\mathbf{B}}(\mathbf{r}, t)}{\partial t} \quad (2.1)$$

$$\nabla \times \tilde{\mathbf{H}}(\mathbf{r}, t) = \tilde{\mathbf{J}}_c(\mathbf{r}, t) + \tilde{\mathbf{J}}_s(\mathbf{r}, t) + \frac{\partial \tilde{\mathbf{D}}(\mathbf{r}, t)}{\partial t} \quad (2.2)$$

$$\nabla \cdot \tilde{\mathbf{B}}(\mathbf{r}, t) = 0 \quad (2.3)$$

$$\nabla \cdot \tilde{\mathbf{D}}(\mathbf{r}, t) = \tilde{\rho}(\mathbf{r}, t), \quad (2.4)$$

where the tildes represent functions of space and time. The variables are defined as follows

$\tilde{\mathbf{E}}$	Electric field intensity:	$\text{V m}^{-1}$
$\tilde{\mathbf{H}}$	Magnetic field intensity:	$\text{A m}^{-1}$
$\tilde{\mathbf{D}}$	Electric flux density:	$\text{C m}^{-2}$
$\tilde{\mathbf{B}}$	Magnetic flux density:	$\text{Wb m}^{-2}$
$\tilde{\mathbf{J}}_c$	Conduction current density:	$\text{A m}^{-2}$
$\tilde{\mathbf{J}}_s$	Source current density:	$\text{A m}^{-2}$
$\tilde{\rho}$	Electric charge density:	$\text{C m}^{-3}$
$\mathbf{r}$	Position vector:	$\text{m}$

Maxwell's equations are supplemented with the following relations

$$\tilde{\mathbf{J}}_c = \sigma \tilde{\mathbf{E}} \quad (2.5)$$

$$\tilde{\mathbf{D}} = \epsilon \tilde{\mathbf{E}} \quad (2.6)$$

$$\tilde{\mathbf{B}} = \mu \tilde{\mathbf{H}}, \quad (2.7)$$

where

$\sigma$	Conductivity:	$\text{S m}^{-1}$
$\varepsilon$	Permittivity:	$\text{F m}^{-1}$
$\mu$	Permeability:	$\text{H m}^{-1}$

The conductivity  $\sigma$ , the permittivity  $\varepsilon$  and the permeability  $\mu$  can in general be functions of the applied field (non-linear); functions of space (inhomogeneous); and dependent on the direction of the field (anisotropic). However, in our analysis we shall only consider linear homogenous isotropic media. We further assume that all media is source free, therefore  $\tilde{\rho} = 0$  and  $\tilde{\mathbf{J}}_s = 0$ .

The partial differentials in Maxwell's equations can be simplified by taking the time-harmonic case. Thus, the field expressions become

$$\tilde{\mathbf{E}}(\mathbf{r}, t) = \mathbf{E}(\mathbf{r})e^{j\omega t} \quad (2.8)$$

$$\tilde{\mathbf{H}}(\mathbf{r}, t) = \mathbf{H}(\mathbf{r})e^{j\omega t} \quad (2.9)$$

where  $\omega$  is the angular frequency,  $j = \sqrt{-1}$  and  $t$  is the time in seconds. Substitution into Maxwell's equations and remembering that  $\tilde{\rho} = 0$  and  $\tilde{\mathbf{J}}_s = 0$  gives

$$\nabla \times \mathbf{E} = -j\omega\mu\mathbf{H} \quad (2.10)$$

$$\nabla \times \mathbf{H} = j\omega\varepsilon \left( 1 - j \frac{\sigma}{\omega\varepsilon} \right) \mathbf{E} \quad (2.11)$$

$$\nabla \cdot (\mu\mathbf{H}) = 0 \quad (2.12)$$

$$\nabla \cdot (\varepsilon\mathbf{E}) = 0, \quad (2.13)$$

where for simplicity the  $\mathbf{r}$  dependence and the  $e^{j\omega t}$  factor have been omitted.

## 2.2 THE DIELECTRIC SLAB WAVEGUIDE

To enable our analysis of rectangular dielectric waveguides we firstly consider the simplest form of dielectric guiding structure, the slab waveguide, refer to Figure 2.1. The structure consists of a guiding region (region 1) of relative permittivity  $\epsilon_1$  surrounded by a region of lower permittivity  $\epsilon_2$  (region 2). The guiding region is infinite in extent in both the  $y$  and  $z$  directions, with propagation in the positive  $z$  direction (out of the page). The  $z$  dependence is of the form  $\exp(-\gamma_z z)$ , where the longitudinal propagation constant is defined by  $\gamma_z = \alpha_z + j\beta_z$ . Therefore,

$$\mathbf{E}(\mathbf{r}) = \mathbf{E}(x, y)e^{-\gamma_z z}$$

and

$$\mathbf{H}(\mathbf{r}) = \mathbf{H}(x, y)e^{-\gamma_z z}.$$

For the slab guide we simplify the problem by assuming the fields are independent of the  $y$  coordinate. Therefore,  $\mathbf{E}(x, y) = \mathbf{E}(x)$  and  $\mathbf{H}(x, y) = \mathbf{H}(x)$ . Substitution into equations (2.10) and (2.11) gives two sets of uncoupled equations. Thus,

$$\gamma_z E_y = -j\omega\mu H_x \quad (2.14)$$

$$\frac{dE_y}{dx} = -j\omega\mu H_z \quad (2.15)$$

$$-\gamma_z H_x - \frac{dH_z}{dx} = j\omega(\epsilon' - j\epsilon'')E_y \quad (2.16)$$

and

$$\gamma_z H_y = j\omega(\epsilon' - j\epsilon'')E_x \quad (2.17)$$

$$\frac{dH_y}{dx} = j\omega(\epsilon' - j\epsilon'')E_z \quad (2.18)$$

$$-\gamma_z E_x - \frac{dE_z}{dx} = -j\omega\mu H_y. \quad (2.19)$$

The  $\sigma\mathbf{E}$  term in phase with the magnetic field in equation (2.11) suggests purely ohmic losses due to free carrier collisions. However, for good dielectrics, the loss

mechanism is somewhat more complicated. The  $(\epsilon - j\sigma/\omega\epsilon)$  term in equation (2.11) has therefore been replaced with the complex permittivity  $\epsilon' - j\epsilon''$ . Where the real part is due to the polarizability of the material; and the imaginary part represents losses due to carrier collision, and any absorptions associated with resonances in the electronic, atomic and permanent polarizabilities of the medium [6].

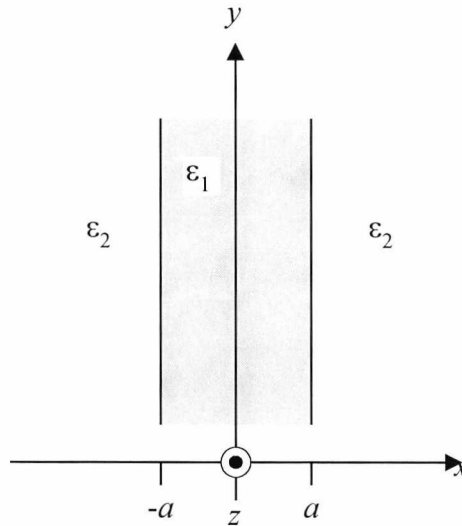


Figure 2.1. Geometry of dielectric slab waveguide.

Equations (2.14), (2.15) and (2.16) do not have an electric field component in the  $z$  direction and therefore define the transverse electric (TE) mode solutions. Eliminating  $H_x$  and  $H_z$  from equations (2.14), (2.15) and (2.16) gives the characteristic equation for the TE mode solutions

$$\frac{d^2 E_y}{dx^2} + k_x^2 E_y = 0. \quad (2.20)$$

Similarly, equations (2.17), (2.18) and (2.19) have no magnetic field component in the  $z$  direction and therefore define the transverse magnetic (TM) mode solutions. Eliminating  $E_x$  and  $E_y$  from equations (2.17), (2.18) and (2.19) gives the TM mode characteristic equation

$$\frac{d^2 H_y}{dx^2} + k_x^2 H_y = 0. \quad (2.21)$$

The eigenvalue defined by the transverse propagation constant  $k_x$  in equations (2.20) and (2.21) is given by the dispersion relation

$$k_x^2 = \gamma_z^2 - \gamma^2 \quad (2.22)$$

with

$$\gamma^2 = -\omega^2 \mu (\epsilon' - j\epsilon''). \quad (2.23)$$

In our analysis, we assume that all of the materials are nonmagnetic, therefore, we let the permeability equal that of free space,  $\mu = \mu_0$ . Remembering that  $\epsilon = \epsilon_0 \epsilon_n$ , where  $\epsilon_n$  is the complex relative permittivity,  $\epsilon_n = \epsilon'_n - j\epsilon''_n$ , of the medium and  $\epsilon_0$  is that of free space, we obtain from equation (2.23)

$$\gamma_n^2 = -k_0^2 \epsilon'_n (1 - j \tan \delta_n), \quad (2.24)$$

where the free space wavenumber is defined by  $k_0^2 = \omega^2 \mu_0 \epsilon_0$  and the loss tangent by

$$\tan \delta_n = \frac{\epsilon''_n}{\epsilon'_n}. \quad (2.25)$$

Therefore, the transverse propagation constant  $k_{xn}$  in region  $n$  becomes

$$k_{xn}^2 = \gamma_z^2 - \gamma_n^2. \quad (2.26)$$

We note that since  $\gamma_n$  is in general a complex quantity the transverse propagation is also complex, that is  $k_{xn} = k'_{xn} + jk''_{xn}$ .

We now consider the TE mode solutions defined by  $\gamma_z$ .

### 2.2.1 TE Mode Solutions

For guided TE modes on slab waveguides with no dielectric losses the transverse field  $E_y$  is split into two forms: a sinusoidal standing wave function within the guiding region and an exponentially decaying function in the surrounding regions. When the guide has losses, the solution has sinusoidal and exponential components in both regions. However, if the loss tangent of both the guiding and surrounding area is small then the real part of  $k_{x1}$  will be much greater than the imaginary part, resulting in a field profile that is predominantly sinusoidal within the guiding region. Thus, we set the electric field function in region 1 equal to the following [7, 8, 9, 10]

$$E_y(x) = A_1 \cos(k_{x1}x) \quad \text{for } |x| \leq a \quad (2.27)$$

for modes with even symmetry and

$$E_y(x) = A_1 \sin(k_{x1}x) \quad \text{for } |x| \leq a \quad (2.28)$$

for modes with odd symmetry; where  $A_1$  is a complex valued amplitude constant.

With similar reasoning, we find that in region 2 the imaginary part of  $k_{x2}$  is much greater than the real part. This results in field profiles that are predominantly exponential. Clearly, the power flow in the guided mode must be finite. We therefore choose exponential field functions that decay to zero for large  $x$ , thus

$$E_y(x) = \pm A_2 \exp[\alpha_{x2}(x+a)] \quad \text{for } x < -a \quad (2.29)$$

and

$$E_y(x) = A_2 \exp[-\alpha_{x2}(x-a)] \quad \text{for } x > a, \quad (2.30)$$

where  $\alpha_{x2}^2 = -k_{x2}^2$  and  $A_2$  is a complex constant. From equation (2.15) we have

$$H_z = \frac{j}{\omega\mu} \frac{dE_y}{dx}. \quad (2.31)$$

Therefore, the longitudinal magnetic field for the TE mode solutions within the guiding region is given by

$$H_z(x) = -\frac{j}{\omega\mu} k_{x1} A_1 \sin(k_{x1}x) \text{ for } |x| \leq a \quad (2.32)$$

for modes with even symmetry and

$$H_z(x) = \frac{j}{\omega\mu} k_{x1} A_1 \cos(k_{x1}x) \text{ for } |x| \leq a \quad (2.33)$$

for modes with odd symmetry.

In the surrounding region the magnetic fields are given by

$$H_z(x) = \pm \frac{j}{\omega\mu} \alpha_{x2} A_2 \exp[\alpha_{x2}(x+a)] \text{ for } x < -a \quad (2.34)$$

and

$$H_z(x) = -\frac{j}{\omega\mu} \alpha_{x2} A_2 \exp[-\alpha_{x2}(x-a)] \text{ for } x > a. \quad (2.35)$$

For continuity the tangential fields must be continuous at the two boundaries, we therefore have the following boundary conditions:

$$E_y(|a^-|) = E_y(|a^+|) \quad (2.36)$$

and

$$H_z(|a^-|) = H_z(|a^+|), \quad (2.37)$$

where the + and – superscripts denote the left and right sides of the  $x=\pm a$  boundaries.

Applying the boundary conditions at the  $x=a$  boundary yields

$$A_1 \cos(k_{x1}a) = A_2 \quad (2.38)$$

and

$$k_{x1}A_1 \sin(k_{x1}a) = \alpha_{x2}A_2 \quad (2.39)$$

for even modes; and

$$A_1 \sin(k_{x1}a) = A_2 \quad (2.40)$$

and

$$k_{x1}A_1 \cos(k_{x1}a) = -\alpha_{x2}A_2 \quad (2.41)$$

for odd modes.

Dividing equation (2.39) by equation (2.38) gives the guidance condition for the TE modes with even symmetry:

$$k_{x1} \tan(k_{x1}a) = \alpha_{x2}. \quad (2.42)$$

Similarly, dividing equation (2.41) by equation (2.40) gives the guidance condition for TE odd modes:

$$k_{x1} \cot(k_{x1}a) = -\alpha_{x2}. \quad (2.43)$$

On squaring equation (2.42) and remembering that  $k_{x1}^2 = \gamma_z^2 - \gamma_1^2$  and  $\alpha_{x2}^2 = \gamma_2^2 - \gamma_z^2$  we obtain

$$k_{x1}^2 [1 + \tan^2(k_{x1}a)] = \gamma_2^2 - \gamma_1^2 \quad (2.44)$$

for even modes and similarly

$$k_{x1}^2 [1 + \cot^2(k_{x1}a)] = \gamma_2^2 - \gamma_1^2 \quad (2.45)$$

for the odd modes. Finally, using equation (2.26) we obtain the guidance condition for TE even mode solutions:

$$k_{x1}^2 [1 + \tan^2(k_{x1}a)] = k_0^2 (\epsilon'_1 - \epsilon'_2) - jk_0^2 (\epsilon'_1 \tan \delta_1 - \epsilon'_2 \tan \delta_2) \quad (2.46)$$

and

$$k_{x1}^2 [1 + \cot^2(k_{x1}a)] = k_0^2 (\epsilon'_1 - \epsilon'_2) - jk_0^2 (\epsilon'_1 \tan \delta_1 - \epsilon'_2 \tan \delta_2) \quad (2.47)$$

for TE odd mode solutions.

The solution of the above two equations is not trivial since both equations, when expanded for complex  $k_{x1}$ , result in coupled transcendental equations for  $k'_{x1}$  and  $k''_{x1}$  [7,11]. These can of course be solved by iterative methods, however, by making a few simple approximations, equations (2.46) and (2.47) can be greatly simplified for structures with small loss tangents [12].

Expanding the first term of the left-hand side of equation (2.46) gives

$$(k'_{x1} + jk''_{x1})^2 \cong k'^2_{x1} + j2k'_{x1}k''_{x1}, \quad (2.48)$$

where the  $(k''_{x1})^2$  terms have been neglected. This approximation is valid if the loss tangent of both the guiding and surrounding regions is small.

The  $\tan(k_{x1}a)$  term is expanded thus

$$\tan[(k'_{x1} + jk''_{x1})a] = \frac{\sin(k'_{x1}a)\cos(k'_{x1}a) + j\sinh(k''_{x1}a)\cosh(k''_{x1}a)}{\cos^2(k'_{x1}a) + \sinh^2(k''_{x1}a)}. \quad (2.49)$$

If  $k''_{x1}a$  is small then  $\cosh(k''_{x1}a) \cong 1$  and  $\sinh(k''_{x1}a) \cong k''_{x1}a$ , therefore

$$\tan[(k'_{x1} + jk''_{x1})a] \cong \tan(k'_{x1}a) + j \frac{k''_{x1}a}{\cos^2(k'_{x1}a)}. \quad (2.50)$$

Squaring gives

$$\tan^2[(k'_{x1} + jk''_{x1})a] = \tan^2(k'_{x1}a) + j2 \frac{k''_{x1}a \sin(k'_{x1}a)}{\cos^3(k'_{x1}a)}, \quad (2.51)$$

where again the  $(k''_{x1})^2$  terms have been ignored. The left-hand side of equation (2.46) now becomes

$$k'^2_{x1} [1 + \tan^2(k'_{x1}a)] + j2 \left\{ \frac{k'^2_{x1} k''_{x1} a \tan(k'_{x1}a)}{\cos^2(k'_{x1}a)} + \frac{k'^2_{x1} k''_{x1}}{k'_{x1}} [1 + \tan^2(k'_{x1}a)] \right\}, \quad (2.52)$$

where once more the  $(k''_{x1})^2$  terms have been neglected. By equating the real parts in equation (2.46) we obtain

$$k'^2_{x1} [1 + \tan^2(k'_{x1}a)] = k_0^2 (\epsilon'_1 - \epsilon'_2) \quad (2.53)$$

and for the imaginary parts

$$2 \left\{ \frac{k'^2_{x1} k''_{x1} a \tan(k'_{x1}a)}{\cos^2(k'_{x1}a)} + \frac{k'^2_{x1} k''_{x1}}{k'_{x1}} [1 + \tan^2(k'_{x1}a)] \right\} = k_0^2 (\epsilon'_2 \tan \delta_2 - \epsilon'_1 \tan \delta_1). \quad (2.54)$$

The above equation can be simplified by making use of equation (2.53), thus

$$2 \left\{ k''_{x1} a \tan(k'_{x1} a) + \frac{k''_{x1}}{k'_{x1}} \right\} k_0^2 (\epsilon'_1 - \epsilon'_2) = k_0^2 (\epsilon'_2 \tan \delta_2 - \epsilon'_1 \tan \delta_1). \quad (2.55)$$

Finally, by solving for  $k''_{x1}$  an approximate expression for the imaginary part of the complex transverse propagation constant  $k_{x1}$  is obtained

$$k''_{x1} = k'_{x1} \frac{\epsilon'_2 \tan \delta_2 - \epsilon'_1 \tan \delta_1}{2(\epsilon'_1 - \epsilon'_2)[1 + k'_{x1} a \tan(k'_{x1} a)]}. \quad (2.56)$$

In a similar way the following equations are obtained for the TE odd modes

$$k'^2_{x1} [1 + \cot^2(k'_{x1} a)] = k_0^2 (\epsilon'_1 - \epsilon'_2) \quad (2.57)$$

and

$$k''_{x1} = k'_{x1} \frac{\epsilon'_2 \tan \delta_2 - \epsilon'_1 \tan \delta_1}{2(\epsilon'_1 - \epsilon'_2)[1 - k'_{x1} a \cot(k'_{x1} a)]}. \quad (2.58)$$

We notice from equations (2.56) and (2.58) that the imaginary part of  $k_{x1}$  is expressed purely in terms of  $k'_{x1}$ . Therefore, by making the above approximations, the coupled transcendental equations in (2.46) and (2.47) are replaced by two uncoupled equations for the real part of  $k_{x1}$ , and two simple expressions relating  $k''_{x1}$  to  $k'_{x1}$ . This greatly simplifies the problem, with now only one uncoupled transcendental equation to solve for each mode. Furthermore, equations (2.53) and (2.57) are exactly those obtained for lossless guiding structures, as is readily seen by setting the imaginary components in equations (2.46) and (2.47) equal to zero. Any technique can thus be complemented with the present method to allow for dielectric losses.

The solution of the lossless guidance condition in equations (2.53) and (2.57) is well known [7, 8, 9, 10], however, for the sake of completeness, a few comments will be made.

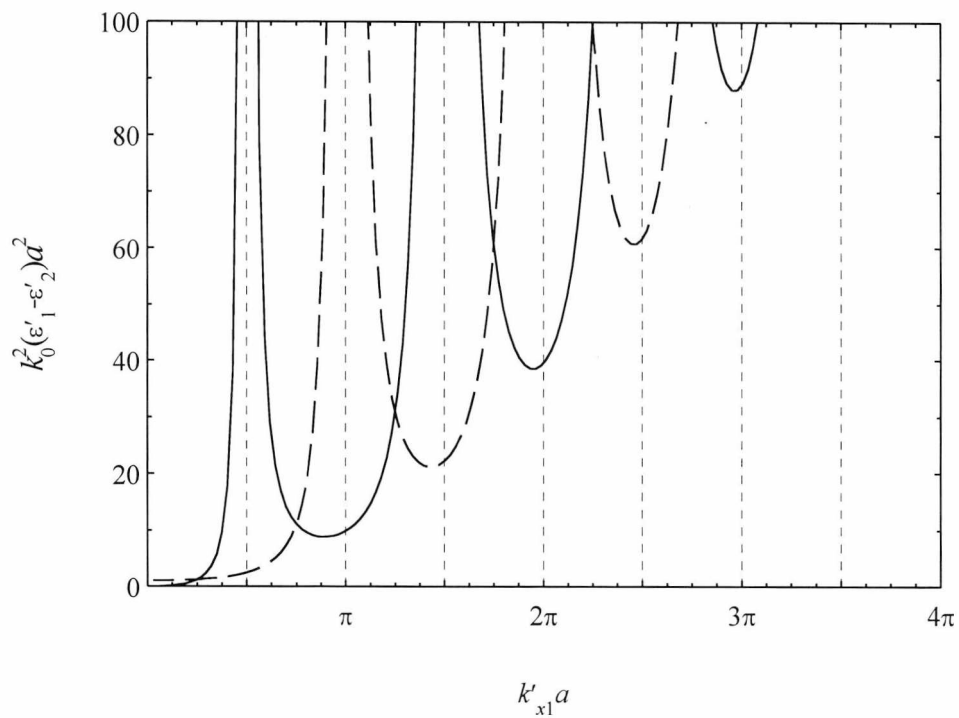


Figure 2.2. Graph of guidance condition for TE slab guide. Solid lines show even mode solutions, dashed lines show odd mode solutions.

Since the guidance condition has been squared to eliminate the  $\alpha_{x2}$  dependence, both positive and negative solutions for the real part for  $\alpha_{x2}$  are obtained from equations (2.53) and (2.57). Clearly, negative values result in field solutions that diverge away from the guiding region. These so-called improper or leaky modes carry infinite power and are of limited practical significance. Fortunately, the solutions for proper modes are easily distinguished. Figure 2.2 shows plots of the right-hand side of equations (2.53) and (2.57), where, for simplicity, both sides have been multiplied by  $a^2$ . Even mode solutions are shown as solid lines, odd modes as dashed lines. The range for which TE even mode solutions are defined is as follows

$$n\pi < k'_{x1}a < \frac{\pi}{2}(2n+1) \quad n=0, 1, 2, \dots, m_e-1 \quad (2.59)$$

where  $m_e$  is the number of modes with even symmetry supported by the guide. The range for which TE odd solutions are defined is as follows

$$\frac{\pi}{2}(2n-1) < k'_{x1}a < n\pi \quad n=1, 2, \dots, m_0 \quad (2.60)$$

where  $m_0$  is the number of antisymmetrical modes supported by the guide. The total number of modes the guide supports is given by  $m_e + m_o$ . In general,  $TE_n$  refers to the  $(n+1)$ th mode of the waveguide. For example,  $TE_0$  is the lowest order even mode,  $TE_1$  is the lowest order odd mode,  $TE_2$  is the next highest order even mode, etc.

The lower limits of equations (2.59) and (2.60) also define the cut-off frequencies of the modes. For example, the cut-off frequency of the lowest order odd mode is given by  $k'_{x1}a = \pi/2$ . Substitution of this value into equation (2.57) allows us to solve for  $k_0$  and therefore the frequency. We see that the fundamental, or lowest order even mode, has a cut-off frequency of zero. Practically, this is not possible, since  $\alpha'_{x2} \rightarrow 0$  as  $f \rightarrow 0$  and therefore, in the limit, the fields carry infinite power.

### 2.2.2 TM Mode Solutions

The analysis of TM modes is slightly more complicated than for TE solutions, however the method is just the same. Again, we start by assuming the following field solutions over the three regions

$$H_y(x) = B_1 \cos(k_{x1}x) \quad \text{for } |x| \leq a \quad (2.61)$$

for modes with even symmetry and

$$H_y(x) = B_1 \sin(k_{x1}x) \quad \text{for } |x| \leq a \quad (2.62)$$

for modes with odd symmetry. In the surrounding regions we assume

$$H_y(x) = \pm B_2 \exp[\alpha_{x2}(x+a)] \quad \text{for } x < -a \quad (2.63)$$

and

$$H_y(x) = B_2 \exp[-\alpha_{x2}(x-a)] \text{ for } x > a. \quad (2.64)$$

From equation (2.18) we have

$$E_z = -\frac{j}{\omega(\epsilon' - j\epsilon'')} \frac{dH_y}{dx}. \quad (2.65)$$

Therefore, the longitudinal electric field for the TM mode solutions within the guiding region is given by

$$E_z(x) = \frac{j}{\omega\epsilon'_1(1-j\tan\delta_1)} k_{x1} B_1 \sin(k_{x1}x) \text{ for } |x| \leq a \quad (2.66)$$

for modes with even symmetry and

$$E_z(x) = -\frac{j}{\omega\epsilon'_1(1-j\tan\delta_1)} k_{x1} B_1 \cos(k_{x1}x) \text{ for } |x| \leq a \quad (2.67)$$

for modes with odd symmetry. In the surrounding region the electric fields are given by

$$E_z(x) = \pm \frac{j}{\omega\epsilon'_2(1-j\tan\delta_2)} \alpha_{x2} B_2 \exp[\alpha_{x2}(x+a)] \text{ for } x < -a \quad (2.68)$$

and

$$E_z(x) = \frac{j}{\omega\epsilon'_2(1-j\tan\delta_2)} \alpha_{x2} B_2 \exp[-\alpha_{x2}(x-a)] \text{ for } x > a. \quad (2.69)$$

Following a similar procedure to the TE mode solutions, we finally obtain the TM guidance condition for even modes:

$$k_{x1}^2 \left[ 1 + \frac{\epsilon_2'^2 (1 - j \tan \delta_2)^2}{\epsilon_1'^2 (1 - j \tan \delta_1)^2} \tan^2(k_{x1} a) \right] = k_0^2 (\epsilon_1' - \epsilon_2') - j k_0^2 (\epsilon_1' \tan \delta_1 - \epsilon_2' \tan \delta_2) \quad (2.70)$$

and for odd modes:

$$k_{x1}^2 \left[ 1 + \frac{\epsilon_2'^2 (1 - j \tan \delta_2)^2}{\epsilon_1'^2 (1 - j \tan \delta_1)^2} \cot^2(k_{x1} a) \right] = k_0^2 (\epsilon_1' - \epsilon_2') - j k_0^2 (\epsilon_1' \tan \delta_1 - \epsilon_2' \tan \delta_2). \quad (2.71)$$

Equations (2.70) and (2.71) are more complicated than equations (2.46) and (2.47) since the ratio of complex permittivity enters the expression. However, we can make the same assumptions that were made for the TE case. Therefore, using equations (2.48) and (2.51) and noting that

$$\frac{\epsilon_2'^2 (1 - j \tan \delta_2)^2}{\epsilon_1'^2 (1 - j \tan \delta_1)^2} \cong \frac{\epsilon_2'^2}{\epsilon_1'^2} + j 2 \frac{\epsilon_2'^2}{\epsilon_1'^2} (\tan \delta_1 - \tan \delta_2) \quad (2.72)$$

we obtain, after some work, the guidance condition:

$$k_{x1}'^2 \left[ 1 + \frac{\epsilon_2'^2}{\epsilon_1'^2} \tan^2(k_{x1}' a) \right] = k_0^2 (\epsilon_1' - \epsilon_2') \quad (2.73)$$

with the imaginary part of the complex propagation constant  $k_{x1}$  given by

$$k_{x1}'' = k_{x1}' \frac{\left[ k_0^2 \left( \epsilon_1' - \frac{\epsilon_2'}{2} \right) - k_{x1}'^2 \right] \tan \delta_2 - \left[ k_0^2 \left( \frac{3\epsilon_1'}{2} - \epsilon_2' \right) - k_{x1}'^2 \right] \tan \delta_1}{k_0^2 (\epsilon_1' - \epsilon_2') + \left[ k_{x1}'^2 \left( \frac{\epsilon_2'^2}{\epsilon_1'^2} - 1 \right) + k_0^2 (\epsilon_1' - \epsilon_2') \right] a k_{x1}' \tan(k_{x1}' a)}, \quad (2.74)$$

where products of all small terms ( $\tan \delta_n$  and  $k_{x1}''$ ) have been neglected.

Similarly, for the odd modes we obtain

$$k'_{x1} \left[ 1 + \frac{\epsilon'_2{}^2}{\epsilon'_1{}^2} \cot^2(k'_{x1}a) \right] = k_0^2 (\epsilon'_1 - \epsilon'_2) \tag{2.75}$$

and

$$k''_{x1} = k'_{x1} \frac{\left[ k_0^2 \left( \epsilon'_1 - \frac{\epsilon'_2}{2} \right) - k'_{x1}{}^2 \right] \tan \delta_2 - \left[ k_0^2 \left( \frac{3\epsilon'_1}{2} - \epsilon'_2 \right) - k'_{x1}{}^2 \right] \tan \delta_1}{k_0^2 (\epsilon'_1 - \epsilon'_2) - \left[ k'_{x1}{}^2 \left( \frac{\epsilon'_2{}^2}{\epsilon'_1{}^2} - 1 \right) + k_0^2 (\epsilon'_1 - \epsilon'_2) \right] ak'_{x1} \cot(k'_{x1}a)} \tag{2.76}$$

Once more we notice that  $k'_{x1}$  is given from the lossless solution, with  $k''_{x1}$  calculated directly from  $k'_{x1}$ .

Figure 2.3 shows plots of equations (2.73) and (2.75). Since the ratio of permittivity enters the equation, different curves result for different permittivity ratios, however, here we let  $\epsilon'_1=2.07$  and  $\epsilon'_2=1$ . Even mode solutions are shown as solid lines, odd modes as dashed lines. The range for which TM even and odd mode solutions are defined is identical to that of the TE modes, equations (2.59) and (2.60), respectively.

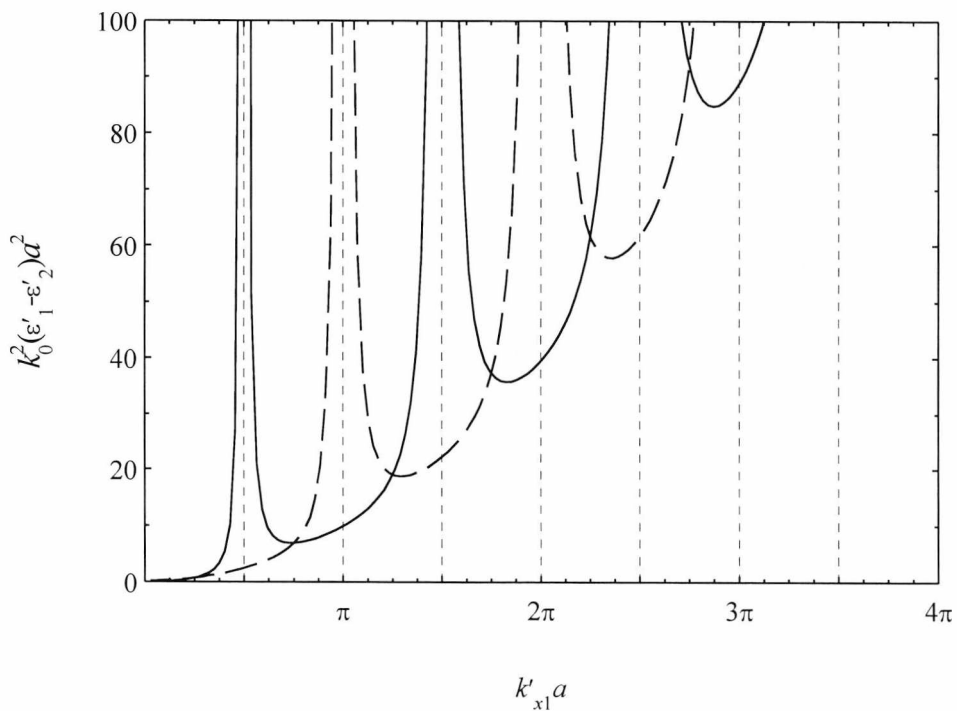


Figure 2.3. Graph of guidance condition for TM slab guide with  $\epsilon'_1=2.07$  and  $\epsilon'_2=1$ . Solid lines show even mode solutions; dashed lines show odd mode solutions.

### 2.2.3 Field Profiles

The field profiles of dielectric slab waveguides can be calculated by substituting the eigenvalues back into the field equations. For simplicity, we set the amplitude constant  $A_1$  in the field equations equal to unity,  $A_2$  is then given by

$$A_2 = \cos(k_{x1}a) \quad (2.77)$$

for even modes and

$$A_2 = \sin(k_{x1}a) \quad (2.78)$$

for odd modes. Since, for small loss tangents, the imaginary parts of  $k_{x1}$  and  $\alpha_{x2}$  are small in comparison to the real part, the field profiles are almost identical to the lossless fields. Therefore, for field profile evaluations,  $k_{x1}$  is set to  $k'_{x1}$  and similarly  $\alpha_{x2}$  is set to  $\alpha'_{x2}$ .

Figure 2.4 and Figure 2.5 show both even and odd mode electric,  $E_y$ , and magnetic,  $H_z$ , field profiles, respectively. The  $H_x$  fields are not shown since they are proportional to the electric field, equation (2.14). The profiles are for TE mode solutions with  $2a=0.9\lambda_0$ ,  $\epsilon'_1=2.07$  and  $\epsilon'_2=1$ . Solving equations (2.53) and (2.57) for these parameters gives  $k'_{x1(e)}a=1.162$  and  $k'_{x1(o)}a=2.259$ , where the (e) and (o) subscripts represent even and odd mode solutions, respectively.

Figure 2.6 shows plots of the even and odd mode electric field profiles  $E_x$  for TM solutions. Again, solid lines represent the even modes, dashed lines the odd. The slab guide has the following parameters:  $2a=0.9\lambda_0$ ,  $\epsilon'_1=2.07$  and  $\epsilon'_2=1$ . We notice from Figure 2.6 that the electric field is discontinuous at the  $|a|$  boundary due to the different values of  $\epsilon_n$  in each region, refer to equation (2.17). Solving equations (2.73) and (2.75) gives  $k'_{x1(e)}a=1.329$  and  $k'_{x1(o)}a=2.482$ .

It should be noted that the sum of two or more solutions of equations (2.20) and (2.21) is also a solution, the complete field profile is therefore given by

$$E_t = \sum_{i=1}^n A_i \mathbf{E}_i, \quad (2.79)$$

where  $\mathbf{E}_i$  and  $A_i$  are the field function and amplitude constant for the  $i$ th mode, respectively. Since the modes on dielectric slab waveguides are orthogonal to each other [8, 9],  $A_i$  cannot be related to  $A_{i+1}$ . Fortunately,  $A_i$  can be determined from the longitudinal boundary conditions, as we shall see in Chapter 5.

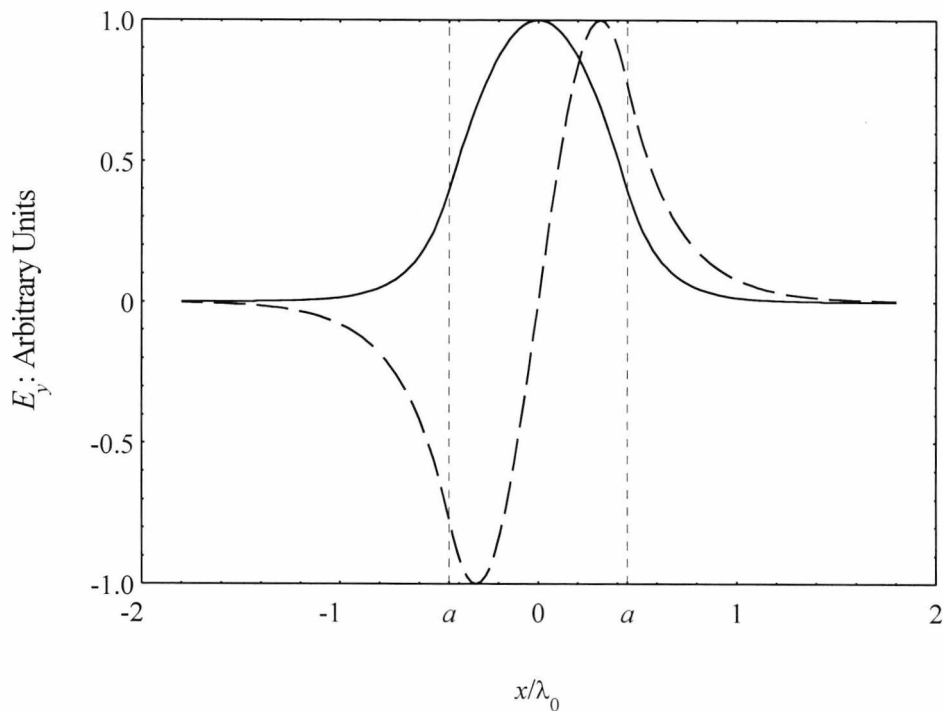


Figure 2.4.  $E_y$  electric field profiles for TE mode slab guide.  $2a=0.9\lambda_0$ ,  $\epsilon'_1=2.07$  and  $\epsilon'_2=1$ . Solid lines show the  $TE_0$  mode and dashed lines show the  $TE_1$ .

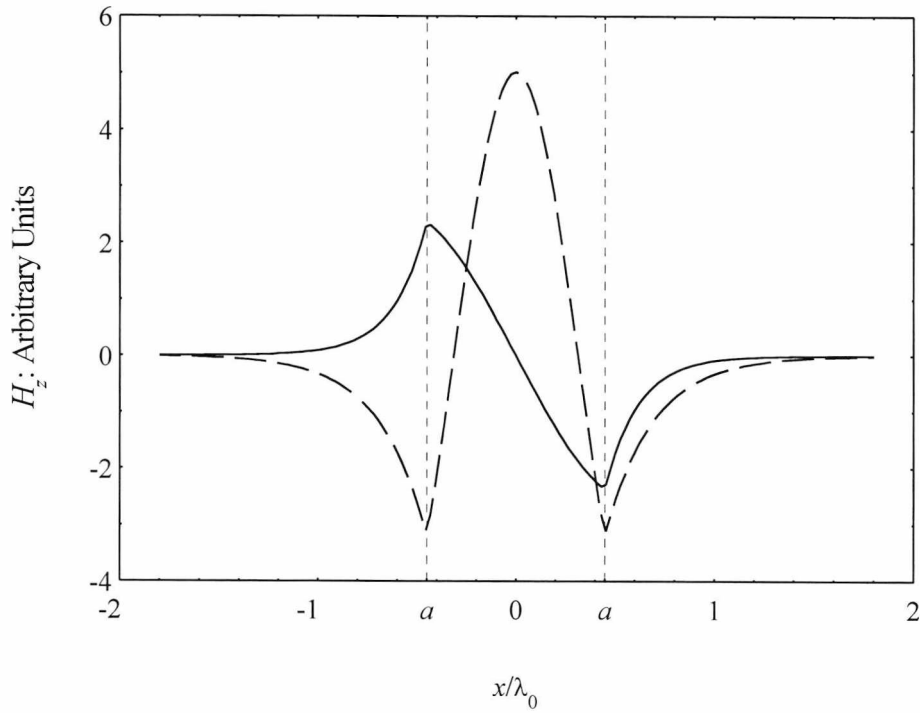


Figure 2.5.  $H_z$  magnetic field profiles for TE mode slab guide.  $2a=0.9\lambda_0$ ,  $\epsilon'_1=2.07$  and  $\epsilon'_2=1$ . Solid lines show the  $TE_0$  mode and dashed lines show the  $TE_1$ .

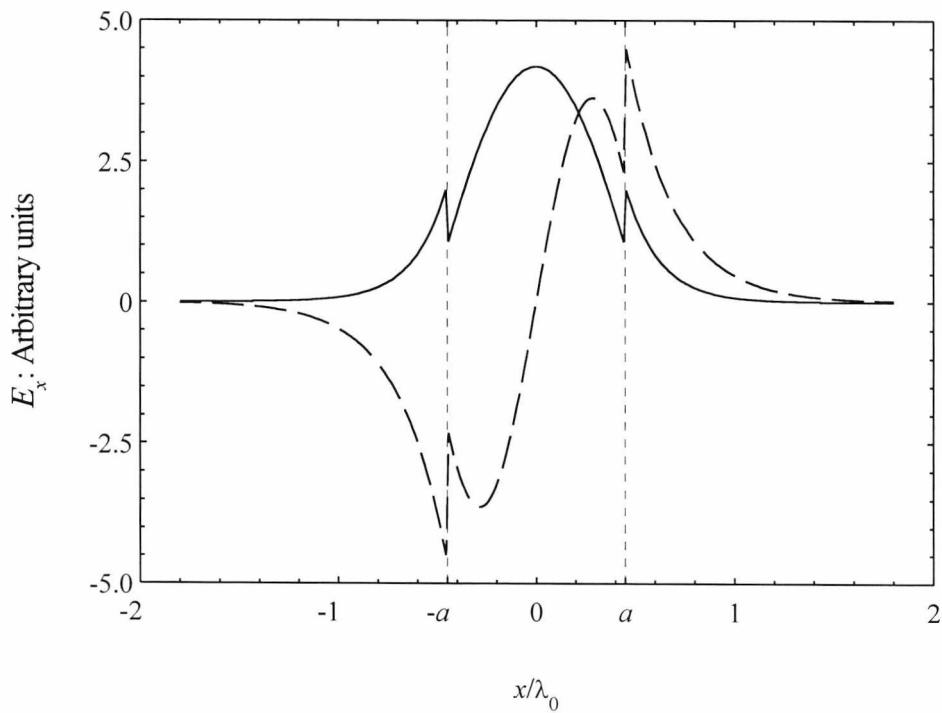


Figure 2.6.  $E_x$  electric field profile for TM mode slab guide.  $2a=0.9\lambda_0$ ,  $\epsilon'_1=2.07$  and  $\epsilon'_2=1$ . Solid lines show the  $TM_0$  mode and dashed lines show the  $TM_1$ .

### 2.2.4 Complex Propagation Constant

In general, the longitudinal propagation constant  $\gamma_z$  is of more importance than  $k'_{x1}$ . We therefore use the dispersion relation in equation (2.26) to obtain

$$\gamma_z = \alpha_z + j\beta_z = \sqrt{(k'_{x1} + jk''_{x1})^2 - k_0^2 \epsilon'_1 (1 - j \tan \delta_1)} \quad (2.80)$$

Ignoring the  $(k''_{x1})^2$  terms and using the binomial expansion to the first order gives

$$\beta_z = \sqrt{\epsilon'_1 k_0^2 - k'^2_{x1}} \quad (2.81)$$

and

$$\alpha_z = \frac{k_0^2 \epsilon'_1 \tan \delta_1 + 2k'_{x1} k''_{x1}}{2\beta_z} \quad (2.82)$$

Figure 2.7 shows plots of the normalised propagation constant  $(\beta_z/k_0)^2$  for both TE and TM mode solutions against normalised guide width  $2a/\lambda_0$ , where  $\lambda_0$  is the free space wavelength. Solid lines show TE solutions, dashed lines show TM solutions. We notice from Figure 2.7 that TM modes have smaller propagation constants than TE modes of the same order and operating frequency. This results in field profiles that are more extensive in the surrounding region and thus, if  $\tan \delta_2 < \tan \delta_1$ , the attenuation constant of the mode will be less. This is readily seen from Figure 2.8 where  $\tan \delta_2 = 0$ . Figure 2.7 and Figure 2.8 use the approximate expressions derived in sections 2.2.1 and 2.2.2 for the solution of  $\gamma_z$ . We therefore compare the approximate values with iterative solutions of equations (2.46) and (2.70).

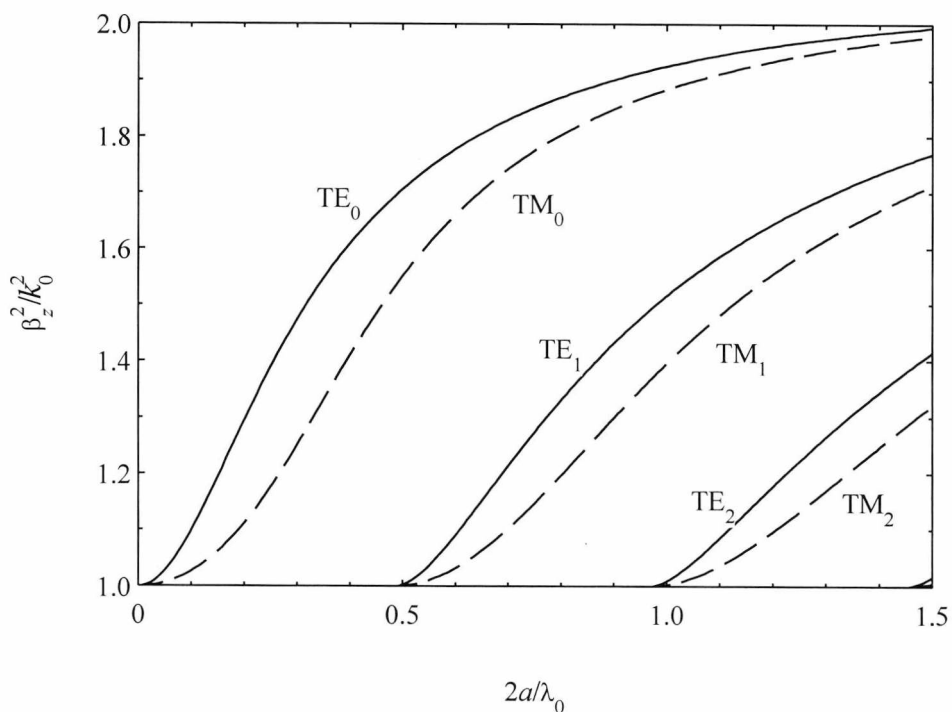


Figure 2.7. Normalised propagation constant for TE (solid lines) and TM (dashed lines) modes against normalised guide width  $2a/\lambda_0$  for  $\epsilon'_1=2.07$ ,  $\tan\delta_1=3\times 10^{-4}$ ,  $\epsilon'_2=1$  and  $\tan\delta_2=0$ .

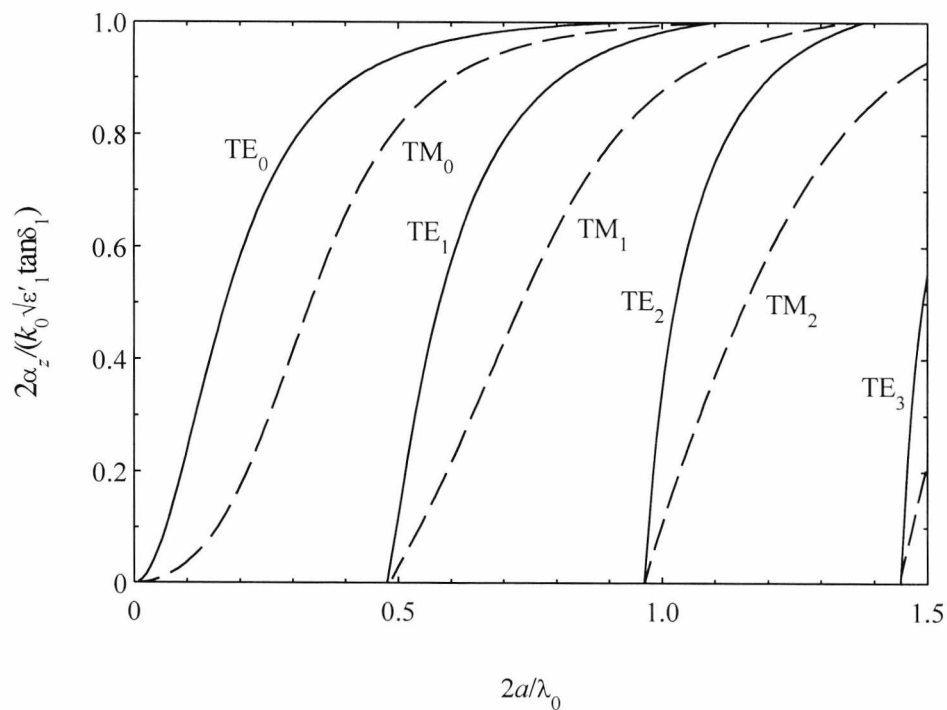


Figure 2.8. Normalised attenuation constant for TE (solid lines) and TM (dashed lines) modes slab waveguide for  $\epsilon'_1=2.07$ ,  $\tan\delta_1=3\times 10^{-4}$ ,  $\epsilon'_2=1$  and  $\tan\delta_2=0$ .

Figure 2.9 and Figure 2.10 show plots of the relative error of the approximate method against  $\tan\delta_1$ , for the real and imaginary parts of  $k_{x1}$ , respectively. In both of the curves the  $TE_0$  mode is shown for guide widths of  $0.8\lambda_0$  and  $0.2\lambda_0$ , with  $\epsilon_1=2.07$ ,  $\epsilon_2=1$  and  $\tan\delta_2=0$ . We see that the error in  $k_{x1}$  for both the real and imaginary parts is less than a few percent, even for waveguides with loss tangents equal to 0.1. Moreover, for guides where the loss tangent is less than 0.001, which is the case for useful low-loss guiding structures, the error is negligible. Figure 2.11 and Figure 2.12 show plots of the relative error for  $TM_0$  mode solutions, where,  $\epsilon_1=2.07$ ,  $\epsilon_2=1$  and  $\tan\delta_2=0$ . Again the error is only a few percent for  $\tan\delta_1=0.1$  and negligible for  $\tan\delta_1=0.001$ .

Due to their infinite geometry, dielectric slab waveguides are only approximations of practical guiding structures. However, by combining the values of several different slab guides, more complicated structures can be analysed. Methods using this approach have several advantages over numerical techniques, namely simplicity and computational ease. Consequently, they are often the chosen approach for the analysis of dielectric waveguides. We therefore consider the effective dielectric constant method in the next section.

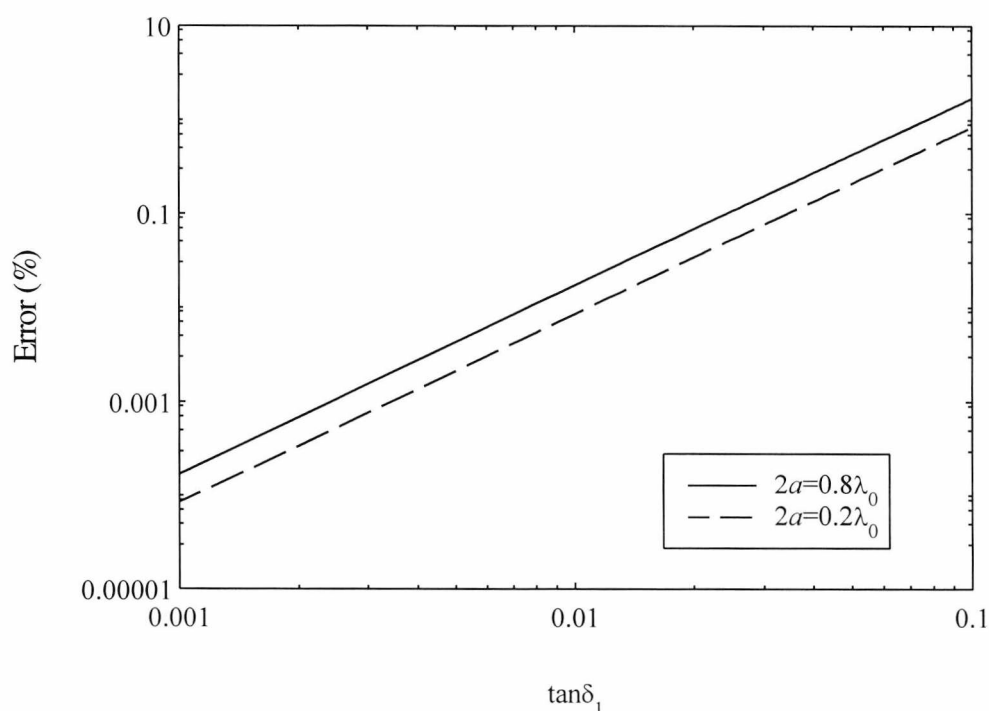


Figure 2.9. Relative error between approximate method and iterative method for the calculation of  $TE_0$  mode  $k''_{x1}$  (imaginary part) with  $\epsilon'_1=2.07$ ,  $\epsilon'_2=1$  and  $\tan\delta_2=0$ .

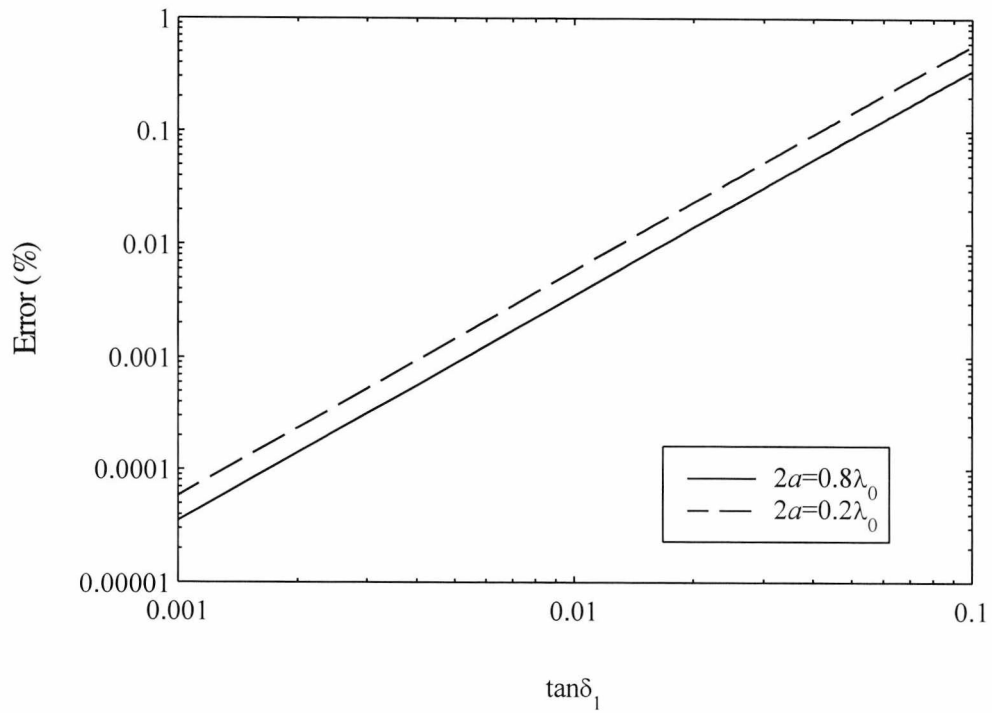


Figure 2.10. Relative error between approximate method and iterative method for the calculation of  $TE_0$  mode  $k'_{x1}$  (real part) with  $\epsilon'_1=2.07$ ,  $\epsilon'_2=1$  and  $\tan\delta_2=0$ .

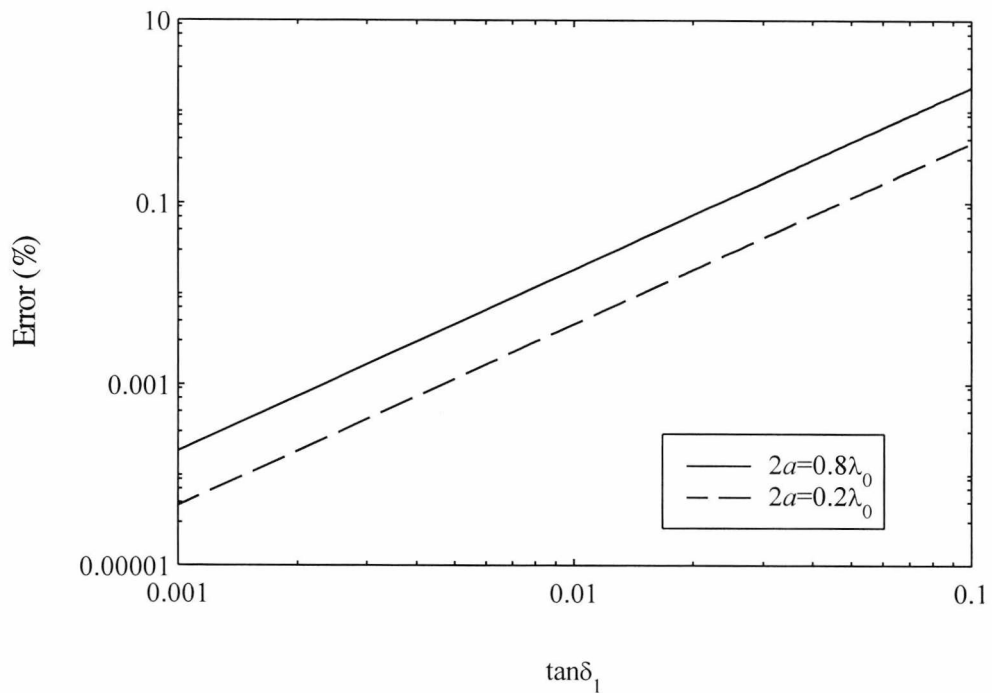


Figure 2.11. Relative error between approximate method and iterative method for the calculation of  $TM_0$  mode  $k''_{x1}$  (imaginary part) with  $\epsilon'_1=2.07$ ,  $\epsilon'_2=1$  and  $\tan\delta_2=0$ .

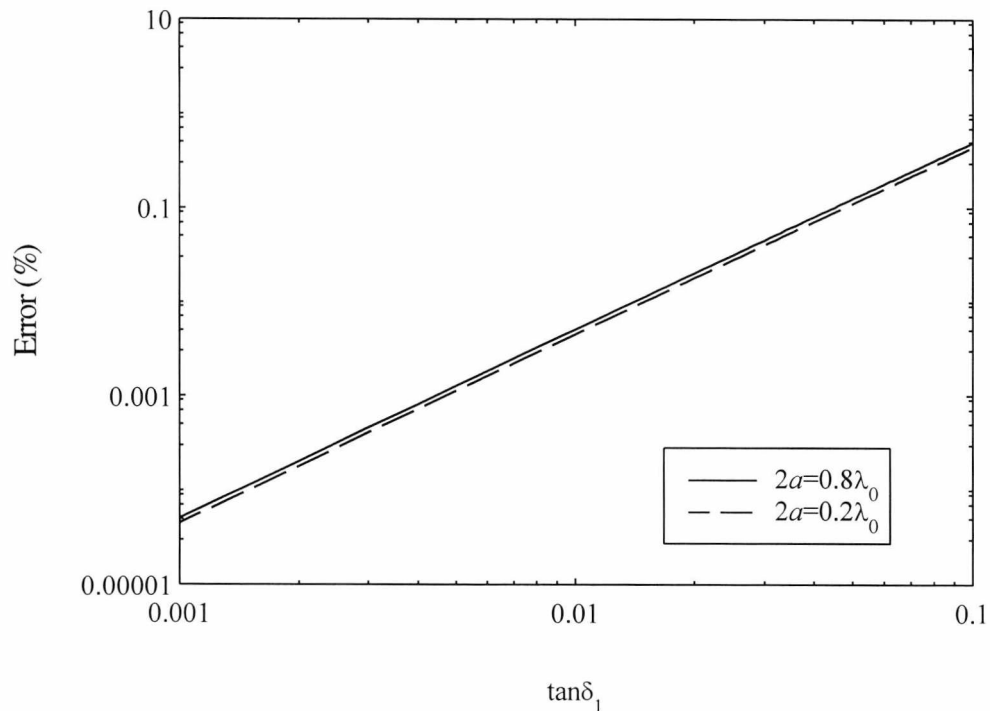


Figure 2.12. Relative error between approximate method and iterative method for the calculation of  $TM_0$  mode  $k'_{x1}$  (real part) with  $\epsilon'_1=2.07$ ,  $\epsilon'_2=1$  and  $\tan\delta_2=0$ .

### 2.3 THE EFFECTIVE DIELECTRIC CONSTANT METHOD

The effective dielectric constant (EDC) method was first introduced in 1972 by Knox and Toullos [3] as a modification to Marcatili's method [1] for the solution of dielectric waveguides with rectangular cross-sections. Since then the method has been applied to many different dielectric guiding structures including optical fibres [13, 14], nonlinear waveguides [15], composite structures [16] and trapped image guides [17]. Theoretical understandings of the method were given by Peng and Oliner [18, 19]. They showed that the EDC method was a lowest order formulation of their mode-matching technique. By considering the scalar modes, Kumar et al. [20] derived a structure that the EDC method actually solves. More recently, Chiang [14] showed that the EDC method solves the reduced vector wave equation. Moreover, by using standard perturbation theory and expanding the fields in asymptotic form Chiang [21] analysed the inherent errors of the EDC method and added a modification to achieve better accuracy. Further analysis resulted in the dual effective-index method (DEIM) [22].

For completeness, we firstly outline the effective dielectric constant method and then add a simple modification to allow for waveguides with dielectric losses.

### 2.3.1 The EDC Method

Modes on rectangular guides form two classes:  $E^y_{mn}$  modes that have their electric fields predominantly in the  $y$  direction; and  $E^x_{mn}$  modes that have their electric fields predominantly in the  $x$  direction. The subscripts  $m$  and  $n$  denote the number of field maxima in the  $x$  and  $y$  direction, respectively.

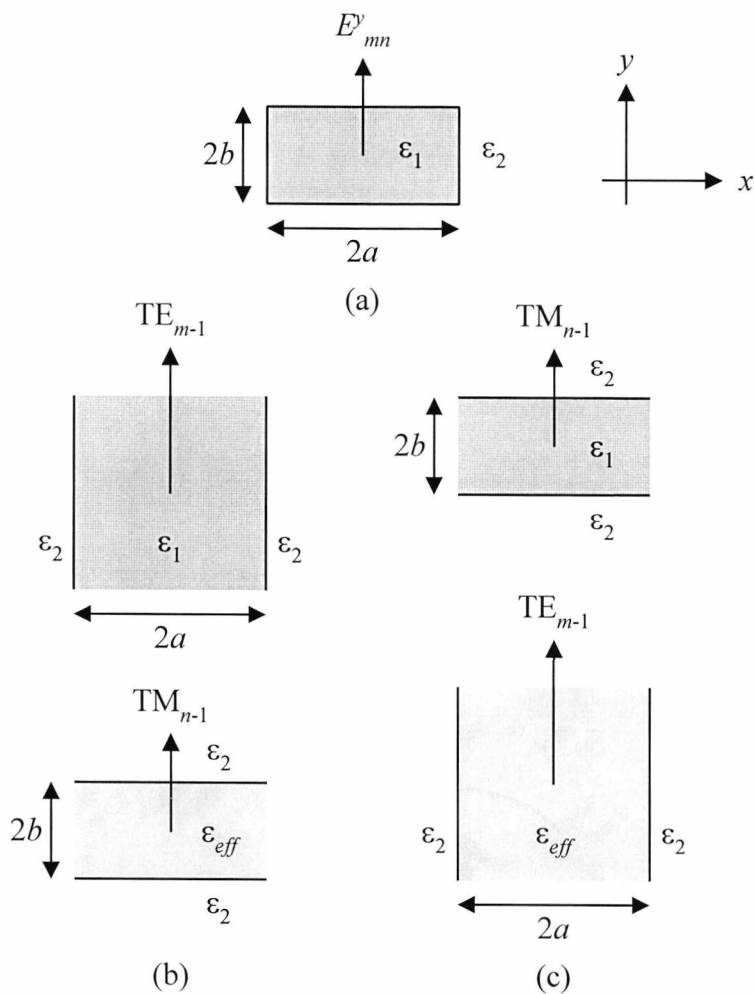


Figure 2.13. The EDC method for  $E^y_{mn}$  modes. (a) Rectangular dielectric waveguide. (b) The  $\beta_{y(2)}$  method. (c) The  $\beta_{y(1)}$  method. Arrows show the direction of the electric field.

To analyse  $E_{mn}^y$  solutions of the structure shown in Figure 2.13(a) we firstly construct a slab waveguide of width  $2b$  and relative permittivity  $\epsilon_1$ , see Figure 2.13(c). The solution of the  $TM_{n-1}$  mode of this structure is then given from equation (2.73) or equation (2.75). For guided modes on lossless structures  $\gamma_z$  will be purely imaginary:  $\gamma_z = j\beta_z$ . Therefore, we can define an effective permittivity for the  $n-1$  mode:

$$\epsilon_{eff} = \frac{\beta_z^2}{k_0^2}. \quad (2.83)$$

The effective permittivity can now be used to construct a second slab waveguide of width  $2a$ , see Figure 2.13(c). The longitudinal propagation constant, denoted by  $\beta_{y(1)}$ , of the  $TE_{m-1}$  mode solution of this structure is then a good approximation of the value for the dielectric waveguide shown in Figure 2.13(a). For simplicity, we express the procedure for the EDC method in the convenient shorthand notation [5]:

$$\beta_{y(1)} = \left[ TM_{m-1}^{2b}(\epsilon_2 | \epsilon_1 | \epsilon_2), TE_{n-1}^{2a}(\epsilon_2 | \epsilon_{eff} | \epsilon_2) \right] \text{ for } E_{mn}^y. \quad (2.84)$$

Of course we could calculate the  $TE_{m-1}$  solution of a slab of width  $2a$  and relative permittivity  $\epsilon_1$  and then, using the effective permittivity, evaluate the  $TM_{n-1}$  solution of a second slab of width  $2b$ , see Figure 2.13(b). We denote this solution by

$$\beta_{y(2)} = \left[ TE_{n-1}^{2a}(\epsilon_2 | \epsilon_1 | \epsilon_2), TM_{m-1}^{2b}(\epsilon_2 | \epsilon_{eff} | \epsilon_2) \right] \text{ for } E_{mn}^y. \quad (2.85)$$

However, it has been shown [22] that better solutions are achieved by evaluating the slab structure with the narrower dimension first – in our case  $2b$ . For  $E_{mn}^x$  solutions a similar procedure is followed but with the polarisation reversed, see Figure 2.14. Again, better solutions are achieved by evaluating the structure with the narrower dimension first. We therefore have

$$\beta_{x(1)} = \left[ TE_{n-1}^{2b}(\epsilon_2 | \epsilon_1 | \epsilon_2), TM_{m-1}^{2a}(\epsilon_2 | \epsilon_{eff} | \epsilon_2) \right] \text{ for } E_{mn}^x \quad (2.86)$$

and

$$\beta_{x(2)} = \left[ TM_{m-1}^{2a}(\epsilon_2 | \epsilon_1 | \epsilon_2), TE_{n-1}^{2b}(\epsilon_2 | \epsilon_{eff} | \epsilon_2) \right] \text{ for } E_{mn}^x. \quad (2.87)$$

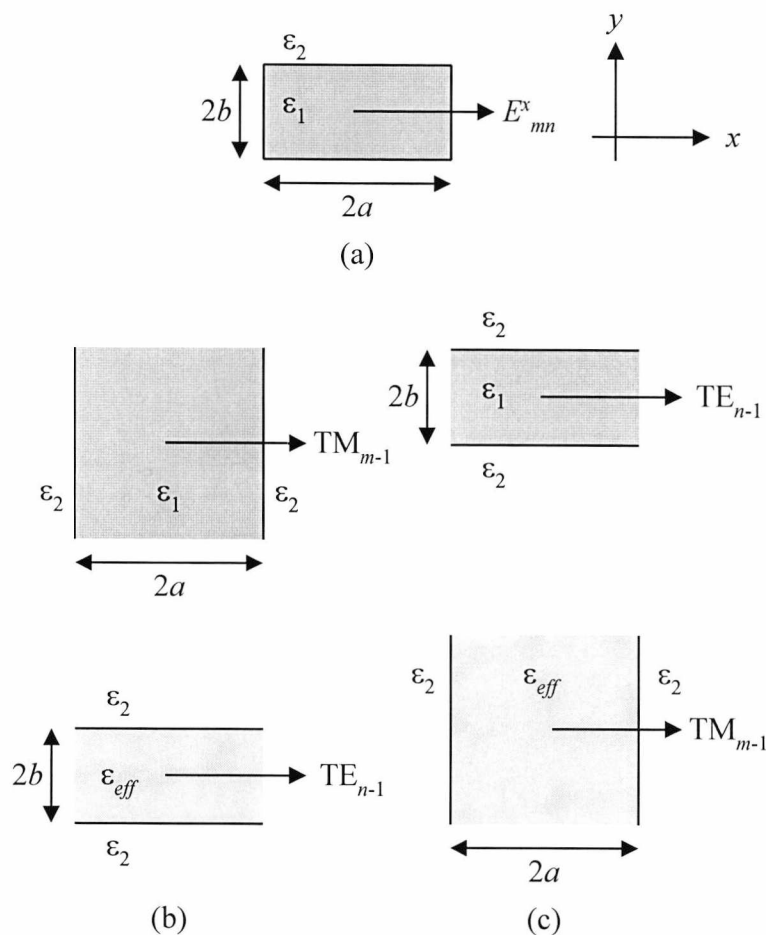


Figure 2.14. The EDC method for  $E^x_{mn}$  modes. (a) Rectangular dielectric waveguide. (b) The  $\beta_{x(2)}$  method. (c) The  $\beta_{x(1)}$  method. Arrows show the direction of the electric field.

### 2.3.2 The EDC Method with Dielectric Losses

In section 2.2 we derived expressions for the attenuation constants of dielectric slab waveguides with complex permittivities. By using these values to define an effective loss tangent, the EDC method can be modified to allow for dielectric losses [12]. For example, to calculate the complex propagation constant  $\gamma_z$  for the  $E^y_{11}$  mode of the rectangular dielectric waveguide shown in Figure 2.15(a), we first calculate the complex transverse propagation constant of the  $TM_0$  mode of a slab guide of width  $2b$  and complex permittivity  $\epsilon'_1(1-j\tan\delta_1)$  from equations (2.73) and (2.74). Thus,

$$k'^2_{y1} \left[ 1 + \frac{\epsilon'^2_2}{\epsilon'^2_1} \tan^2(k'_{y1} b) \right] = k_0^2 (\epsilon'_1 - \epsilon'_2) \tag{2.88}$$

and

$$k''_{y1} = k'_{y1} \frac{\left[ k_0^2 \left( \epsilon'_1 - \frac{\epsilon'_2}{2} \right) - k'^2_{y1} \right] \tan \delta_2 - \left[ k_0^2 \left( \frac{3\epsilon'_1}{2} - \epsilon'_2 \right) - k'^2_{y1} \right] \tan \delta_1}{k_0^2 (\epsilon'_1 - \epsilon'_2) + \left[ k'^2_{y1} \left( \frac{\epsilon'^2_2}{\epsilon'^2_1} - 1 \right) + k_0^2 (\epsilon'_1 - \epsilon'_2) \right] b k'_{y1} \tan(k'_{y1} b)} \quad (2.89)$$

Where in this case we have used  $k_{y1}$  instead of  $k_{x1}$  since the transverse component is now in the  $y$  direction. Since  $k_{y1}$  is complex, we define a complex effective permittivity:

$$\epsilon_{eff} = \epsilon'_{eff} (1 - j \tan \delta_{eff}) = \frac{-\gamma_z^2}{k_0^2} \quad (2.90)$$

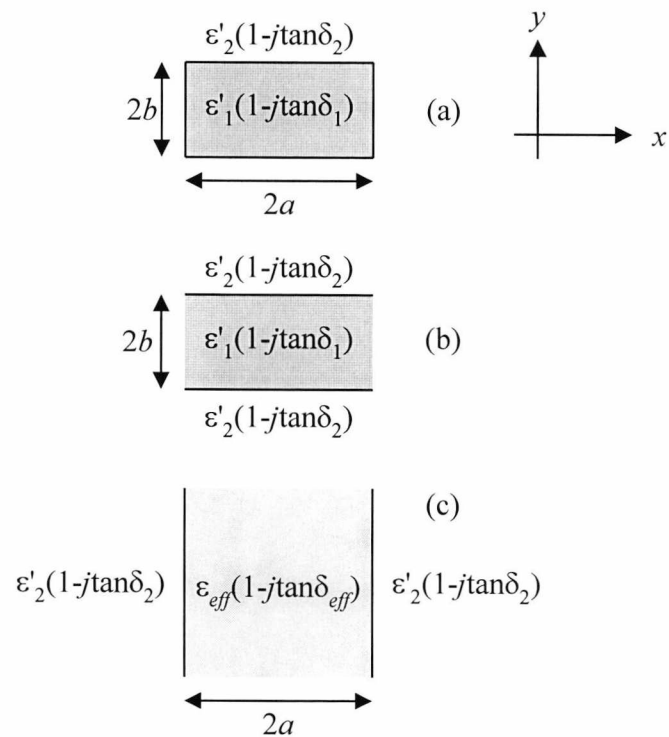


Figure 2.15. The EDC method for waveguides with dielectric losses.

Using equation (2.81) and equation (2.82) and remembering that  $\gamma_z = \alpha_z + j\beta_z$  yields

$$\epsilon'_{eff} = \frac{\epsilon'_1 k_0^2 - k_{y1}'^2}{k_0^2} \quad (2.91)$$

and

$$\tan \delta_{eff} = \frac{k_0^2 \epsilon'_1 \tan \delta_1 + 2k_{y1}' k_{y1}''}{\epsilon'_{eff} k_0^2}. \quad (2.92)$$

We now construct a second slab of width  $2a$  and permittivity  $\epsilon'_{eff}(1-j\tan\delta_{eff})$ , Figure 2.15(c). Using equation (2.53) and (2.56) we obtain

$$k_{x1}'^2 [1 + \tan^2(k'_{x1} a)] = k_0^2 (\epsilon'_{eff} - \epsilon'_2) \quad (2.93)$$

and

$$k_{x1}'' = k_{x1}' \frac{\epsilon'_2 \tan \delta_2 - \epsilon'_{eff} \tan \delta_{eff}}{2(\epsilon'_{eff} - \epsilon'_2) [1 + k'_{x1} a \tan(k'_{x1} a)]}. \quad (2.94)$$

Finally, the complex propagation is given by  $\gamma_{y(1)} = \alpha_{y(1)} + j\beta_{y(1)}$  with

$$\beta_{y(1)} = \sqrt{\epsilon'_{eff} k_0^2 - k_{x1}'^2} \quad (2.95)$$

and

$$\alpha_{y(1)} = \frac{k_0^2 \epsilon'_{eff} \tan \delta_{eff} + 2k_{x1}' k_{x1}''}{2\beta_z}. \quad (2.96)$$

The above procedure outlines the  $\beta_{y(1)}$  method, but equally applies to the  $\beta_{y(2)}$ ,  $\beta_{x(1)}$  and  $\beta_{x(2)}$  methods. The technique is only valid for low-loss materials since the approximate solutions described in section 2.2 have been used. Of course, the exact complex propagation constants for the individual slab guides can be evaluated using

iterative techniques. However, in section 2.2.4 the relative error of the approximate solutions was shown to be negligible for low-loss materials.

### 2.3.3 The Dual Effective-Index Method (DEIM)

Better results are achieved by using the dual effective-index method (DEM). This technique is described elsewhere [22], however a brief overview of the derivation is given below. It can be shown from Maxwell's equations that the vector modes of a rectangular dielectric waveguide satisfy the full vector wave equation:

$$\nabla^2 \mathbf{E}_t + (\epsilon k_0^2 - \beta_z^2) \mathbf{E}_t + \nabla_t \left[ \mathbf{E}_t \frac{\nabla_t(\epsilon)}{\epsilon} \right] = 0, \quad (2.97)$$

where  $\mathbf{E}_t = E_x \hat{\mathbf{x}} + E_y \hat{\mathbf{y}}$ . Therefore,

$$\left( \frac{\partial^2}{\partial x^2} + \frac{\partial^2}{\partial y^2} \right) E_x + (\epsilon k_0^2 - \beta_z^2) E_x + \frac{\partial}{\partial x} \left( \frac{1}{\epsilon} \frac{\partial \epsilon}{\partial x} E_x + \frac{1}{\epsilon} \frac{\partial \epsilon}{\partial y} E_y \right) = 0 \quad (2.98)$$

$$\left( \frac{\partial^2}{\partial x^2} + \frac{\partial^2}{\partial y^2} \right) E_y + (\epsilon k_0^2 - \beta_z^2) E_y + \frac{\partial}{\partial y} \left( \frac{1}{\epsilon} \frac{\partial \epsilon}{\partial x} E_x + \frac{1}{\epsilon} \frac{\partial \epsilon}{\partial y} E_y \right) = 0 \quad (2.99)$$

where  $E_x$ ,  $E_y$  and  $\epsilon$  are all functions of  $x$  and  $y$ . There will be two different forms of solution to equation (2.97).  $E_{mn}^y$  modes where  $E_y$  is dominant and  $E_{mn}^x$  modes where  $E_x$  is dominant. These modes are similar to the TE and TM modes of dielectric slab waveguides.

Here we only consider structures of uniform permittivity and therefore the gradient of  $\epsilon$  is zero in all of the regions. However, at the boundary between the guiding region and the surrounding medium  $\nabla \epsilon$  will be non zero. The effect of the boundary then is to couple the terms in equation (2.97). It has been shown [23] that the field component in the  $y$  direction is of order

$$\Delta = \frac{\sqrt{\varepsilon_1} - \sqrt{\varepsilon_2}}{\sqrt{\varepsilon_1}} \quad (2.100)$$

smaller than the  $x$  component for the  $x$  polarised mode and vice versa for the  $y$  polarised mode. This would suggest that for dielectric waveguides with  $\Delta \ll 1$  the coupling terms in equation (2.97) can be neglected. However, even for larger values of  $\Delta$  the approximation still gives good results. Therefore, we obtain two separate equations for the  $E_{mn}^x$  and  $E_{mn}^y$  modes:

$$\left( \frac{\partial^2}{\partial x^2} + \frac{\partial^2}{\partial y^2} \right) E_x + (\varepsilon k_0^2 - \beta_z^2) E_x + \frac{\partial}{\partial x} \left( \frac{1}{\varepsilon} \frac{\partial \varepsilon}{\partial x} E_x \right) = 0 \quad (2.101)$$

and

$$\left( \frac{\partial^2}{\partial x^2} + \frac{\partial^2}{\partial y^2} \right) E_y + (\varepsilon k_0^2 - \beta_z^2) E_y + \frac{\partial}{\partial y} \left( \frac{1}{\varepsilon} \frac{\partial \varepsilon}{\partial y} E_y \right) = 0, \quad (2.102)$$

respectively, where the electric field is now linearly polarised. The above expressions are the reduced vector wave equations and are the first source of error in the EDC method.

The next step is to assume a variable separable profile. Thus, for the  $E_{mn}^x$  mode we let

$$E_x(x, y) = E_m(x) E_n(y) \quad (2.103)$$

and

$$\varepsilon(x, y) = \varepsilon'(x) + \varepsilon''(y) \quad (2.104)$$

According to the  $\beta_{x(1)}$  EDC method we firstly solve for a slab of width  $2b$ . This is expressed mathematically as

$$\left( \frac{\partial^2}{\partial y^2} \right) E_n(y) + (\varepsilon''(y) k_0^2 - \varepsilon_{eff} k_0^2) E_n(y) = 0 \quad (2.105)$$

with

$$\varepsilon''(y) = \begin{cases} \varepsilon_2 & \text{for } -\infty < y < -b \\ \varepsilon_1 & \text{for } -b \leq y \leq b \\ \varepsilon_2 & \text{for } b < y < \infty \end{cases} \quad (2.106)$$

Substituting equation (2.103) and (2.104) into (2.101) and subtracting equation (2.105) from the result yields

$$\frac{d^2 E_m(x)}{dx^2} + (\varepsilon'(x)k_0^2 + \varepsilon_{eff}k_0^2 - \beta_{x(1)}^2)E_m(x) + \frac{d}{dx} \left[ \frac{E_m(x)}{\varepsilon'(x) + \varepsilon_{eff}} \frac{d}{dx} (\varepsilon'(x) + \varepsilon_{eff}) \right] = 0 \quad (2.107)$$

Thus, following the method of the EDC technique, we require

$$\varepsilon'(x) = \begin{cases} \varepsilon_2 - \varepsilon_{eff} & \text{for } -\infty < y < -b \\ 0 & \text{for } -b \leq y \leq b \\ \varepsilon_2 - \varepsilon_{eff} & \text{for } b < y < \infty \end{cases} \quad (2.108)$$

Therefore, the actual profile that the EDC method analyses is shown in Figure 2.16. This is the second source of error in the EDC technique.

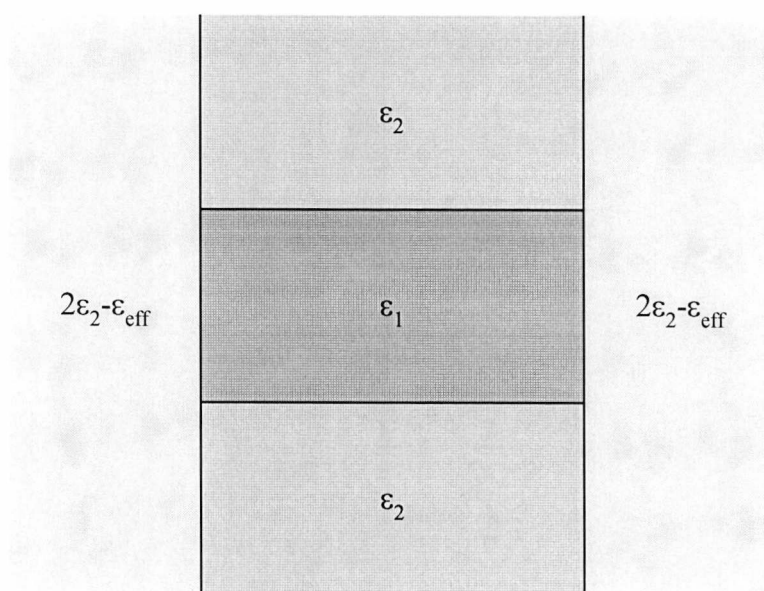


Figure 2.16. Actual structure the EDC method analyses for  $E_{mn}^x$  modes.

By allowing the normalised frequency to approach infinity, Chiang used asymptotic field expansions in standard perturbation formulas to analyse the error associated with the above approximations. By eliminating the errors, the DEIM is obtained [22]:

$$(\beta_z^x)^2 = \frac{(R^2\beta_{x(1)}^2 - \beta_{x(2)}^2) + R(\beta_{y(1)}^2 - \beta_{y(2)}^2)}{R^2 - 1} \quad \text{for } E_{mn}^x \quad (2.109)$$

and

$$(\beta_z^y)^2 = \frac{(R^2\beta_{y(1)}^2 - \beta_{y(2)}^2) + R(\beta_{x(1)}^2 - \beta_{x(2)}^2)}{R^2 - 1} \quad \text{for } E_{mn}^y \quad (2.110)$$

where  $R = a/b$ . We see that now the propagation constants are given by combining the four different techniques of applying the EDC method.

### 2.3.4 The DEIM with losses

By substituting  $\alpha_{x(1)} + j\beta_{x(1)}$  for  $\beta_{x(1)}$ ,  $\alpha_{y(1)} + j\beta_{y(1)}$  for  $\beta_{y(1)}$ , etc, into equations (2.109) and (2.110) we obtain, for small losses [24],

$$\beta_z^x = \sqrt{\frac{(R^2\beta_{x(1)}^2 - \beta_{x(2)}^2) + R(\beta_{y(1)}^2 - \beta_{y(2)}^2)}{R^2 - 1}} \quad (2.111)$$

$$\alpha_z^x = \frac{(R^2\beta_{x(1)}\alpha_{x(1)} - \beta_{x(2)}\alpha_{x(2)}) + R(\beta_{y(1)}\alpha_{y(1)} - \beta_{y(2)}\alpha_{y(2)})}{(R^2 - 1)\beta_z^x} \quad (2.112)$$

for  $E_{mn}^x$  solutions and

$$\beta_z^y = \sqrt{\frac{(R^2\beta_{y(1)}^2 - \beta_{y(2)}^2) + R(\beta_{x(1)}^2 - \beta_{x(2)}^2)}{R^2 - 1}} \quad (2.113)$$

$$\alpha_z^y = \frac{(R^2\beta_{y(1)}\alpha_{y(1)} - \beta_{y(2)}\alpha_{y(2)}) + R(\beta_{x(1)}\alpha_{x(1)} - \beta_{x(2)}\alpha_{x(2)})}{(R^2 - 1)\beta_z^y} \quad (2.114)$$

for  $E_{mn}^y$  solutions. This is a justifiable step, since the asymptotic field profiles used in [22] to obtain equation (2.109) and (2.110) will not be significantly changed if small dielectric losses are introduced. Thus, equations (2.112) and (2.114) are valid expressions. At first sight, the above equations for the attenuation constants seem complicated, since both the propagation and attenuation constants of the four slab waveguides are required. However, when we remember that  $\alpha_{y(1)}$ ,  $\alpha_{y(2)}$ ,  $\alpha_{x(1)}$  and  $\alpha_{x(2)}$  are given directly from the lossless propagation constants we see that only a small amount of additional computation is required to allow for dielectric losses.

Figure 2.17 and Figure 2.18 show curves of the attenuation constant for  $E_{11}^y$  and  $E_{11}^x$  modes using the conventional EDC method ( $\beta_{y(1)}$  and  $\beta_{x(1)}$ ) and the DEIM, respectively. In each case the waveguide has the following parameters:  $2a=7.112\text{mm}$ ,  $2b=3.556\text{mm}$ ,  $\epsilon_2=1$  and  $\epsilon_1=2.07(1-j3\times 10^{-4})$ . For comparison, the curves are compared with finite element results using Hewlett Packard's HFSS software. As can be seen, both methods are in excellent agreement for the higher frequency range where the fields are more confined. However, the DEIM gives significantly better results for the lower frequency range where the fields are less confined to the dielectric. For completeness the propagation constant using both methods is compared with finite element results, see Figure 2.19. Again, the DEIM results are in good agreement with HFSS values. Further results can be found in [12].

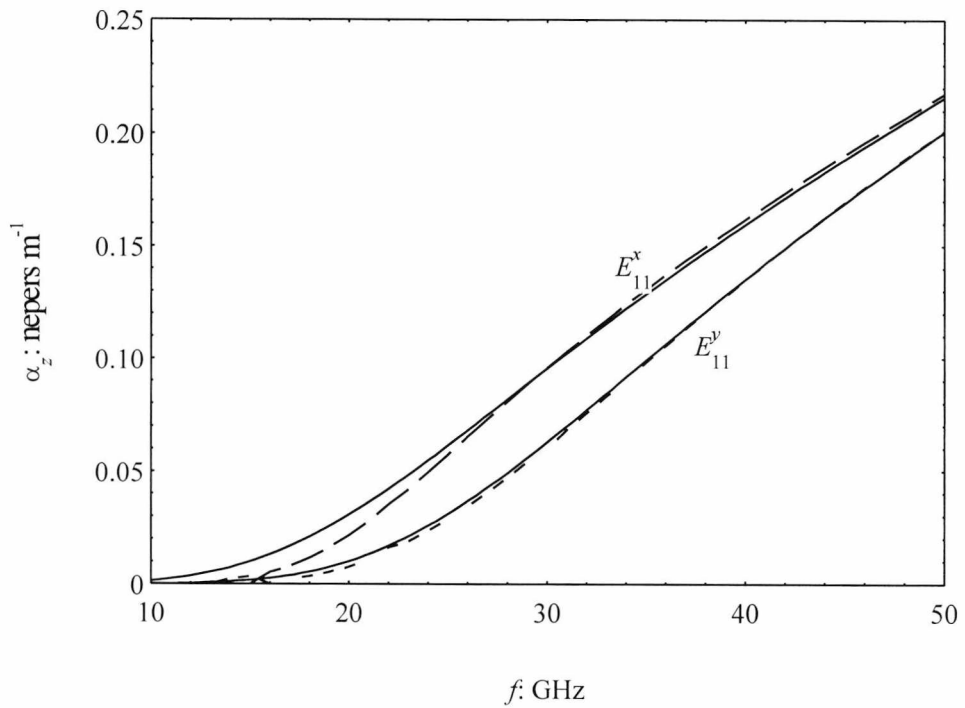


Figure 2.17 Attenuation constant using the conventional EDC method ( $\beta_{y(1)}$  and  $\beta_{x(1)}$ ) for dielectric waveguide with  $2a=7.112$ ,  $2b=3.556$ ,  $\epsilon_2=1$  and  $\epsilon_1=2.07(1-j3\times 10^{-4})$ . Solid lines show EDC method, dashed lines show HFSS finite element results.

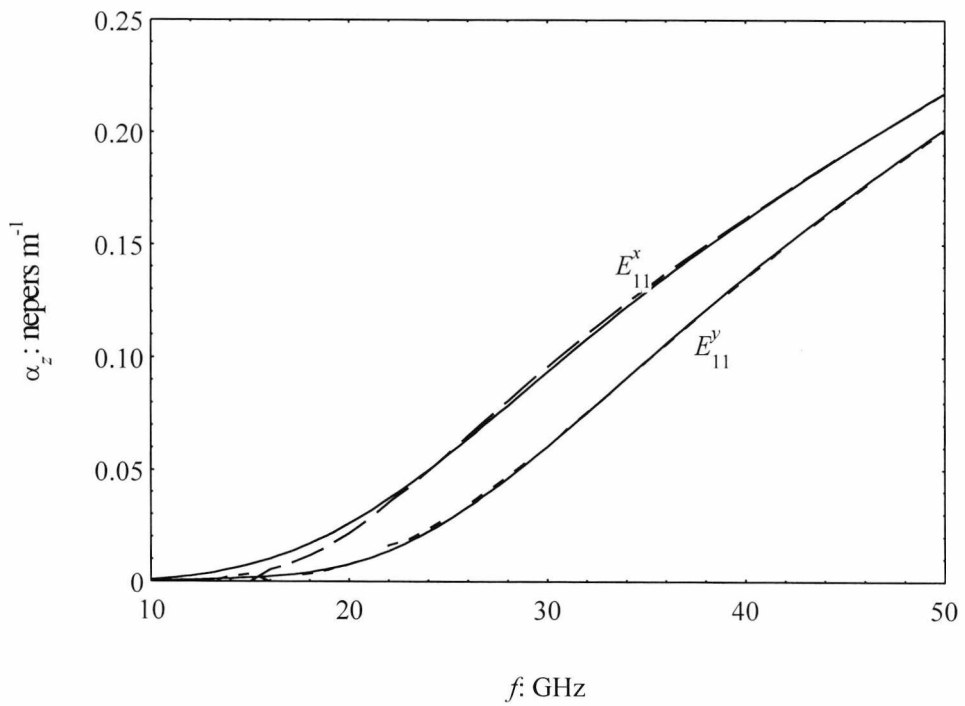


Figure 2.18. Attenuation constant using the DEIM with losses for dielectric waveguide with  $2a=7.112$ ,  $2b=3.556$ ,  $\epsilon_2=1$  and  $\epsilon_1=2.07(1-j3\times 10^{-4})$ . Solid lines show DEIM, dashed lines show HFSS finite element results.

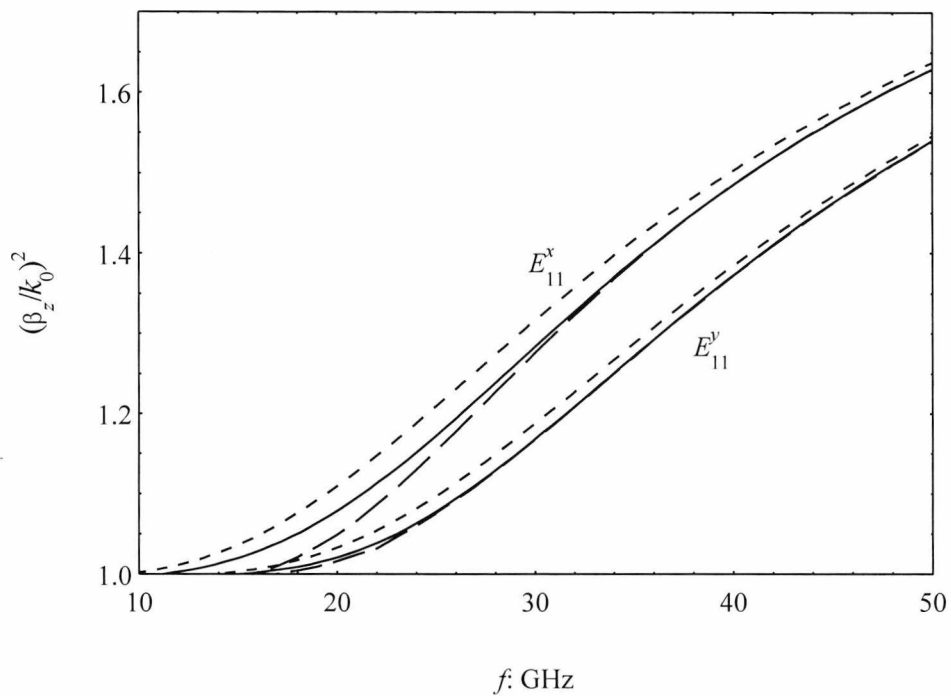


Figure 2.19. Propagation constant using conventional EDC method (dotted lines), DEIM (solid lines) and HFSS finite element (dashed lines) for  $2a=7.112$ ,  $2b=3.556$ ,  $\epsilon_2=1$  and  $\epsilon_1=2.07(1-j3\times 10^{-4})$ .

## 2.4 SUMMARY

In summary, approximate expressions for the attenuation constant  $\alpha_z$  of both TE and TM slab waveguides have been presented. The problem was greatly simplified by converting the coupled transcendental guidance equations into a single transcendental equation, and an expression linking  $\alpha_z$  directly to the lossless  $\beta_z$  and the waveguide parameters. Moreover, the expressions apply to structures where both the guiding and surrounding regions have dielectric losses. By introducing an effective loss tangent the approximate expressions were applied to the effective dielectric constant (EDC) method and the dual effective-index method (DEIM) and were shown to be in good agreement with HFSS finite element simulations. Furthermore, very little additional computation is required to calculate  $\alpha_z$  since the attenuation constants are given directly from the lossless solutions. Therefore, the well-established EDC method is easily complemented with the present expressions to allow for the calculation of  $\alpha_z$  at millimetre-wave frequencies where the attenuation cannot be neglected.

---

**REFERENCES**

- 1 E. A. J. Marcatili, "Dielectric rectangular waveguide and directional coupled for integrated optics," *Bell Syst. Tech. J.*, vol. 48, 1969, pp. 2071-2102.
- 2 J. E. Goell, "A circular-harmonic computer analysis of rectangular dielectric waveguides," *Bell Syst. Tech. J.*, vol. 48, 1969, pp. 2133-2160.
- 3 R. M. Knox and P. P. Toullos, "Integrated circuits for the millimeter through optical frequency range," *Proc. Symp. Submillimeter Waves* (Polytechnic Press, Brooklyn), 1970, pp. 497-516.
- 4 S. M. Saad, "Review of numerical methods for the analysis of arbitrarily-shaped microwave and optical dielectric waveguides," *IEEE Trans. Microwave Theory Tech.*, vol. MTT-33, No. 10, 1985, pp. 894-899.
- 5 K. S. Chiang, "Dual effective-index method for the analysis of rectangular waveguides," *Appl. Opt.*, vol. 25, no. 13, July 1986, pp. 2169-2174.
- 6 A. von Hippel, "Dielectrics and Waves," *Artech House*, 1954.
- 7 N. S. Kapany & J. J. Burke, "Optical Waveguides," *Academic Press*, Chapter 1, 1972.
- 8 D. Marcuse, "Theory of dielectric optical waveguides," *Academic Press*, Chapter 1, 1974.
- 9 G. Owyang, "Foundations of optical waveguides," *Edward Arnold*, Chapter 2, 1981.

- 
- 10 D. Lee, "Electromagnetic principles of integrated optics," *John Wiley & Sons*, Chapter 4, 1986.
  - 11 M. Tsuji, K. Kawai, H Shigesawa & K Takiyama, "Submillimeter Guided-Wave Experiments with Polyethylene Slab Waveguides," *IEEE Trans. Microwave Theory Tech.*, vol. MTT-27, Nov. 1979, pp. 873-878.
  - 12 P. R. Young and R. J. Collier, "Extension to the effective-index method to include the calculation of losses in dielectric waveguides," *Electron. Lett.*, vol. 33, No. 13, June 1997, pp. 1151-1152.
  - 13 K. S. Chiang, "Analysis of optical fibres by the effective-index method," *Appl. Opt.*, Vol. 25, 1986, pp. 348-354.
  - 14 K. S. Chiang, "Geometric birefringence in a class of step-index fiber," *J. Lightwave Technol.*, vol. LT-5, No. 6, June 1987, pp. 737-744.
  - 15 K. S. Chiang and R. A. Sammut, "Effective-index method for spatial solitons in planar waveguides with Kerr-type nonlinearity," *J. Opt. Soc. Am. B*, vol. 10, 1993, pp. 704-708.
  - 16 K. S. Chiang, "Effective-index method for the analysis of optical waveguide couplers and arrays: An asymptotic theory," *J. Lightwave Technol.*, vol. 9, No. 1, January 1991, pp. 62-72.
  - 17 W. B. Zhou and T Itoh, "Analysis of trapped image guides using effective dielectric constant and surface impedances," *IEEE Trans. Microwave Theory Tech.*, vol. MTT-30, no. 12, December 1982, pp. 2163-2166.
  - 18 S. T. Peng and A. A. Oliner, "Guidance and leakage properties of a class of open dielectric waveguides: Part I – Mathematical formulations," *IEEE Trans. Microwave Theory Tech.*, vol. MTT-29, No. 9, September 1981, pp. 843-854.

- 
- 19 S. T. Peng and A. A. Oliner, "Guidance and leakage properties of a class of open dielectric waveguides: Part II – New physical effects," *IEEE Trans. Microwave Theory Tech.*, vol. MTT-29, No. 9, September 1981, pp. 855-869.
  - 20 A. Kumur, D. F. Clark and B Culshaw, "Explanation of errors inherent in the effective-index method for analyzing rectangular-core waveguides," *Opt. Lett.*, vol. 13, 1988, pp. 1129-1131.
  - 21 K. S. Chiang, "Performance of the effective-index method for the analysis of dielectric waveguides," *Opt. Lett.*, vol. 16, no. 10, May 15, 1991, pp. 714-716.
  - 22 K. S. Chiang, " Analysis of the effective-index method for the vector modes of rectangular-core dielectric waveguides," *IEEE Trans. Microwave Theory Tech.*, vol. 44, no. 5, May 1996,pp. 692-700.
  - 23 A. W. Snyder and J. D. Love, "Optical Waveguide Theory," *Chapman and Hall*, 1983.
  - 24 P. R. Young and R. J. Collier, "Solution of lossy dielectric waveguides using the dual effective-index method," *Electron. Lett.*, vol. 33, No. 21, October 1997, pp. 1788-1789.

---

### 3. PROPAGATION CHARACTERISTICS OF COUPLED DIELECTRIC WAVEGUIDES

---

Composite structures are used extensively in dielectric waveguide components such as directional couplers [1, 2, 3], filters [4, 5, 6] and, as we shall see in Chapter 6, phase shifters [7], variable attenuators [8] and wavemeters [9]. For each of these components, accurate values for the modal propagation constants are required. In general, solutions of coupled structures are obtained using coupled mode theories [10, 11, 12]. The coupled mode is approximated by a weighted sum of the modes that exist on the isolated structures. However, these methods are only valid for large separations or well-confined modes [13, Appendix A]. Furthermore, the coupled mode theory does not work well for asymmetrical guides [13, Appendix A]. Marcuse [14] presented an exact technique for the solution of compound slab waveguides with width and permittivity asymmetry. Unfortunately, his method is cumbersome, requiring numerical techniques to find the eigenvalue of a  $8 \times 8$  determinant. Exact transcendental characteristic equations have been presented for symmetrical coupled slabs [15, 16] and coupled slabs with width asymmetry [17]. However, no expression has been obtained for the general case.

In this section, we derive an exact transcendental characteristic equation for the general asymmetrical coupled slab waveguide with dielectric losses. Approximate solutions for the attenuation constant of symmetrical coupled guides are then obtained. Using these expressions in the EDC method together with the concept of an effective loss tangent, we calculate the complex propagation constants of lossy coupled rectangular dielectric waveguides. Finite element simulations are then compared with the EDC results.

### 3.1 ASYMMETRICAL COUPLED SLAB WAVEGUIDES

Consider two parallel slab waveguides,  $A$  and  $B$ , with thicknesses  $2a$  and  $2b$ , respectively (Figure 3.1). Guide  $A$  occupies the region  $-(D+2a) < x < -D$  and has a relative permittivity  $\epsilon_a$ . Guide  $B$  occupies the region  $D < x < (D+2b)$  and has a relative permittivity  $\epsilon_b$ . The regions outside the waveguides defined by  $x < -(D+2a)$  and  $x > (D+2b)$  both have a relative permittivity  $\epsilon_2$ . The middle region, between the two guides, is defined by  $-D < x < D$  and also has a relative permittivity  $\epsilon_2$ . All five regions have permeability  $\mu_0$ . We make the same assumptions as in section 2.2, therefore we have two possible mode polarisations

$$\text{TE: } \frac{d^2}{dx^2} E_y(x) + k_x^2 E_y(x) = 0 \quad (3.1)$$

$$\text{TM: } \frac{d^2}{dx^2} H_y(x) + k_x^2 H_y(x) = 0 \quad (3.2)$$

where

$$\begin{aligned} k_x^2 = -\alpha_{x2}^2 = \gamma_z^2 - \gamma_2^2 & \quad \text{for } x < -(2a + D), \ x < |D| \text{ and } x > (2b + D), \\ k_x^2 = k_{xa}^2 = \gamma_z^2 - \gamma_a^2 & \quad \text{for } -(2a + D) < x < -D, \\ k_x^2 = k_{xb}^2 = \gamma_z^2 - \gamma_b^2 & \quad \text{for } D < x < (2b + D). \end{aligned} \quad (3.3)$$

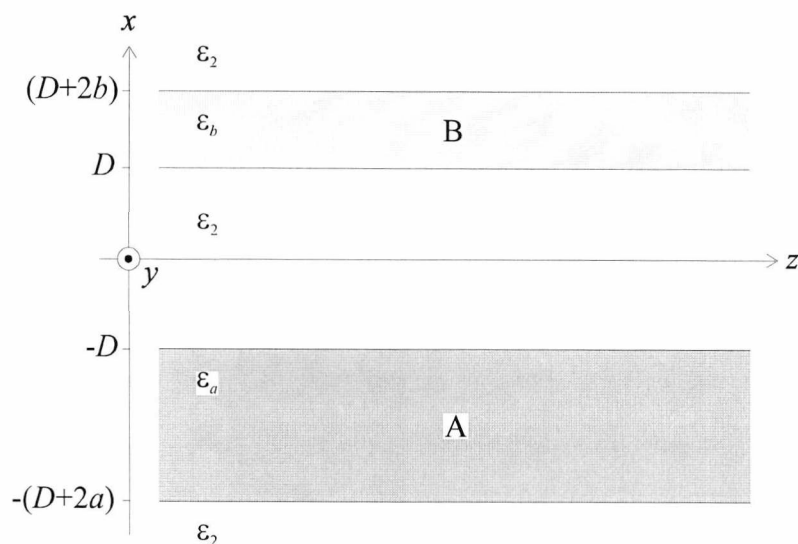


Figure 3.1. Geometry of two parallel dielectric slab waveguides.

Clearly the above expressions are normally complex, however, for the meantime, we assume that the dielectric losses are zero. Then

$$\alpha_{x2} = \sqrt{\beta_z^2 - \epsilon_2 k_0^2} \quad (3.4)$$

$$k_{xa} = \sqrt{\epsilon_a k_0^2 - \beta_z^2} \quad (3.5)$$

$$k_{xb} = \sqrt{\epsilon_b k_0^2 - \beta_z^2}. \quad (3.6)$$

### 3.1.1 TE Mode Solutions

For simplicity, we first consider TE mode solutions of equation (3.1). We therefore choose the following functions for  $E_y(x)$  over the five regions:

$$E_y(x) = E_1 e^{\alpha_{x2}[x+(D+2a)]} \quad \text{for } x < -(D+2a), \quad (3.7)$$

$$E_y(x) = E_2 \cos\{k_{xa}[x+(D+2a)] - \phi_a\} \quad \text{for } -(D+2a) < x < -D, \quad (3.8)$$

$$E_y(x) = E_3 \cosh[\alpha_{x2}x] + E_4 \sinh[\alpha_{x2}x] \quad \text{for } -D < x < D, \quad (3.9)$$

$$E_y(x) = E_5 \cos\{k_{xb}[x-D] - \phi_b\} \quad \text{for } D < x < (D+2b), \quad (3.10)$$

$$E_y(x) = E_6 e^{-\alpha_{x2}[x-(2b+D)]} \quad \text{for } x > (D+2b), \quad (3.11)$$

where  $E_1 \dots E_6$  are amplitude constants and  $\phi_a$  and  $\phi_b$  are constant phase terms. It should be noted that if  $\epsilon_a > \epsilon_b$  then  $k_{xb}$  can become imaginary, similarly if  $\epsilon_b > \epsilon_a$  then  $k_{xa}$  can become imaginary. If either  $k_{xa}$  or  $k_{xb}$  becomes imaginary, the transverse field

variation in the respective waveguide will become a hyperbolic function similar to that in the middle region. This effect is discussed in more detail in section 3.2.

Substituting  $E_y(x)$  into equation (2.15) yields:

$$H_z(x) = \frac{j\alpha}{\omega\mu_o} E_1 e^{\alpha_{x2}[x+(D+2a)]} \quad \text{for } x < -(D+2a), \quad (3.12)$$

$$H_z(x) = -\frac{jk_{xa}}{\omega\mu_o} E_2 \sin\{k_{xa}[x+(D+2a)] - \phi_a\} \quad \text{for } -(D+2a) < x < -D, \quad (3.13)$$

$$H_z(x) = \frac{j\alpha_{x2}}{\omega\mu_o} E_3 \sinh[\alpha_{x2}x] + \frac{j\alpha_{x2}}{\omega\mu_o} E_4 \cosh[\alpha_{x2}x] \quad \text{for } -D < x < D, \quad (3.14)$$

$$H_z(x) = -\frac{jk_{xb}}{\omega\mu_o} E_5 \sin\{k_{xb}[x-D] - \phi_b\} \quad \text{for } D < x < (D+2b), \quad (3.15)$$

$$H_z(x) = -\frac{j\alpha_{x2}}{\omega\mu_o} E_6 e^{-\alpha_{x2}[x-(2b+D)]} \quad \text{for } x > (D+2b). \quad (3.16)$$

From equation (2.14) we see that  $H_x$  is proportional to  $E_y$  and therefore carries no additional information. We require  $E_y(x)$  and  $H_z(x)$  to be continuous, hence dividing  $E_y(x)$  by  $H_z(x)$  at the four boundaries gives:

$$\alpha_{x2} = k_{xa} \tan(\phi_a) \quad \text{for } x = -(D+2a), \quad (3.17)$$

$$k_{xa} \tan(2k_{xa}a - \phi_a) = \alpha_{x2} \frac{E_3 \sinh(\alpha_{x2}D) - E_4 \cosh(\alpha_{x2}D)}{E_3 \cosh(\alpha_{x2}D) - E_4 \sinh(\alpha_{x2}D)} \quad \text{for } x = -D, \quad (3.18)$$

$$k_{xb} \tan(\phi_b) = \alpha_{x2} \frac{E_3 \sinh(\alpha_{x2}D) + E_4 \cosh(\alpha_{x2}D)}{E_3 \cosh(\alpha_{x2}D) + E_4 \sinh(\alpha_{x2}D)} \quad \text{for } x = D, \quad (3.19)$$

$$\alpha_{x_2} = k_{xb} \tan(2k_{xb}b - \phi_b) \quad \text{for } x = (2b + D). \quad (3.20)$$

Combining equation (3.17) with (3.18) yields

$$\frac{\tan(2k_{xa}a - \phi_a)}{\tan(\phi_a)} = \frac{E_3 \sinh(\alpha_{x_2}D) - E_4 \cosh(\alpha_{x_2}D)}{E_3 \cosh(\alpha_{x_2}D) - E_4 \sinh(\alpha_{x_2}D)}, \quad (3.21)$$

and equation (3.19) with (3.20)

$$\frac{\tan(\phi_b)}{\tan(2k_{xb}b - \phi_b)} = \frac{E_3 \sinh(\alpha_{x_2}D) + E_4 \cosh(\alpha_{x_2}D)}{E_3 \cosh(\alpha_{x_2}D) + E_4 \sinh(\alpha_{x_2}D)}. \quad (3.22)$$

On elimination of  $E_3$  and  $E_4$  from the above two equations we find that

$$\frac{T_b \cosh(\alpha_{x_2}D) - \sinh(\alpha_{x_2}D)}{T_a \cosh(\alpha_{x_2}D) - \sinh(\alpha_{x_2}D)} = \frac{\cosh(\alpha_{x_2}D) - T_b \sinh(\alpha_{x_2}D)}{T_a \sinh(\alpha_{x_2}D) - \cosh(\alpha_{x_2}D)} \quad (3.23)$$

$$\text{where } T_a = \frac{\tan(2k_{xa}a - \phi_a)}{\tan(\phi_a)} \quad \text{and} \quad T_b = \frac{\tan(\phi_b)}{\tan(2k_{xb}b - \phi_b)}.$$

After rearranging equation (3.23) we eventually obtain

$$\tanh(2\alpha_{x_2}D) = \frac{T_a + T_b}{T_a T_b + 1}. \quad (3.24)$$

Solving for  $2D$  finally gives the guidance condition:

$$2D = \frac{1}{2\alpha_{x_2}} \ln \left[ \frac{\sin(2k_{xa}a) \sin(2k_{xb}b)}{\sin(2\phi_a - 2k_{xa}a) \sin(2k_{xb}b - 2\phi_b)} \right]. \quad (3.25)$$

Where from equation (3.17)

$$\phi_a = \tan^{-1} \left( \frac{\alpha_{x2}}{k_{xa}} \right) \quad (3.26)$$

and from (3.20)

$$\phi_b = 2k_{xb}b - \tan^{-1} \left( \frac{\alpha_{x2}}{k_{xb}} \right). \quad (3.27)$$

We see from equation (3.4), and equations (3.5) and (3.6) that  $\alpha_{x2}$ ,  $k_{xa}$  and  $k_{xb}$  are all functions of  $\beta_z$ . Thus, the right hand side of equation (3.25) is a function of a single variable - the longitudinal propagation constant  $\beta_z$ . Therefore if  $a$ ,  $b$ ,  $D$ ,  $\epsilon_a$ , and  $\epsilon_b$  are specified, we can solve equation (3.25) for all possible solutions of  $\beta_z$ .

### 3.1.2 Symmetrical Coupled Slab Waveguides

If the guides are identical then  $k_{xa} = k_{xb}$  and thus from equations (3.26) and (3.27) we see that  $\phi_b = 2k_{xa}a - \phi_a$ . Accordingly, equation (3.25) becomes

$$2D = \frac{1}{\alpha_{x2}} \ln \left| \frac{\sin(2k_{xa}a)}{\sin(2\phi_a - 2k_{xa}a)} \right| \quad (3.28)$$

which is identical to [15, 16].

If the guides are different, the argument of the ln function on the right-hand side of equation (3.25) can become negative. This would imply that the distance  $2D$  could be complex, which obviously has no physical meaning. Furthermore, if the argument of the ln function is less than unity, the right-hand side of equation (3.25) will be negative, again implying a complex distance. We therefore consider only positive

purely real values for the right-hand side of equation (3.25). As mentioned previously, either  $k_{xa}$  or  $k_{xb}$  can become imaginary, resulting in either  $\phi_a$  or  $\phi_b$  becoming respectively complex with real parts given by  $\pm(n+1/2)\pi$ , where  $n=0,1,2,\dots$  [18, 19]. Therefore, both the numerator and denominator of the argument are purely imaginary and thus the argument of the  $\ln$  function remains real. We assume that all solutions of equation (3.25) are in the region  $k_o < \beta_z < k_o \sqrt{\epsilon}$  where  $\epsilon=\epsilon_a$  if  $\epsilon_a \geq \epsilon_b$  and  $\epsilon=\epsilon_b$  if  $\epsilon_a < \epsilon_b$ .

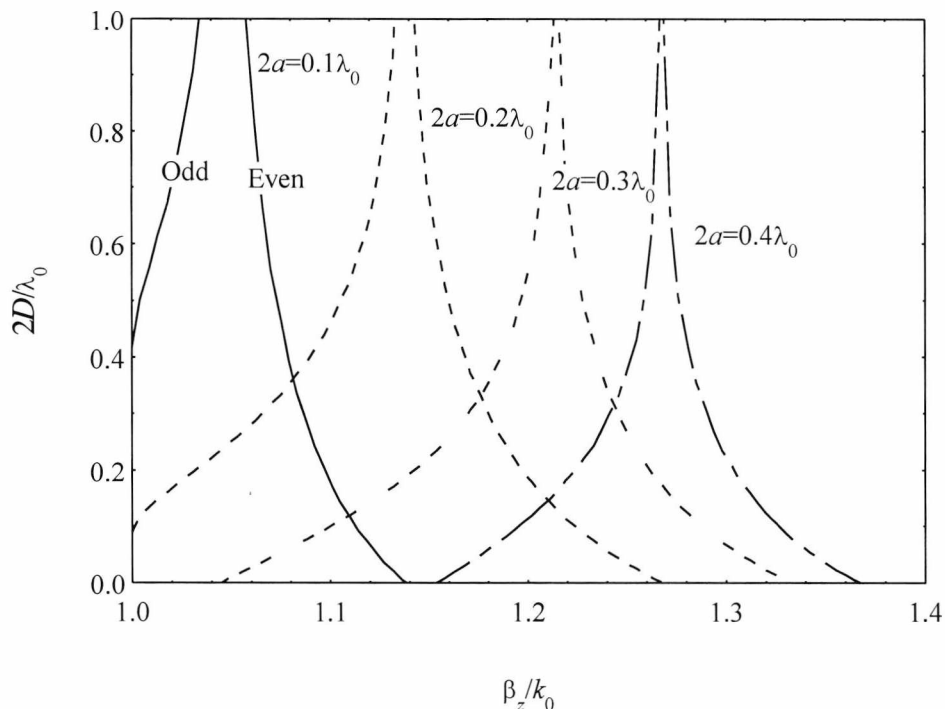


Figure 3.2. Normalised separation  $2D/\lambda_0$  against  $\beta_z/k_0$  for several different  $2a/\lambda_0$  ratios. Note  $a=b$  and  $\epsilon_a=\epsilon_b=2.07$ .

Figure 3.2 shows the normalised separation  $2D/\lambda_0$  plotted against the normalised propagation constant  $\beta_z/k_0$  (sometimes referred to as the effective refractive index  $n_{eff}$ ) for different  $2a/\lambda_0$  ratios. Both guides are identical, *i.e.*  $a=b$  and  $\epsilon_a=\epsilon_b=2.07$ . From Figure 3.2 we see that, for the given  $2a/\lambda_0$  ratios, there are two solutions to equation (3.25). The solution with the largest value of  $\beta_z/k_0$  corresponds to the lowest order (even) mode. The solution with the smallest value of  $\beta_z/k_0$  corresponds to the next higher order (odd) mode. This can be readily seen by substituting  $\beta_z$  into the field equations. It should be noted that for further increases in frequency, higher order modes will propagate, see Figure 3.7 and Figure 3.8. However, in general, coupled

structures are limited to the two mode case. We clarify Figure 3.2 with an example. For a structure with  $a=b=0.5\text{mm}$ ,  $2D=6.0\text{mm}$  and  $\lambda_0=10.0\text{mm}$ , Figure 3.2 shows that two modes exist: an odd mode with  $\beta_z/k_0=1.012$  and an even mode with  $\beta_z/k_0=1.068$ .

Solutions with values of  $\beta_z/k_0$  approaching unity correspond to modes near to low frequency cut-off. It is seen that in the low frequency case,  $2a/\lambda_0=0.1$ , that the odd mode is cut-off until the guide separation  $2D$  is larger than  $0.4\lambda_0$ . Another interesting feature is that the even and odd mode propagation constants tend to a constant value for increasing separation. Furthermore, they converge more quickly for the higher frequency cases. All these effects can be easily explained when we consider the limiting cases of zero separation and infinite separation, refer to Section 3.1.4.

### 3.1.3 Asymmetrical Coupled Slab Waveguides

We now look at the asymmetrical case. For simplicity, we assume that either the permittivity or the width of guide B is less or equal to that of guide A. It is further assumed that  $\epsilon_a=2.07$ . Figure 3.3 and Figure 3.5 show the effects of width asymmetry, Figure 3.4 and Figure 3.6 show the effects of permittivity asymmetry. Figure 3.3 and Figure 3.4 are for  $2a=0.4\lambda_0$ , Figure 3.5 and Figure 3.6 are for  $2a=0.1\lambda_0$ . We see that there is a strong similarity between varying asymmetry in permittivity and width. For an increase in both permittivity and width asymmetry the guide separation has less of an affect on the odd and even mode propagation constants. Furthermore, the difference in these propagation constants increases with asymmetry. We also see that in the low frequency case, the odd mode is completely cut-off until a given separation is reached. Moreover, this cut-off separation increases with increasing asymmetry. Again all these effects become clear when we look at the limiting cases in the next section.

For completeness, Appendix A gives a comparison between the present technique and the improved coupled mode theory. It is shown that the coupled mode theory gives good results for large separations, however the values display significant error for small separations and large asymmetries. Since the difference in the even and odd mode propagation constant is often the important parameter, the coupled mode theory should not be used for asymmetrical guides with small separations. Therefore, since the present technique is exact and easy to implement, it provides a superior alternative to the coupled mode theory.

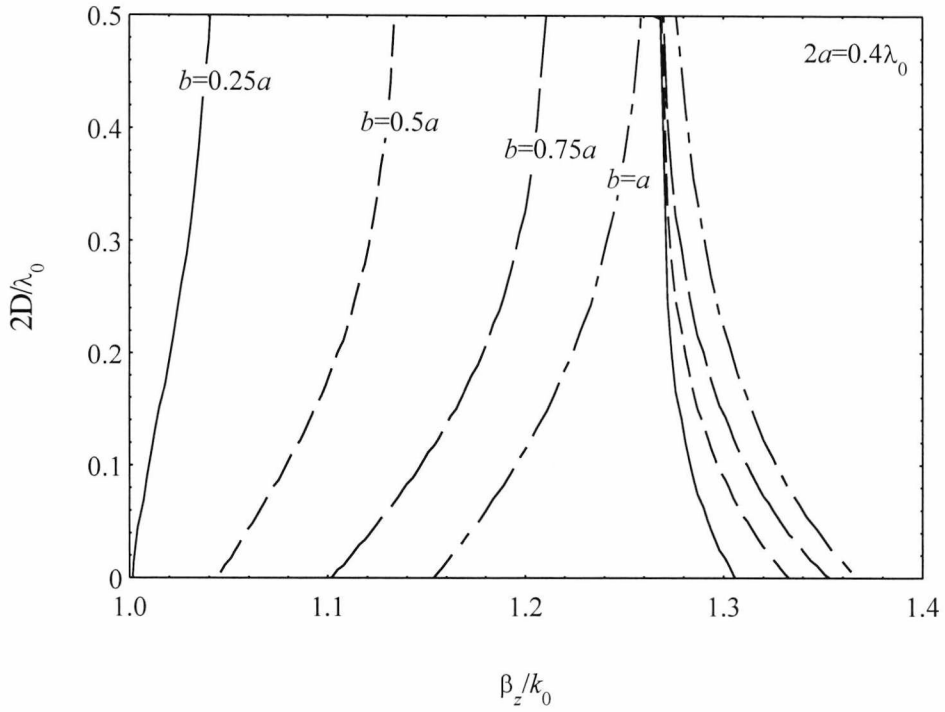


Figure 3.3. Effects of width asymmetry.  $2a=0.4\lambda_0$  and  $\epsilon_a=\epsilon_b=2.07$ .

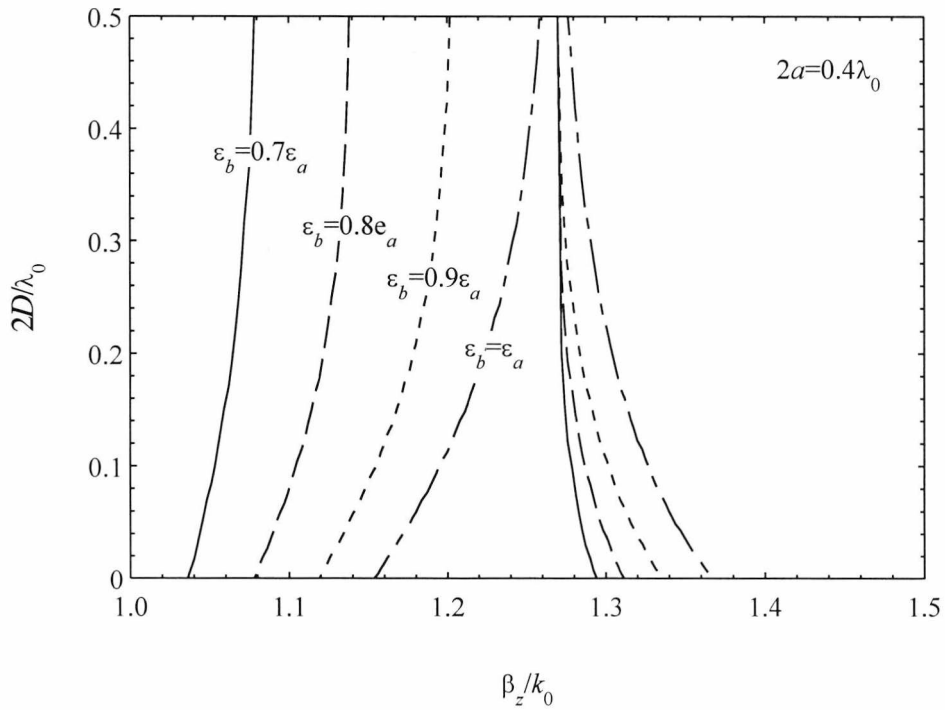


Figure 3.4. Effects of permittivity asymmetry.  $2a=2b=0.4\lambda_0$  and  $\epsilon_a=2.07$ .

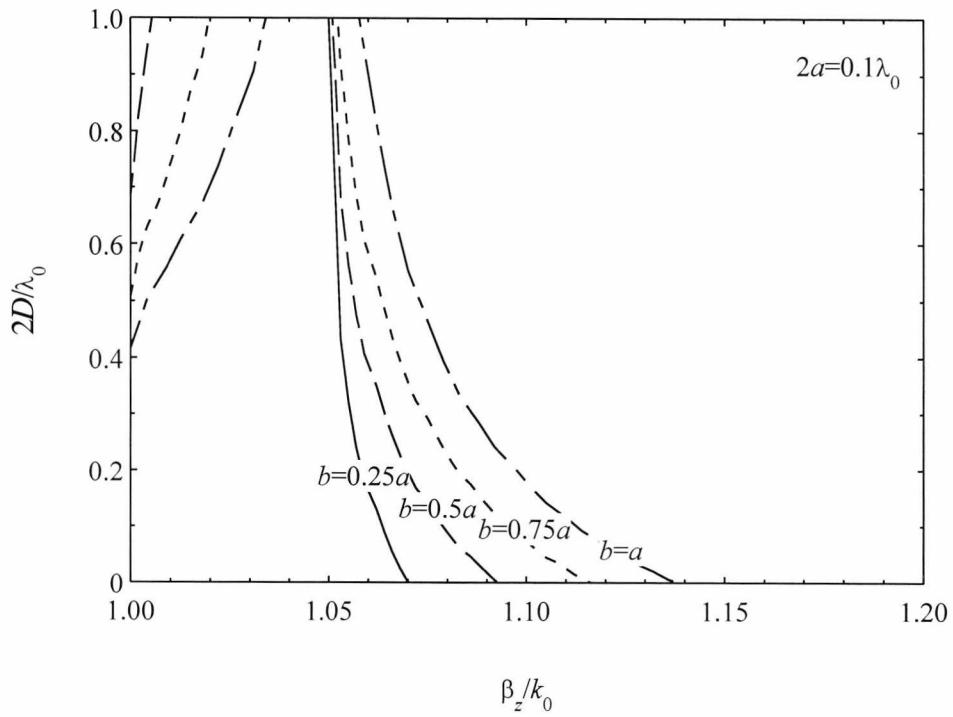


Figure 3.5. Effects of width asymmetry.  $2a=0.1\lambda_0$  and  $\epsilon_a=\epsilon_b=2.07$ .

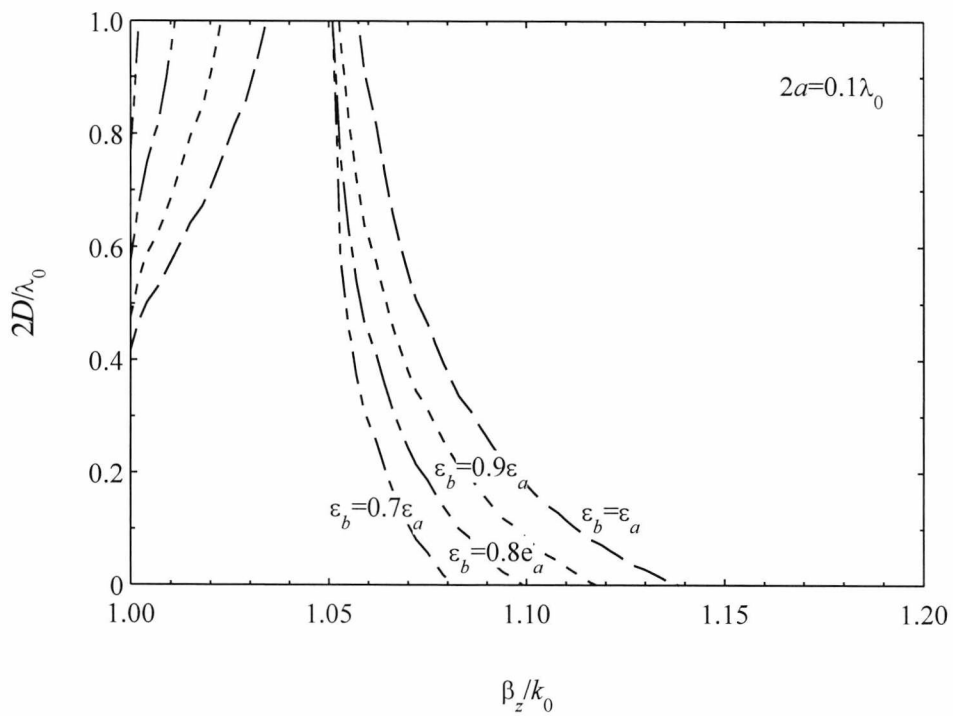


Figure 3.6. Effects of permittivity asymmetry.  $2a=2b=0.1\lambda_0$  and  $\epsilon_a=2.07$ .

### 3.1.4 Limiting Cases ( $2D=0$ and $2D \rightarrow \infty$ )

We now look at the two limiting cases of zero separation and infinite separation. Suppose we have an infinite value of  $D$ , then the right-hand side of equation (3.25) must also be infinite. This condition is satisfied when

$$\sin(2\phi_a - 2k_{xa}a)\sin(2k_{xb}b - 2\phi_b) \rightarrow 0, \quad (3.29)$$

which is achieved when either

$$2\phi_a - 2k_{xa}a = 2 \tan^{-1}\left(\frac{\alpha}{k_{xa}}\right) - 2k_{xa}a = \pm n\pi \quad (3.30)$$

or

$$2k_{xb}b - 2\phi_b = 2 \tan^{-1}\left(\frac{\alpha}{k_{xb}}\right) - 2k_{xb}b = \pm n\pi \quad n=0,1,2,3,\dots \quad (3.31)$$

Equations (3.30) and (3.31) are exactly the guidance conditions for slab waveguides in isolation with widths  $2a$  and  $2b$ , respectively [20]. From a physical standpoint, this is expected since the coupled modes become more like the isolated modes as the separation is increased. We can describe this mathematically if we denote the solutions for a given separation by  $TE_m$ . We then see that  $TE_{2m} \rightarrow TE_m^{2a}$  and  $TE_{2m+1} \rightarrow TE_m^{2b}$  as  $2D \rightarrow \infty$ . Where  $TE_m^{2a}$  is the longitudinal propagation constant of guide A, when in isolation, and  $TE_m^{2b}$  is the propagation constant of guide B, in isolation, see Figure 3.7. It should be noted that the above is only true if  $TE_m^{2a} > TE_m^{2b}$ . If, however,  $TE_m^{2a} < TE_m^{2b}$  then  $TE_{2m} \rightarrow TE_m^{2b}$  and  $TE_{2m+1} \rightarrow TE_m^{2a}$  as  $2D \rightarrow \infty$ . If both guides are identical then equations (3.30) and (3.31) are equivalent and therefore  $TE_{2m} \rightarrow TE_m^{2a}$  for even  $m$  and  $TE_{2m+1} \rightarrow TE_m^{2a}$  for odd  $m$ , as  $2D \rightarrow \infty$ . This is clearly seen in Figure 3.8.

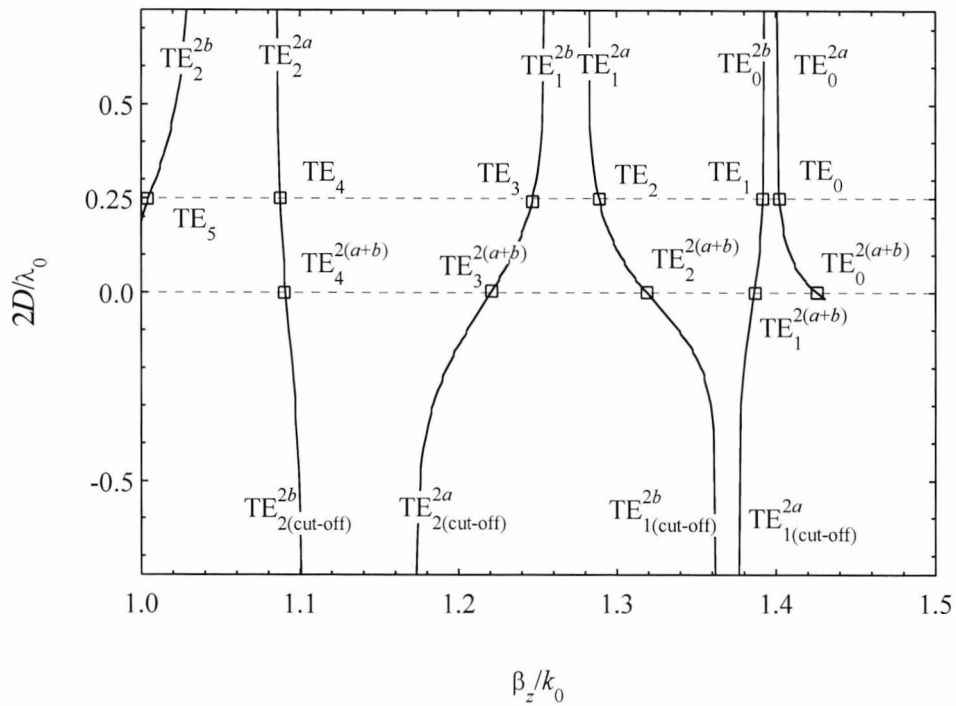


Figure 3.7. Isolated and coupled solutions of two asymmetrical slab waveguides.  $2a=1.2\lambda_0$ ,  $b=0.9a$  and  $\epsilon_a=\epsilon_b=2.07$ .

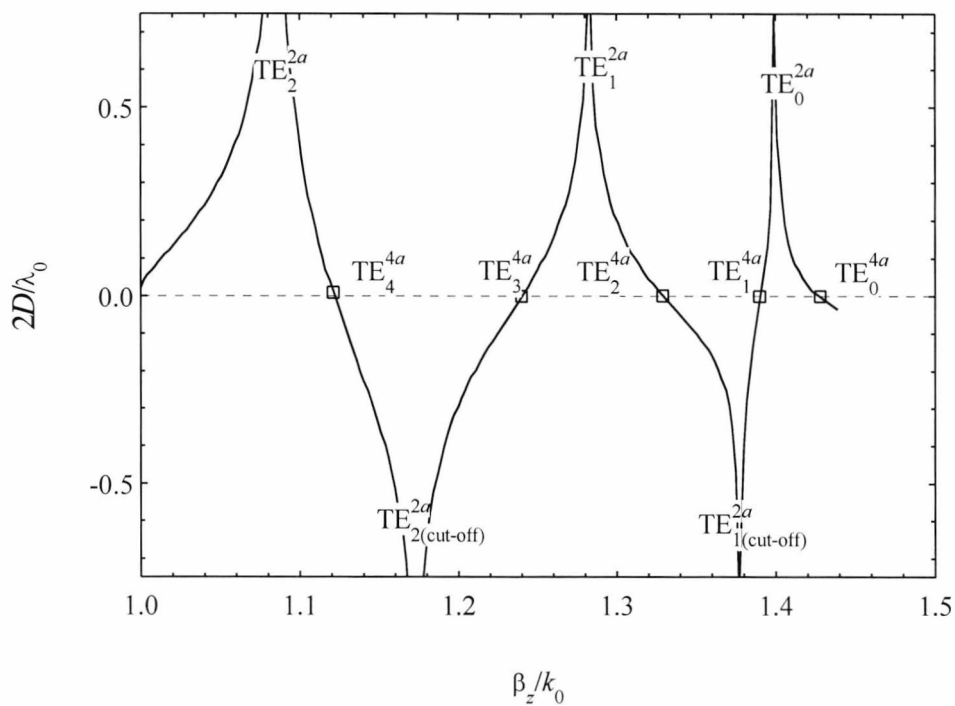


Figure 3.8. Isolated and coupled solutions of two symmetrical slab waveguides.  $2a=2b=1.2\lambda_0$  and  $\epsilon_a=\epsilon_b=2.07$ .

We now consider the case when  $2D=0$ . Under this condition, the right-hand side of equation (3.25) must also equal zero. Therefore,

$$\sin(2k_{xa}a)\sin(2k_{xb}b) = \sin(2\phi_a - 2k_{xa}a)\sin(2k_{xb}b - 2\phi_b) \quad (3.32)$$

If the guides are of the same material then  $k_{xa}=k_{xb}$  and  $\phi_b = 2k_{xa}b - \phi_a$ . Thus

$$\sin(2k_{xa}a)\sin(2k_{xa}b) = \sin(2\phi_a - 2k_{xa}a)\sin(2\phi_a - 2k_{xa}b). \quad (3.33)$$

Intuitively we would expect the solution of equation (3.33) to be identical to a slab structure of width  $2(a+b)$ , that is [20]

$$2\phi_a - 2k_{xa}(a+b) = 2 \tan^{-1}\left(\frac{\alpha}{k_{xa}}\right) - 2k_{xa}(a+b) = \pm n\pi. \quad (3.34)$$

Solving the above equation for  $\phi_a$  and substituting back into equation (3.33) shows that the above expression is indeed a solution of equation (3.33). Therefore, for zero separation, the solution of the guidance condition is identical to that of a slab structure of width  $2(a+b)$ .

We can now understand why the odd mode for  $2a=0.1\lambda_0$ , in Figure 3.2, is completely cut-off for separations less than  $0.4\lambda_0$ . The mode cannot exist for zero separation as can be readily seen by solving equation (3.34). However, as  $2D \rightarrow \infty$ , we see from equations (3.30) and (3.31) that the mode can propagate. Therefore, it seems reasonable to suppose that the mode can start propagating at some separation between these two limits. We obtain an expression for the cut-off separation by allowing  $\beta_z \rightarrow \sqrt{\epsilon_2}k_0$ . Unfortunately,

$$\lim_{\beta_z \rightarrow \sqrt{\epsilon_2}k_0} \{2\alpha_{x2}\} = 0$$

and

$$\lim_{\beta_z \rightarrow \sqrt{\epsilon_2} k_0} \left\{ \ln \left[ \frac{\sin(2k_{xa}a) \sin(2k_{xb}b)}{\sin(2\phi_a - 2k_{xa}a) \sin(2k_{xb}b - 2\phi_b)} \right] \right\} = 0$$

and thus equation (3.25) becomes meaningless. However, L'Hôpital's rule states that if both  $f(x)$  and  $g(x)$  are zero for  $x=a$  then

$$\lim_{x \rightarrow a} \frac{f(x)}{g(x)} = \lim_{x \rightarrow a} \frac{f'(x)}{g'(x)}.$$

Therefore, letting

$$g(\beta_z) = 2\alpha_{x2}$$

and

$$f(\beta_z) = \ln \left[ \frac{\sin(2k_{xa}a) \sin(2k_{xb}b)}{\sin(2\phi_a - 2k_{xa}a) \sin(2k_{xb}b - 2\phi_b)} \right]$$

we obtain, after some work,

$$\begin{aligned} 2D_{cut-off} &= \lim_{\beta_z \rightarrow \sqrt{\epsilon_2} k_0} \left\{ \frac{1}{2\alpha_{x2}} \ln \left[ \frac{\sin(2k_{xa}a) \sin(2k_{xb}b)}{\sin(2\phi_a - 2k_{xa}a) \sin(2k_{xb}b - 2\phi_b)} \right] \right\} \\ &= \frac{1}{k_0 \sqrt{\epsilon_a - \epsilon_2}} \cot(2ak_0 \sqrt{\epsilon_a - \epsilon_2}) + \frac{1}{k_0 \sqrt{\epsilon_b - \epsilon_2}} \cot(2bk_0 \sqrt{\epsilon_b - \epsilon_2}) \end{aligned} \quad (3.35)$$

For symmetrical guides we find that

$$2D_{cut-off} = \lim_{k_z \rightarrow \sqrt{\epsilon_2} k_0} \left\{ \frac{1}{\alpha_{x2}} \ln \left| \frac{\sin(2k_{xa}a)}{\sin(2\phi_a - 2k_{xa}a)} \right| \right\} = \frac{2}{k_0 \sqrt{\epsilon_a - \epsilon_2}} \cot(2ak_0 \sqrt{\epsilon_a - \epsilon_2}). \quad (3.36)$$

We note that  $2D_{cut-off}$  can become negative, suggesting that the mode propagates for all physical values of  $2D$ .

In Figure 3.2, we have limited the range to (0..1). However, equation (3.25) does have solutions with negative values, see Figure 3.7 and Figure 3.8. As we discussed in the previous section, negative distance has no physical meaning. Nevertheless, these solutions are of some interest. We find that for infinite negative separation,  $2k_{xa}a=n\pi$  or  $2k_{xb}b=n\pi$ . From section 2.2.1, we see that this is exactly the value of the transitional point from proper to improper modes. Therefore, if we plot the whole range of equation (3.25) we find that the negative peaks describe the cut-off frequencies of the isolated modes, see Figure 3.7 and Figure 3.8.

In section 2.2.1, we saw that the guidance condition solved for modes where the fields diverged away from the guiding structure. These so-called improper modes carry infinite power but can be of some use in describing waveguides beyond cut-off [21]. Equation (3.25) can be used to solve for improper modes by replacing  $\alpha_{x2}$  with  $-\alpha_{x2}$  in equations (3.25), (3.26) and (3.27). However, their solution will not be covered here.

### 3.1.5 TM Mode Solutions

TM mode solutions follow in a similar way to section 3.1.1. By using equation (3.2) and matching the tangential electric and magnetic fields at the four boundaries we obtain:

$$\alpha_{x2} \frac{\epsilon_a}{\epsilon_2} = k_{xa} \tan(\phi_a) \quad \text{for } x = -(D + 2a), \quad (3.37)$$

$$k_{xa} \tan(2k_{xa}a - \phi_a) = \alpha_{x2} \frac{E_3 \sinh(\alpha_{x2}D) - E_4 \cosh(\alpha_{x2}D)}{E_3 \cosh(\alpha_{x2}D) - E_4 \sinh(\alpha_{x2}D)} \quad \text{for } x = -D, \quad (3.38)$$

$$k_{xb} \tan(\phi_b) = \alpha_{x2} \frac{E_3 \sinh(\alpha_{x2}D) + E_4 \cosh(\alpha_{x2}D)}{E_3 \cosh(\alpha_{x2}D) + E_4 \sinh(\alpha_{x2}D)} \quad \text{for } x = D, \quad (3.39)$$

$$\alpha_{x2} \frac{\epsilon_b}{\epsilon_2} = k_{xb} \tan(2k_{xb}b - \phi_b) \quad \text{for } x = (2b + D). \quad (3.40)$$

Thus, by combining the above equations we have

$$2D = \frac{1}{2\alpha_{x2}} \ln \left[ \frac{\sin(2k_{xa}a) \sin(2k_{xb}b)}{\sin(2\phi_a - 2k_{xa}a) \sin(2k_{xb}b - 2\phi_b)} \right] \quad (3.41)$$

with

$$\phi_a = \tan^{-1} \left( \frac{\alpha_{x2} \epsilon_a}{k_{xa} \epsilon_2} \right) \quad (3.42)$$

and

$$\phi_b = 2k_{xb}b - \tan^{-1} \left( \frac{\alpha_{x2} \epsilon_b}{k_{xb} \epsilon_2} \right). \quad (3.43)$$

Notice that equation (3.41) is identical to equation (3.25) except that the argument of the arc tangent in  $\phi_a$  and  $\phi_b$  is now multiplied by the permittivity ratio. The relationships derived in section 3.1.4 therefore become

$2D \rightarrow \infty$ :

$$2\phi_a - 2k_{xa}a = 2 \tan^{-1} \left( \frac{\alpha_{x2} \epsilon_a}{k_{xa} \epsilon_2} \right) - 2k_{xa}a = \pm n\pi \quad (3.44)$$

or

$$2k_{xb}b - 2\phi_b = 2 \tan^{-1} \left( \frac{\alpha_{x2} \epsilon_b}{k_{xb} \epsilon_2} \right) - 2k_{xb}b = \pm n\pi \quad n=0,1,2,3,\dots \quad (3.45)$$

$2D=0$  for symmetrical guides:

$$2\phi_a - 2k_{xa}(a+b) = 2 \tan^{-1} \left( \frac{\alpha_{x2} \epsilon_a}{k_{xa} \epsilon_2} \right) - 2k_{xa}(a+b) = \pm n\pi \quad (3.46)$$

Cut-off separation:

$$2D_{cut-off} = \frac{\epsilon_a}{\epsilon_2} \frac{1}{k_0 \sqrt{\epsilon_a - \epsilon_2}} \cot(2ak_0 \sqrt{\epsilon_a - \epsilon_2}) + \frac{\epsilon_b}{\epsilon_2} \frac{1}{k_0 \sqrt{\epsilon_b - \epsilon_2}} \cot(2bk_0 \sqrt{\epsilon_b - \epsilon_2}) \quad (3.47)$$

The  $2D$ - $\beta_z$  curves and the field profiles are essentially the same for TM modes. However, for completeness, we compare the TM mode solutions with those of the TE modes. Figure 3.9 shows plots of the guidance condition for both TE and TM modes at two different operating frequencies. We see that the TM mode propagation constants are less than the corresponding TE solutions. The TM mode field profiles are therefore more extensive in the surrounding regions. Figure 3.10 and Figure 3.11 show TE and TM solutions for permittivity and width asymmetry, respectively. Again we see that the TM mode propagation constants are less than the corresponding TE solutions.

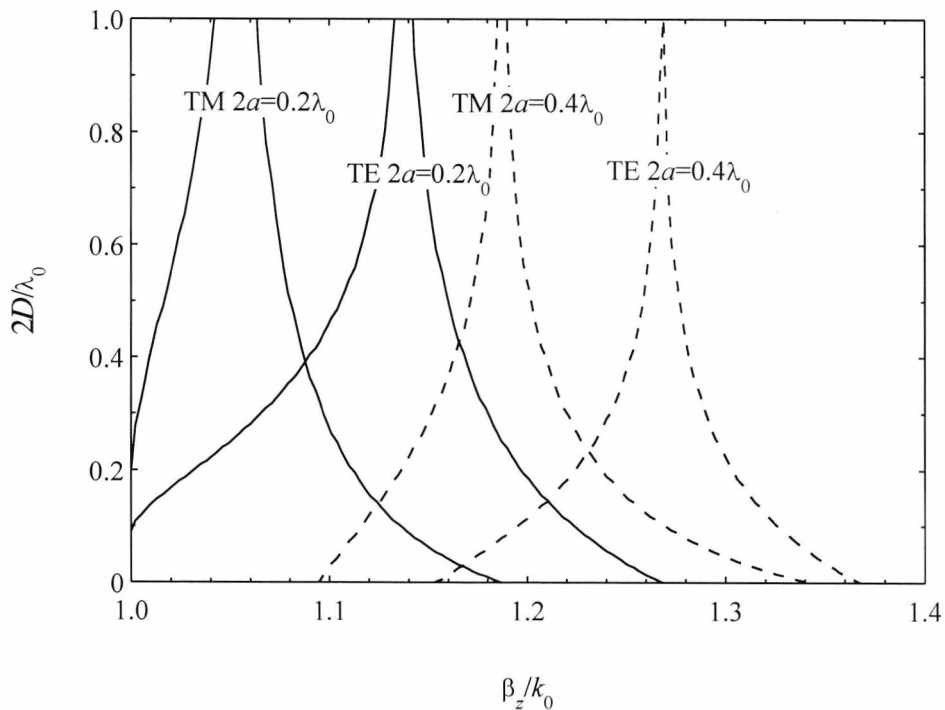


Figure 3.9. Normalised separation  $2D/\lambda_0$  against  $\beta_z/k_0$  for TE and TM modes. Note  $a=b$  and  $\epsilon_a=\epsilon_b=2.07$ .

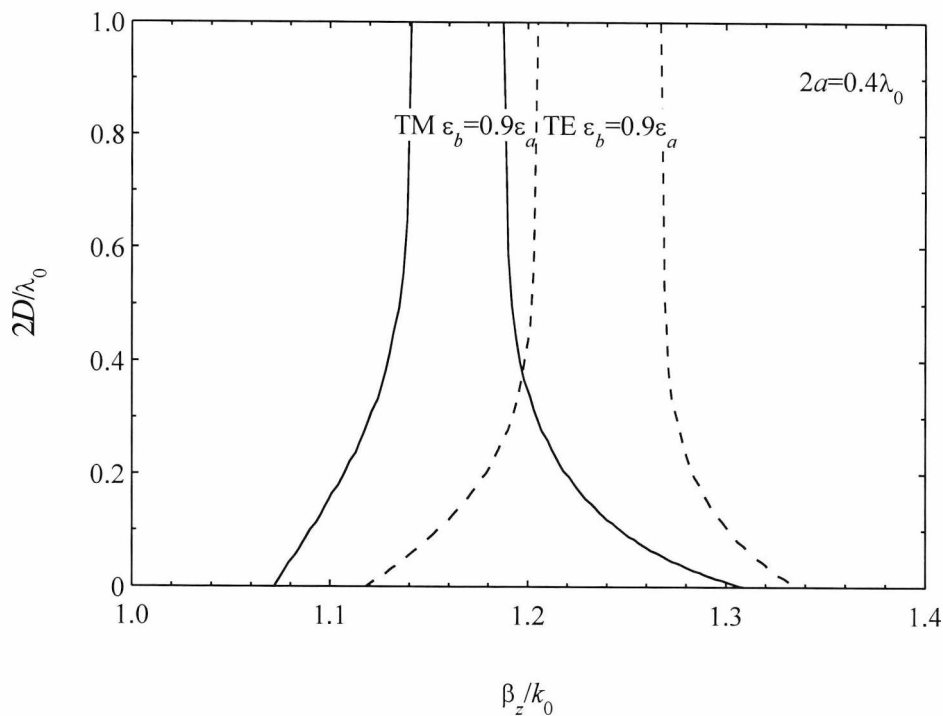


Figure 3.10. Normalised separation  $2D/\lambda_0$  against  $\beta_z/k_0$  for TE and TM modes with permittivity asymmetry. Note  $2a=0.4\lambda_0$  and  $\epsilon_a=\epsilon_b=2.07$ .

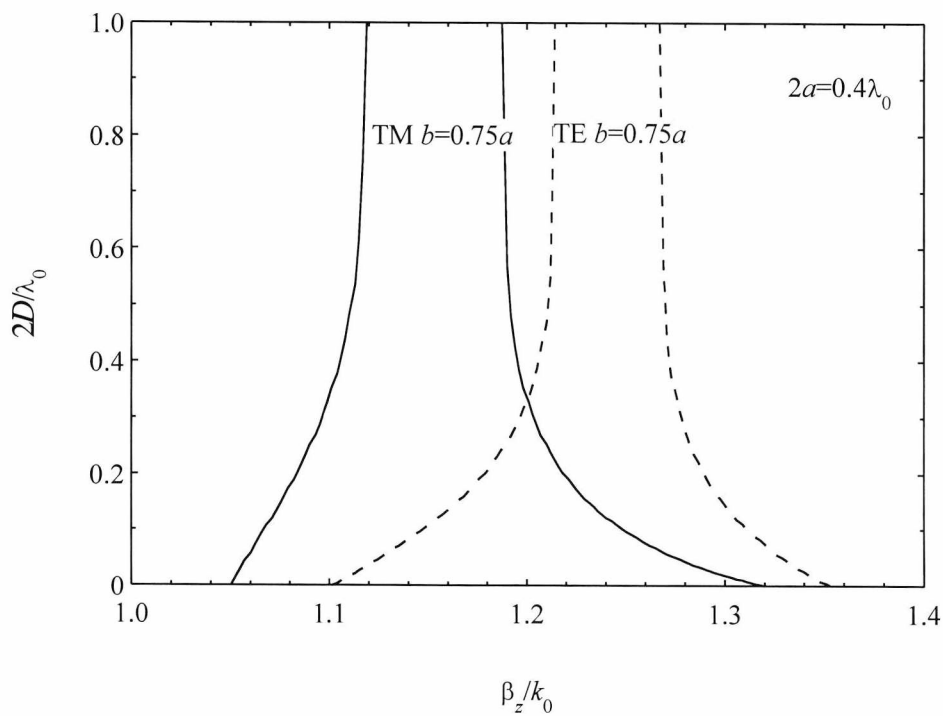


Figure 3.11. Normalised separation  $2D/\lambda_0$  against  $\beta_z/k_0$  for TE and TM modes with width asymmetry. Note  $2a=0.4\lambda_0$  and  $\epsilon_a=\epsilon_b=2.07$ .

### 3.2 FIELD PROFILES

If the longitudinal propagation constants for the various modes that a guide supports are known, then  $\alpha_{x2}$ ,  $k_{xa}$ ,  $k_{xb}$ ,  $\phi_a$  and  $\phi_b$  can all be calculated from equations (3.4), (3.5), (3.6), (3.26) and (3.27), respectively. Therefore, if the amplitude constants  $E_1 \dots E_6$  are specified then the electric field profile over the whole structure can be evaluated. Since the electric field must be continuous, we equate the field functions at four boundaries. Thus:

$$E_1 = E_2 \cos(\phi_a) \quad \text{for } x = -(D + 2a). \quad (3.48)$$

$$E_3 \cosh(\alpha_{x2}D) - E_4 \sinh(\alpha_{x2}D) = E_2 \cos(2k_{xa}a - \phi_a) \quad \text{for } x = -D \quad (3.49)$$

and therefore

$$E_3 = \frac{E_2 \cos(2k_{xa}a - \phi_a)}{\cosh(\alpha_{x2}D) - \Gamma \sinh(\alpha_{x2}D)} \quad (3.50)$$

and

$$E_4 = \frac{E_2 \cos(2k_{xa}a - \phi_a)}{\frac{\cosh(\alpha_{x2}D)}{\Gamma} - \sinh(\alpha_{x2}D)} \quad (3.51)$$

where from equation (3.21)

$$\Gamma = \frac{E_4}{E_3} = \frac{\tan(2k_{xa}a - \phi_a) \cosh(\alpha_{x2}D) - \tan(\phi_a) \sinh(\alpha_{x2}D)}{\tan(2k_{xa}a - \phi_a) \sinh(\alpha_{x2}D) - \tan(\phi_a) \cosh(\alpha_{x2}D)}. \quad (3.52)$$

$$E_5 = \frac{E_3 \cosh(\alpha_{x2}D) + E_4 \sinh(\alpha_{x2}D)}{\cos(\phi_b)} \quad \text{for } x = D. \quad (3.53)$$

$$E_6 = E_5 \cos(2k_{xb}b - \phi_b) \quad \text{for } x = (2b + D). \quad (3.54)$$

It should be noted that for odd modes the sinh function is the dominant component of the field function in the middle region and therefore  $E_4 \gg E_3$ . For even modes, the cosh function is the dominant component hence  $E_3 \gg E_4$ . Furthermore, for symmetrical guides  $E_3 = 0$  for odd modes and  $E_4 = 0$  for even modes.

Clearly for a two-mode structure, there will be two electric field profiles: one for the lowest order even mode and one for the next higher order odd mode. We thus indicate the odd profile by  $E_{y(o)}(x)$  and the even profile by  $E_{y(e)}(x)$ . Since the modes are orthogonal [22], the relation between the odd mode amplitude constants,  $E_{1(o)} \dots E_{6(o)}$ , and the even mode amplitude constants,  $E_{1(e)} \dots E_{6(e)}$ , cannot be determined without considering the longitudinal boundary conditions, see Chapter 5. We therefore set  $E_{2(e)}=1$  and  $E_{5(o)}=1$ ; the reason for this choice will become apparent when we plot the electric field.

Field plots are shown in Figure 3.12 and Figure 3.13. In each case  $2a=\lambda_0/2$  and  $\epsilon_a=2.0$ . Figure 3.12 shows the effects of guide separation  $2D$  and width asymmetry  $a/b$ , with both guides having a permittivity,  $\epsilon_a=\epsilon_b=2.0$ . Figure 3.12 (a), (b) and (c) show the symmetrical case with  $2D=\lambda_0/4$ ,  $2D=\lambda_0/2$  and  $2D=\lambda_0$ , respectively. Figure 3.12 (d), (e) and (f) are for the same guide separations as above but with a width asymmetry of  $a/b=2$ . Similarly, Figure 3.12 (g), (h) and (I) are for  $a/b=4$  and Figure 3.12 (j), (k) and (l) are for  $a/b=8$ . Figure 3.13 shows the effects of guide separation and permittivity asymmetry, with both guides having the same width,  $2a=2b=\lambda_0/2$ . For comparison, Figure 3.12 (a), (b) and (c) are repeated in Figure 3.13 (a), (b) and (c), respectively. In a similar fashion to Figure 3.12, Figure 3.13 (d), (e) and (f) are for a permittivity asymmetry of  $\epsilon_b=1.8$ . Figure 3.13 (g), (h), and (I) are for  $\epsilon_b=1.6$ . Finally, Figure 3.13 (j), (k) and (l) are for  $\epsilon_b=1.4$ .

We can see from Figure 3.12 and Figure 3.13 that the even field is similar to the profile for guide A in isolation with varying degrees of perturbation depending on the magnitude and type of asymmetry, and also the guide separation. Similarly, the odd field profile is identical to the field for guide B when in isolation with varying perturbation depending on the asymmetry and separation. However, the odd field profile is more strongly perturbed than the even mode. In fact for smaller separations, the odd mode appears to be close to cut-off, and indeed can become cut-off for low operating frequencies, see section 3.1.2 and 3.1.3. This becomes clear when we consider that for a mode to be odd the field must go positive within guide A. If the field outside the isolated mode for guide B is extensive, the amplitude of the field at the  $x=-D$  boundary of guide A will be relatively large. Therefore, for the field to become positive there must be a large perturbation. These effects decrease with separation since the field in the middle region will have decayed by a greater amount. For very large separations, no perturbation is seen for either the odd or the even modes since both the fields have decayed by a considerable amount. The above facts become important when we consider discontinuities in Chapter 5. There it is shown that for large asymmetries and separations it is pointless to consider the structure as a coupled guide.

The field profile in guide B becomes hyperbolic for certain values of permittivity asymmetry, although this is difficult to see from Figure 3.13. From equation (3.6),

$$k_{xb} = k_0 \sqrt{\epsilon_b - \frac{\beta_z^2}{k_0^2}}$$

Thus if  $\beta_z/k_0 > \sqrt{\epsilon_b}$  then  $k_{xb}$  will be imaginary. We can see from Figure 3.4, that if  $2b=2a=0.4\lambda_0$ ,  $\epsilon_a=2.07$  and  $\epsilon_b=0.8\epsilon_a$  then the even mode solutions for varying separation will all result in an imaginary  $k_{xb}$  and thus the field profile for the even mode will have a hyperbolic function within guide B. For a two mode structure, the odd mode field profile in either guide can never become hyperbolic. This can be explained if we note that the odd mode longitudinal propagation constant tends to the value of guide B when in isolation with increasing separation  $2D$ . For guide B, in isolation, the solution is in the range  $k_0 < \beta_z < \sqrt{\epsilon_b}k_0$ . Therefore the odd mode

solution can never be greater than  $\sqrt{\epsilon_b} k_0$  and thus  $k_{xb}$  can never become imaginary. For width asymmetry,  $k_{xb}$  can never become imaginary since we assume  $\epsilon_a = \epsilon_b$ .

For completeness, the magnetic fields of both the even and odd mode symmetrical solutions are shown in Figure 3.14 and Figure 3.15, respectively. The fields are plotted as vectors with the arrows length determining the magnitude.

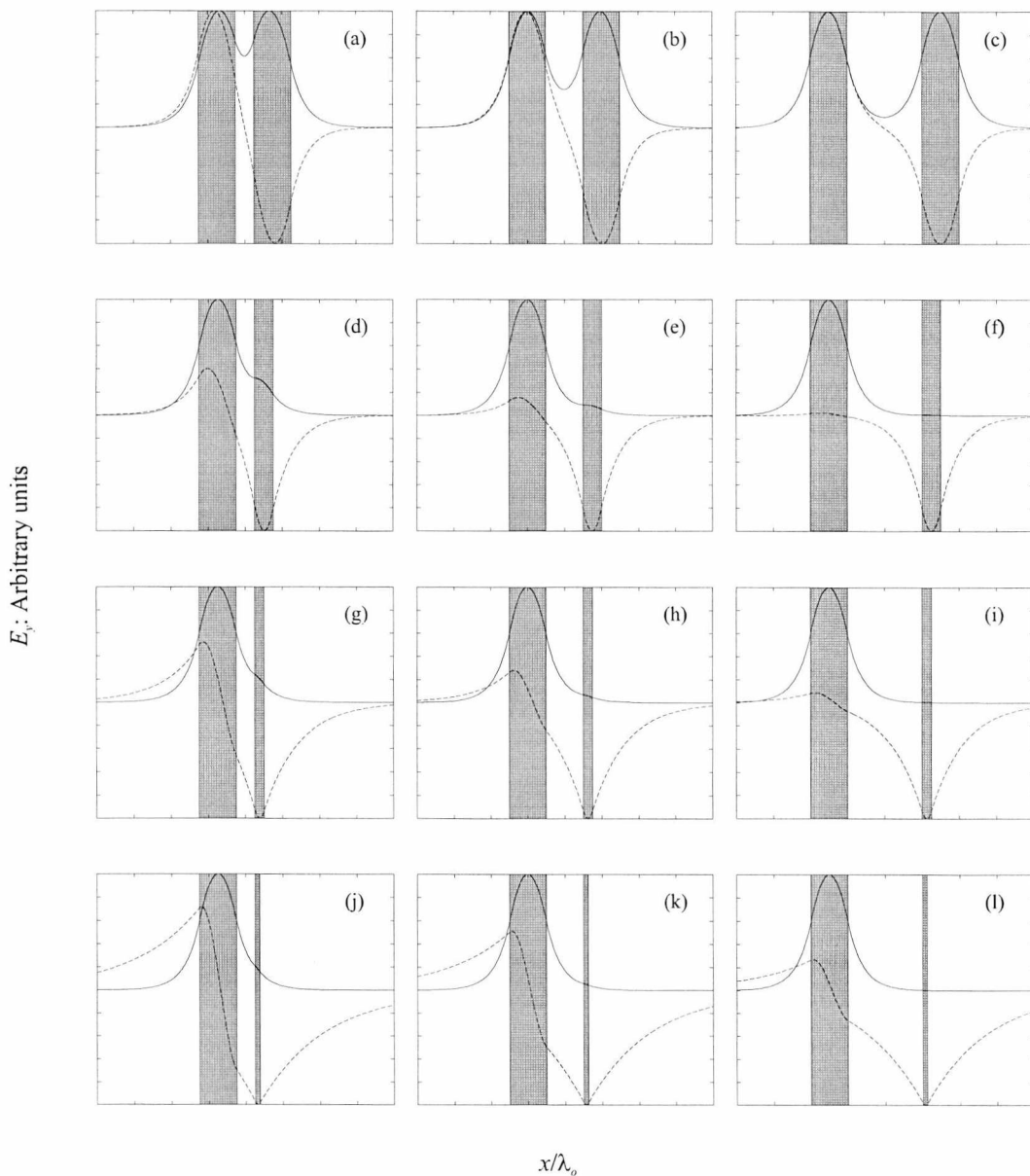


Figure 3.12. Effects of separation and width asymmetry on the modal electric field profiles for TE coupled slab waveguide. Solid lines show the even modes, dashed lines show the odd.

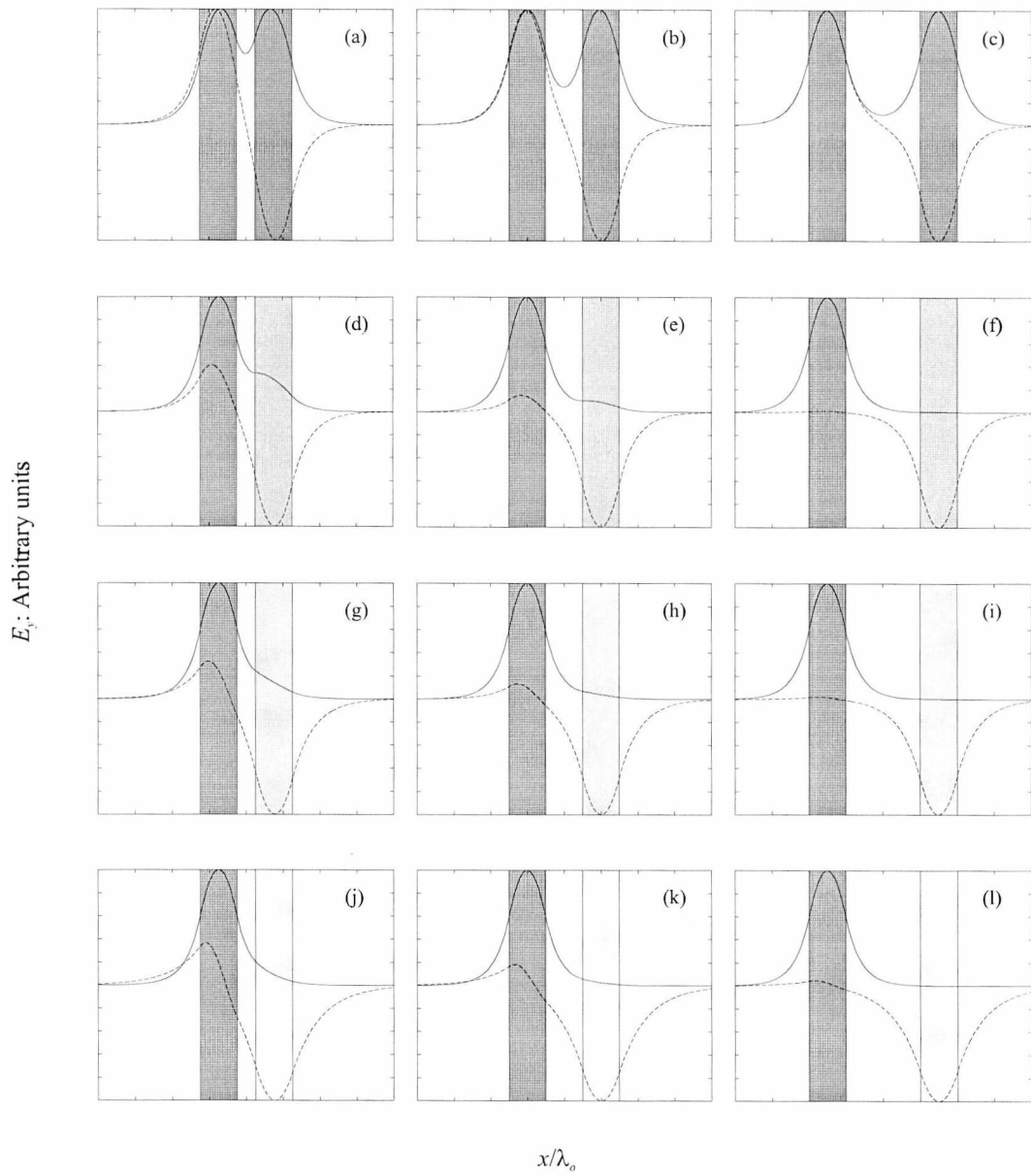


Figure 3.13. Effects of separation and permittivity asymmetry on the modal electric field profiles for TE coupled slab waveguide. Solid lines show the even modes, dashed lines show the odd.

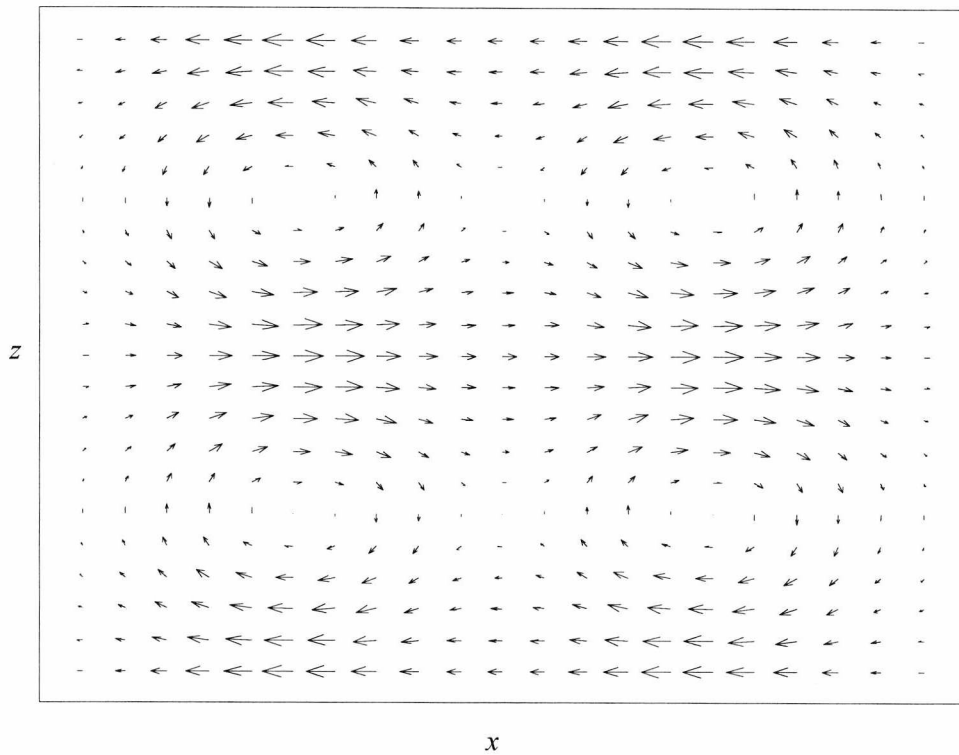


Figure 3.14. Vector field plot of the even mode magnetic field of a symmetrical coupled slab waveguide with  $\epsilon_a=\epsilon_b=2.07$ ,  $2a=2b=0.4\lambda_0$  and  $2D=0.4\lambda_0$ .

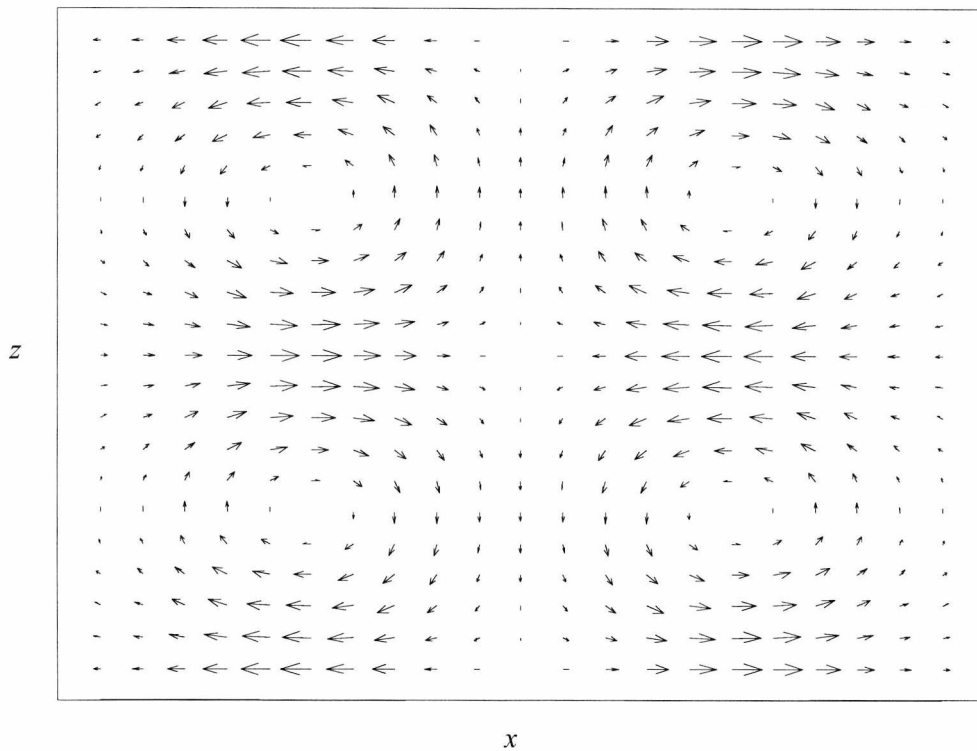


Figure 3.15. Vector field plot of the odd mode magnetic field of a symmetrical coupled slab waveguide with  $\epsilon_a=\epsilon_b=2.07$ ,  $2a=2b=0.4\lambda_0$  and  $2D=0.4\lambda_0$ .

### 3.3 SYNCHRONOUS SOLUTIONS

So far we have looked at either width or permittivity asymmetry; it is of course possible for there to be asymmetry in both. Here we look at the case when the guides are different but have identical isolated propagation constants. Structures of this type are said to be synchronous [10]. From equation (2.53), we find that

$$b = \frac{1}{k_{xb}} \tan^{-1} \left\{ \frac{\sqrt{k_0^2 (\epsilon_b - \epsilon_2) - k_{xb}^2}}{k_{xb}} \right\} \quad (3.55)$$

for TE even modes and

$$b = \frac{1}{k_{xb}} \tan^{-1} \left\{ \frac{\epsilon_b \sqrt{k_0^2 (\epsilon_b - \epsilon_2) - k_{xb}^2}}{\epsilon_2 k_{xb}} \right\} \quad (3.56)$$

for TM odd modes.

Therefore if  $a$ ,  $\epsilon_a$  and  $\epsilon_b$  are given, we can calculate  $\beta_z$  from equation (2.53) and then, using equation (3.55), obtain a value for  $b$  such that the guides are synchronous. For example, if  $2a=0.4\lambda_0$ ,  $\epsilon_a=2.07$  and  $\epsilon_b=1.8$  then we find that  $\beta_z/k_0=1.268$  and therefore  $b=1.924a$ .

Figure 3.16 shows the even and odd mode field profiles for  $2a=0.4\lambda_0$ ,  $\epsilon_a=2.07$ ,  $\epsilon_b=1.8$  and  $b=1.924a$ . We notice that although there is a high degree of asymmetry, the fields have almost equal amplitudes in each of the guides. This is in contrast to the asynchronous asymmetry in Figure 3.12 and Figure 3.13 where the even mode is dominant in guide A and the odd mode is dominant in guide B. Again, this has important implications to the coupling of energy, as we shall see in Chapter 5.

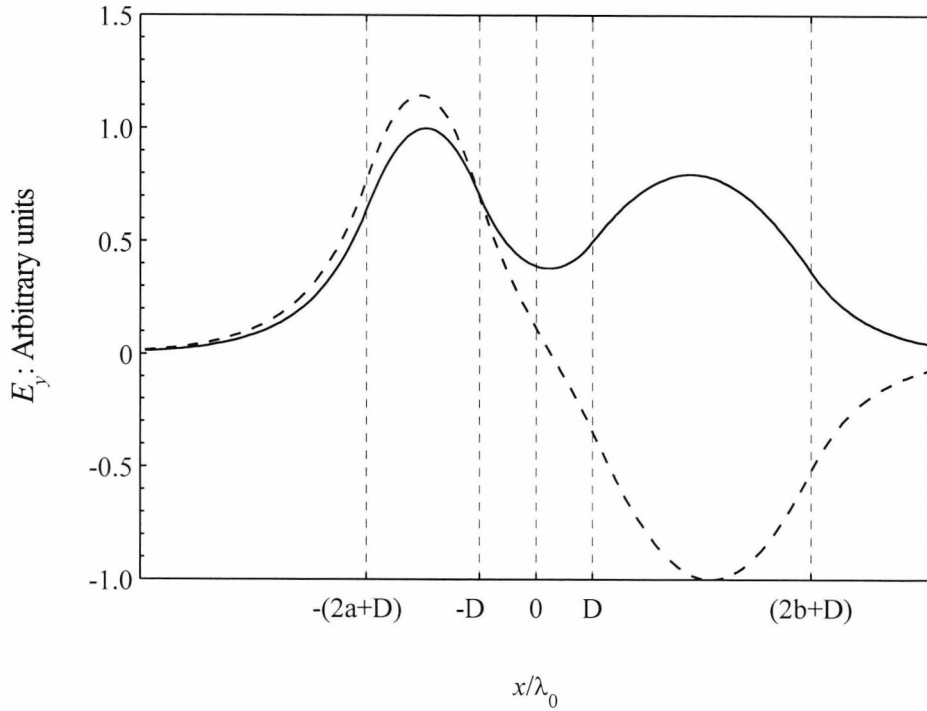


Figure 3.16. Field profile for synchronous guides.  $2a=0.4\lambda_0$ ,  $\epsilon_a=2.07$ ,  $\epsilon_b=1.8$  and  $b=1.924a$ . Solid lines show the  $TE_0$  mode and dashed lines show the  $TE_1$  mode.

### 3.4 LOSSES IN COUPLED SLAB GUIDES

We found in section 3.1 that the guidance condition for asymmetrical coupled slab waveguides for structures with no dielectric losses was given by

$$2D = \frac{1}{2\alpha_{x2}} \ln \left[ \frac{\sin(2k_{xa}a) \sin(2k_{xb}b)}{\sin(2\phi_a - 2k_{xa}a) \sin(2k_{xb}b - 2\phi_b)} \right] \quad (3.57)$$

with

$$\phi_a = \tan^{-1} \left( \frac{\alpha_{x2}}{k_{xa}} \rho_a \right) \quad (3.58)$$

and

$$\phi_b = 2k_{xb}b - \tan^{-1}\left(\frac{\alpha_{x2}}{k_{xb}}\rho_b\right). \quad (3.59)$$

Where

$$\rho_a = 1 \text{ and } \rho_b = 1$$

for TE modes and

$$\rho_a = \frac{\epsilon_a}{\epsilon_2} \text{ and } \rho_b = \frac{\epsilon_b}{\epsilon_2}$$

for TM modes. At millimetre-wave frequencies the losses may become significant. We therefore allow  $\epsilon_a$ ,  $\epsilon_b$  and  $\epsilon_2$  to become complex, i.e.

$$\epsilon_a = \epsilon'_a(1 - j \tan \delta_a), \quad \epsilon_b = \epsilon'_b(1 - j \tan \delta_b) \text{ and } \epsilon_2 = \epsilon'_2(1 - j \tan \delta_2).$$

Thus,  $\alpha_{x2}$ ,  $k_{xa}$  and  $k_{xb}$  are now given by equation (3.3) with  $\gamma_z = \alpha_z + j\beta_z$ . Expanding equation (3.57) forms a pair of coupled transcendental equations for  $\alpha_z$  and  $\beta_z$ . These can be solved numerically, however for small losses we can obtain an approximate expression for the symmetrical structure. The complete derivation of the approximate expressions is lengthy, therefore only an outline is given here.

For symmetrical structures with dielectric losses equation (3.57) becomes

$$2D = \frac{1}{2(\alpha'_{x2} + j\alpha''_{x2})} \ln \left[ \frac{\sin^2(2k'_{xa}a + j2k''_{xa}a)}{\sin^2(2\phi'_a - 2k'_{xa}a + j2\phi''_a - j2k''_{xa}a)} \right] \quad (3.60)$$

with

$$\phi_a = \tan^{-1} \left( \frac{\alpha'_{x2} + j\alpha''_{x2}}{k'_{xa} + jk''_{xa}} \rho_a \right). \quad (3.61)$$

Where

$$\rho_a = 1$$

for TE solutions and

$$\rho_a = \frac{\epsilon'_a(1 - j \tan \delta_a)}{\epsilon'_2(1 - j \tan \delta_2)}$$

for TM.

Multiplying equation (3.60) by  $\alpha_{x2}$  and taking the exponent of both sides yields

$$\exp(4\alpha'_{x2}D + j4\alpha''_{x2}D) = \frac{\sin^2(2k'_{xa}a + j2k''_{xa}a)}{\sin^2(2\phi'_a - 2k'_{xa}a + j2\phi''_a - j2k''_{xa}a)}. \quad (3.62)$$

If we assume that  $k'_{xa} \gg k''_{xa}$ ,  $\alpha'_{x2} \gg \alpha''_{x2}$  and  $\phi'_a \gg \phi''_a$  then we can expand the trigonometric and hyperbolic functions to the first order and neglect the products of all small terms. We then find, after some algebra, that the real part of equation (3.60) is given by

$$\exp(4\alpha'_{x2}D) = \frac{\sin^2(2k'_{xa}a)}{\sin^2(2\phi'_a - 2k'_{xa}a)} \quad (3.63)$$

and the imaginary part by

$$\exp(4\alpha'_{x2}D)4\alpha''_{x2}D = \frac{4\sin(2k_{xa}a)[k''_{xa}a\sin(2\phi'_a) - \sin(2k_{xa}a)\cos(2\phi'_a - 2k'_{xa}a)\phi''_a]}{\sin^3(2\phi'_a - 2k'_{xa}a)}. \quad (3.64)$$

Equation (3.64) can be simplified further by making use of equation (3.63). Thus

$$\alpha''_{x2} = \frac{[k''_{xa}a\sin(2\phi'_a) - \sin(2k_{xa}a)\cos(2\phi'_a - 2k'_{xa}a)\phi''_a]}{\sin(2\phi'_a - 2k'_{xa}a)\sin(2k_{xa}a)D}. \quad (3.65)$$

Using standard expressions for the arc tangent of a complex number [18, 19] we find that, after the appropriate approximations,

$$\phi''_a = \frac{1}{4} \ln \left( 1 + \frac{2\alpha''_{x2}k'_{xa} - 2\alpha'_{x2}k''_{xa}}{\alpha_{x2}^{\prime 2} + k_{xa}^{\prime 2}} \right) - \frac{1}{4} \ln \left( 1 - \frac{2\alpha''_{x2}k'_{xa} - 2\alpha'_{x2}k''_{xa}}{\alpha_{x2}^{\prime 2} + k_{xa}^{\prime 2}} \right). \quad (3.66)$$

Expanding to the first order gives

$$\phi''_a = \frac{\alpha''_{x2}k'_{xa} - \alpha'_{x2}k''_{xa}}{\alpha_{x2}^{\prime 2} + k_{xa}^{\prime 2}} \quad (3.67)$$

Substituting equation (3.67) into equation (3.65) yields

$$\frac{\alpha''_{x2}}{k''_{xa}} = \frac{a(\epsilon'_a - \epsilon'_2)k_0^2 \sin(2\phi'_a) + \alpha'_{x2} \sin(2k'_{xa}a) \cos(2\phi'_a - 2k'_{xa}a)}{[\cos(2\phi'_a - 2k'_{xa}a)k'_{xa} + D(\epsilon'_a - \epsilon'_2)k_0^2 \sin(2\phi'_a - 2k'_{xa}a)] \sin(2k'_{xa}a)}, \quad (3.68)$$

where we have made use of  $\alpha_{x2}^{\prime 2} + k_{xa}^{\prime 2} = (\epsilon'_a - \epsilon'_2)k_0^2$ .

For TM mode solutions, the analysis is much more complex; we therefore simplify the problem by setting the loss tangent of the surrounding regions equal to zero,  $\tan\delta_2=0$ . Then, in a similar way to the TE case, we find that

$$\phi_a'' = \varepsilon_2' \varepsilon_a' \frac{k_{xa}' \alpha_{x2}'' + k_{xa}' \alpha_{x2}' \tan \delta_a - \alpha_{x2}' k_{xa}''}{\varepsilon_2'^2 k_{xa}'^2 + \varepsilon_a'^2 k_{xa}''^2}. \quad (3.69)$$

Substitution into equation (3.65) gives

$$\frac{\alpha_{x2}''}{k_{xa}''} = \frac{a(\varepsilon_a'^2 \alpha_{x2}' + \varepsilon_2'^2 k_{xa}'^2) k_0^2 \sin(2\phi_a') + \varepsilon_2' (\alpha_{x2}' k_0^2 \varepsilon_a' - 2\alpha_{x2}' k_{xa}'^2) \sin(2k_{xa}' a) \cos(2\phi_a' - 2k_{xa}' a)}{[D(\varepsilon_a'^2 \alpha_{x2}' + \varepsilon_2'^2 k_{xa}'^2) k_0^2 \sin(2\phi_a' - 2k_{xa}' a) - \varepsilon_2' (k_{xa}' k_0^2 \varepsilon_a' + 2k_{xa}' \alpha_{x2}'^2) \cos(2\phi_a' - 2k_{xa}' a) k_{xa}'] \sin(2k_{xa}' a)} \quad (3.70)$$

We require the attenuation constant  $\alpha_z$ . Therefore, equating the imaginary parts of equation (3.3) gives

$$2k_{xa}' k_{xa}'' = -\varepsilon_a' k_0^2 \tan \delta_a - 2\beta_z \alpha_z \quad (3.71)$$

and

$$2\alpha_{x2}' \alpha_{x2}'' = \varepsilon_2' k_0^2 \tan \delta_2 + 2\beta_z \alpha_z, \quad (3.72)$$

where the products and squares of all small terms have been neglected. Dividing equation (3.72) by equation (3.71) and solving for  $\alpha_z$  we obtain

$$\alpha_z = -k_0^2 \frac{\left( \alpha_{x2}' \frac{\alpha_{x2}''}{k_{xa}''} \varepsilon_a' \tan \delta_a + k_{xa}' \varepsilon_2' \tan \delta_2 \right)}{2\beta_z \left( \alpha_{x2}' \frac{\alpha_{x2}''}{k_{xa}''} + k_{xa}' \right)} \quad (3.73)$$

for TE modes, where  $\alpha_{x2}''/k_{xa}''$  is given by equation (3.68). Also,

$$\alpha_z = -k_0^2 \frac{\left( \alpha'_{x2} \frac{\alpha''_{x2}}{k''_{xa}} \epsilon'_a \tan \delta_a \right)}{2\beta_z \left( \alpha'_{x2} \frac{\alpha''_{x2}}{k''_{xa}} + k'_{xa} \right)} \quad (3.74)$$

for TM modes, where  $\alpha''_{x2}/k''_{xa}$  is given by equation (3.70).

We notice that equation (3.63) is identical to the symmetrical guidance condition for a lossless guide, equation (3.28). Therefore, we can solve for a given structure in the usual manner and then use the above approximate expressions to calculate  $\alpha_z$  directly from  $\beta_z$  and the waveguide parameters. Equation (3.73) and (3.74) are complicated expressions, however they can be evaluated more easily than the original coupled transcendental equation in (3.60). Furthermore, a test on the convergence of the expressions reveals a similar range of validity as the single guide. Unfortunately, a study of the approximate expressions for asymmetrical coupled slab waveguides using the above method results in huge expressions and consequently is of little use. Therefore, solutions for lossy asymmetrical structures are best obtained by solving equation (3.25) numerically for the complex roots.

Figure 3.17 and Figure 3.18 show typical curves for the normalised attenuation constant of a symmetrical coupled structure. Figure 3.17 shows TE solutions and Figure 3.18 shows TM. In both cases  $2a=2b$ ,  $\epsilon_2=1$ ,  $\epsilon'_a=\epsilon'_b=2.07$  and  $\tan\delta_a=\tan\delta_b=3.0 \times 10^{-4}$ . We notice several interesting features from Figure 3.17 and Figure 3.18. Firstly, as expected, the attenuation constant is less for the low frequency solutions. Secondly, in a similar way to the real part of the propagation constant,  $\alpha_z$  converges to the isolated attenuation constant for increasing  $2D$  and is equal to a guide of width  $4a$  when  $2D=0$ . This is as expected since the equations in section 3.1.4 are all valid for guides with complex permittivities. Finally, the odd mode solutions increase with  $2D$ , reach a maximum and then decrease slightly as they converge to the isolated value. For the even modes,  $\alpha_z$  decreases as  $2D$  increases, reaches a minimum and then increases with  $2D$ , finally converging to the isolated value. This means that for some values of  $2D$  the even mode of the coupled structure has a lower attenuation constant than that of the isolated dielectric waveguide. This may have some implications on low-loss propagation.

Figure 3.19 and Figure 3.20 show curves of the attenuation constant for asymmetrical structures with  $2a=0.4\lambda_0$ ,  $\epsilon_2=1$ ,  $\epsilon'_a=\epsilon'_b=2.07$  and  $\tan\delta_a=\tan\delta_b=3.0\times 10^{-4}$ . Again Figure 3.19 shows TE solutions, Figure 3.20 shows TM. In a similar way to the real part, we find that the attenuation constant of the odd mode converges to that of the isolated value of guide B (the smaller guide), and the even mode to that of guide A.

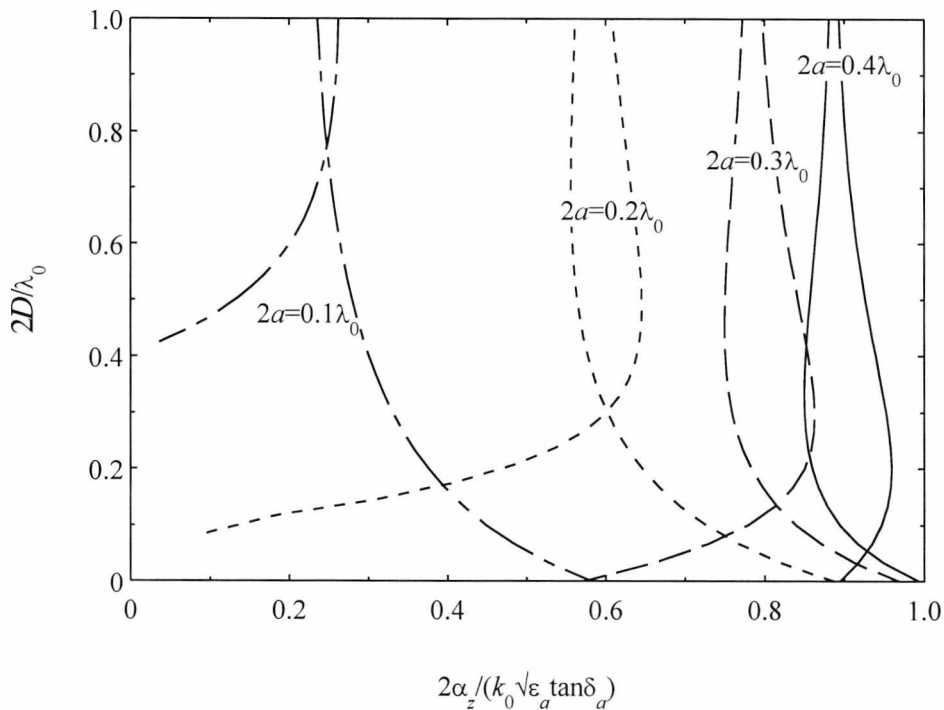


Figure 3.17. Normalised attenuation constant for TE mode symmetrical coupled slab waveguide.  $2a=2b$ ,  $\epsilon_2=1$ ,  $\epsilon'_a=\epsilon'_b=2.07$  and  $\tan\delta_a=\tan\delta_b=3.0\times 10^{-4}$ .

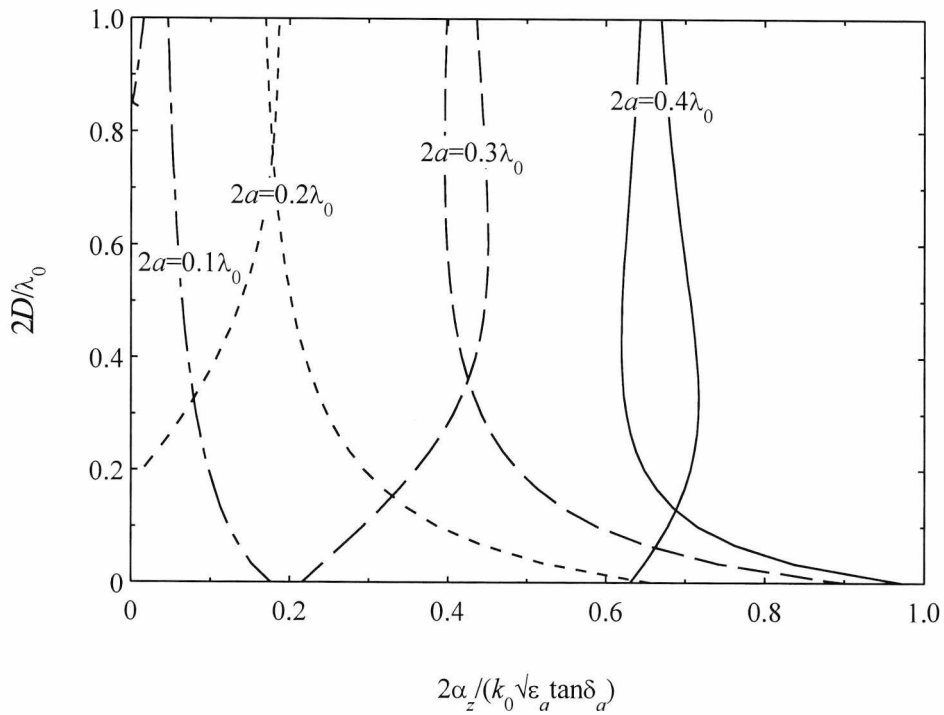


Figure 3.18. Normalised attenuation constant for TM symmetrical coupled slab waveguide.  $2a=2b$ ,  $\epsilon_2=1$ ,  $\epsilon'_a = \epsilon'_b = 2.07$  and  $\tan\delta_a = \tan\delta_b = 3.0 \times 10^{-4}$ .

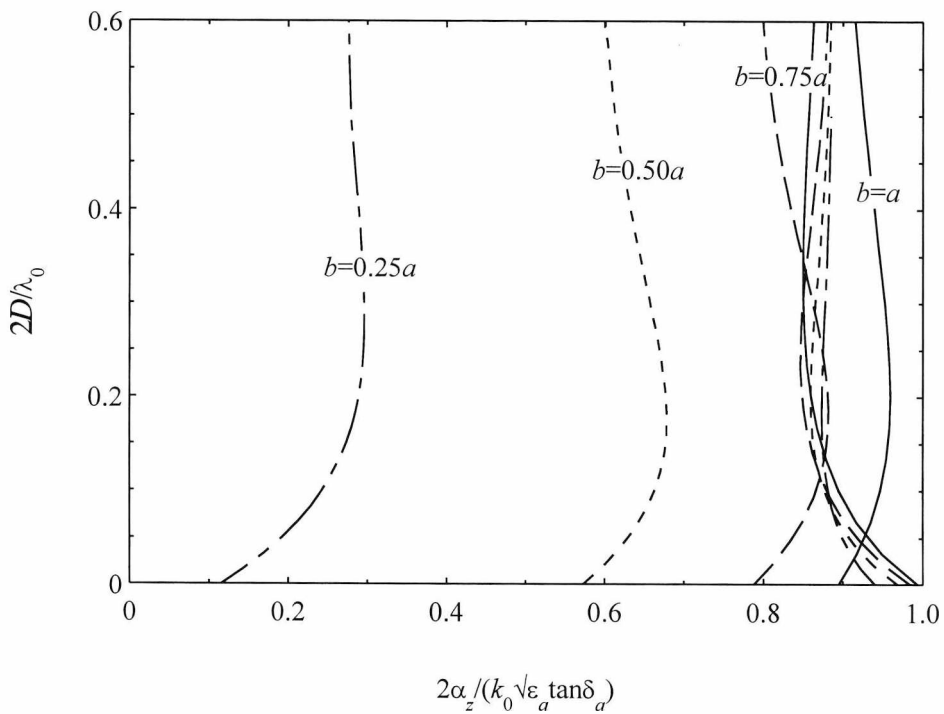


Figure 3.19. Normalised attenuation constant for TE width asymmetrical coupled slab waveguide.  $2a=0.4\lambda_0$ ,  $\epsilon_2=1$ ,  $\epsilon'_a = \epsilon'_b = 2.07$  and  $\tan\delta_a = \tan\delta_b = 3.0 \times 10^{-4}$ .

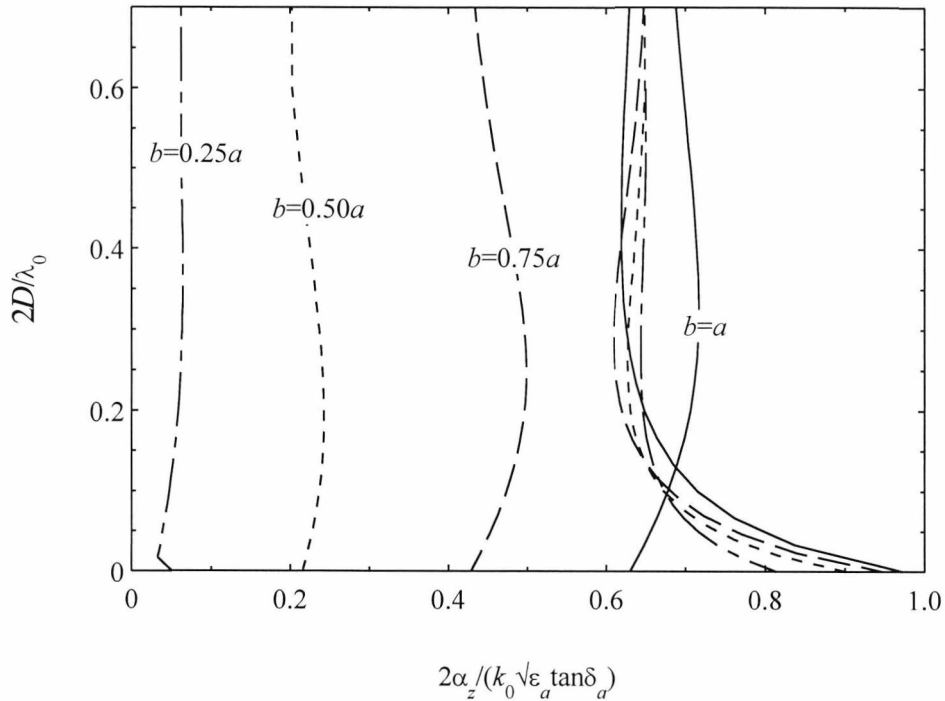


Figure 3.20. Normalised attenuation constant for TM width asymmetrical coupled slab waveguide.  $2a=0.4\lambda_0$ ,  $\epsilon_2=1$ ,  $\epsilon'_a=\epsilon'_b=2.07$  and  $\tan\delta_a=\tan\delta_b=3.0\times 10^{-4}$ .

### 3.5 THE EDC METHOD FOR COUPLED GUIDES

As in Chapter 2, we use the slab guide solutions in the effective dielectric constant method to obtain results for the more useful finite dimensioned rectangular dielectric waveguide. Only the conventional EDC method is considered since it is envisaged that the expressions in equation (2.109) and (2.110) are different for coupled structures. This is because the asymptotic field profiles used in Chiang's DEIM [23] will not be the same for coupled guides. It should be noted that the EDC method has been applied to coupled structures before [24], however, the analysis has relied on coupled mode theory and is therefore only valid for symmetrical guides with large separations. Again, we use the convenient shorthand notation:

$$\beta_{y(1)} = [TE^{coup}(\epsilon_2 | \epsilon_a | \epsilon_2 | \epsilon_b | \epsilon_2), TM^{2d}(\epsilon_2 | \epsilon_{eff} | \epsilon_2)] \quad (3.75)$$

$$\beta_{x(1)} = [TM^{coup}(\epsilon_2 | \epsilon_a | \epsilon_2 | \epsilon_b | \epsilon_2), TE^{2d}(\epsilon_2 | \epsilon_{eff} | \epsilon_2)] \quad (3.76)$$

That is, we first evaluate the TE (TM) complex propagation constants of a coupled slab waveguide. This gives us an effective permittivity and loss tangent. We then use these values to construct a second slab waveguide of width  $2d$  and complex permittivity  $\epsilon_{eff}(1-j\tan\delta_{eff})$ . The TM (TE) solutions of this second structure are then an approximate value for the complex propagation constant of the coupled structure, Figure 3.21.

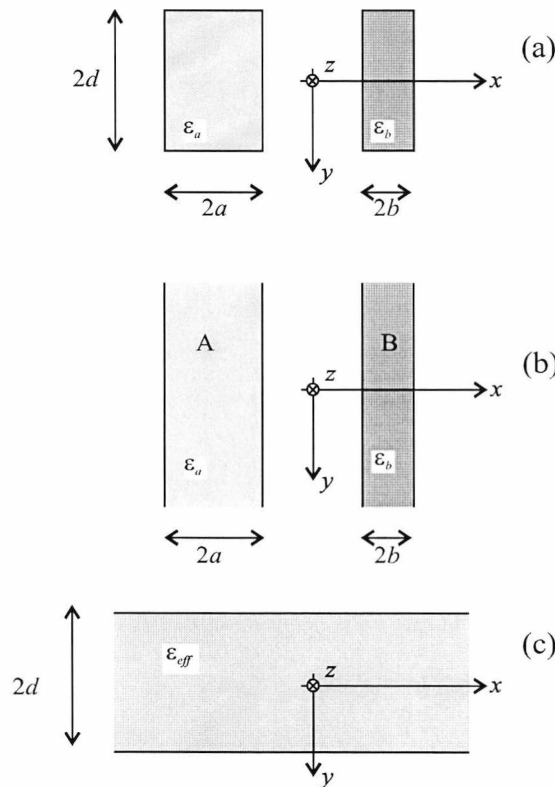


Figure 3.21. The EDC method for coupled dielectric guides. (a) Coupled structure. (b) Coupled slab guide. (c) Single slab of permittivity  $\epsilon_{eff}$ .

Figure 3.22, Figure 3.24, Figure 3.26 and Figure 3.28 show solutions using the EDC method for  $E^x$  mode propagation with  $f=25.0, 30.0, 35.0$  and  $40.0$  GHz, respectively. Similarly, Figure 3.23, Figure 3.25, Figure 3.27 and Figure 3.29 show  $E^y$  modes for  $f=25.0, 30.0, 35.0$  and  $40.0$  GHz, respectively. In each case  $2a=2b=3.556$  mm,  $2d=7.112$  mm,  $\epsilon_a=\epsilon_b=2.07$ ,  $\tan\delta_a=\tan\delta_b=3.0\times 10^{-4}$  and  $\epsilon_2=1$ . Solid lines show EDC solutions and, for comparison, the boxes show HFSS finite element results. We see that both the real and imaginary part of the propagation constant are in good agreement, particularly as the frequency increases. We further observe that the even mode solutions for both the attenuation and propagation constant are in better agreement than the odd modes. This is as expected since the odd mode is always more closer to cut-off than the even mode.

Solutions for asymmetrical structures were also considered. Figure 3.30 and Figure 3.31 show width asymmetry results for  $E^x$  and  $E^y$  modes, respectively. In each case  $f=25.0$  GHz,  $2a=3.556$  mm,  $2b=1.778$  mm,  $2d=7.112$  mm,  $\epsilon_a=\epsilon_b=2.07$ ,  $\tan\delta_a=\tan\delta_b=3.0\times 10^{-4}$  and  $\epsilon_2=1$ . Similarly, Figure 3.32 and Figure 3.33 show permittivity asymmetry results for  $E^x$  and  $E^y$  modes, respectively. In each case  $f=30.0$  GHz,  $2a=2b=3.556$  mm,  $2d=7.112$  mm,  $\epsilon_a=2.254$ ,  $\epsilon_b=2.07$ ,  $\tan\delta_a=1.5\times 10^{-4}$ ,  $\tan\delta_b=3.0\times 10^{-4}$  and  $\epsilon_2=1$ . Once more, solid lines show EDC solutions and boxes show HFSS results. Again, we observe good agreement between the EDC results and those from the HFSS finite element solver. However, we see from Figure 3.30 and Figure 3.31 that some of the HFSS solutions appear to be erroneous. These points are probable spurious modes, since HFSS solves for all of the modes that the structure can support. This includes modes that exist in the surrounding medium and may not necessarily be the guided modes of the waveguide. This of course highlights a major advantage that the EDC method has over commercial finite element electromagnetic packages, namely its simplicity. Each point in the HFSS results took about 45 minutes to compute on workstation. Furthermore, quite some time was needed for experimentation to obtain any sensible results. In contrast, the results using the EDC method only took a few seconds on a standard desktop PC.

Further results can be seen in the Appendix B.

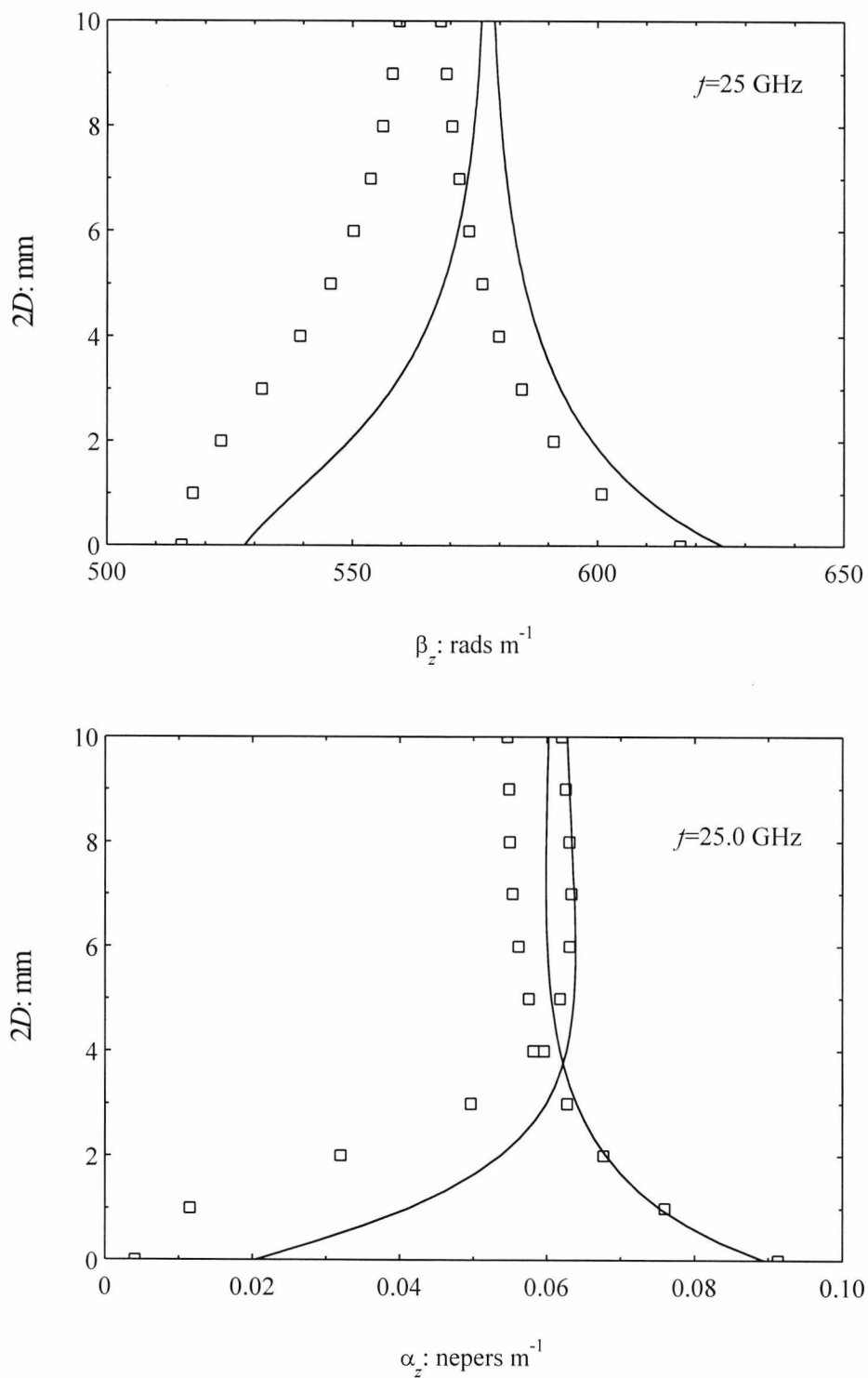


Figure 3.22.  $E^x$  modes for coupled dielectric waveguide with  $f=25$  GHz,  $2a=2b=3.556$  mm,  $2d=7.112$  mm,  $\epsilon_a=\epsilon_b=2.07(1-j3.0 \times 10^{-4})$  and  $\epsilon_2=1.0$ . Solid lines are EDC solutions boxes are HFSS solutions.

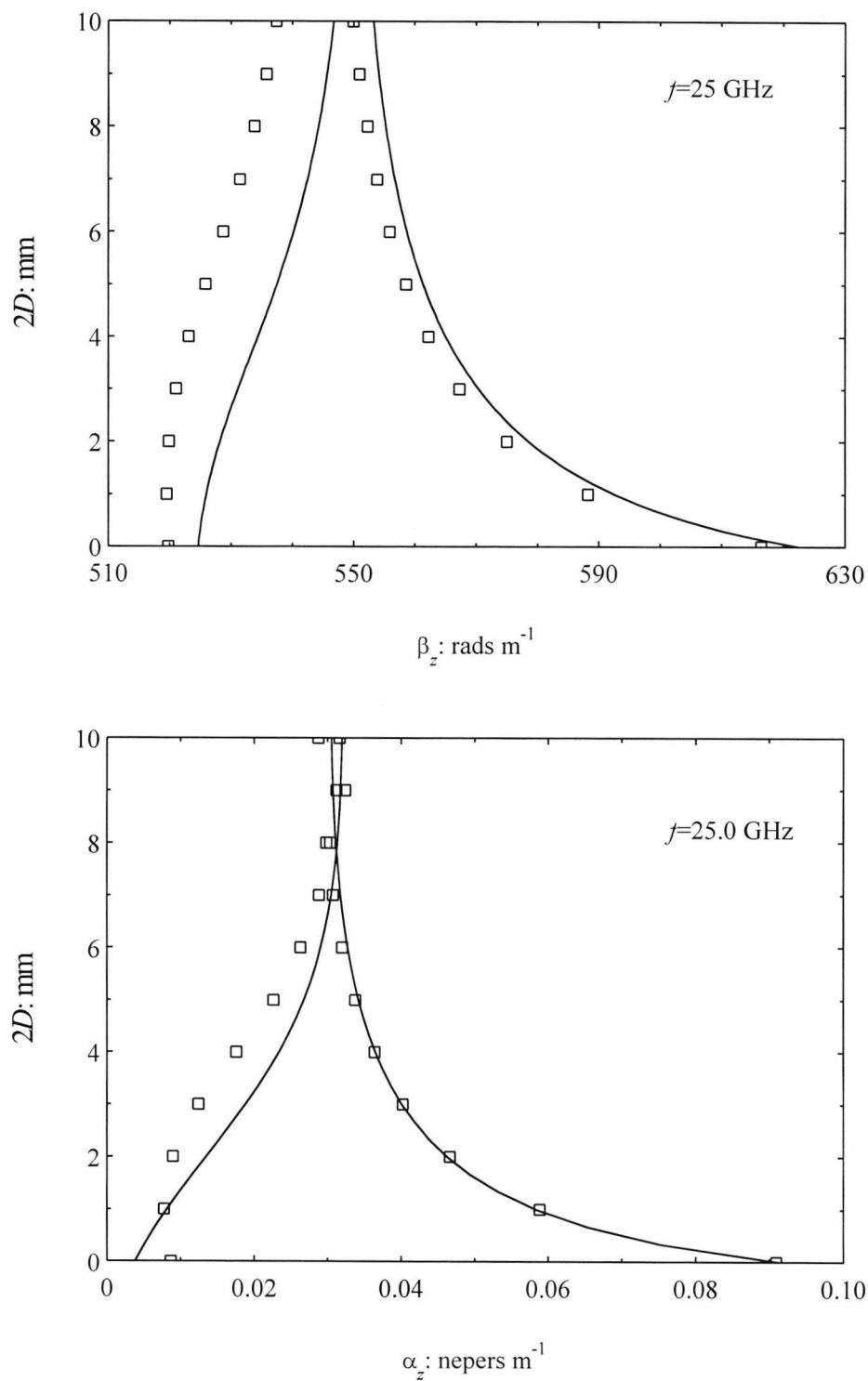


Figure 3.23.  $E^y$  modes for coupled dielectric waveguide with  $f=25$  GHz,  $2a=2b=3.556$  mm,  $2d=7.112$  mm,  $\epsilon_a=\epsilon_b=2.07(1-j3.0\times 10^{-4})$  and  $\epsilon_2=1.0$ . Solid lines are EDC solutions boxes are HFSS solutions.

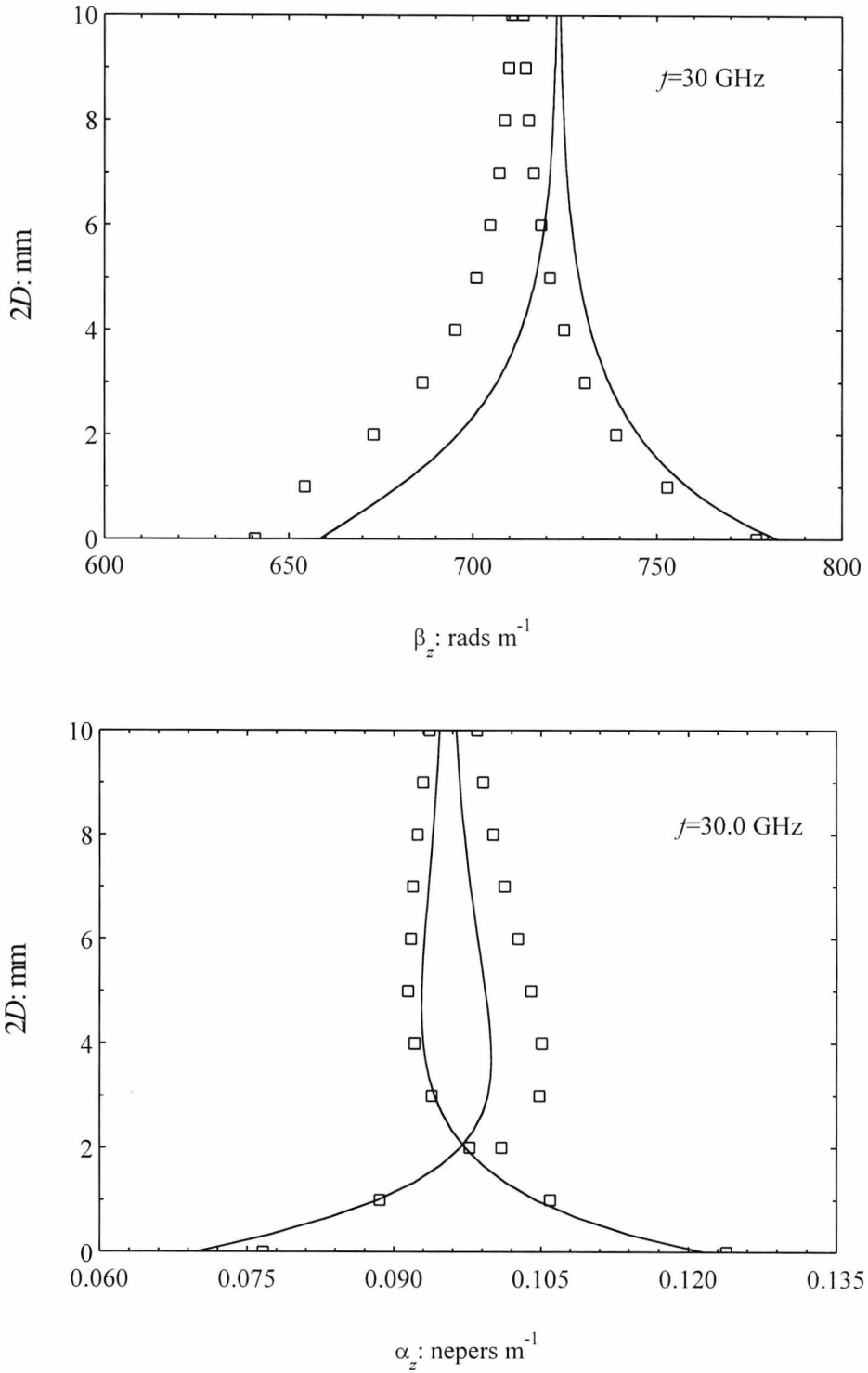


Figure 3.24.  $E^x$  modes for coupled dielectric waveguide with  $f=30$  GHz,  $2a=2b=3.556$  mm,  $2d=7.112$  mm,  $\epsilon_a=\epsilon_b=2.07(1-j3.0\times 10^{-4})$  and  $\epsilon_2=1.0$ . Solid lines are EDC solutions boxes are HFSS solutions.

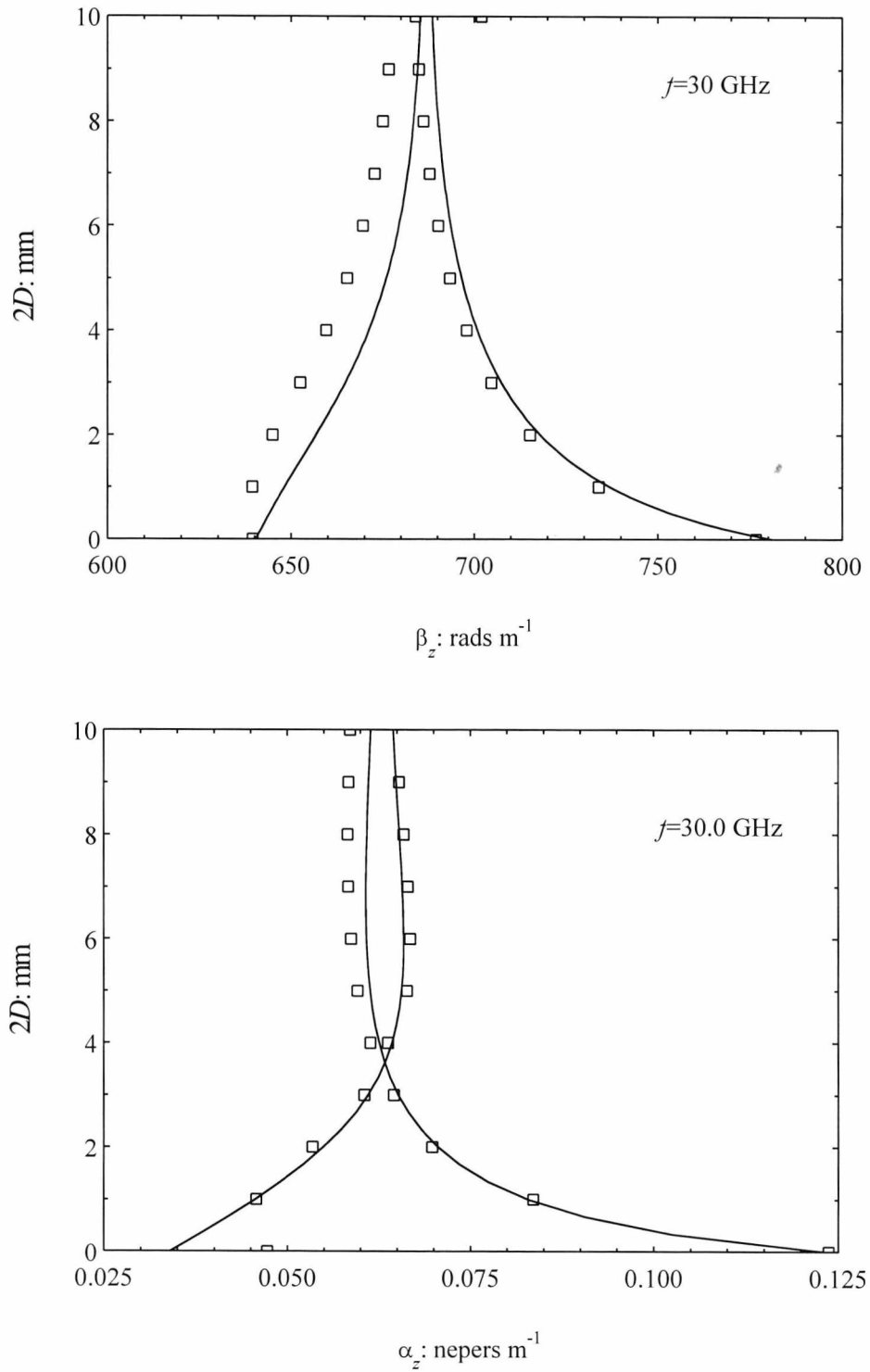


Figure 3.25.  $E^y$  modes for coupled dielectric waveguide with  $f=30$  GHz,  $2a=2b=3.556$  mm,  $2d=7.112$  mm,  $\epsilon_a=\epsilon_b=2.07$  and  $\epsilon_2=1.0$ . Solid lines are EDC solutions boxes are HFSS solutions.

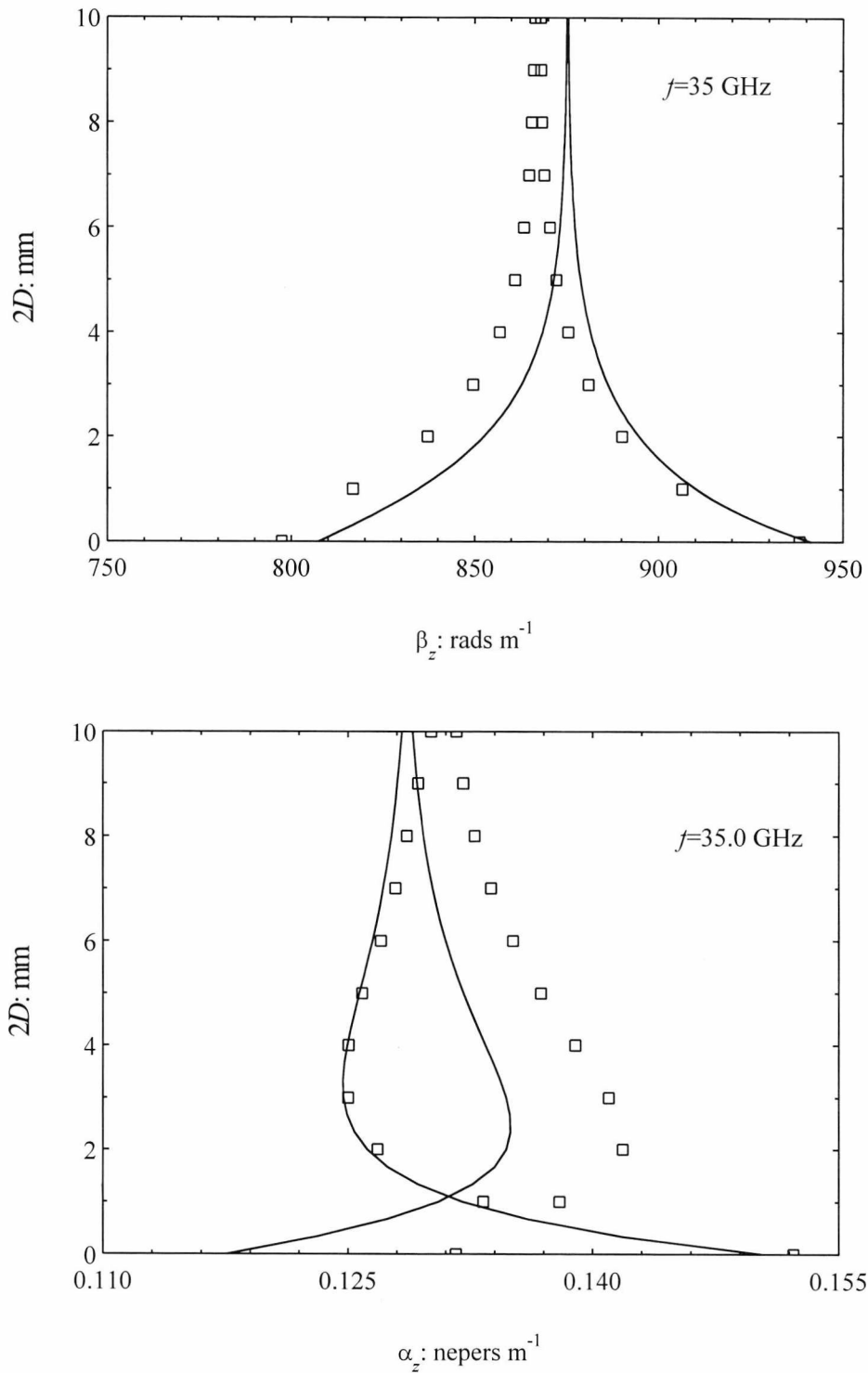


Figure 3.26.  $E^x$  modes for coupled dielectric waveguide with  $f=35$  GHz,  $2a=2b=3.556$  mm,  $2d=7.112$  mm,  $\epsilon_a=\epsilon_b=2.07(1-j3.0\times 10^{-4})$  and  $\epsilon_2=1.0$ . Solid lines are EDC solutions boxes are HFSS solutions.

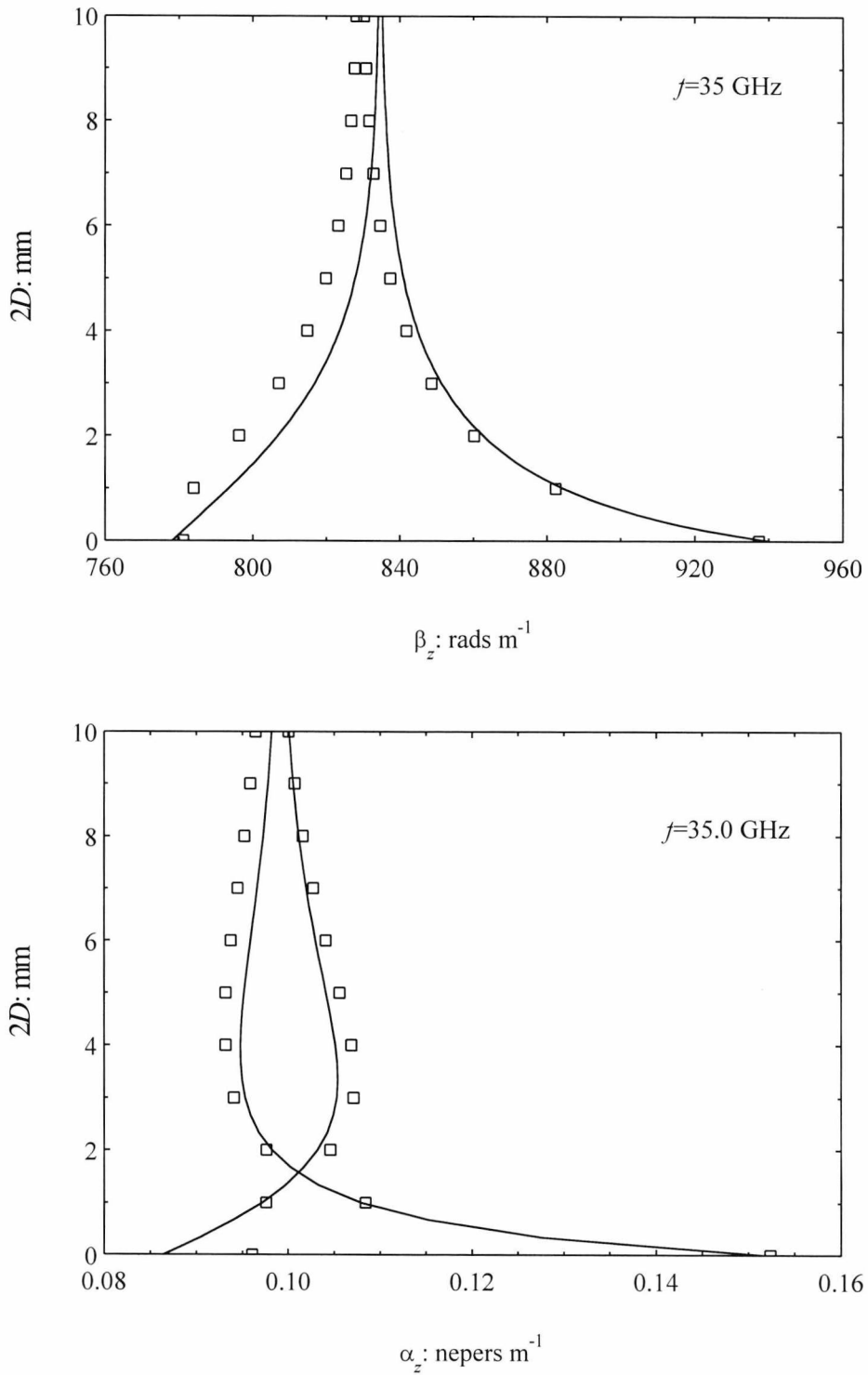


Figure 3.27.  $E^y$  modes for coupled dielectric waveguide with  $f=35$  GHz,  $2a=2b=3.556$  mm,  $2d=7.112$  mm,  $\epsilon_a=\epsilon_b=2.07(1-j3.0\times 10^{-4})$  and  $\epsilon_2=1.0$ . Solid lines are EDC solutions boxes are HFSS solutions.

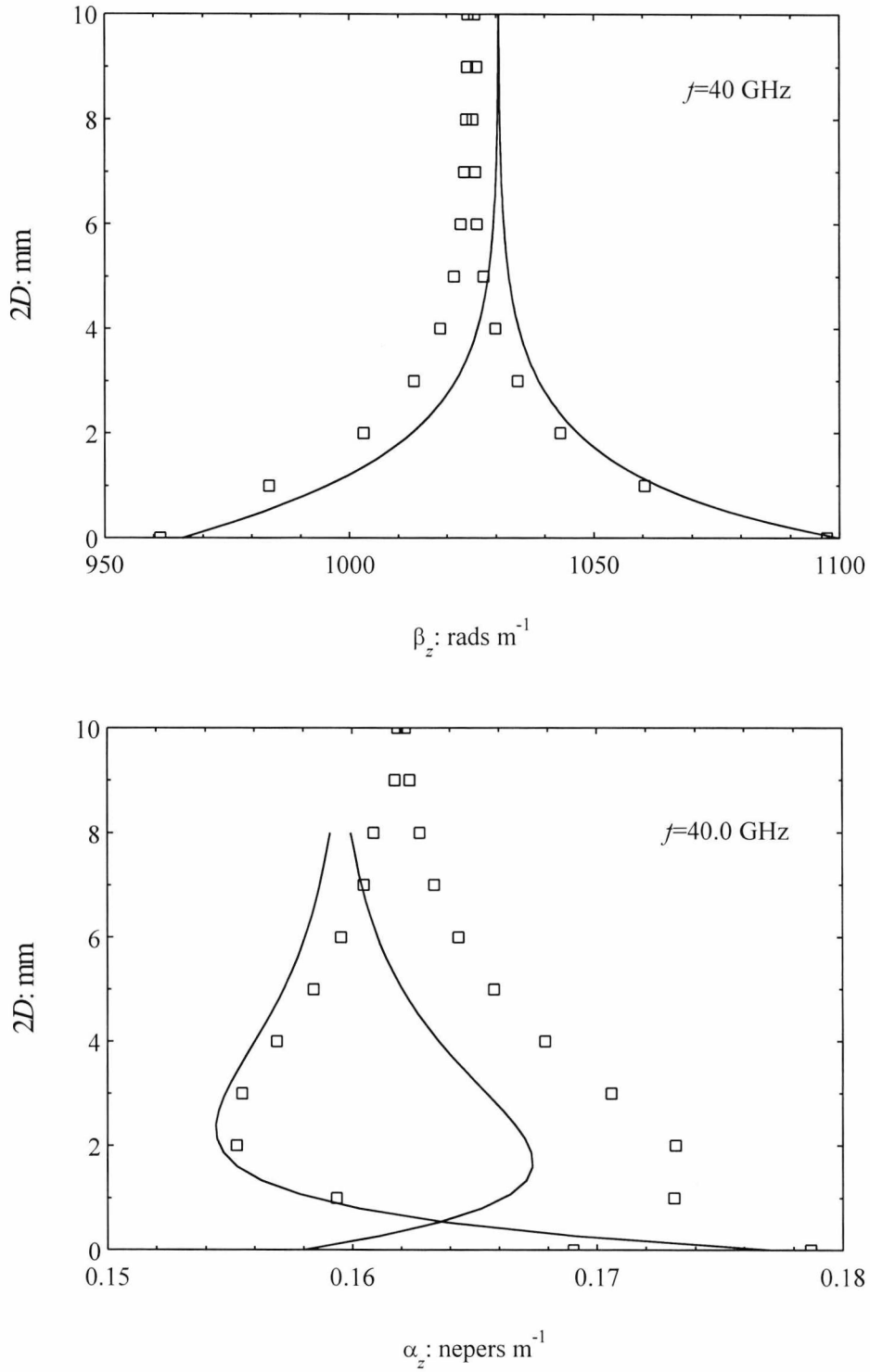


Figure 3.28.  $E^x$  modes for coupled dielectric waveguide with  $f=40$  GHz,  $2a=2b=3.556$  mm,  $2d=7.112$  mm,  $\epsilon_a=\epsilon_b=2.07(1-j3.0\times 10^{-4})$  and  $\epsilon_2=1.0$ . Solid lines are EDC solutions boxes are HFSS solutions.

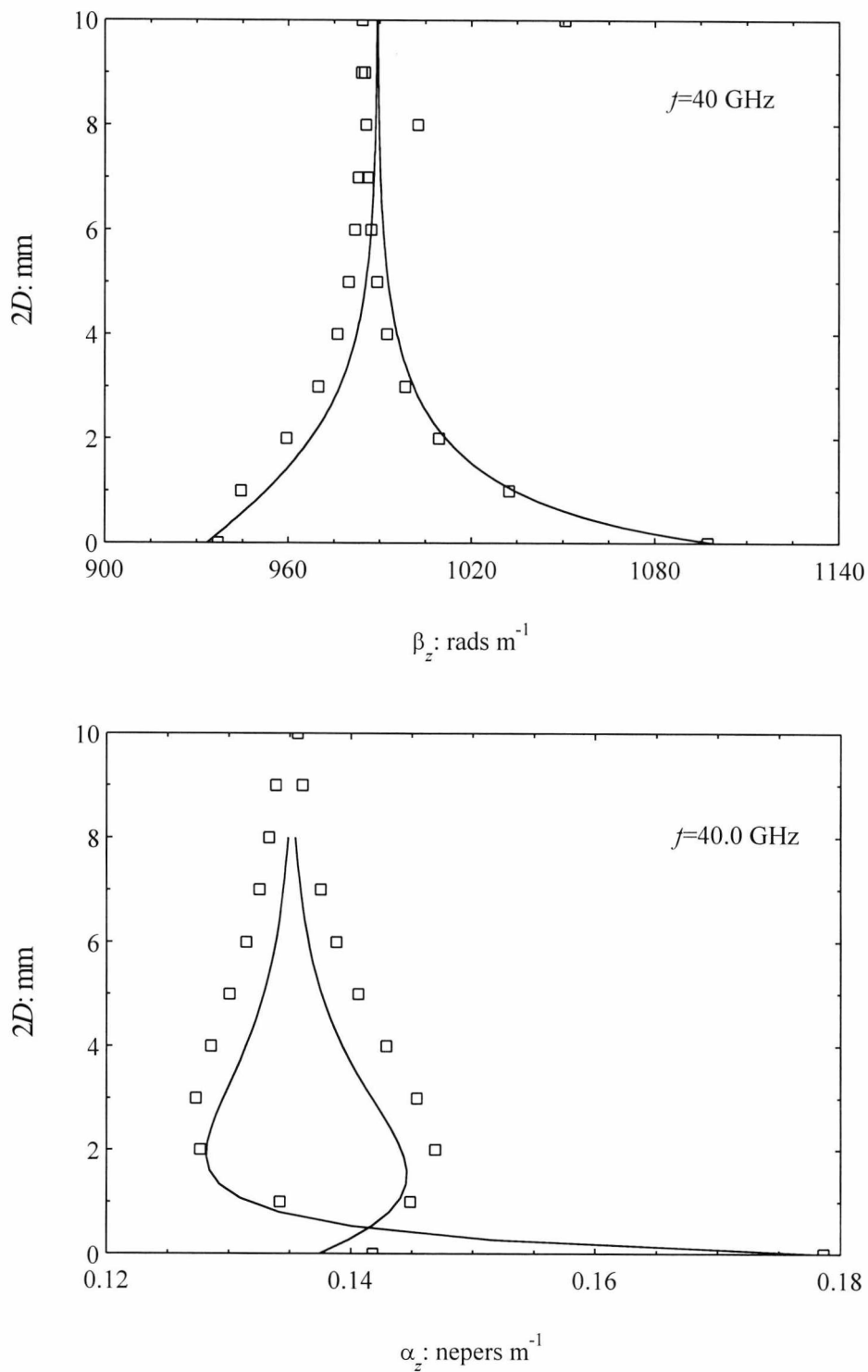


Figure 3.29.  $E^y$  modes for coupled dielectric waveguide with  $f=40$  GHz,  $2a=2b=3.556$  mm,  $2d=7.112$  mm,  $\epsilon_a=\epsilon_b=2.07(1-j3.0\times 10^{-4})$  and  $\epsilon_2=1.0$ . Solid lines are EDC solutions boxes are HFSS solutions.

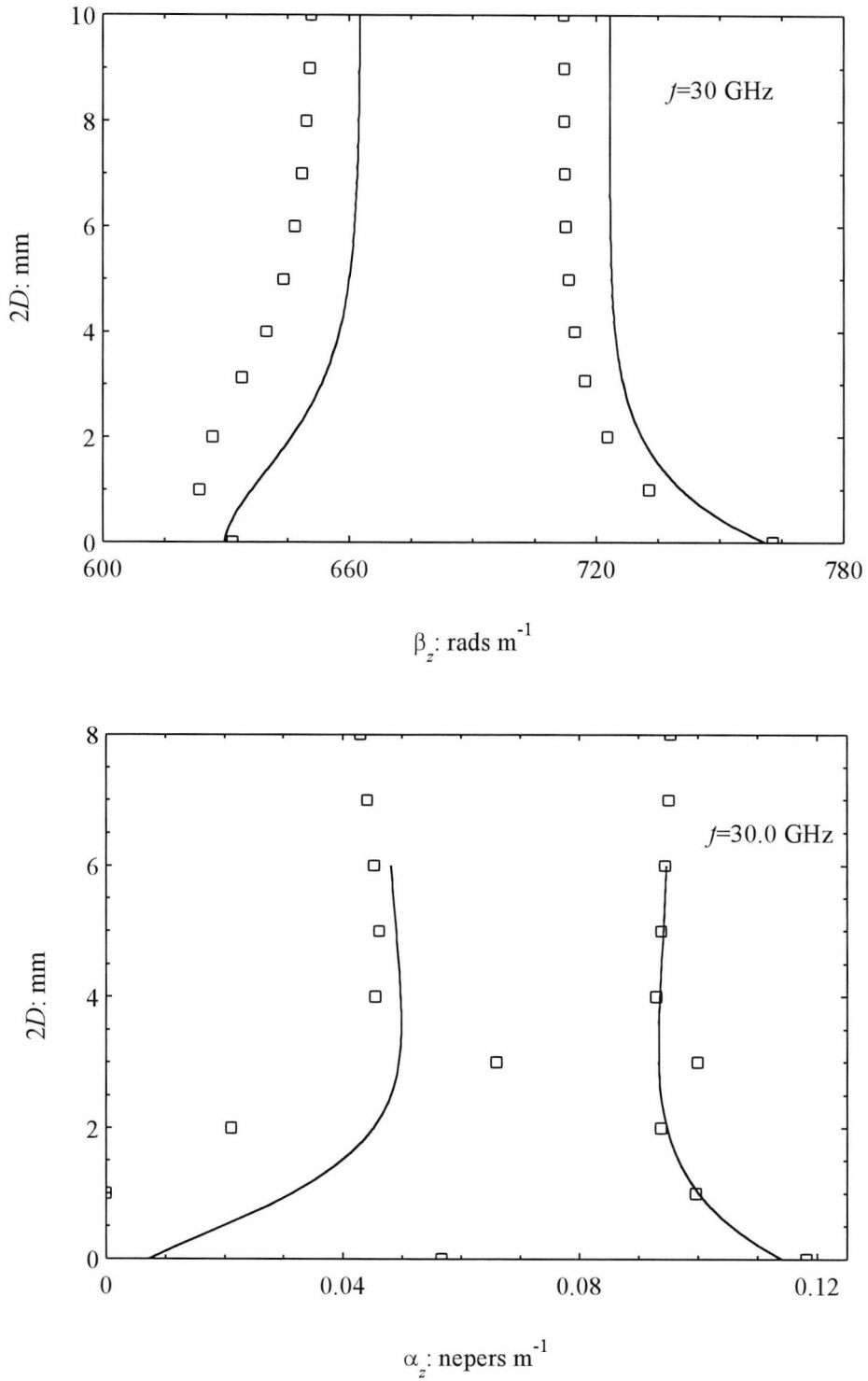


Figure 3.30.  $E^x$  modes for coupled dielectric waveguide with  $f=30$  GHz,  $2a=3.556$  mm,  $2b=1.778$  mm,  $2d=7.112$  mm,  $\epsilon_a=\epsilon_b=2.07(1-j3.0\times 10^{-4})$  and  $\epsilon_2=1.0$ . Solid lines are EDC solutions boxes are HFSS solutions.

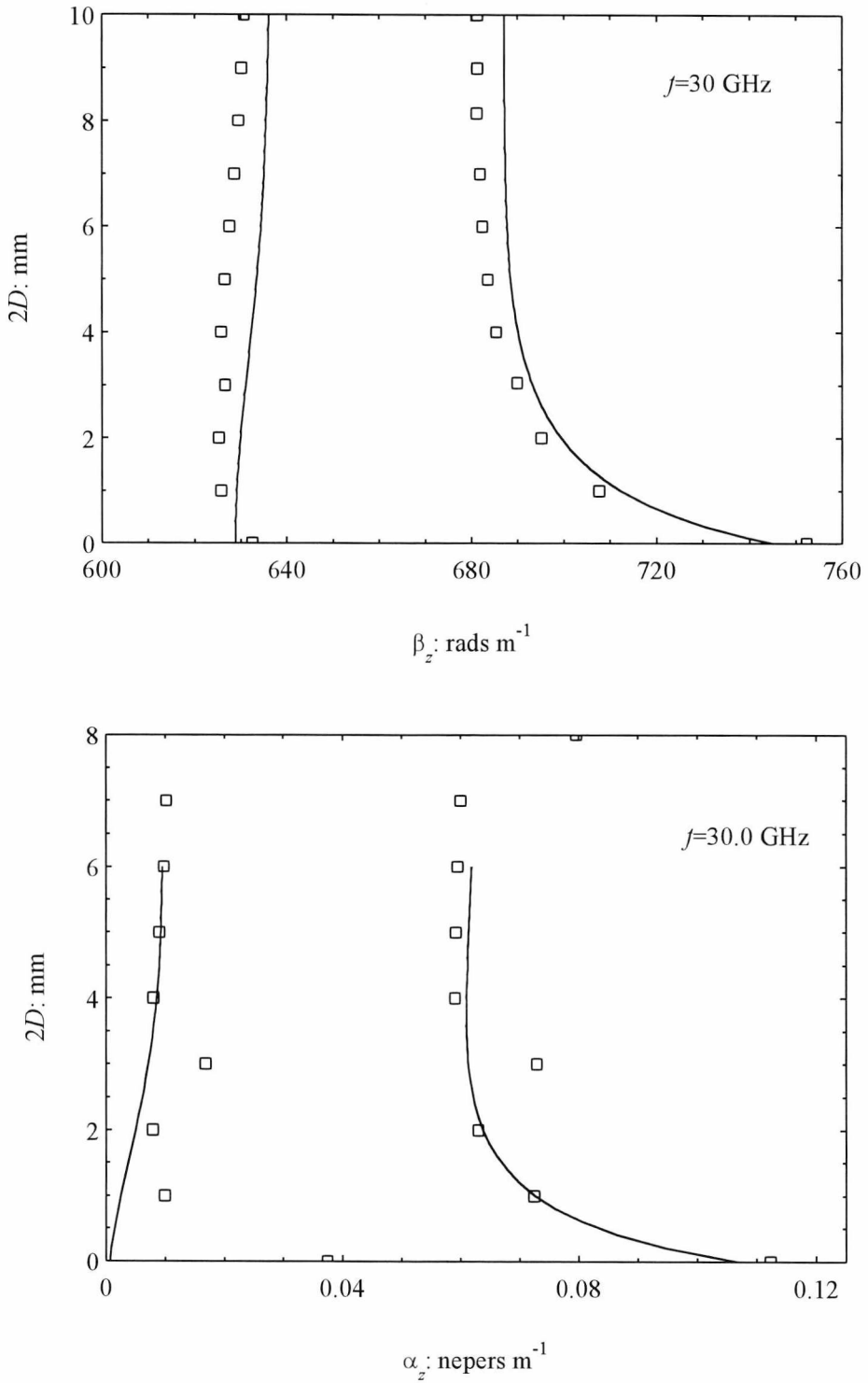


Figure 3.31.  $E^y$  modes for coupled dielectric waveguide with  $f=30 \text{ GHz}$ ,  $2a=3.556 \text{ mm}$ ,  $2b=1.778 \text{ mm}$ ,  $2d=7.112 \text{ mm}$ ,  $\epsilon_a=\epsilon_b=2.07(1-j3.0 \times 10^{-4})$  and  $\epsilon_2=1.0$ . Solid lines are EDC solutions boxes are HFSS solutions.

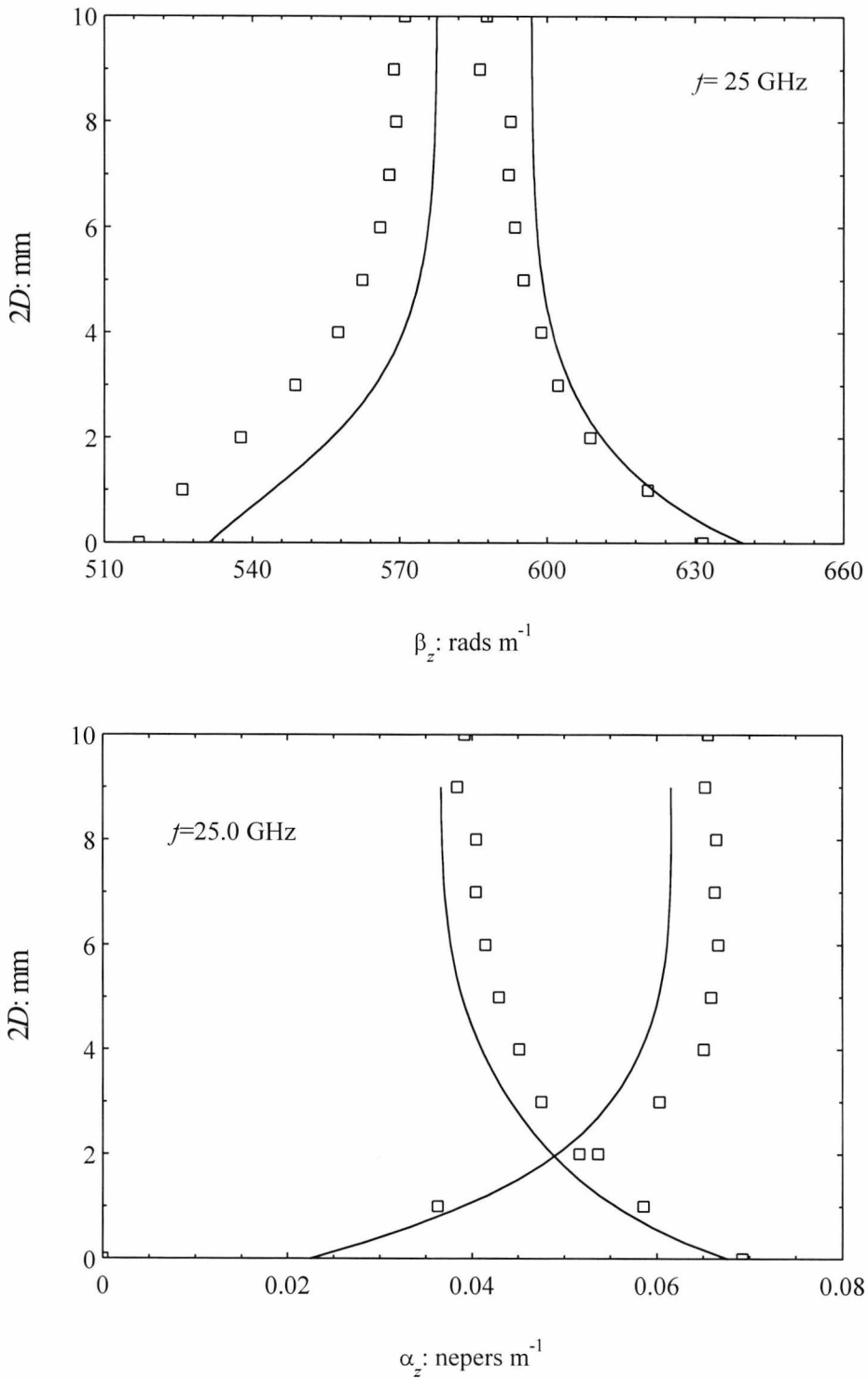


Figure 3.32.  $E^x$  modes for coupled dielectric waveguide with  $f=25 \text{ GHz}$ ,  $2a=2b=3.556 \text{ mm}$ ,  $2d=7.112 \text{ mm}$ ,  $\epsilon_a=2.254(1-j1.5 \times 10^{-4})$ ,  $\epsilon_b=2.07(1-j3.0 \times 10^{-4})$  and  $\epsilon_2=1.0$ . Solid lines are EDC solutions boxes are HFSS solutions.

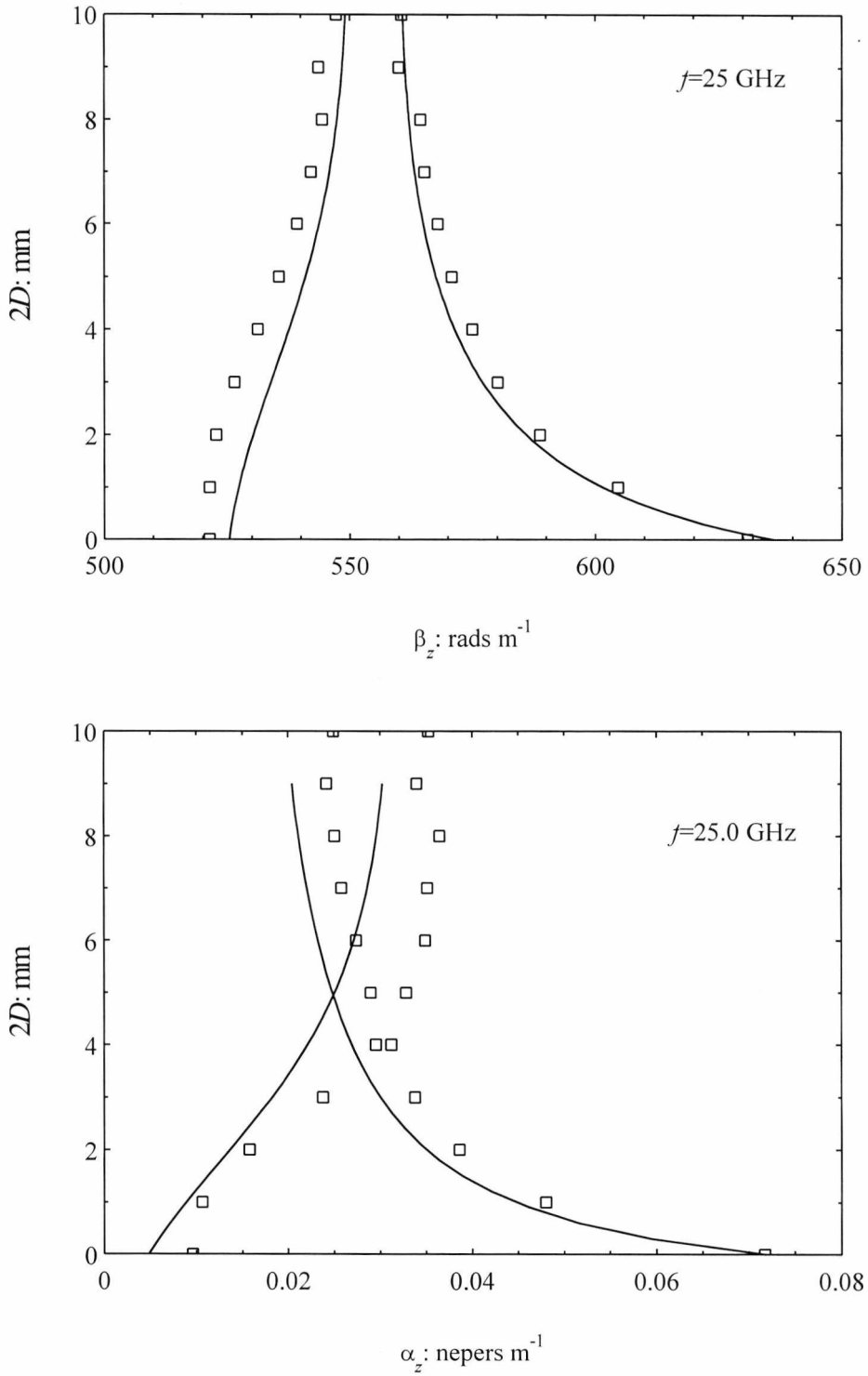


Figure 3.33.  $E^y$  modes for coupled dielectric waveguide with  $f=25$  GHz,  $2a=2b=3.556$  mm,  $2d=7.112$  mm,  $\epsilon_a=2.254(1-j1.5\times 10^{-4})$ ,  $\epsilon_b=2.07(1-j3.0\times 10^{-4})$  and  $\epsilon_2=1.0$ . Solid lines are EDC solutions boxes are HFSS solutions.

### 3.6 SUMMARY

In summary, an exact transcendental characteristic equation was presented for asymmetrical coupled slab waveguides with both width and permittivity asymmetry. The solution of this new equation is simpler than previous methods and, unlike coupled mode theories, is exact. Moreover, because the method is exact the solutions are valid for all guide separations and asymmetries. It was shown that coupled structures can become monomode for certain guide separations. Furthermore, expressions were derived for the cut-off separation. This phenomenon is exploited in Chapter 6 to design very low-loss phase-shifters.

Approximate expressions were obtained for the losses in symmetrical coupled waveguides and numerical results for asymmetrical coupled guides were given. It was shown that, for certain separations, the even mode had an attenuation constant less than that of the isolated waveguide. This may have implications for low-loss propagation.

Coupled slab solutions were used in the EDC method and were shown to be in good agreement with finite element results for both the propagation and attenuation constant. Both symmetrical and asymmetrical structures were considered and shown to be in similar agreement with HFSS results. However, due to the complexity of the problem, the finite element results appeared to display erroneous points for the case of permittivity asymmetry. This clearly highlights the advantages that the EDC technique has over finite element techniques, namely its speed and simplicity.

The expressions derived in this chapter form the basis of Chapter 6 where we use symmetrical and asymmetrical guides for the design of dielectric waveguide components.

---

**REFERENCES**

- 1 P. K. Ikäläinen and G. Matthaei, "Design of broad-band dielectric waveguide 3-dB couplers," *IEEE Trans Microwave Theory Tech.*, vol. MTT-35, no. 7, July 1987, pp. 621-628.
- 2 J. Rodríguez and A. Prieto, "Wide-band directional couplers in dielectric waveguide," *IEEE Trans Microwave Theory Tech.*, vol. MTT-35, no. 8, August 1987, pp. 681-686.
- 3 Y. Shen, D. Xu and C. Ling, "The design of an ultra-broad-band 3 dB coupler in dielectric waveguide," *IEEE Trans Microwave Theory Tech.*, vol. MTT-38, no. 6, June 1990, pp. 785-787.
- 4 G. L. Matthaei, D. C. Park, Y. M. Kim and D. L. Johnson, "A study of the filter properties of single and parallel-coupled dielectric-waveguide gratings," *IEEE Trans Microwave Theory Tech.*, vol. MTT-31, no. 10, October 1983, pp. 825-835.
- 5 P. K. Ikäläinen and G. Matthaei, "Design of dielectric waveguide bandpass filters using parallel-coupled gratings," *IEEE Trans Microwave Theory Tech.*, vol. MTT-34, no. 6, June 1986, pp. 681-688.
- 6 J. A. G. Malherbe and J. C. Olivier, "A bandstop filter constructed in coupled nonradiative dielectric waveguide," *IEEE Trans Microwave Theory Tech.*, vol. MTT-34, no. 12, December 1986, pp. 1408-1412.
- 7 P. R. Young, R. J. Collier and P. G. G. Bianconi, "A low loss phase shifter for dielectric waveguide using asymmetrical guides," *27<sup>th</sup> European microwave conference proceedings*, vol. 1, 1997, pp. 631-635.

- 
- 8 P. R. Young and R. J. Collier, "The design of dielectric waveguide components using the propagation characteristics of two parallel asymmetrical slab waveguides," *M+RF 96 conference proceedings*, 1996, pp. 373-383.
  - 9 P. R. Young and R. J. Collier, "A novel wavemeter for dielectric waveguide," *27<sup>th</sup> European microwave conference proceedings*, vol. 2, 1997, pp. 891-896.
  - 10 D. Marcuse, "The Coupling of Degenerate Modes in Two Parallel Dielectric Waveguides," *Bell Syst. Tech. J.*, Vol. 50, No. 6, pp 1791-1816, July-August 1971.
  - 11 A. W. Snyder, "Coupled-mode Theory for Optical Fibers," *J. Opt. Soc. Am.*, Vol. 62, No. 11, pp. 1267-1277, November 1972.
  - 12 A. Yariv, "Coupled-Mode Theory for Guided-Wave Optics," *J. Quant. Electron.*, Vol QE-9, No. 9, pp 919-933, September 1973.
  - 13 A Hardy, W Streifer, "Coupled Mode Theory of Parallel Waveguides," *J Lightwave Tech.*, Vol. LT-3, No. 5, pp 1135-1146, October 1985.
  - 14 D. Marcuse, "Directional couplers made of nonidentical asymmetric slabs. Part I: Synchronous couplers," *J. Lightwave Tech.*, vol. LT-5, no. 1, January 1987, pp. 113-118.
  - 15 Z. H. Wang and S. R. Seshadri, "Asymptotic theory of guided modes on two parallel, identical dielectric waveguides," *J. Opt. Soc. Am. A*, vol. 5, no. 6, June 1988, pp. 782-792.
  - 16 S. R. Seshadri, "Asymptotic theory of power transport by guided modes in two parallel, identical planar dielectric waveguides," *J. Appl. Phys.*, 72 (11), December 1992, pp. 5039-5046.

- 
- 17 W. V. McLevige, T. Itoh and R. Mittra, "New waveguide structures for the millimeter-wave and optical integrated circuits," *IEEE Trans. Microwave Theory Tech.*, vol. MTT-23, no. 10, October 1975, pp. 788-794.
  - 18 M. L. Boas, "Mathematical methods in the physical sciences," 2<sup>nd</sup> Ed., *John Wiley & Sons*, 1983, Chapter 2.
  - 19 E. Kreyszig, "Advanced engineering mathematics," *John Wiley & Sons*, 1993, Chapter 12.
  - 20 D. L. Lee, "Electromagnetic principles of integrated optics," *John Wiley & Sons*, 1986, Chapter 4.
  - 21 D. Marcuse, "Theory of dielectric optical waveguides," *Academic Press*, 1974, Chapter 1.
  - 22 G. H. Owyang, "Foundations of optical waveguides," *Edward Arnold*, 1981, Chapter 2.
  - 23 K. S. Chiang, "Analysis of the effective-index method for the vector modes of rectangular-core dielectric waveguides," *IEEE Trans. Microwave Theory Tech.*, vol. 44, no. 5, May 1996, pp. 692-700.
  - 24 K. S. Chiang, "Effective-index method for the analysis of optical waveguide couplers and arrays; An asymptotic theory," *J. Lightwave Technol.*, vol. 9, no. 1, January 1991, pp. 62-72.

---

## 4. DIELECTRIC WAVEGUIDE MEASUREMENTS

---

In this chapter, we obtain experimental verifications of the techniques presented in chapters 2 and 3. Two methods are considered for the measurement of the propagation characteristics of dielectric waveguides. Namely, the insertion loss method [1] and the resonant cavity method [2]. However, due to its advantages, experimental results are only obtained using the resonant cavity approach. For simplicity, experimental results are carried out at 10 GHz and 30 GHz. At these frequencies, the physical dimensions of the waveguides and cavities are much larger than at millimetre wavelengths making the task far simpler. Measurements are shown to be in good agreement with the techniques of chapters 2 and 3. Furthermore, the results are shown to be in excellent agreement with HFSS finite element results.

### 4.1 THE INSERTION LOSS TECHNIQUE

The insertion loss technique is the simplest method for the measurement of the propagation characteristics of dielectric waveguides. A simplified schematic of the technique is shown in Figure 4.1. Energy is launched into a dielectric waveguide via a waveguide horn. The received power at the other end of the waveguide is then measured via another horn. Due to the discontinuities between the waveguide and the horns, standing waves are set up along the guide. This allows us to measure the guided wavelength with a field probe and therefore calculate  $\beta_z$ . The attenuation constant  $\alpha_z$  is obtained directly from the received power.



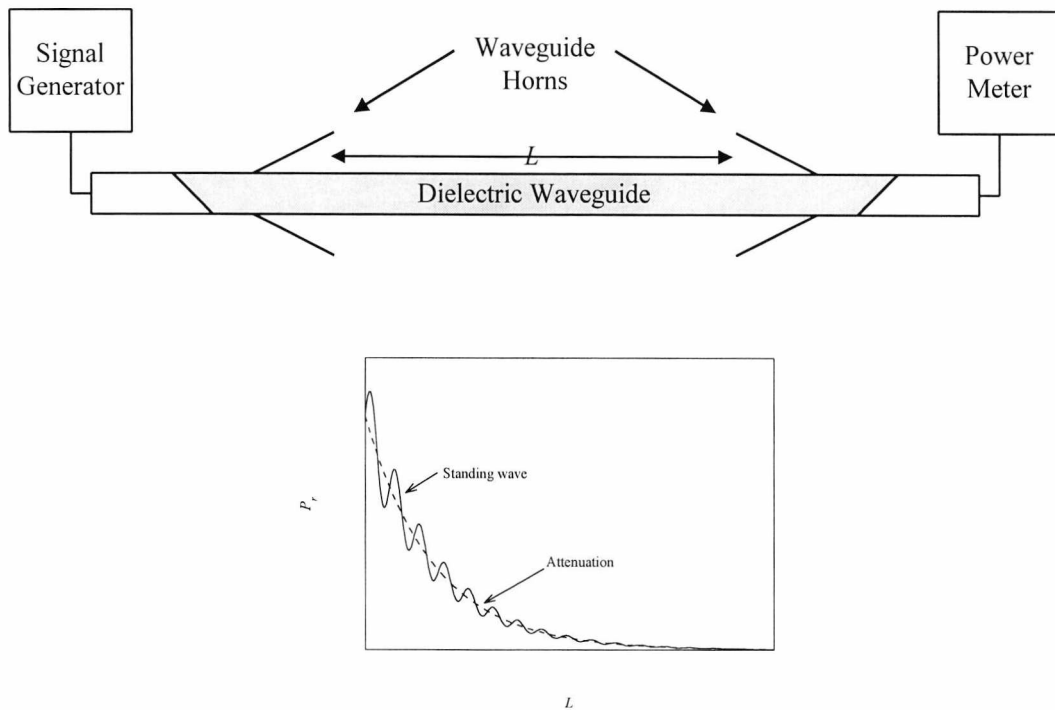


Figure 4.1. The insertion loss technique.

Unfortunately, the insertion loss technique has several disadvantages for measuring small attenuation constants. Firstly, very large lengths of dielectric waveguide are required since the losses are very small. Secondly, the standing waves set up in the dielectric waveguide because of the waveguide to horn transitions (see Figure 4.1) affect the attenuation measurement. Therefore, to account for the standing waves, measurements must be obtained for many different waveguide lengths. Finally, exciting sufficient amounts of energy in some of the dielectric waveguide modes can be a problem, particularly for coupled structures.

## 4.2 THE OPEN RESONANT CAVITY TECHNIQUE

Due to the disadvantages of the insertion loss technique, particularly the large lengths of dielectric waveguide that are required, the resonant cavity technique as described by Chandler [2] was used to obtain experimental results for the waveguide parameters. The technique involves two parallel conducting plates situated either end of a dielectric waveguide, refer to Figure 4.2. Energy is coupled in to and out of the waveguide by small coupling holes in the two end plates. By measuring the quality factor of the received power the attenuation constant can be determined.

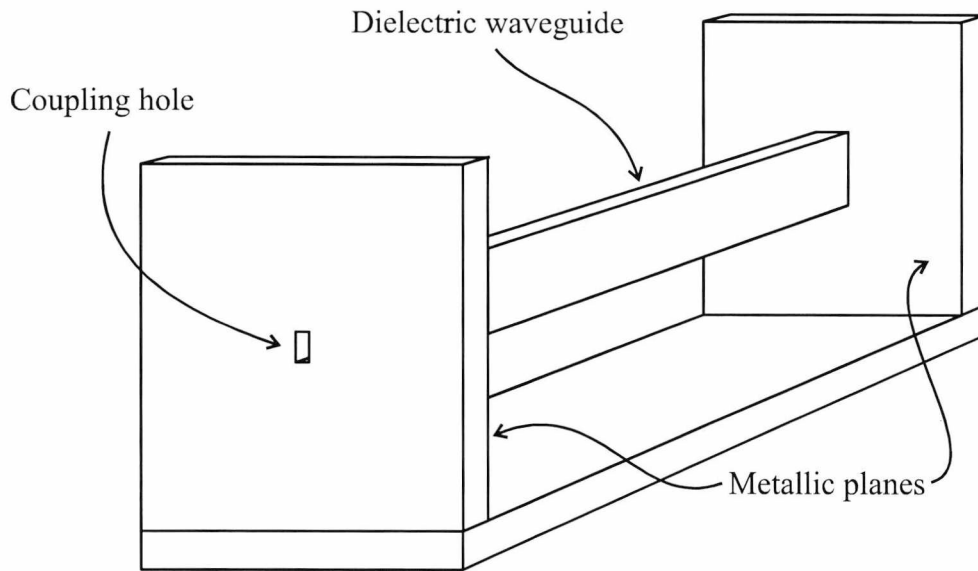


Figure 4.2. The open resonant cavity technique.

If very little energy is coupled to external circuits, the measured quality factor of the cavity can be defined as

$$\frac{1}{Q} = \frac{1}{Q_d} + \frac{1}{Q_w} + \frac{1}{Q_r} \quad (4.1)$$

Where:

$Q_d$  is associated with losses in the waveguide due to dielectric absorptions. It should be noted that here we mean absorptions for guided modes. There will of course be dielectric absorptions for any radiation modes [3, 4] that may exist in the cavity. However, some of the continuum of radiation modes inherently have attenuation constants associated with them, even for the lossless case. Therefore, the losses due to radiation mode absorption are considered with the radiation quality factor  $Q_r$  (see below).

$Q_w$  is due to the finite conductivity of the end plates.

$Q_r$  is associated with the radiation losses. These arise from four main mechanisms. Firstly, inhomogeneities in the dielectric guide and any obstacles

in the cavity cause mode conversion and coupling into radiation modes. Secondly, imperfections in the end plates and any deviation from the parallel also cause mode conversions and therefore radiation. Thirdly, the finite extent of the end plates results in radiation from the tail end of the evanescent wave. Finally, there will be radiation from the coupling holes, since energy will be coupled into a continuum of radiation modes as well as the guided modes. Fortunately, if the end plates are sufficiently large so that the evanescent field has decayed approximately to zero, and the waveguide and end plates are carefully machined all but the latter of these can be neglected.

$Q_r$  and  $Q_w$  are both dependent on the cavity length  $L$ . This is easily explained when we consider the definition of the quality factor:

$$Q = \omega \frac{\bar{E}_S}{\bar{P}_L}, \quad (4.2)$$

where  $\bar{E}_S$  is the time-averaged energy stored and  $\bar{P}_L$  is the average power loss. If the cavity length is increased by a factor  $K$  then the stored energy in the guided modes will also increase by a factor  $K$ . However, the energy loss from the finite conductivity of the end plates remains the same since the transverse field profile is independent of the cavity length. This is not strictly true, since the energy from the coupling holes will excite not only the guided modes of the waveguide, but also a continuum of radiation modes. Fortunately, if the cavity is sufficiently long, the radiation modes from each end plate will not interfere with each other and thus the transverse field incident on the end plates is not a function of the cavity length. Furthermore, the amount of radiated energy will remain constant if the cavity is of sufficient length. Therefore, the energy loss from radiation, and the finite conductivity of the end plates remains constant, resulting in both  $Q_r$  and  $Q_w$  increasing by a factor  $K$ . The losses in the dielectric will clearly increase by a factor  $P$ , therefore  $Q_d$  remains constant.

We therefore express equation (4.1) in the following form

$$\frac{1}{Q} = \frac{1}{Q_d} + \frac{1}{Q_p} \quad (4.3)$$

with

$$\frac{1}{Q_p} = \frac{1}{Q_r} + \frac{1}{Q_w}. \quad (4.4)$$

For very long cavity lengths  $Q_p \gg Q_d$  and thus  $Q \cong Q_d$ . However, long cavities make mounting the dielectric waveguide difficult. Furthermore, materials such as PTFE (Polytetrafluoroethylene) are very flexible and tend to bend if the length is excessive. This problem can be overcome by measuring the  $Q$  for two different lengths  $L_1$  and  $L_2$ . Then

$$\frac{1}{Q}\Big|_{L=L_1} = \frac{1}{Q_d} + \frac{1}{Q_p}\Big|_{L=L_1} \quad (4.5)$$

and

$$\frac{1}{Q}\Big|_{L=L_2} = \frac{1}{Q_d} + \frac{1}{Q_p}\Big|_{L=L_2} \quad (4.6)$$

but since  $Q_p$  is directly proportional to length,

$$Q_p\Big|_{L=L_2} = \frac{L_2}{L_1} \cdot Q_p\Big|_{L=L_1}. \quad (4.7)$$

Thus

$$\frac{1}{Q_d} = \frac{L_2 Q\Big|_{L=L_2} - L_1 Q\Big|_{L=L_1}}{(L_2 - L_1) Q\Big|_{L=L_1} Q\Big|_{L=L_2}}. \quad (4.8)$$

It should be noted that both lengths should be sufficiently long so that the transverse field at the end plates is the same in both cases (see above).

The attenuation constant of the dielectric waveguide is of more importance than the quality factor. Shimabukuro [5] and Yeh [5, 6] showed that the attenuation constant is related to the quality factor of the cavity by

$$\alpha_z = \frac{v_p}{v_g} \frac{\beta_z}{2Q_d}, \quad (4.9)$$

where

$$v_p = \frac{\omega}{\beta_z} \quad (4.10)$$

and

$$v_g = \frac{\partial \omega}{\partial \beta_z}. \quad (4.11)$$

$\beta_z$  can be determined by measuring the guide wavelength  $\lambda_g$ . Therefore,

$$\beta_z = \frac{2\pi}{\lambda_g} = \frac{n\pi}{L}, \quad (4.12)$$

where  $n$  is the number of half wavelengths within the cavity. The phase velocity  $v_p$  and the group velocity  $v_g$  can be determined by constructing a  $\omega$ - $\beta$  diagram. This requires the measurement of the guide wavelength of the various different resonant peaks. The phase velocity is then given from equation (4.10) and the group velocity from equation (4.11).

#### 4.2.1 Dielectric Waveguides

The basic configuration of the measurement system is shown in Figure 4.3. Measurements were obtained for two different dielectric waveguides. One made from PTFE, the other from Polyethylene. In each case, the waveguide dimensions were  $2a=7.112\text{mm}$  by  $2b=3.556\text{mm}$ . Both  $E_{11}^y$  and  $E_{11}^x$  mode propagation was investigated with the different polarisations achieved simply by rotating the dielectric waveguide through 90 degrees. The quality factors were measured for two different waveguide lengths  $L=200\text{mm}$  and  $L=100\text{mm}$ . Typical curves of the resonant frequencies can be seen in Figure 4.16. As expected the resonant peaks for the 100mm cavity almost coincide with those of the 200mm. Of course only every other mode exists on the 100mm cavity since the boundary conditions require a field

minima at  $z=100\text{mm}$ , whereas on the 200mm cavity both field minima and maxima can exist at  $z=100\text{mm}$ .

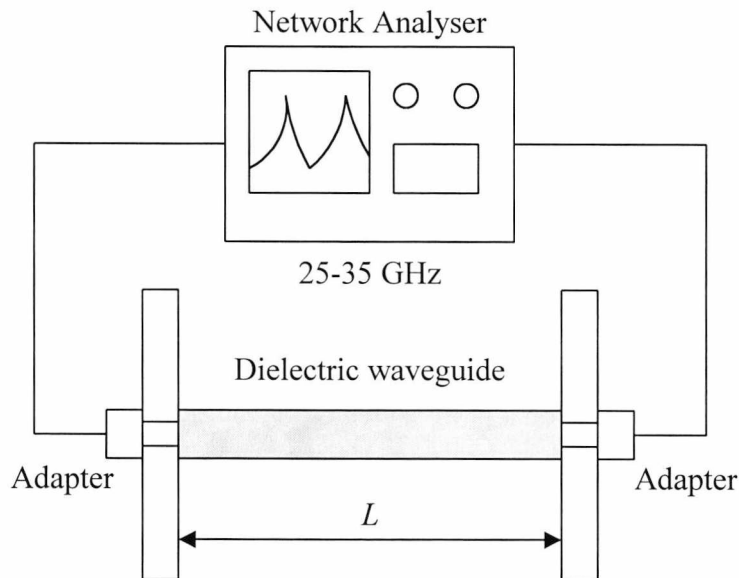


Figure 4.3. Schematic of resonant cavity measurement setup.

As discussed in the previous section both the  $Q$  and  $\beta_z$  are required to obtain the attenuation constant. The propagation constant  $\beta_z$  can be acquired by measuring the guide wavelength for each resonant peak with a field probe. The propagation constant is then given from equation (4.12). Unfortunately this was quite cumbersome. An alternative is obtained by moving a metallic plane close to (and perpendicular to) the waveguide, in the longitudinal direction and counting the number of minima,  $n$ , in the received power. The wavelength is then given by  $\lambda_g=2L/n$ . It should be noted that this is best achieved by setting the source frequency to that of the required resonant mode.

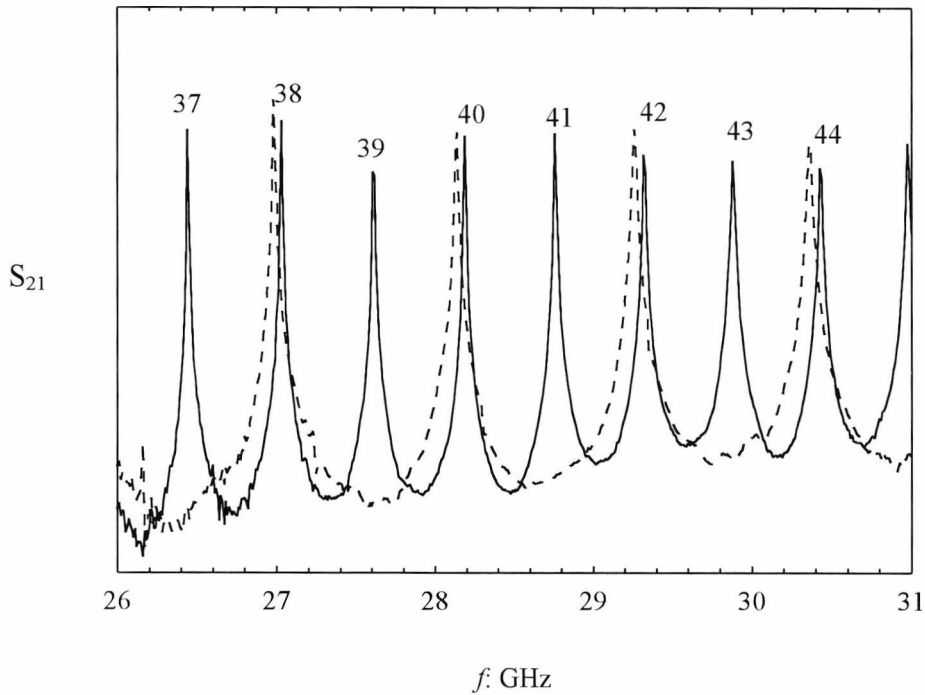


Figure 4.4. Typical Q curves for 200 mm cavity (solid lines) and 100mm cavity (dashed lines). The numbers indicate the number of half wavelengths  $n$  measured in the 200mm cavity for the respective mode.

Figure 4.5 and Figure 4.6 show measured values of  $\beta_z$  for  $E_{11}^y$  and  $E_{11}^x$  propagation in a PTFE waveguide, respectively. As can be seen the theoretical results, using published values for the real part of the permittivity [7], are in excellent agreement with the measured values. Figure 4.7 and Figure 4.8 show results for a polyethylene waveguide and again are in excellent agreement with theoretical results. The very small error observed at the lower frequency results could be due to the inaccuracies that the DEIM exhibits for modes approaching cut-off. However, another factor may also affect the results. Namely that the permittivity of the material is frequency dependent [8] - even though most manufacturers quote a single figure.

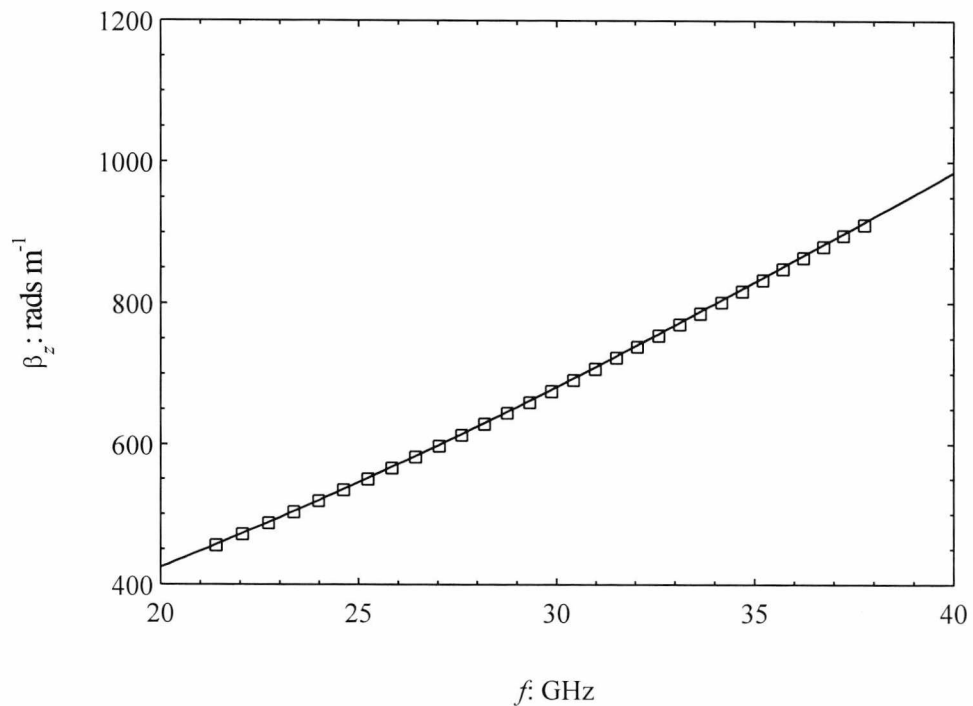


Figure 4.5. Propagation constant for  $E^y_{11}$  mode PTFE waveguide. Solid lines show theoretical results using the DEIM, boxes are experimental results using the Q band cavity. For the theoretical curves  $\epsilon_1=2.07$  [7].

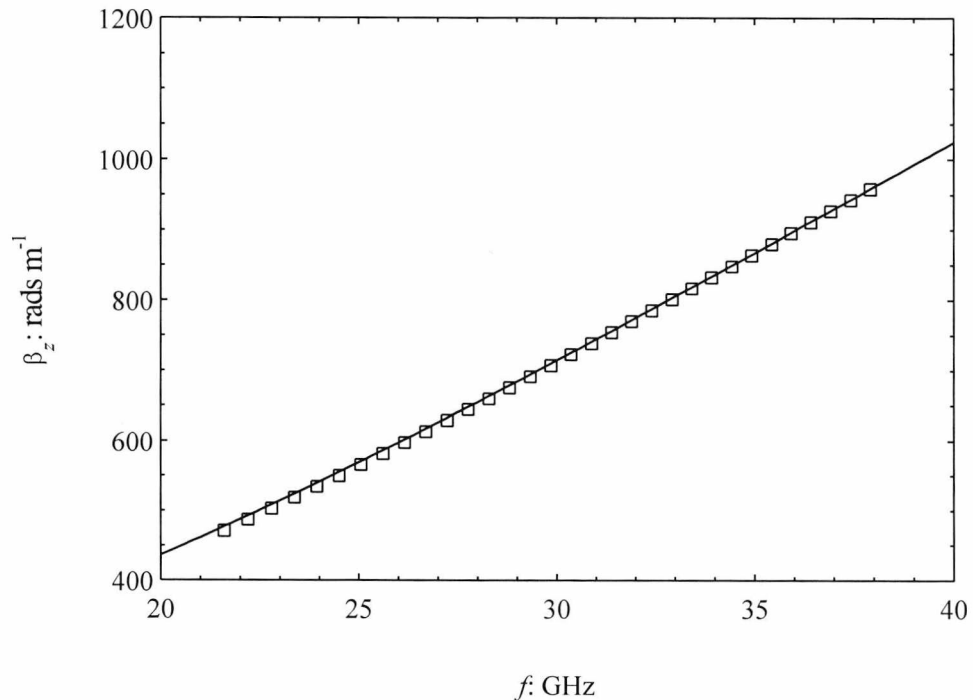


Figure 4.6. Propagation constant for  $E^x_{11}$  mode PTFE waveguide. Solid lines show theoretical results using the DEIM, boxes are experimental results using the Q band cavity. For the theoretical curves  $\epsilon_1=2.07$  [7].

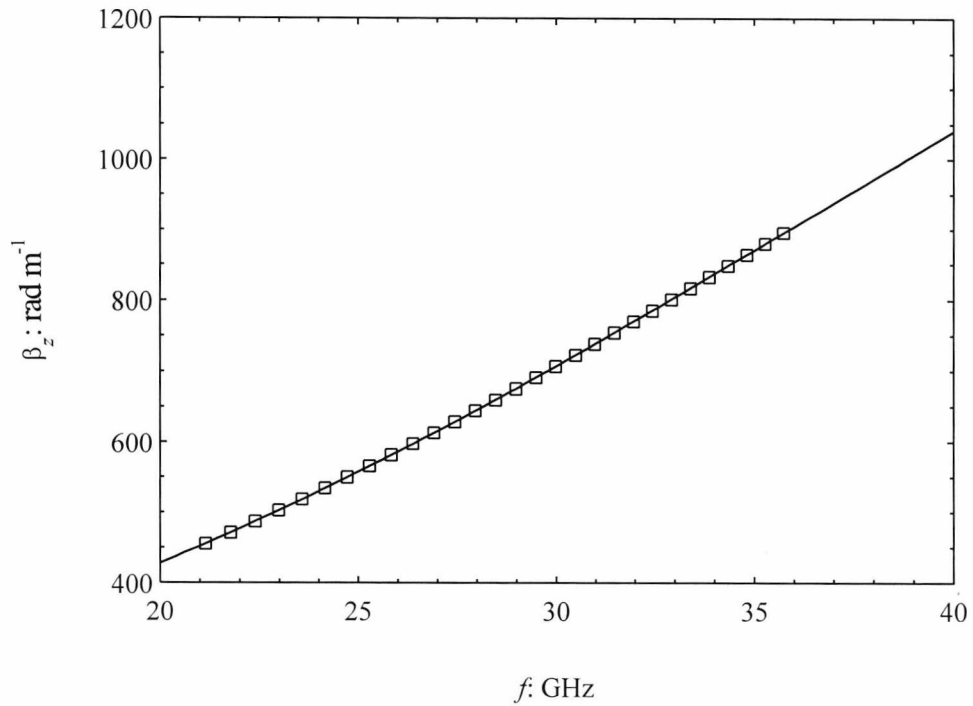


Figure 4.7.  $E_{11}^y$  mode propagation constant for Polyethylene waveguide. Solid lines show theoretical results using the DEIM, boxes are experimental results using the Q band cavity. For the theoretical curves  $\epsilon_1=2.316$  [7].

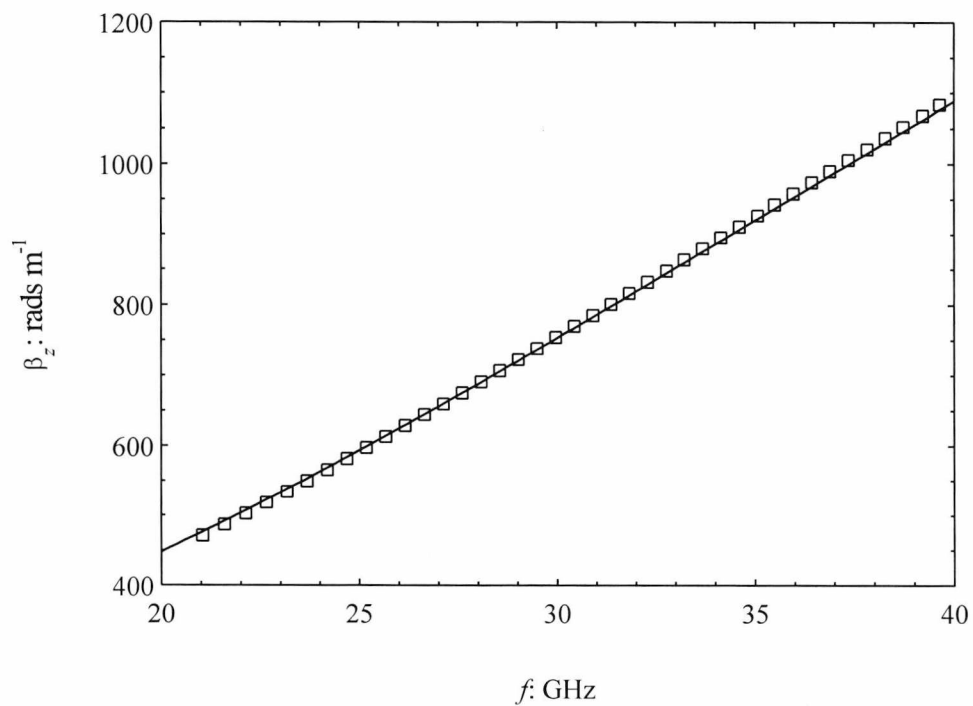


Figure 4.8.  $E_{11}^x$  mode propagation constant for Polyethylene waveguide. Solid lines show theoretical results using the DEIM, boxes are experimental results using the Q band cavity. For the theoretical curves  $\epsilon_1=2.316$  [7].

Figure 4.9 and Figure 4.10 show values of the measured quality factor and attenuation constant for the  $E_{11}^x$  mode PTFE waveguide, respectively. Figure 4.11 and Figure 4.12 show values of the measured quality factor and attenuation constant for the  $E_{11}^y$  mode polyethylene waveguide, respectively. Similarly, Figure 4.13 and Figure 4.14 show results for the  $E_{11}^x$  mode polyethylene waveguide. In each case parabolas were fitted to the measured quality factors,  $Q_1$  and  $Q_2$ , using the least squares method. With the help of these fitted curves  $Q_d$  was calculated from equation (4.8).  $v_p$  and  $\beta_z$  were obtained directly from the measured values of  $\lambda_g$ ,  $v_g$  was calculated by constructing an  $\omega$ - $\beta$  diagram and finally the attenuation constant  $\alpha_z$  was obtained from equation (4.9).

We see from Figure 4.10 that the attenuation constant of the  $E_{11}^x$  PTFE waveguide suggests a loss tangent of about  $2.5$  to  $3.0 \times 10^{-4}$ . Again, from Figure 4.12 and Figure 4.14, we see that the loss tangent of the polyethylene is approximately  $4.5 \times 10^{-4}$ . A review of the literature gives values for the loss tangent of PTFE between  $2.17 \times 10^{-4}$  [5] and  $3.15 \times 10^{-4}$  [7] and  $1.3 \times 10^{-4}$  [7] to  $3.8 \times 10^{-4}$  [5] for polyethylene, at 35 GHz. The measured values are therefore in quite good agreement. The range of values quoted for the loss tangents of these materials is not wholly due to the varying inaccuracies of the different techniques used to acquire them. Another important factor is the material itself. Afsar and Button [8] pointed out that the dielectric parameters, and in particular the loss tangent of a specific material, can be greatly affected by the manufacturing process. Furthermore, Afsar has shown that the loss tangents of both PTFE and polyethylene vary considerable over the 60-300 GHz range. Extrapolation of this data suggests that the loss tangent may well vary by up to 20% over the 20-60 GHz range.

We notice from the results that the values for  $\alpha_z$  begin to diverge at about 30 GHz and we actually find that the attenuation constant becomes negative at 34 GHz. This is of course impossible. There may be several reasons for the increase in error as the frequency is increased. Firstly, higher order modes start to propagate. When the resonant frequency of one of these modes is close to, or equal to, that of the required mode, the resonant curves broaden giving erroneous quality factors. Secondly, we observe that the quality factor of the two lengths of waveguide appear to converge for increasing frequency. This suggests that the dielectric losses become dominant. Therefore, under these conditions, the use of two different lengths is not required.

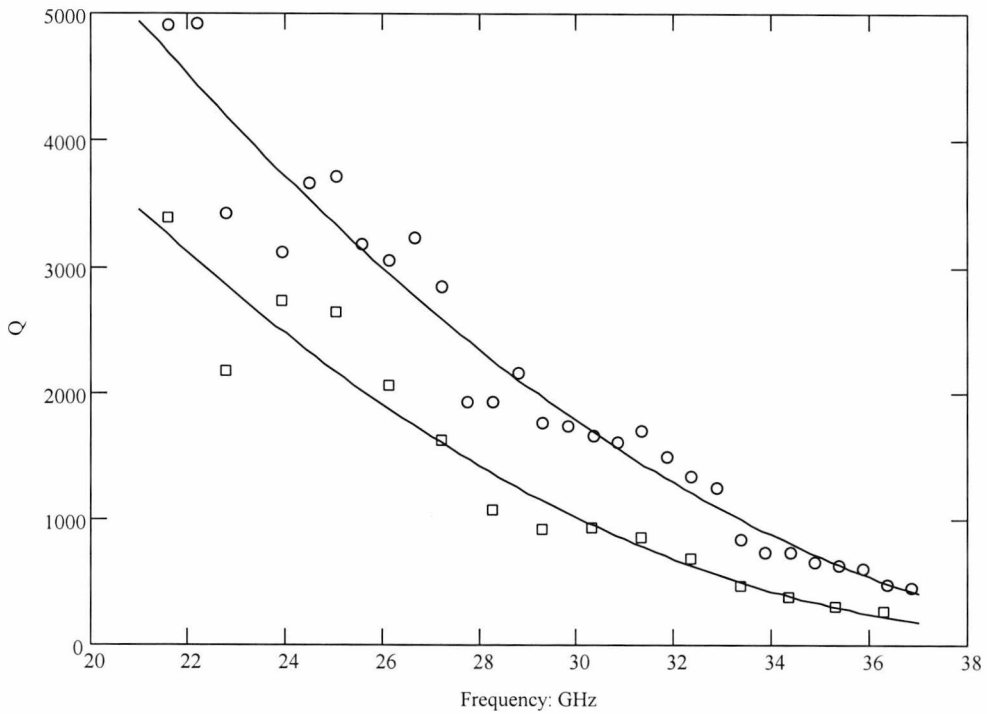


Figure 4.9.  $E_{11}^x$  mode PTFE waveguide quality factors for 200 mm cavity ○ and 100 mm cavity □. Solid lines show least squares fit.

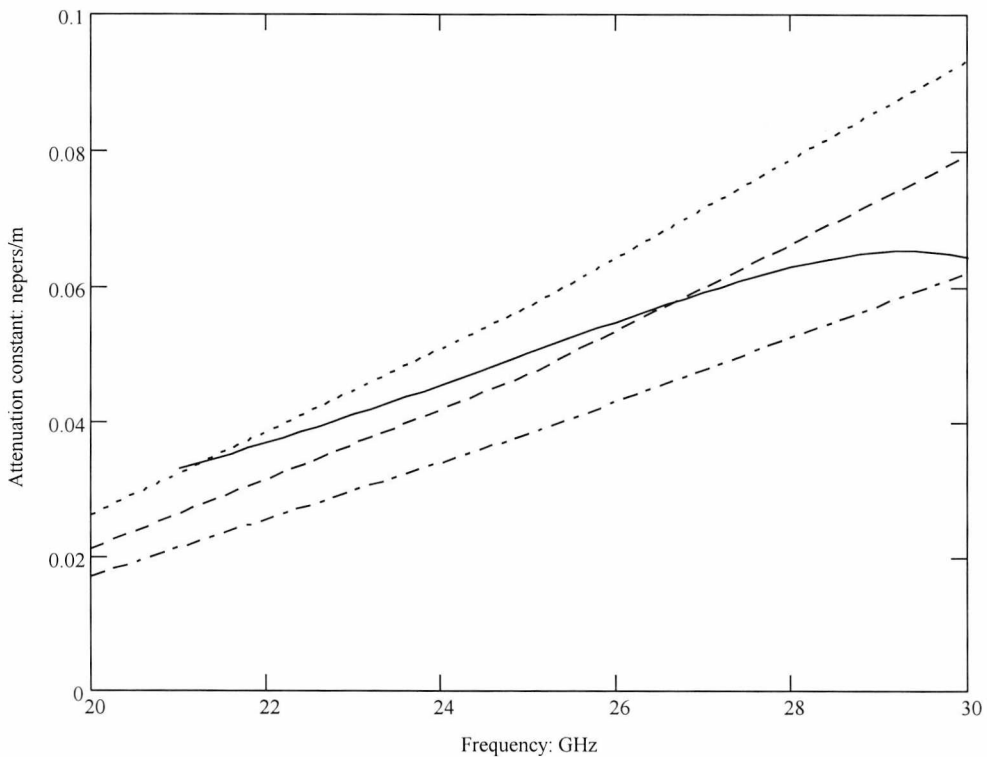


Figure 4.10.  $E_{11}^x$  mode PTFE waveguide attenuation constant (solid line). Dotted, dashed and dot-dashed curves show theoretical results for loss tangents of  $3.0 \times 10^{-4}$ ,  $2.5 \times 10^{-4}$  and  $2.0 \times 10^{-4}$ , respectively. In each case the dual effective loss tangent technique is used.

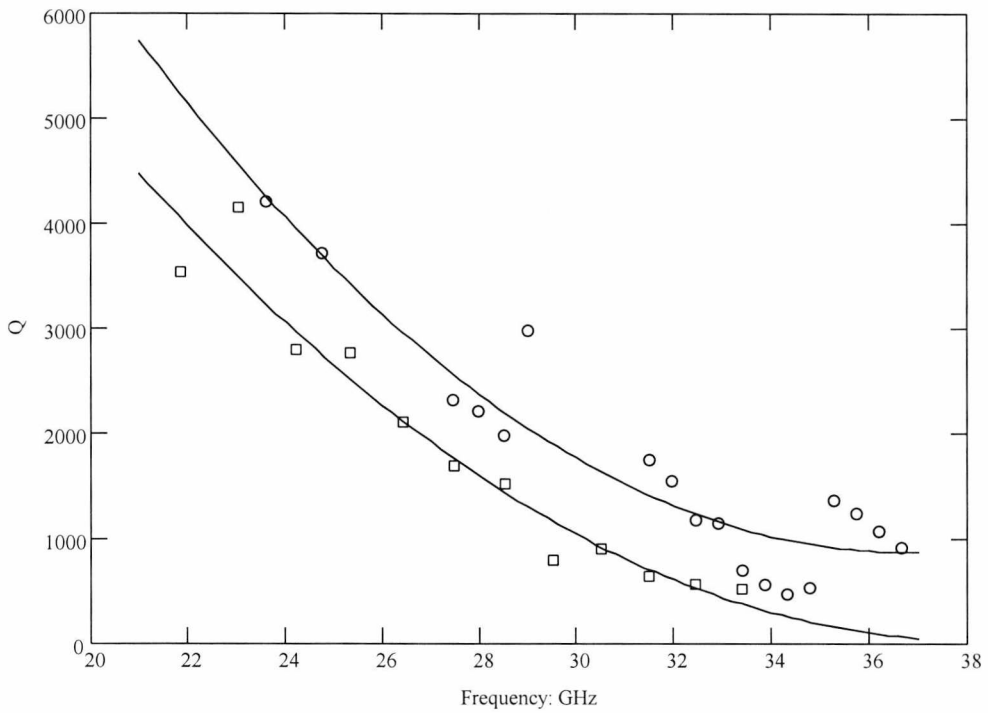


Figure 4.11.  $E^y_{11}$  mode Polyethylene waveguide Quality factors for 200 mm cavity ○ and 100 mm cavity □. Solid lines show least squares fit.

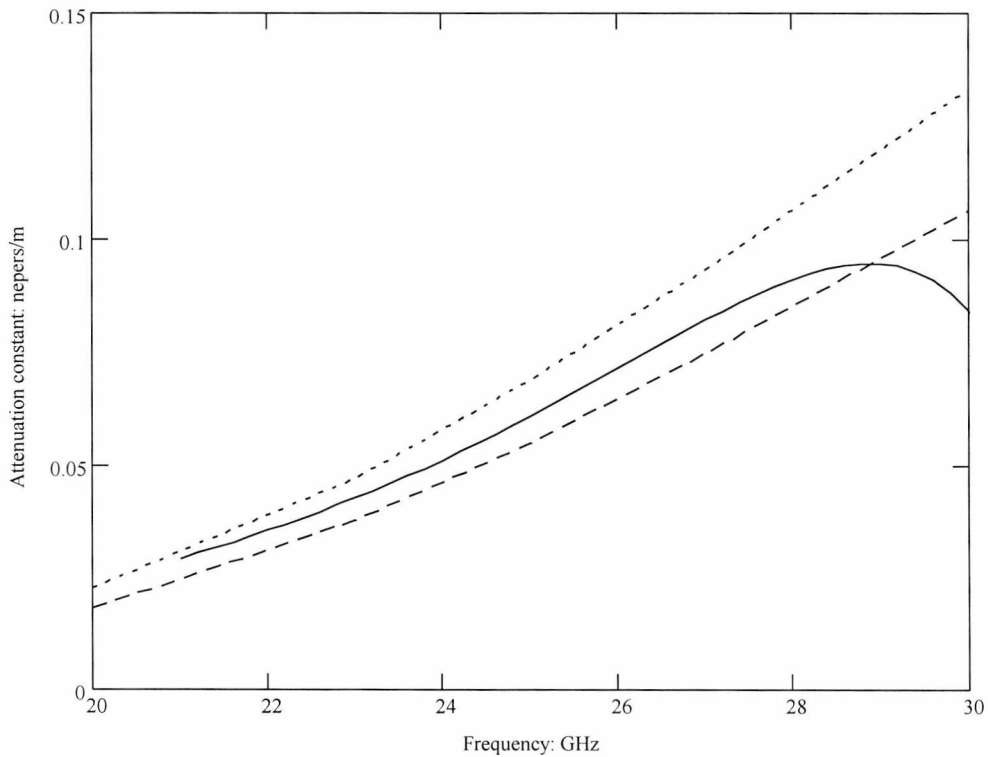


Figure 4.12.  $E^y_{11}$  mode polyethylene waveguide attenuation constant (solid line). Dotted and dashed curves show theoretical results for loss tangents of  $5.0 \times 10^{-4}$  and  $4.0 \times 10^{-4}$ , respectively. In each case, the dual effective loss tangent technique is used.

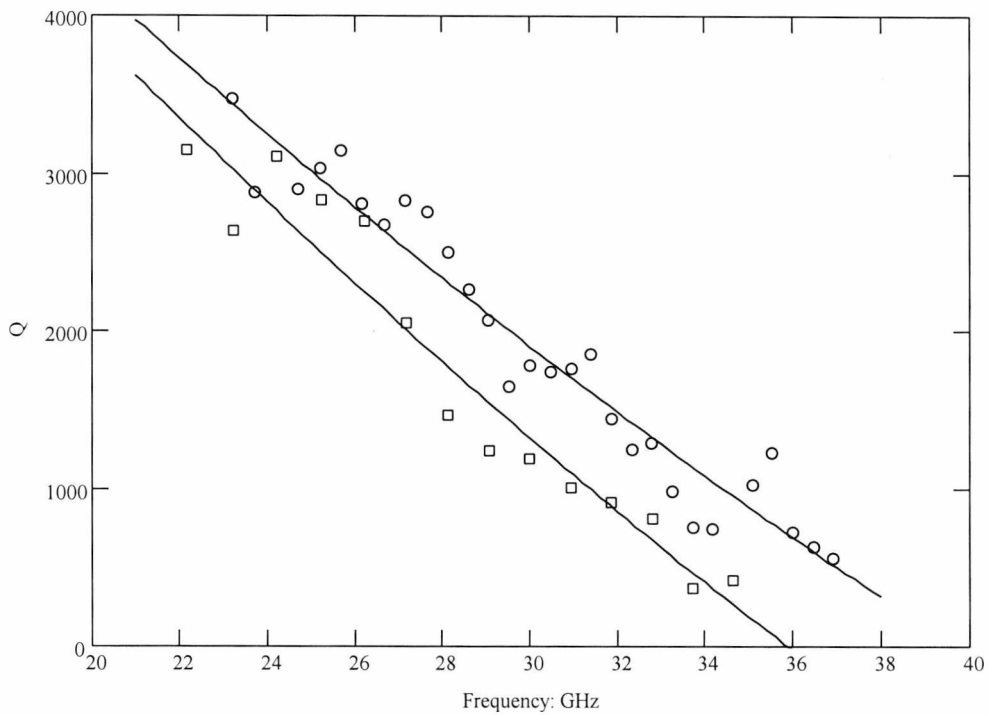


Figure 4.13.  $E_{11}^x$  mode Polyethylene waveguide Quality factors for 200 mm cavity  $\circ$  and 100 mm cavity  $\square$ . Solid lines show least squares fit.

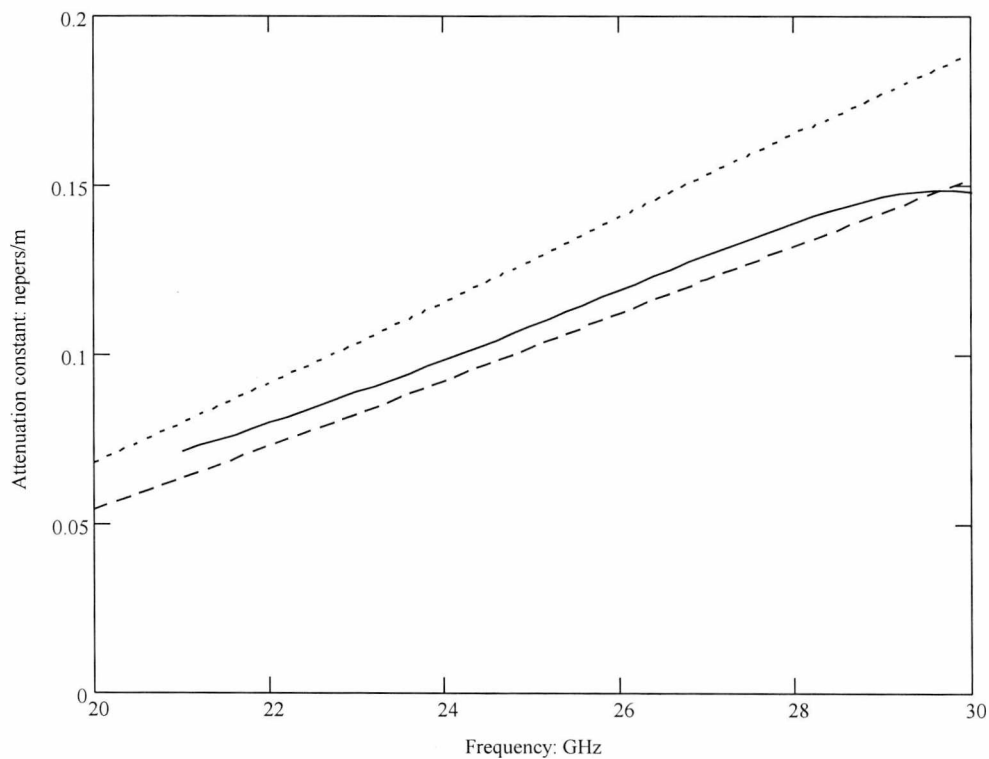


Figure 4.14.  $E_{11}^x$  mode polyethylene waveguide attenuation constant (solid line). Dotted and dashed curves show theoretical results for loss tangents of  $5.0 \times 10^{-4}$  and  $4.0 \times 10^{-4}$ , respectively. In each case, the dual effective loss tangent technique is used.

Another factor that may have affected the accuracy of the measurements is the fact that the network analyser used to obtain the data could only store a maximum of 501 data points. Therefore, for the frequency range 25-35 GHz the smallest sample width is 20 MHz. This gives a maximum measurable  $Q$  of about 750. Clearly this is not adequate, as the  $Q$  factors of low-loss materials can exceed 10,000 for the 25-35GHz range. This problem was overcome by acquiring the measurements over small frequency ranges of 2 GHz. This of course requires additional work since the analyser must be calibrated for each frequency range. Also, it is very difficult to place the dielectric waveguide in the same place for each measurement and thus additional errors are incurred.

#### 4.2.2 Coupled Dielectric Waveguides

In this section, we look at coupled dielectric waveguides. Figure 4.15 shows a photograph of the cavity resonator. Energy is coupled into one of the waveguides, which is fixed to the end plates. The other guide is mounted in an expanded polystyrene cradle; the cradle in turn is connected to a metal base plate that can be moved with the aid of a micrometer. The separation of the two guides can then be easily measured.

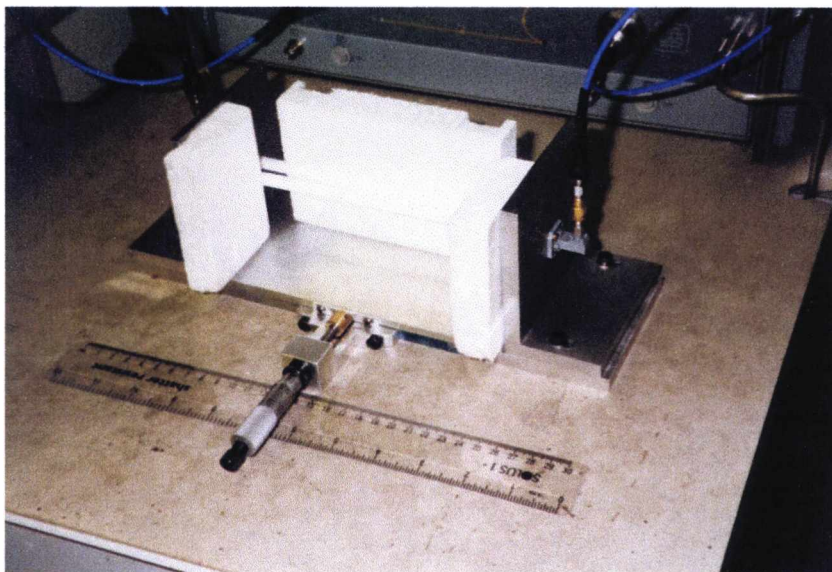


Figure 4.15. Photograph of cavity resonator for coupled waveguide measurements.

Unfortunately, it was found that an accurate measurement of the attenuation constant of coupled dielectric waveguides was extremely difficult due to the following factors:

1. The resonant frequencies change with separation. This is explained when we remember that, for a given cavity mode,  $\beta_z$  must remain constant whatever the separation. Therefore, with reference to Figure 4.16, we see that the resonant frequencies of the modes with even transverse symmetry increase with separation whereas the odd mode frequency decreases. Accordingly, there will be separations where an odd and even mode will have resonant frequencies close to or identical to each other. This results in a spreading of the resonant curves and consequently the Q factor can not be accurately obtained. Figure 4.18 to Figure 4.23 show these effects.
2. Low-loss materials such as PTFE are very flexible. Difficulties therefore arise in maintaining a constant separation along the whole length of the guide. For low-loss materials, measurements for two different cavities are required, resulting in further inconsistencies in the guide separation. We can overcome this by using high loss materials. However, it was found that since the resonant peaks of high loss materials are much broader, they interfere with each other to such an extent that the Q factors become meaningless. Increasing the cavity length so that only the dielectric losses are dominant would alleviate the need for two cavities. However, the problem of flexibility would then be more apparent.
3. The movable guide has to be mounted in an expanded polystyrene cradle. This shifts the resonant peaks since the polystyrene has a relative permittivity different from air. In addition, there is a small decrease in the quality factor due to the loss tangent of the polystyrene and any reflections from the discontinuity. Fortunately, both of these effects are small, as can be seen from Figure 4.17.
4. Unwanted higher order modes are sometimes excited. These interfere with modes that have resonant frequencies close to or equal to them giving meaningless quality factors.
5. Energy is coupled into all the modes that the guides can support. Unfortunately, the amount of energy coupled into some of the modes can be very small for certain separations making measurements of the Q impossible.

With more time and effort, some of the above problems could be overcome. However, only the real part of the propagation constant is considered here. It should be noted that the insertion loss technique could be used to obtain the attenuation constant of coupled structures. Unfortunately, the problem of exciting the correct mode and varying and maintaining the correct separation would make the method impractical.

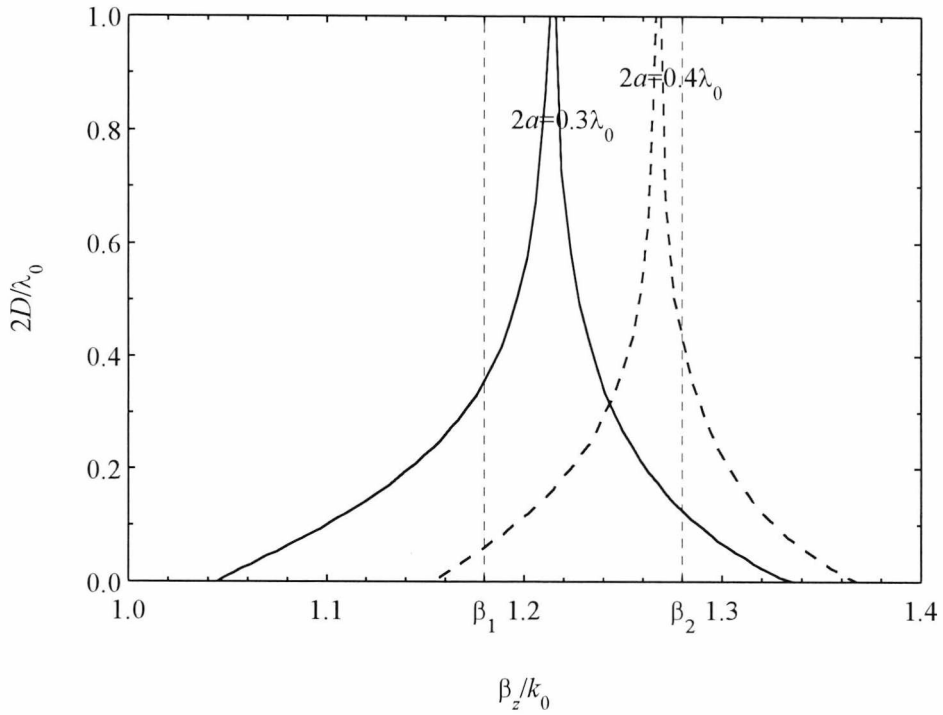


Figure 4.16. Illustration of how the resonant frequencies vary with separation.

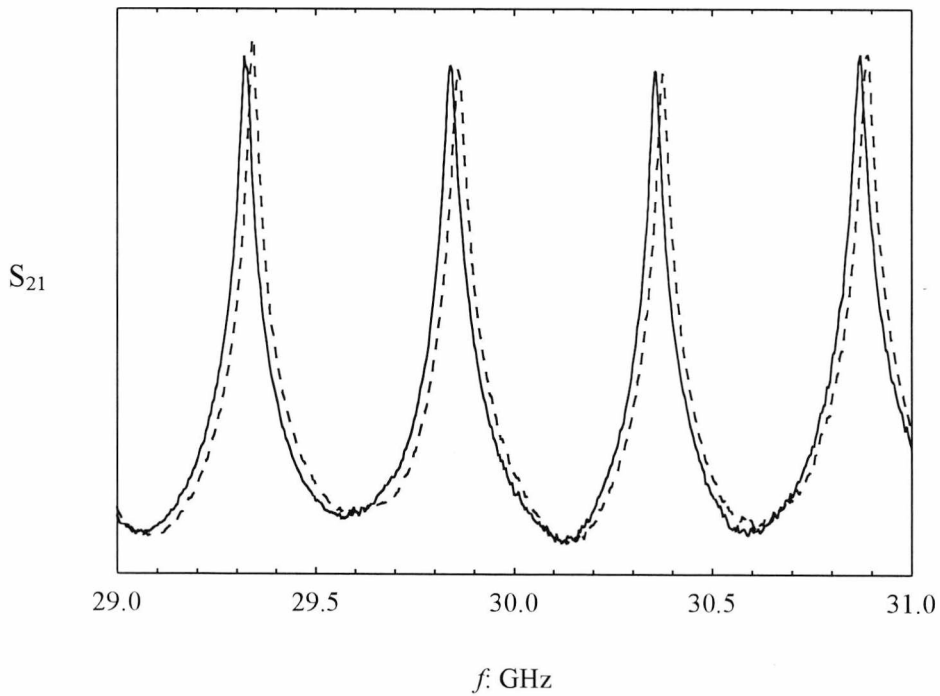


Figure 4.17. Q curves for  $E^x$  mode of a single PTFE waveguide with (solid lines) and without (dashed lines) expanded polystyrene cradle.

Two different coupled cavities were investigated: one at 10 GHz, the other at 30 GHz. The first had a length  $L=300\text{mm}$ , the second  $L=200\text{mm}$ . In both cases, the movable dielectric was mounted in an expanded polystyrene cradle that could be moved by a micrometer. The waveguides for the 10 GHz cavity had dimensions  $2a=2b=10.03\text{mm}$ ,  $2d=22.8\text{mm}$  and were both made of PTFE. The waveguides for the 30 GHz cavity had dimensions  $2a=2b=3.556\text{mm}$ ,  $2d=7.112\text{mm}$  and were, again, both made of PTFE. For completeness Figure 4.18, Figure 4.19 and Figure 4.20 show the transmission of the 10GHz cavity for increasing separation. In each case the frequency range is 8.0 GHz to 10 GHz. From left to right, Figure 4.18 shows separations for  $2D=0$  to 7mm in steps of 1mm. Figure 4.19 shows separations for  $2D=8$  to 15mm; Figure 4.20 shows separations for  $2D=16$  to 23mm. Similarly, Figure 4.21, Figure 4.22 and Figure 4.23 show the transmission for the frequency range 10 GHz to 12 GHz.

For each of the resonant peaks shown in Figure 4.18 to Figure 4.23 the guide wavelength has to be determined. In a similar way to the single guide cavity, the guide wavelength was obtained by moving a metallic plane along the whole length of the guides and counting the number of minima in the transmission. The guide wavelength is not the only parameter that must be determined. The type of the mode, i.e. even or odd, is also important. We can determine this by placing a metallic plane between the two guides and parallel to them. If the plane is in the centre, we find that the even  $E^x$  modes, which do not have electric field zeros at the centre, are cut-off leaving only the odd modes. An alternative method for determining the mode type is obtained if we remember that odd mode resonant frequencies decrease with separation whereas even modes increase. The mode type is then given by simply observing which way the resonant frequency moves as the separation is increased.

Clearly, determining which mode is which as the separation is increased is very difficult, particularly for the high frequency region where higher order modes start to propagate. However, with perseverance, the type and order of each of the resonant modes can be determined for each separation.

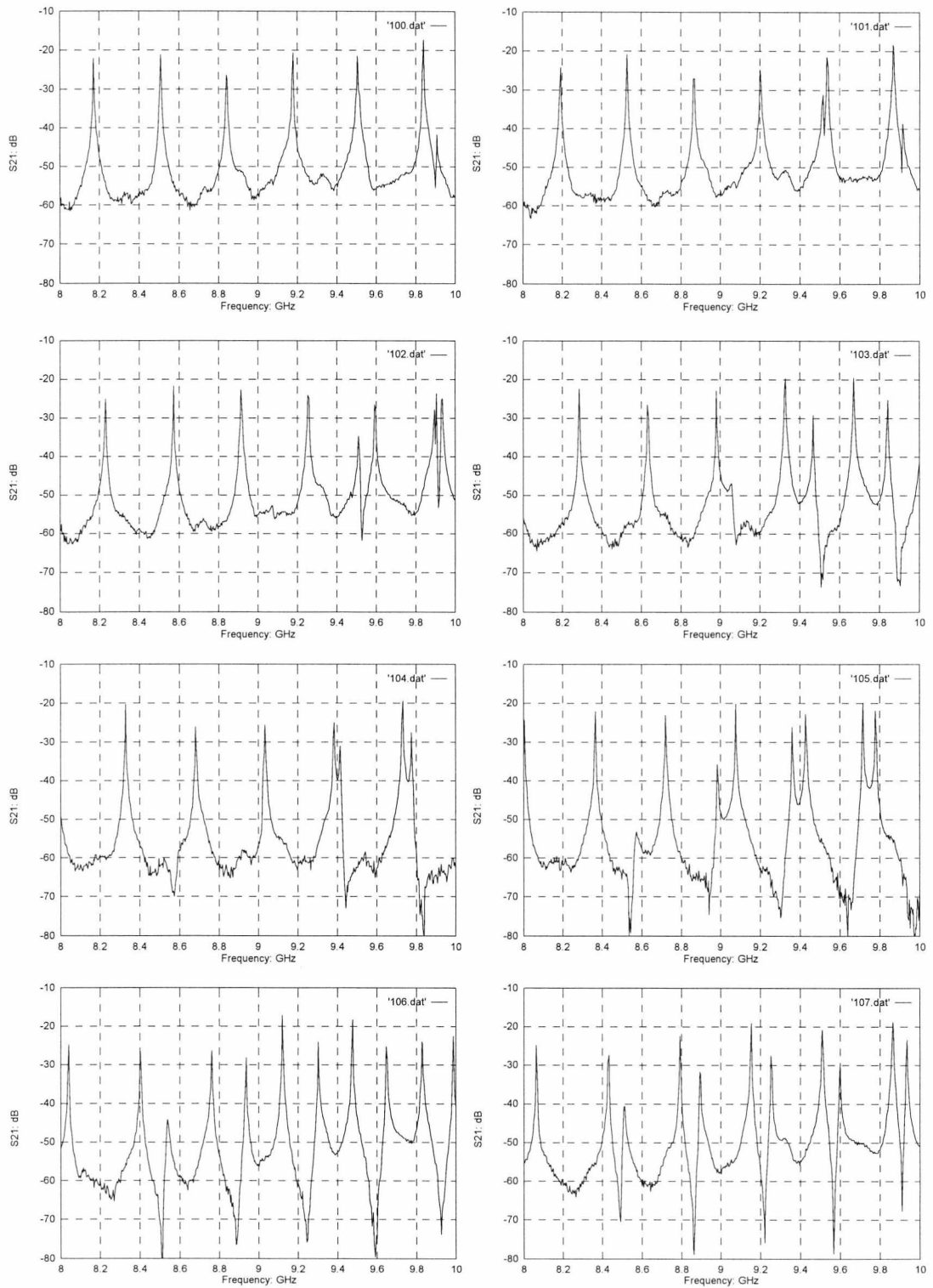


Figure 4.18. 10 GHz coupled cavity transmission curves for separations of  $2D=0$  to 7mm.

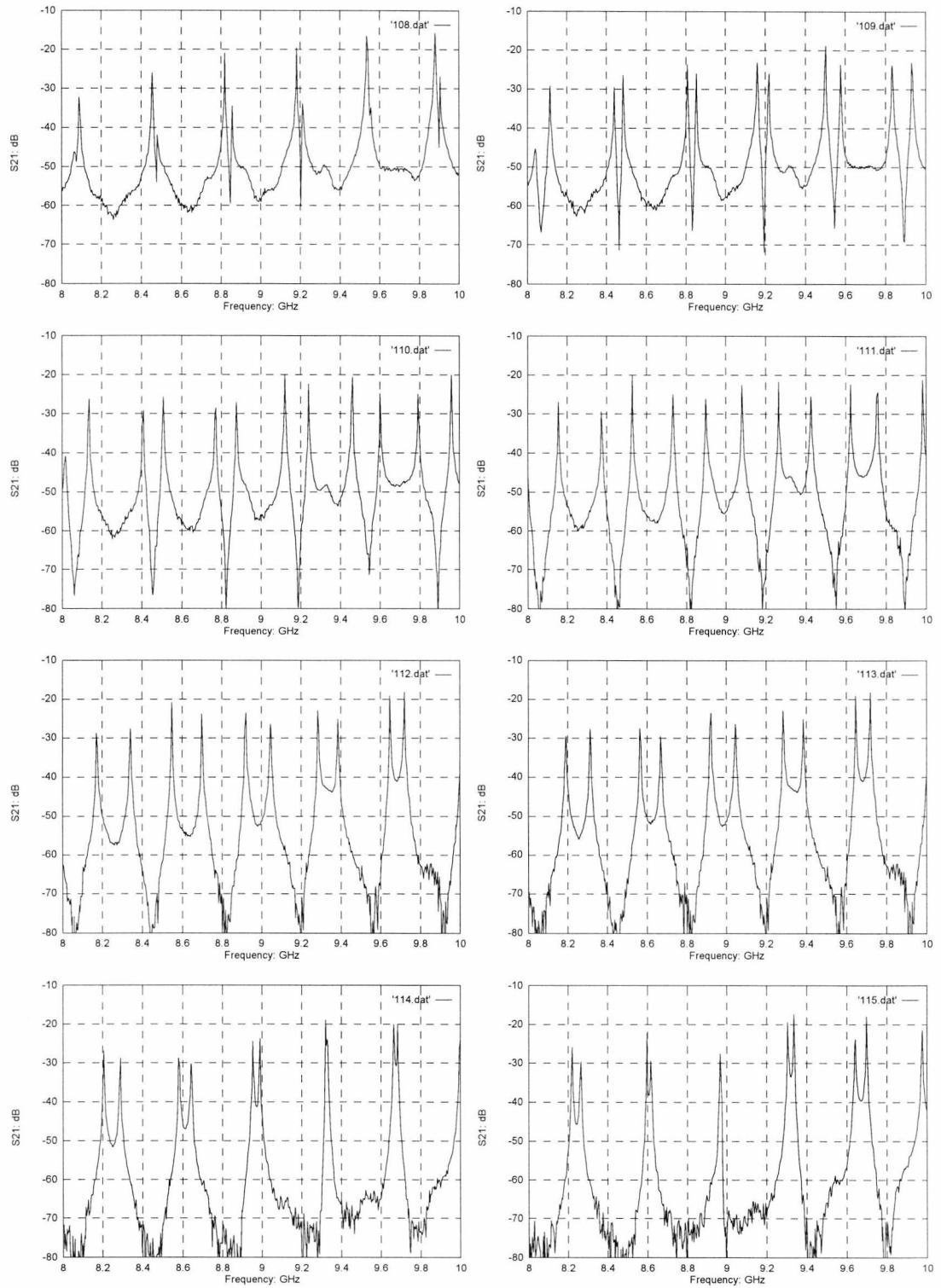


Figure 4.19. 10 GHz coupled cavity transmission curves for separations of  $2D = 8$  to 15mm.

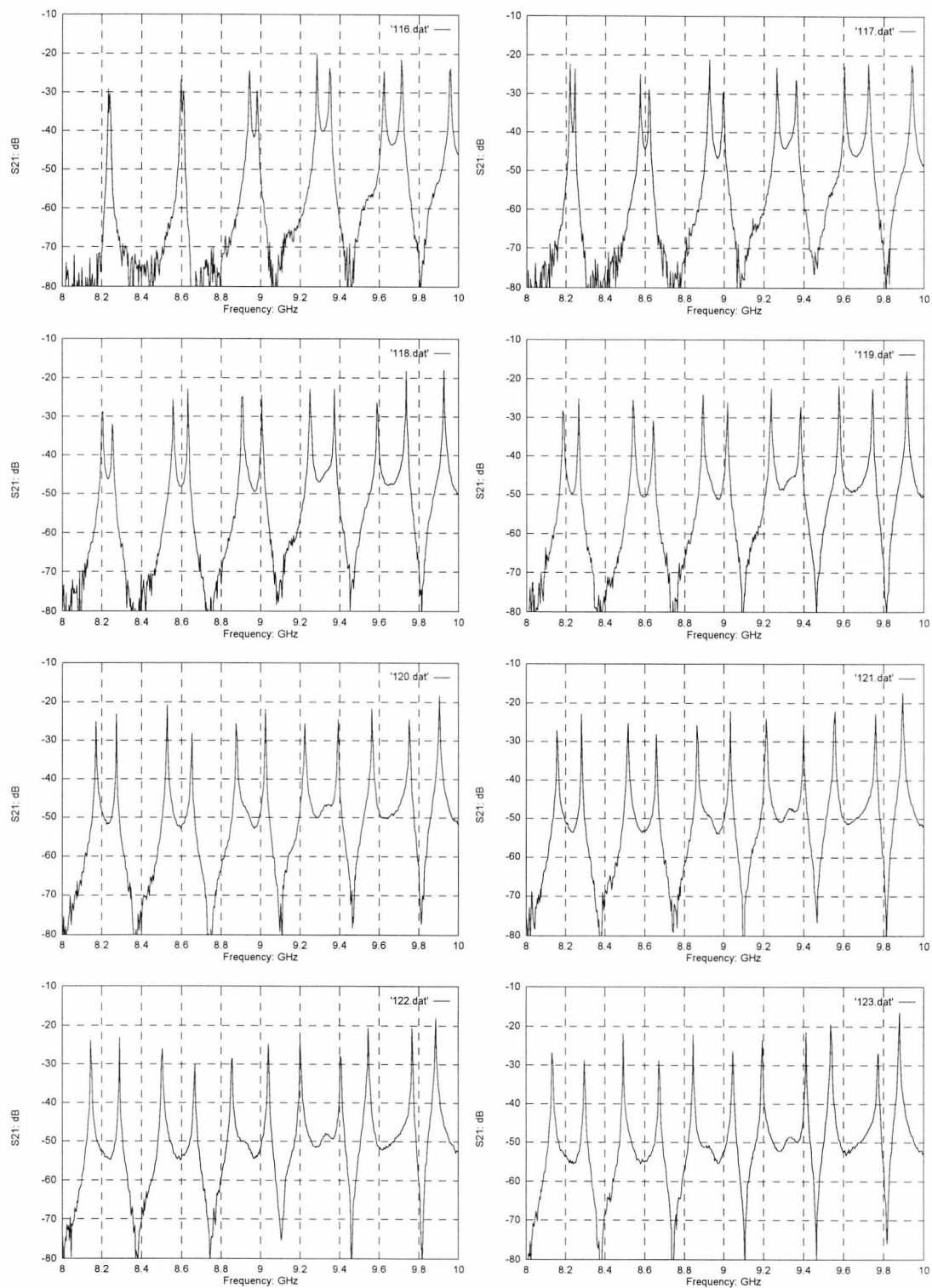


Figure 4.20. 10 GHz coupled cavity transmission curves for separations of  $2D = 16$  to 23mm.

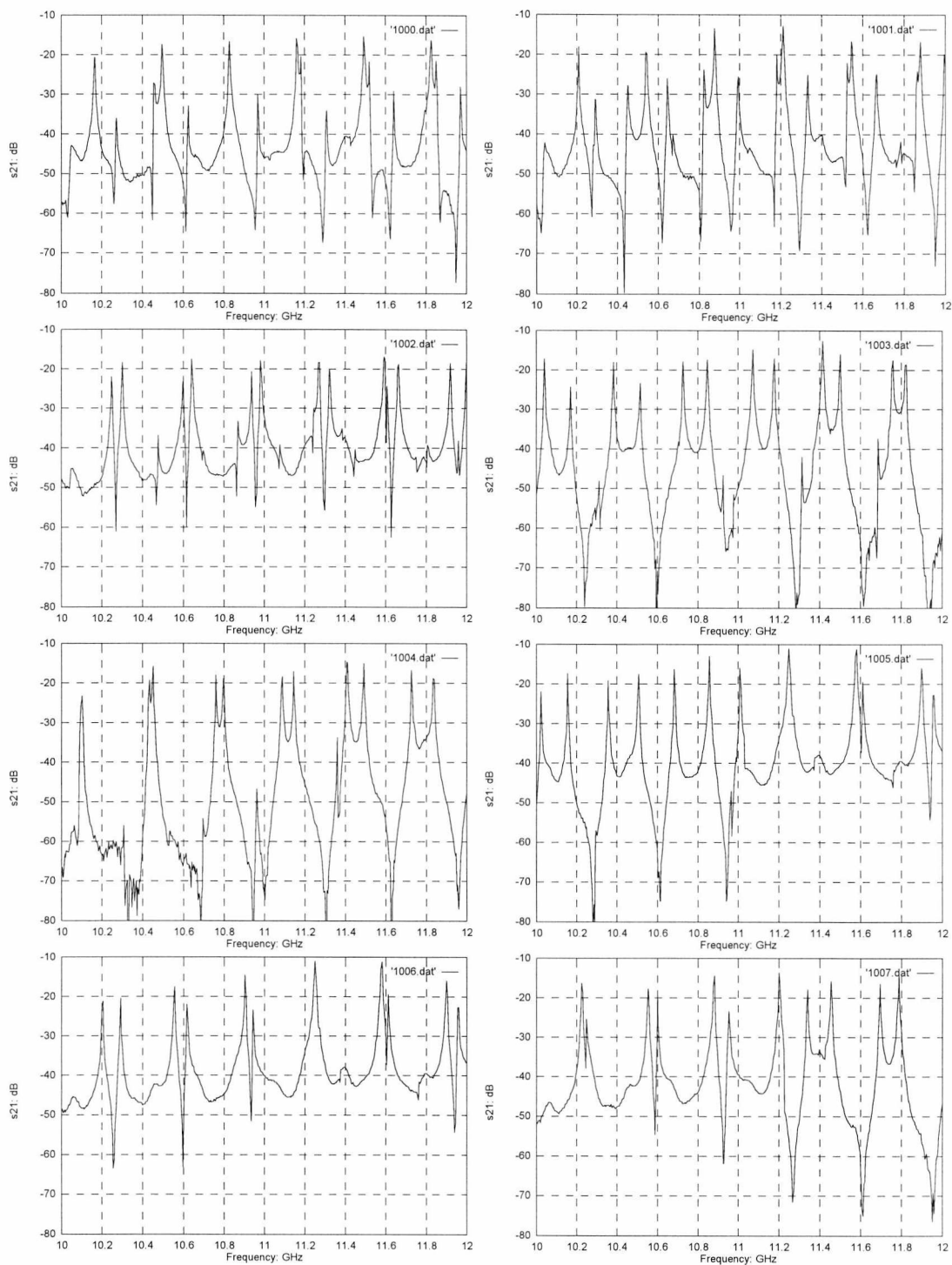


Figure 4.21. 10 GHz coupled cavity transmission curves for separations of  $2D=0$  to 7mm.

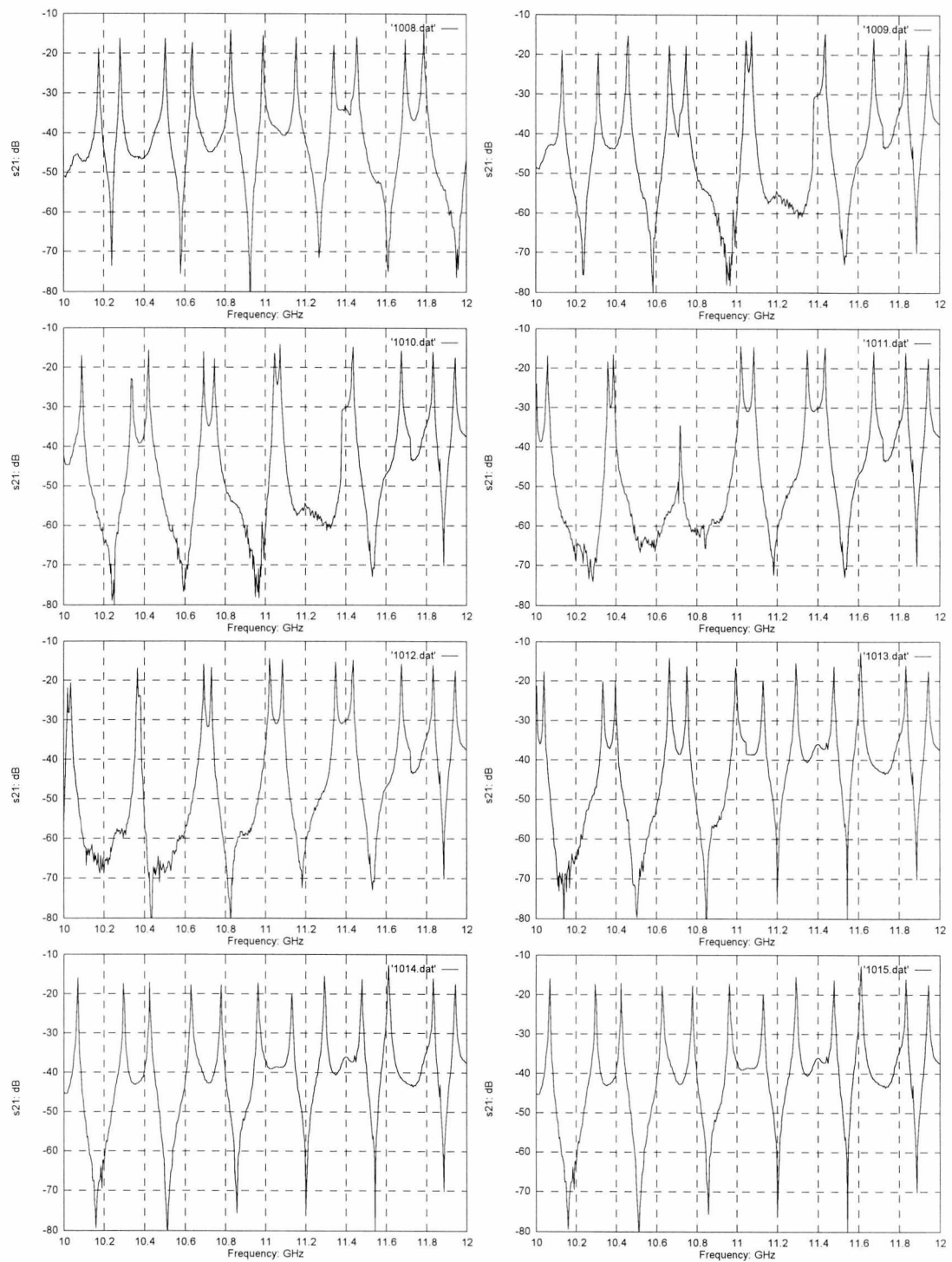


Figure 4.22. 10 GHz coupled cavity transmission curves for separations of  $2D = 8$  to 15mm.

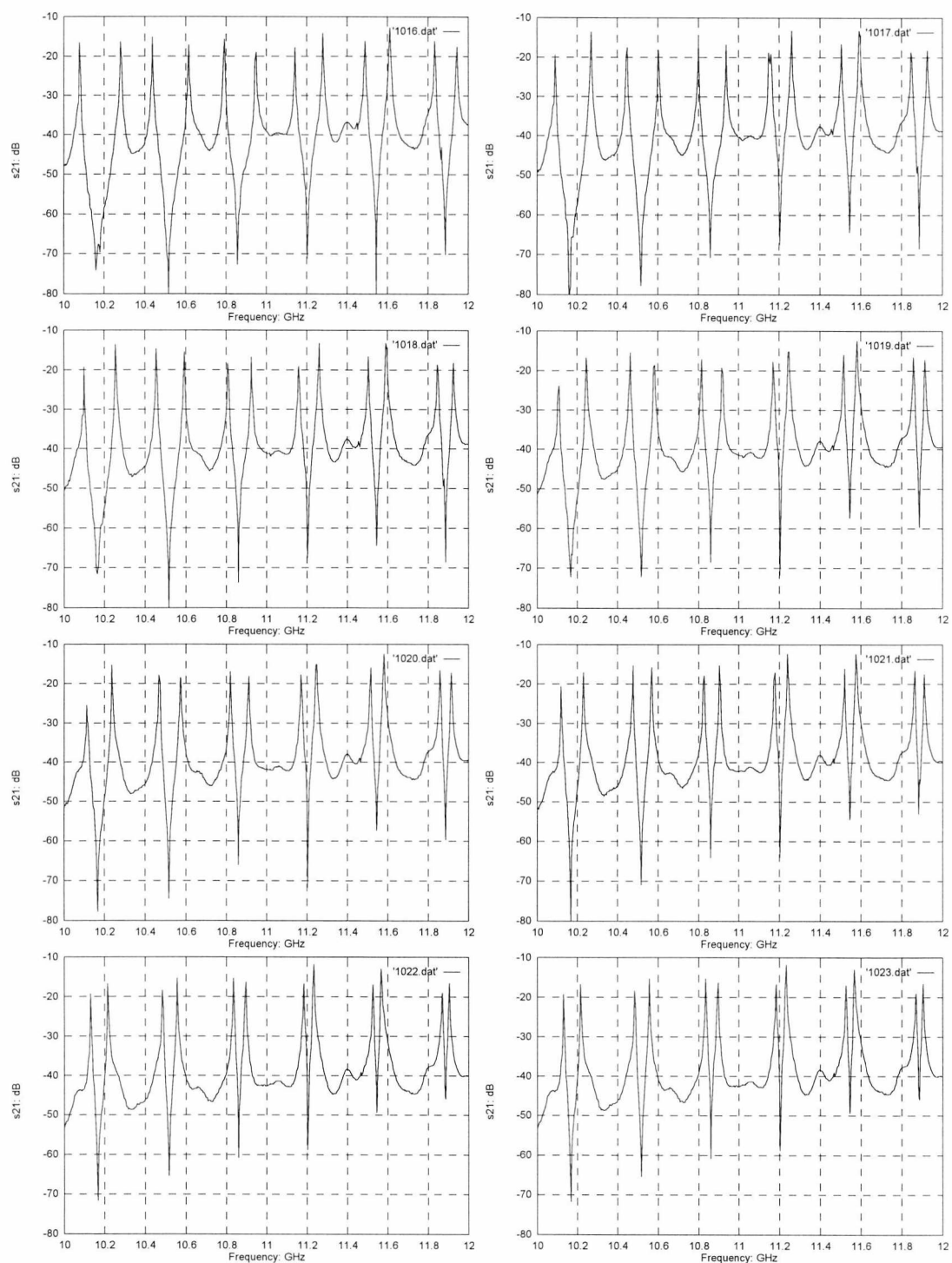


Figure 4.23. 10 GHz coupled cavity transmission curves for separations of  $2D=16$  to 23mm.

Figure 4.24, Figure 4.25 and Figure 4.26 show results for  $E^x$  mode coupled PTFE waveguides at 8.0, 10.0 and 12.0 GHz, respectively. Figure 4.27, Figure 4.28 and Figure 4.29 show results for  $E^x$  mode coupled PTFE waveguides at 25.0, 30.0 and 35.0 GHz, respectively. We see that the EDC method presented in Chapter 3 is in good agreement with the experimental results, particularly for even mode solutions. As expected, the method compares better for the high frequency results. We further see that the HFSS finite element results are in excellent agreement with the measured values. It is therefore envisaged that the attenuation constant using HFSS would also compare well with experimental results. Consequently, the EDC results in Chapter 3 can be trusted.

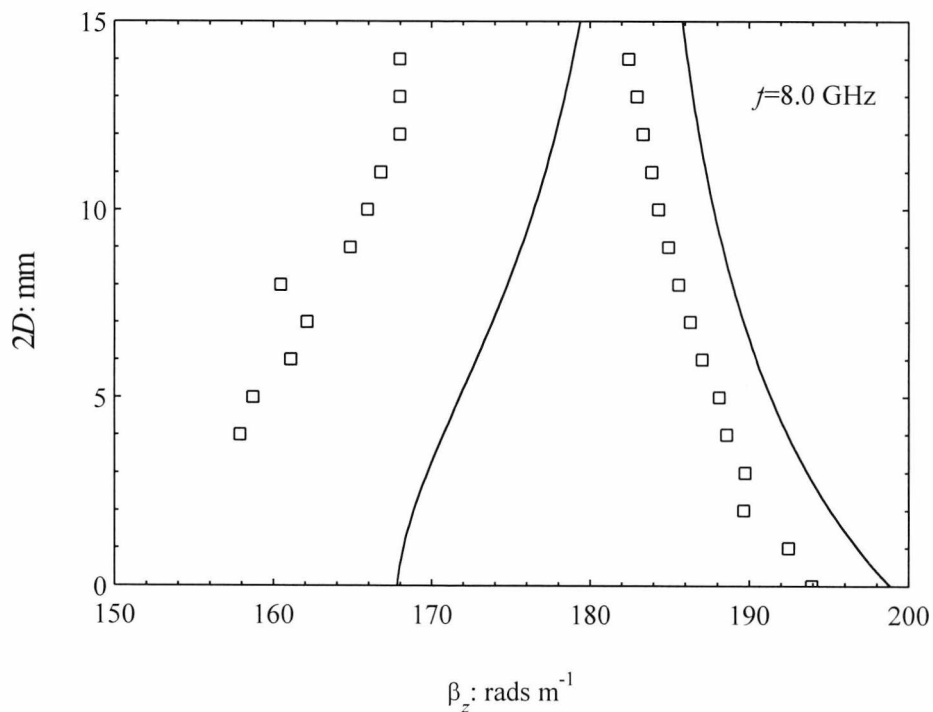


Figure 4.24. Coupled dielectric waveguide measurements for PTFE waveguides:  $\epsilon_a = \epsilon_b = 2.07$ ,  $2a = 2b = 10.03 \text{ mm}$ ,  $2d = 22.8 \text{ mm}$  and  $f = 8.0 \text{ GHz}$ . Solid lines show EDC solutions and boxes show experimental results.

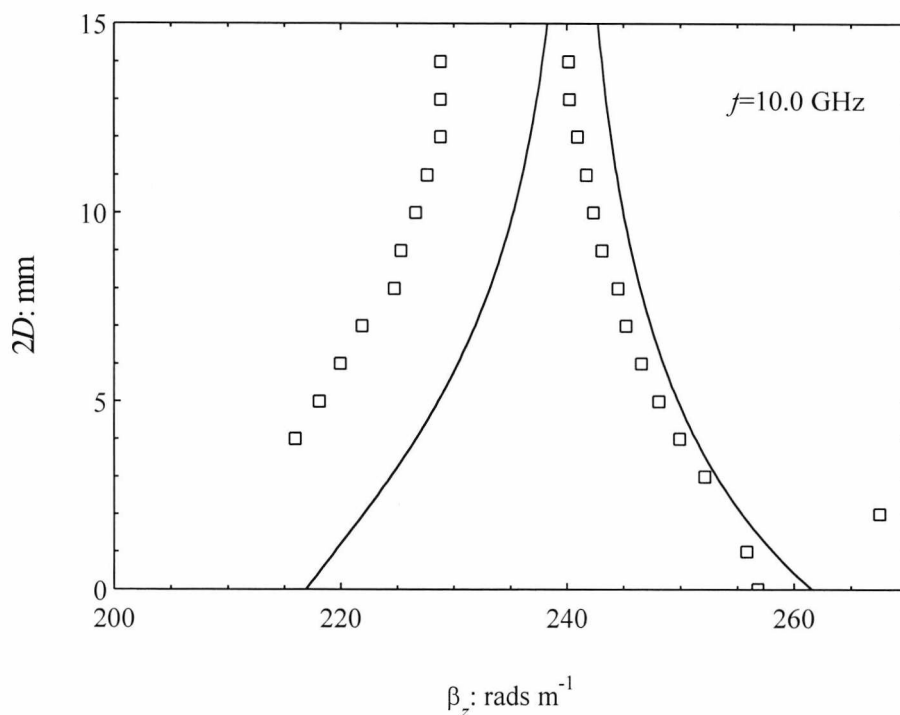


Figure 4.25. Coupled dielectric waveguide measurements for PTFE waveguides:  $\epsilon_a = \epsilon_b = 2.07$ ,  $2a = 2b = 10.03 \text{ mm}$ ,  $2d = 22.8 \text{ mm}$  and  $f = 10.0 \text{ GHz}$ . Solid lines show EDC solutions and boxes show experimental results.

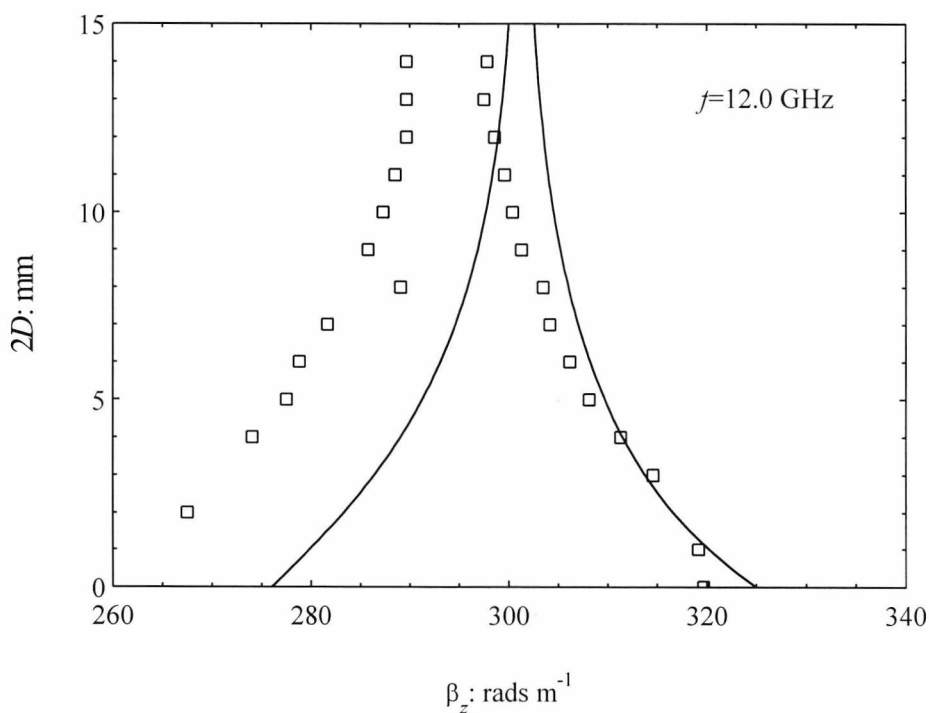


Figure 4.26. Coupled dielectric waveguide measurements for PTFE waveguides:  $\epsilon_a = \epsilon_b = 2.07$ ,  $2a = 2b = 10.03 \text{ mm}$ ,  $2d = 22.8 \text{ mm}$  and  $f = 12.0 \text{ GHz}$ . Solid lines show EDC solutions and boxes show experimental results.

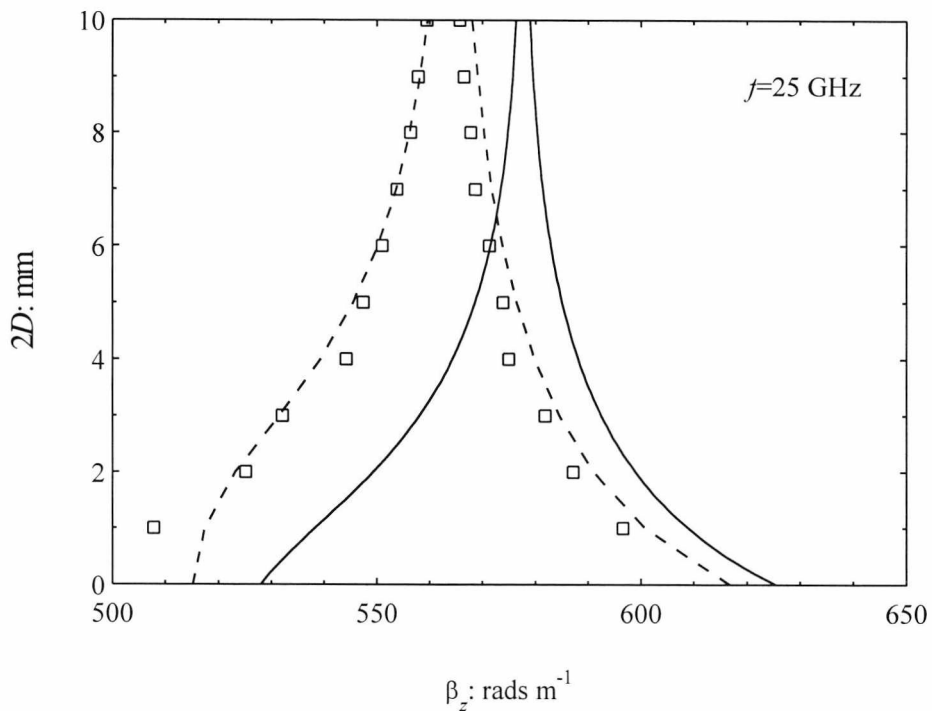


Figure 4.27. Coupled dielectric waveguide measurements for PTFE waveguides:  $\epsilon_a=\epsilon_b=2.07$ ,  $2a=2b=3.556\text{mm}$ ,  $2d=7.112\text{mm}$  and  $f=25\text{GHz}$ . Solid lines show EDC solutions, dashed lines show HFSS solutions and boxes show experimental results.

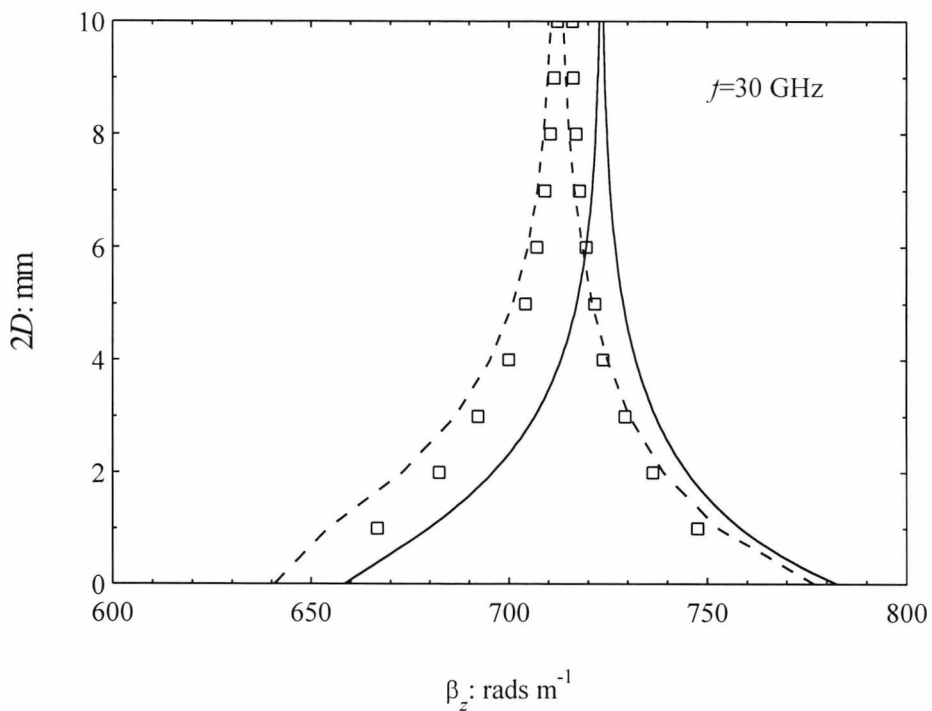


Figure 4.28. Coupled dielectric waveguide measurements for PTFE waveguides:  $\epsilon_a=\epsilon_b=2.07$ ,  $2a=2b=3.556\text{mm}$ ,  $2d=7.112\text{mm}$  and  $f=30\text{GHz}$ . Solid lines show EDC solutions, dashed lines show HFSS solutions and boxes show experimental results.

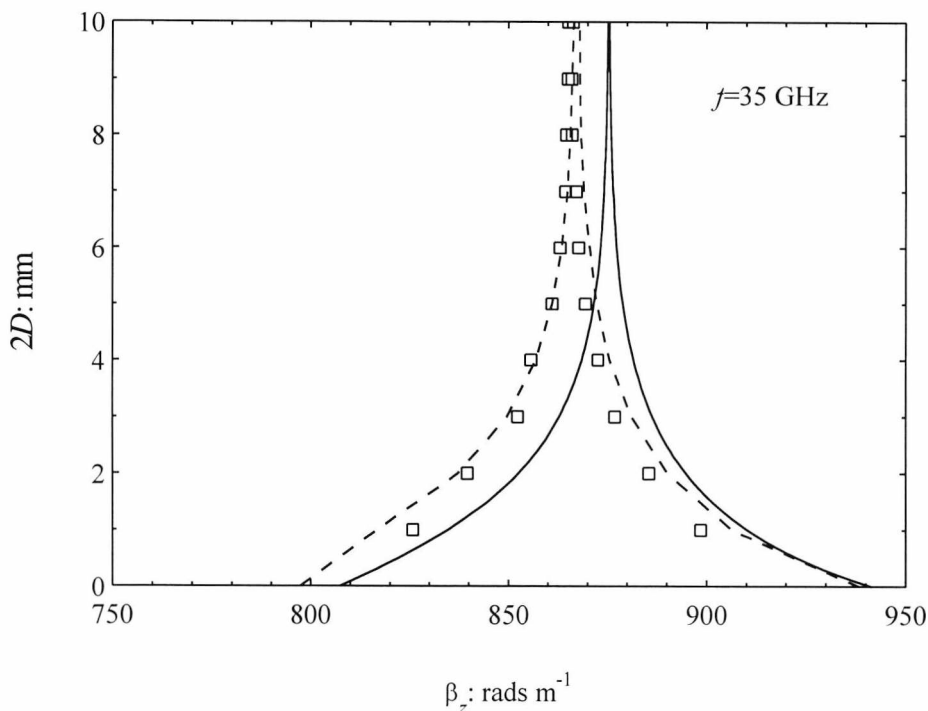


Figure 4.29. Coupled dielectric waveguide measurements for PTFE waveguides:  $\epsilon_a = \epsilon_b = 2.07$ ,  $2a = 2b = 3.556 \text{ mm}$ ,  $2d = 7.112 \text{ mm}$  and  $f = 35 \text{ GHz}$ . Solid lines show EDC solutions, dashed lines show HFSS solutions and boxes show experimental results.

### 4.3 SUMMARY

In summary, values for both the propagation and attenuation constant of PTFE and polyethylene dielectric waveguides were measured using the cavity resonator technique. By using two lengths of cavity, the measurements were obtained without the need for large cavity lengths. For both materials the propagation constant was shown to be in excellent agreement with experimental values, the attenuation constant being in fair agreement.

The problems of measuring the attenuation constant of coupled guides were highlighted and some ideas on how to overcome them were given. Propagation constants for symmetrical coupled waveguides were acquired and shown to be in good agreement with theoretical results using the technique presented in Chapter 3. HFSS finite element simulations for symmetrical structures were also shown to be in excellent agreement with measured propagation constants. It is therefore envisaged that the finite element simulations shown in Chapter 3 are valid for both the symmetrical and asymmetrical cases. We can therefore put some faith in the values of the complex propagation constant obtained using HFSS and therefore the technique in Chapter 3.

---

**REFERENCES**

- 1 R. J. Collier and P. D. White, "Attenuation measurements of dielectric waveguide," *Electron. Lett.*, vol. 10, no. 25/26, December 1974.
- 2 C. Chandler, "Investigation of dielectric rod as waveguides," *J. Appl. Phys.*, vol. 20, 1949, pp. 1188-1192.
- 3 D. Marcuse, "Theory of dielectric optical waveguides," *Academic Press*, 1974, Chapter 1.
- 4 G. Owyang, "Foundations of optical waveguides," *Edward Arnold*, 1981, Chapter 2.
- 5 F. Shimabukuro and C. Yeh, "Attenuation measurements of very low loss dielectric waveguides by the cavity resonator method applicable in the millimeter/submillimeter wavelength range," *IEEE Trans. Microwave Theory Tech.*, vol. 36, no. 7, July 1988, pp. 1160-1166.
- 6 C. Yeh, "Relation between  $\alpha$  and  $Q$ ," *Proc. IRE*, vol. 50, 1962, pp. 2145.
- 7 M. Afsar, "Precision dielectric measurements of nonpolar polymers in the millimeter wavelength range," *IEEE Trans. Microwave Theory Tech.*, vol. MTT-33, no. 12, July 1985, pp. 1410-1415.
- 8 M. Afsar and K. Button, "Millimeter-wave dielectric measurement of materials," *Proc. IEEE*, vol. 73, no. 1, January 1985, pp. 131-153.

---

## 5. DISCONTINUITIES IN DIELECTRIC WAVEGUIDES

---

In chapters 2 and 3, we considered guided modes on single and coupled dielectric waveguides. These modes adequately describe the field profiles of dielectric guides as long as there are no discontinuities nearby. In regions where discontinuities are present, another class of solutions, known as radiation modes, must also be examined. These radiation modes, together with the guided modes, form a complete set, which can describe exactly the field distributions at, and nearby, a discontinuity.

Discontinuities usually exist somewhere in a system. To launch energy into a dielectric waveguide there must be some form of discontinuity, whether it is a waveguide horn or another dielectric waveguide. Furthermore, as we shall see in Chapter 6, dielectric waveguide components based on coupled waveguides introduce discontinuities. Accordingly, in this chapter, we limit ourselves to the important case of discontinuities between single and coupled dielectric waveguide structures.

### 5.1 RADIATION MODES

We saw in Chapter 2 that the electric field of a dielectric waveguide with no discontinuities is given by

$$\mathbf{E}_t = \sum_{i=1}^n A_i \mathbf{E}_i, \quad (5.1)$$

where  $\mathbf{E}_i$  is the transverse field function of the  $i^{\text{th}}$  guided mode and  $A_i$  is a complex constant. We recall that the guided modes decayed exponentially within the air region

and consequently carried finite power in the  $z$  direction. There is, however, another class of modes that carry infinite power. These so-called radiation modes have standing wave functions in both the guiding and surrounding regions. Thus,

$$E = A_1 \cos(k_{x1}x) \quad \text{for } x \leq |a| \quad (5.2)$$

$$E = A_1 \cos(k_{x1}a) \cos(\rho x + \phi) \quad \text{for } x > a, \quad (5.3)$$

where  $\phi$  can be determined by matching the tangential fields at the  $|x|=a$  boundary. The decay constant  $\alpha_{x1}$  that was used in the air region has now been replaced by a propagation constant  $\rho$  [1]:

$$\rho = \sqrt{\varepsilon_2 k_0^2 - \beta_z^2}, \quad (5.4)$$

where here we assume that all the regions are lossless. Since we have not constrained the problem by setting the field to zero at infinity,  $\rho$  is continuous and can take on any positive value. Therefore,

$$0 \leq \rho < \infty. \quad (5.5)$$

Equation (5.4) results in two different types of solution: propagating modes and non-propagating evanescent modes. The propagating radiation modes are defined for  $0 \leq \rho < \sqrt{\varepsilon_2} k_0$ , where  $\beta_z$  is purely real and the evanescent modes for  $\sqrt{\varepsilon_2} k_0 \leq \rho < \infty$ , where  $\beta_z$  becomes purely imaginary.

Although the radiation modes carry infinite power, an expression for its value can be obtained with the help of the Dirac delta function. The Poynting power flow for two different modes,  $\mathbf{E}$  and  $\mathbf{E}'$ , is given by

$$P = \frac{1}{2} \int_S \text{Re} \{ \tilde{\mathbf{E}} \times \tilde{\mathbf{H}}' \} \cdot \hat{\mathbf{n}} da. \quad (5.6)$$

Evaluation of this integral gives a solution of the form [1, 2]

$$P = f(\rho)\delta(\rho - \rho'), \quad (5.7)$$

where  $\rho$  and  $\rho'$  are the transverse propagation constants in the surrounding region for the  $\mathbf{E}$  and  $\mathbf{E}'$  modes, respectively, and  $f(\rho)$  is finite for  $\rho > 0$ . We see that the power is zero for  $\rho \neq \rho'$ , which is as expected since the modes are orthogonal [2]. However, for  $\rho = \rho'$  the power becomes infinite. This suggests an infinite source power for each radiation mode; and therefore a single radiation mode is of little use. Fortunately, when we consider a continuum of radiation modes, finite power levels are realisable. Thus, the complete solution of a dielectric guide can be expressed as

$$\mathbf{E}_t = \sum_{i=1}^n A_i \mathbf{E}_i + \int_0^{\infty} A(\rho) \mathbf{e}(\rho) d\rho, \quad (5.8)$$

where  $A(\rho)$  and  $\mathbf{e}(\rho)$  are the amplitude constant and field functions of the radiation modes, respectively. The above expression completely describes the field function of a dielectric waveguide, even if discontinuities are present. It therefore forms the basis of the next section where transitions from single to coupled slab guides are analysed.

## 5.2 WAVEGUIDE DISCONTINUITIES

Consider a transition between a single guide to a coupled guide, see Figure 5.1. We denote the fields in the single guide, region A, with the superscript  $a$  and the fields in the coupled structure, region B, with  $b$ . Assuming that the structure supports one guided mode in Region A and two in Region B, we have the following continuity expressions

$$\mathbf{E}^a = \mathbf{e}_1^a + \sum_{i=1}^m A_i \mathbf{e}_i^a + \int_0^{\infty} A(\rho) \mathbf{e}^a(\rho) d\rho \quad (5.9)$$

$$\mathbf{H}^a = \mathbf{h}_1^a - \sum_{i=1}^m A_i \mathbf{h}_i^a - \int_0^\infty A(\rho) \mathbf{h}^a(\rho) d\rho \tag{5.10}$$

within region A and

$$\mathbf{E}^b = \sum_{i=1}^n B_i \mathbf{e}_i^b + \int_0^\infty B(\rho) \mathbf{e}^b(\rho) d\rho \tag{5.11}$$

$$\mathbf{H}^b = \sum_{i=1}^n B_i \mathbf{h}_i^b + \int_0^\infty B(\rho) \mathbf{h}^b(\rho) d\rho \tag{5.12}$$

within region B, where, for our case,  $m=1$  and  $n=2$ .

We require the fields to be continuous across the  $z=0$  boundary, i.e.

$$\mathbf{E}^a = \mathbf{E}^b \tag{5.13}$$

and

$$\mathbf{H}^a = \mathbf{H}^b. \tag{5.14}$$

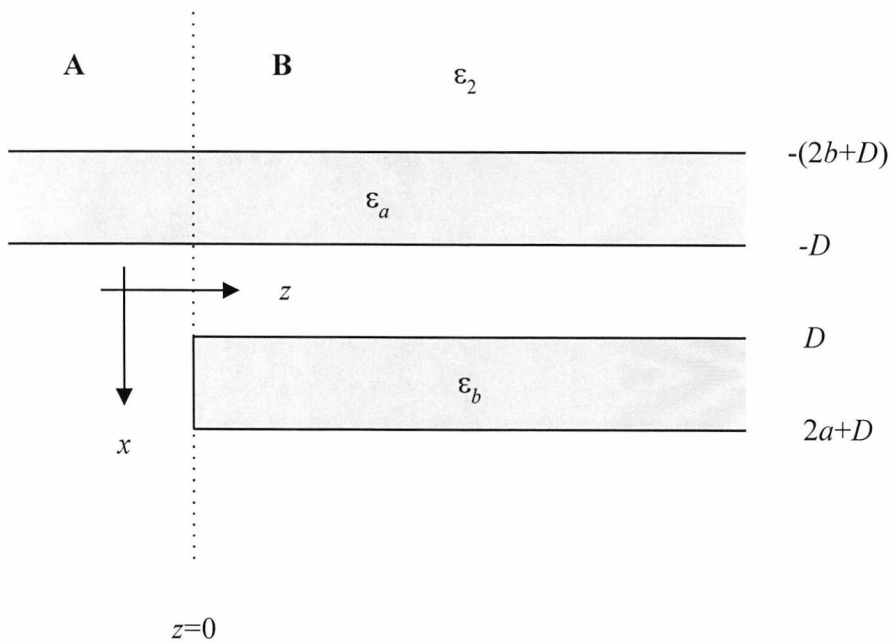


Figure 5.1. Geometry of dielectric slab waveguide discontinuity.

The problem now is to determine the amplitude functions  $A(\rho)$  and  $B(\rho)$  of the radiation fields. This can be achieved by changing the continuous summations in equations (5.13) and (5.14) into discrete ones [3, 4]. We therefore write  $A(\rho)$  and  $B(\rho)$  in terms of a known set of functions such as the Laguerre polynomials [3, 4]. Thus,

$$A(\rho) = \sum_{i=1}^{\infty} a_i f_i(\rho) \quad (5.15)$$

$$B(\rho) = \sum_{i=0}^{\infty} b_i f_i(\rho) \quad (5.16)$$

where  $a_i$  and  $b_i$  are constants and  $f_i(\rho)$  are Laguerre polynomials of degree  $i$ . To allow an numerical implementation the summation over all  $i$  in the above equations is truncated, equation (5.13) and (5.14) then become

$$\mathbf{e}_1^a + \sum_{i=1}^m A_i \mathbf{e}_i^a + \sum_{i=1}^M a_i \mathbf{E}_i^a = \sum_{i=1}^n B_i \mathbf{e}_i^b + \sum_{i=1}^N b_i \mathbf{E}_i^b \quad (5.17)$$

and

$$\mathbf{h}_1^a - \sum_{i=1}^m A_i \mathbf{h}_i^a - \sum_{i=1}^M a_i \mathbf{H}_i^a = \sum_{i=1}^n B_i \mathbf{h}_i^b + \sum_{i=1}^N b_i \mathbf{H}_i^b, \quad (5.18)$$

respectively. Where  $M$  and  $N$  are chosen for the required convergence and  $\mathbf{E}_i^{a,b}$  and  $\mathbf{H}_i^{a,b}$  are given by

$$\mathbf{E}_i^{a,b} = \int_0^{\infty} f_i(\rho) \mathbf{e}^{a,b}(\rho) d\rho \quad (5.19)$$

and

$$\mathbf{H}_i^{a,b} = \int_0^{\infty} f_i(\rho) \mathbf{h}^{a,b}(\rho) d\rho. \quad (5.20)$$

Clearly, equation (5.19) and (5.20) can be difficult to evaluate, particularly for coupled structures. However, Brooke and Kharadly proposed a mathematically

simpler method [5]; in their technique, the open dielectric waveguide is converted to a bounded guide by placing a conducting plane either side of the dielectric structure, refer to Figure 5.2. The continuum of radiation modes in equations (5.17) and (5.18) then become an infinite, but discrete, set of modes. These modes are of two types: fast and evanescent. The fast modes are defined for  $0 \leq \rho < k_0$  and have real propagation constants. In contrast, the evanescent modes, defined by  $k_0 \leq \rho < \infty$ , have purely imaginary propagation constants and are therefore non-propagating. The guided modes of the open structure are now referred to as slow modes but are still defined for  $k_0 < \beta_z < \sqrt{\epsilon_a} k_0$ .

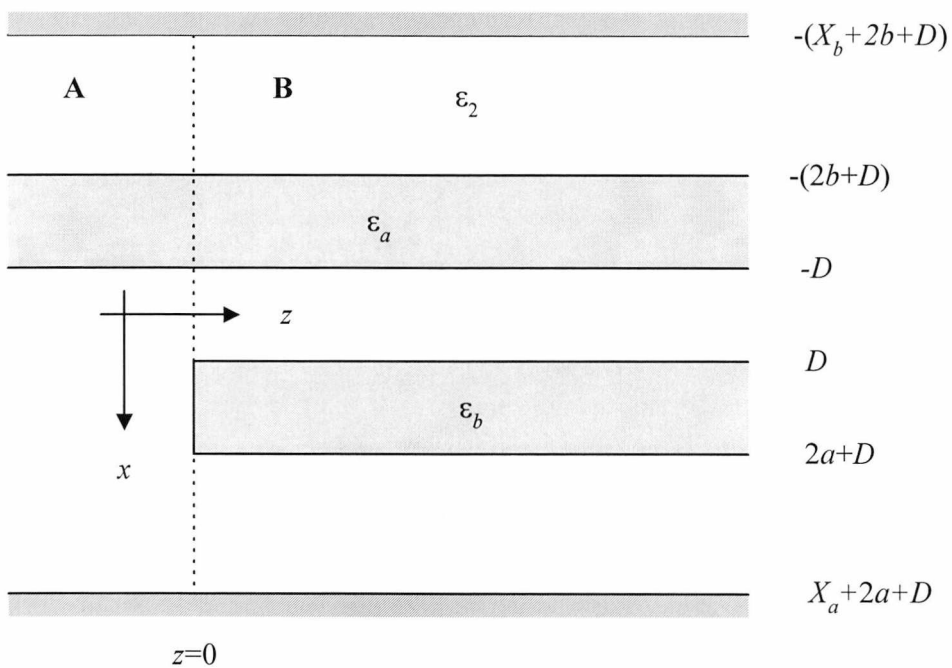


Figure 5.2. Geometry of bounded dielectric slab waveguide discontinuity.

The boundary conditions are now given by

$$\mathbf{e}_1^a + \sum_{i=1}^K A_i \mathbf{e}_i^a = \sum_{i=1}^K B_i \mathbf{e}_i^b \tag{5.21}$$

and

$$\mathbf{h}_1^a - \sum_{i=1}^K A_i \mathbf{h}_i^a = \sum_{i=1}^K B_i \mathbf{h}_i^b \tag{5.22}$$

where the summations are now over all modes: slow, fast and evanescent. Again, the infinite summation of fast and evanescent modes have been truncated to allow a numerical implementation. Also, we choose  $M$  and  $N$  such that  $m+M=n+N=K$ . Applying the orthogonality relations to the above equations we obtain [5]

$$\sum_{i=1}^K B_i (P_{ij}^{ba} + P_{ji}^{ab}) = 2\delta_{j1} P_1^a$$

$$A_j = \delta_{j1} - \sum_{i=1}^K B_i \frac{P_{ji}^{ab}}{P_j^a} \quad j=1, 2, 3, \dots, K \quad (5.23)$$

with

$$P_{ij}^{ba} = \int_S \mathbf{e}_i^b \times \mathbf{h}_j^a \cdot d\mathbf{S} \quad (5.24)$$

$$P_{ji}^{ab} = \int_S \mathbf{e}_j^a \times \mathbf{h}_i^b \cdot d\mathbf{S} \quad (5.25)$$

$$P_j^a = \int_S \mathbf{e}_j^a \times \mathbf{h}_j^a \cdot d\mathbf{S} \quad (5.26)$$

Also, the Kronecker delta function  $\delta_{ij}$  is defined as:

$$\delta_{ij} = \begin{cases} 1 & \text{if } i = j \\ 0 & \text{if } i \neq j \end{cases} \quad (5.27)$$

To evaluate the integrals in the above expressions we must first calculate the field functions for each of the modes on both sides of the  $z=0$  boundary. This is achieved in a similar manner to the open structure; the difference being that now the fields must equal zero at the  $x=(X_a+2a+D)$  and  $x=-(X_b+2b+D)$  boundaries. Therefore, following the same approach to Chapter 2 we find that the guidance condition of the slow mode solutions in the coupled region ( $z>0$ ) is given by

$$\begin{aligned}
 2D = & \frac{1}{2\alpha_{x2}} \ln \left\{ \frac{(T_a + 1) \sin(2k_{xa}a) + (T_a - 1) \sin(2\phi_a - 2k_{xa}a)}{(T_a - 1) \sin(2k_{xa}a) + (T_a + 1) \sin(2\phi_a - 2k_{xa}a)} \right\} \\
 & + \frac{1}{2\alpha_{x2}} \ln \left\{ \frac{(T_b + 1) \sin(2k_{xb}b) + (T_b - 1) \sin(2k_{xb}b - 2\phi_b)}{(T_b - 1) \sin(2k_{xb}b) + (T_b + 1) \sin(2k_{xb}b - 2\phi_b)} \right\}
 \end{aligned} \tag{5.28}$$

where

$$\phi_a = \tan^{-1} \left\{ \rho_a \frac{\alpha_{x2}}{k_{xa} T_a} \right\}, \tag{5.29}$$

$$\phi_b = 2k_{xb}b - \tan^{-1} \left\{ \rho_b \frac{\alpha_{x2}}{k_{xb} T_b} \right\}, \tag{5.30}$$

$$T_a = \tanh(\alpha_{x2} X_a), \tag{5.31}$$

$$T_b = \tanh(\alpha_{x2} X_b). \tag{5.32}$$

Again,  $\rho_a = 1$  and  $\rho_b = 1$  for TE modes;  $\rho_a = \frac{\epsilon_a}{\epsilon_2}$  and  $\rho_b = \frac{\epsilon_b}{\epsilon_2}$  for TM modes.

As expected, when  $X_a$  and  $X_b$  become infinite, equation (5.33) is identical to that of the open structure, equation (3.25).

The fast and evanescent guidance conditions for both the single and coupled guide regions follow in a similar way and are not considered here. The slow mode solutions for the single structure are given by

$$\tan(2k_{xa}a) = -\alpha_{x2} k_{xa} \frac{T_a + \tanh[\alpha_{x2}(X_b + 2b + 2D)]}{\alpha_{x2}^2 - T_a k_{xa}^2 \tanh[\alpha_{x2}(X_b + 2b + 2D)]} \tag{5.34}$$

Solving  $\beta_z$  for each of the waveguide modes and evaluating the corresponding field functions allows us to calculate the amplitude constants in equation (5.23). The field distribution at the boundary is then given.

Figure 5.3 shows field profiles either side of the  $z=0$  boundary for the following waveguide parameters:  $\epsilon_a=\epsilon_b=2.07$ ,  $\epsilon_1=1$ ,  $2a=2b=0.268\lambda_0$ , and  $2D=0$ . Solid lines are for region A, dashed lines are for region B. The number of modes,  $K$ , in equation (5.23) was set to 22. This figure was chosen for adequate convergence [5]. The mode indexes are denoted as follows. In region A, mode 1 is the reflected fundamental mode of the structure, mode 2 is the first order fast/evanescent mode, mode 3 is the next higher order mode, etc. In region B, modes 1 and 2 are the even and odd slow mode solutions, modes 8 to 12 are the first ten fast/evanescent modes with even symmetry and modes 13 to 22 are the first ten fast/evanescent modes with odd symmetry. Both the metal boundaries were placed a distance of 6 wavelengths from the dielectric waveguide, i.e.  $X_a=X_b=6.0\lambda_0$ . Brooke and Kharadly showed that the value of the amplitude constants oscillate about a mean for increasing  $X_a$ . However, in our case, the amplitude of the oscillation was found to be very small and therefore the amplitude constants were only calculated for a single value of  $X_a$ .

We see from Figure 5.4 that the amplitude constants of the fast/evanescent modes in both regions are much smaller than those of the slow modes. Moreover, the magnitude of the reflected fundamental mode in region A is much smaller than the slow mode constants in region B. It is further seen from Figure 5.5 and Figure 5.6 that as the separation is increased the above effects become more apparent. Indeed, as the separation is increased, the modes in region A become more and more orthogonal to the modes on guide B. In the limit,  $2D\rightarrow\infty$ , we find that the energy splits equally between the guided modes of the coupled structure, with the reflected and radiated energy converging to zero. It therefore seems reasonable to neglect the reflected energy. The amplitude constants in region B are then given by

$$B_i = \frac{P_{1i}^{ab}}{P_i^b} \quad i=1,\dots,K \quad (5.35)$$

Using the above expression we find that, for  $2D=0.268\lambda_0$ ,  $B_1=0.592$  and  $B_2=0.408$ . These values compare well with  $B_1=0.587$  and  $B_2=0.416$  using equation (5.23). For  $2D=0$  we have,  $B_1=0.848$  and  $B_2=0.154$  using equation (5.35), and,  $B_1=0.818$  and  $B_2=0.157$  using equation (5.23). Again, the difference is quite small.

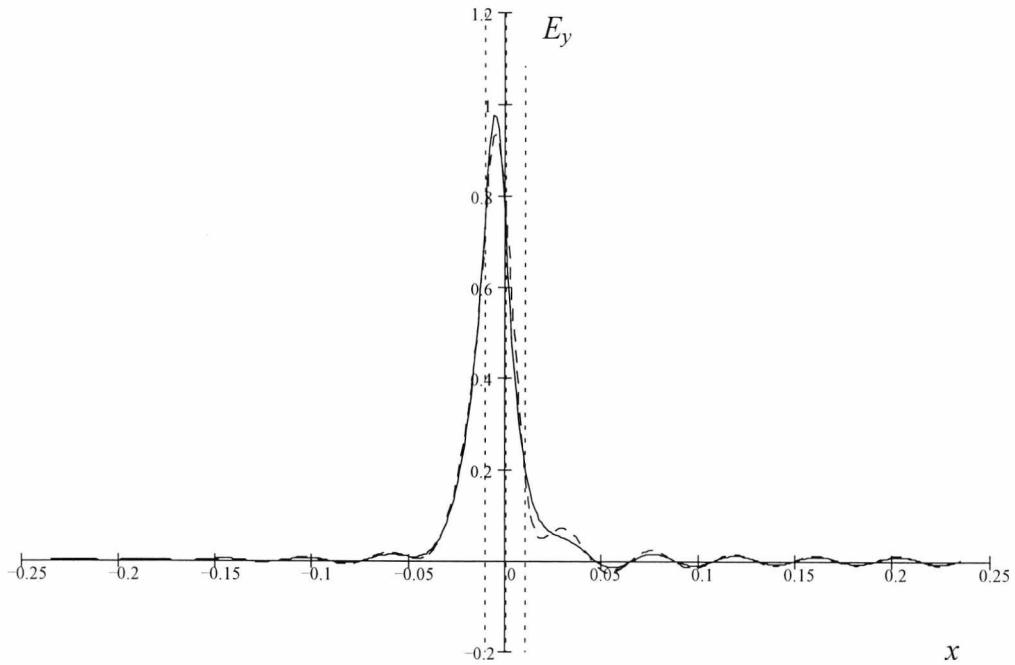


Figure 5.3. Field profiles at discontinuity for  $2a=2b=0.268\lambda_0$ ,  $\epsilon_a=\epsilon_b=2.07$ ,  $2D=0$ ,  $X_a=6\lambda_0$  and  $K=22$ . Solid lines show the field profile in region A ( $z<0$ ), dashed lines show field profiles for region B ( $z>0$ ).

	$ a $	$ b $
1	0.0297	0.8181
2	6.1930E-5	0.1569
3	3.1956E-5	2.2021E-4
4	2.4450E-4	8.5732E-4
5	1.2452E-4	1.7698E-3
6	5.3878E-4	2.8279E-3
7	2.6945E-4	3.8167E-3
8	8.9917E-4	4.6643E-3
9	4.5868E-4	5.3574E-3
10	1.3521E-3	5.9693E-3
11	6.8798E-4	6.1500E-3
12	1.8679E-3	6.2437E-3
13	9.6006E-4	0.0830
14	2.4377E-3	0.0820
15	1.2869E-3	0.0643
16	3.0659E-3	0.0501
17	1.6953E-3	0.0391
18	4.1799E-3	0.0310
19	2.2435E-3	0.0252
20	5.3493E-3	0.0226
21	3.0866E-3	0.0184
22	7.2866E-3	0.0147

Figure 5.4. Amplitude constants for  $2a=2b=0.268\lambda_0$ ,  $\epsilon_a=\epsilon_b=2.07$ ,  $2D=0$ ,  $X_a=6\lambda_0$  and  $K=22$ .

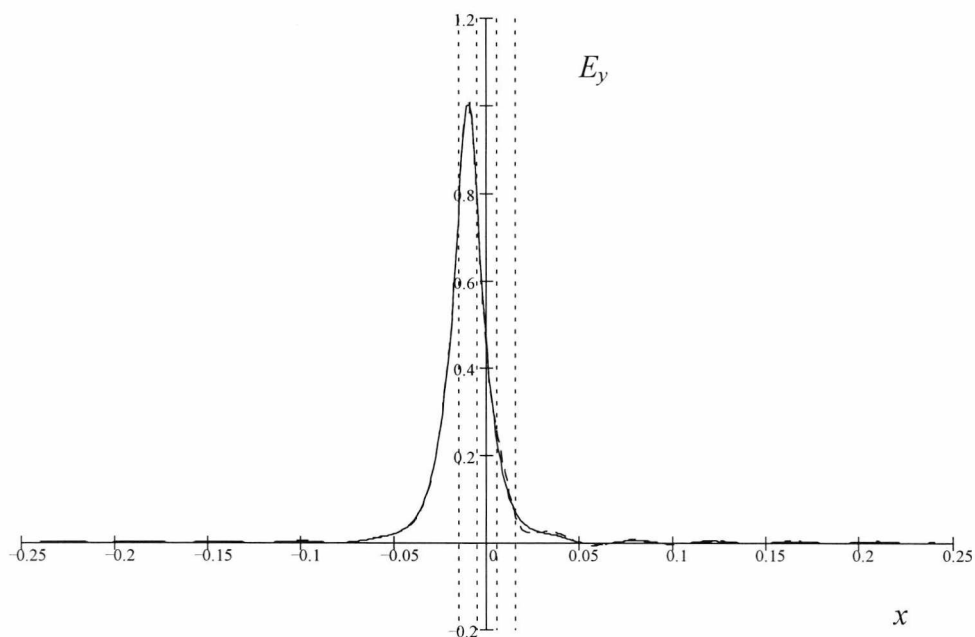


Figure 5.5. Field profiles at discontinuity for  $2a=2b=0.268\lambda_0$ ,  $\epsilon_a=\epsilon_b=2.07$ ,  $2D=0.267\lambda_0$ ,  $X_a=6\lambda_0$  and  $K=22$ . Solid lines show the field profile in region A ( $z<0$ ), dashed lines show field profiles for region B ( $z>0$ ).

	$ a $	$ b $
1	3.1560E-3	0.587
2	3.9982E-5	0.416
3	5.4791E-6	8.2418E-5
4	1.5451E-4	3.0827E-4
5	2.1802E-5	6.3390E-4
6	3.2953E-4	9.8005E-4
7	5.0258E-5	1.3007E-3
8	5.4377E-4	1.5590E-3
9	8.9495E-5	1.7242E-3
10	7.7263E-4	1.7529E-3
11	1.4067E-4	1.6219E-3
12	9.9239E-4	1.2372E-3
13	2.0322E-4	1.7485E-3
14	1.1852E-3	3.1480E-3
15	2.7222E-4	3.9834E-3
16	1.3450E-3	4.3505E-3
17	3.3519E-4	4.3800E-3
18	1.4886E-3	4.2235E-3
19	3.6147E-4	3.9898E-3
20	1.6655E-3	3.7599E-3
21	3.2020E-4	3.5579E-3
22	1.9875E-3	3.3380E-3

Figure 5.6. Amplitude constants for  $2a=2b=0.268\lambda_0$ ,  $\epsilon_a=\epsilon_b=2.07$ ,  $2D=0.267\lambda_0$ ,  $X_a=6\lambda_0$  and  $K=22$ .

Figure 5.7 shows the amplitude constants  $B_1$  and  $B_2$  against separation for a symmetrical structure using equation (5.35). We observe that for increasing separation the amplitudes of both the odd and even modes converge to 0.5. Therefore, as the separation is increased, the energy is split equally between the guided modes of the coupled structure. In contrast, from Figure 5.8 and Figure 5.9 it is seen that when asymmetry is introduced more of the energy is coupled into the even mode of the composite guide. Furthermore, as  $2D$  increases, the amplitude constant  $B_1$  converges to 1.0 and thus all of the energy is coupled into the even mode. As the asymmetry is increased, the above effect is more apparent. It should be noted that if the second waveguide has an isolated propagation constant greater than that of the first then the opposite would occur, i.e. more of the energy would couple to the odd mode. For synchronous structures, the amplitude constants converge to constant, but different values, see Figure 5.10. However, evaluation of the power in each mode shows that the energy is split evenly between the guided modes for increasing separation.

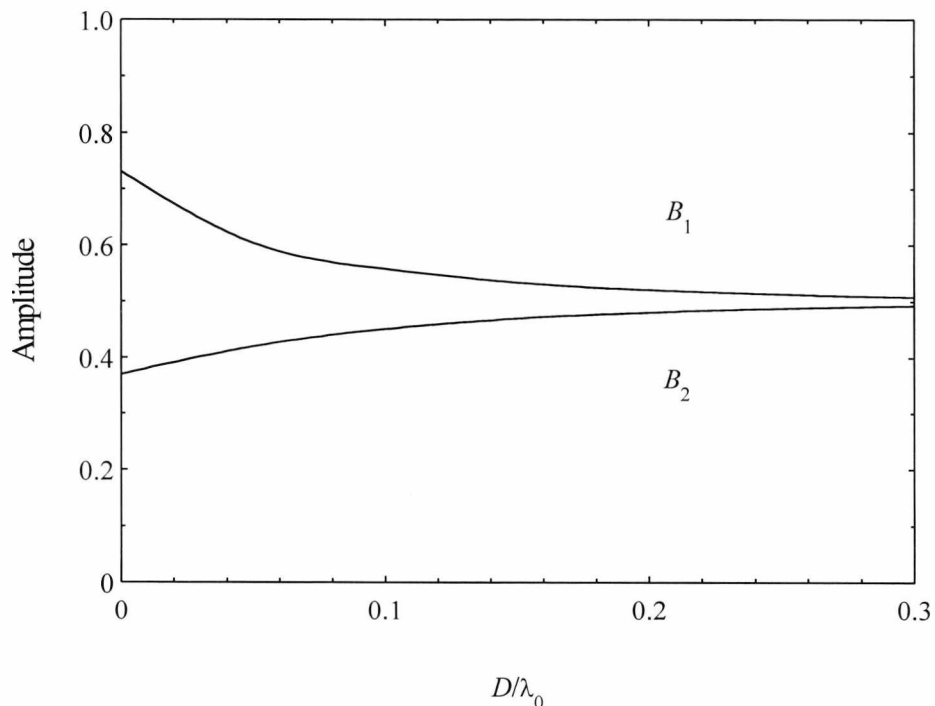


Figure 5.7. Variation of amplitude constants with separation for symmetrical coupled waveguide:  $2a=2b=0.4\lambda_0$  and  $\epsilon_a=\epsilon_b=2.07$ .

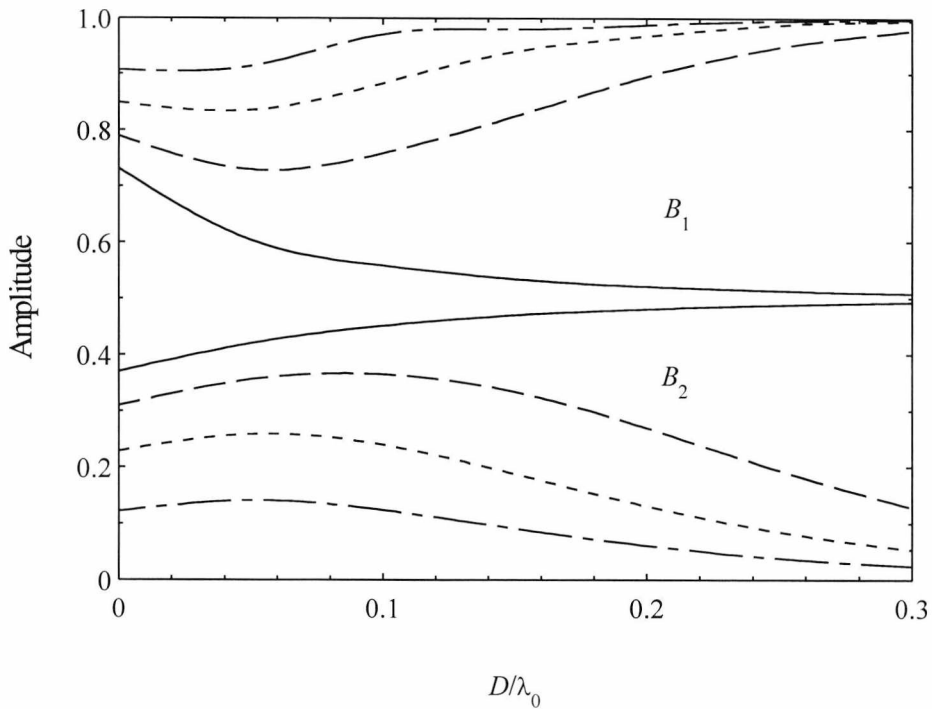


Figure 5.8. Variation of amplitude constants with separation for coupled waveguide with width asymmetry:  $2a=0.4\lambda_0$  and  $\epsilon_a=\epsilon_b=2.07$ . Solid lines are for  $a=b$ , dashed lines are for  $a=0.8b$ , dotted lines are for  $a=0.6b$  and dot-dashed lines are for  $a=0.4b$

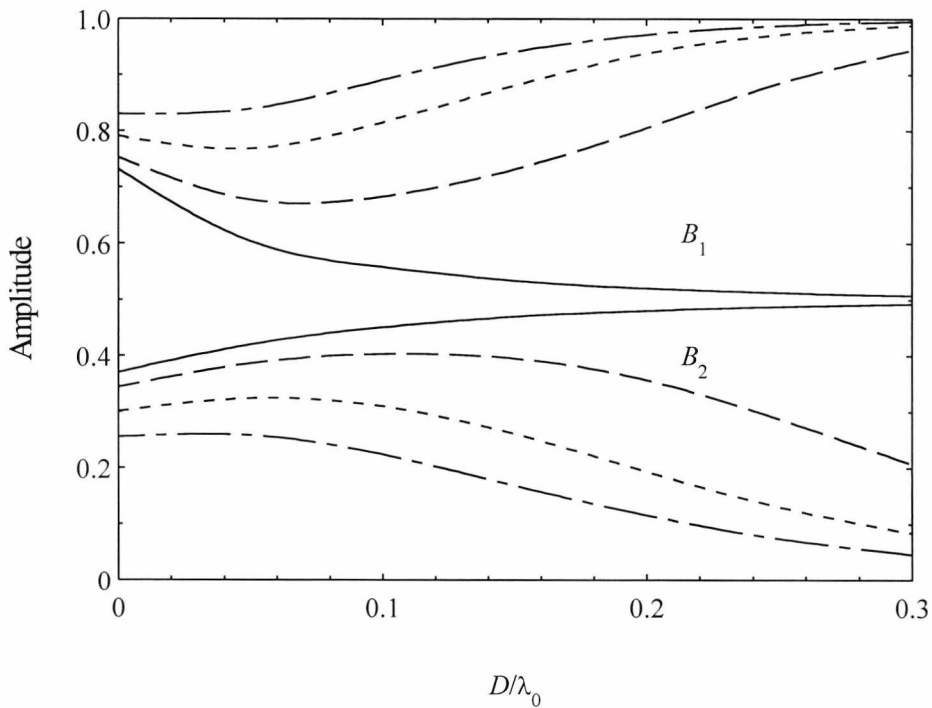


Figure 5.9. Variation of amplitude constants with separation for coupled waveguide with permittivity asymmetry:  $2a=2b=0.4\lambda_0$  and  $\epsilon_a=2.07$ . Solid lines are for  $\epsilon_b=2.07$ , dashed lines are for  $\epsilon_b=2.00$ , dotted lines are for  $\epsilon_b=1.90$  and dot-dashed lines are for  $\epsilon_b=1.80$ .

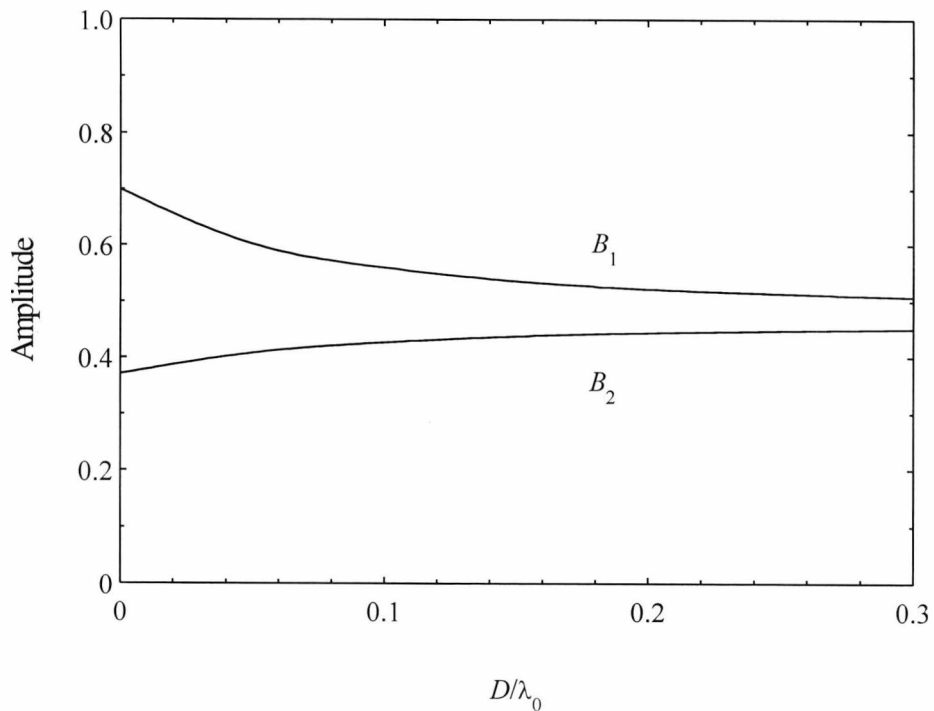


Figure 5.10. Variation of amplitude constants with separation for asymmetrical synchronous coupled waveguide:  $2a=0.4\lambda_0$ ,  $2b=0.568\lambda_0$ ,  $\epsilon_a=2.07$  and  $\epsilon_b=1.9$ .

Greater insight can be obtained if we plot the energy distribution around the discontinuity. Neglecting all radiation modes, the electric field profile in the coupled region is given by

$$E(x, z) = B_1 E_1(x) \exp(-j\beta_{1z} z) + B_2 E_2(x) \exp(-j\beta_{2z} z). \quad (5.36)$$

Therefore, the energy distribution is of the form

$$P(x, z) = \beta_{1z} B_1^2 E_1^2(x) + \beta_{2z} B_2^2 E_2^2(x) + (\beta_{1z} + \beta_{2z}) B_1 E_1(x) B_2 E_2(x) \cos(\Delta\beta_z z), \quad (5.37)$$

where

$$\Delta\beta_z = \beta_{1z} - \beta_{2z}. \quad (5.38)$$

Figure 5.11 shows plots of the energy distribution for a discontinuity of the type shown in Figure 5.1. The areas in red show the highest intensities, with the regions in purple showing the lowest intensities. The longitudinal dimension,  $z$ , is in a direction parallel to the side of the page; the transverse dimension,  $x$ , is parallel to the bottom of the page. Six plots are shown; (a), (b) and (c) are for separations of  $2D=0.0$ ,  $0.1\lambda_0$  and  $0.2\lambda_0$ , respectively. Similarly, (d), (e) and (f) show plots for  $2D=0.3\lambda_0$ ,  $0.4\lambda_0$  and  $0.5\lambda_0$ , respectively. In each case  $2a=2b=0.4\lambda_0$ ,  $\epsilon_a=\epsilon_b=2.07$  and  $\epsilon_2=1$ . Several interesting points can be noted from Figure 5.11.

Firstly, as expected, the energy distribution does not vary with  $z$  in the single structure since the guide is monomode. In contrast, within the coupled region, where two modes exist, the energy distribution oscillates back and forth between the two waveguides, a maximum in one guide coinciding with a minimum in the other. This effect becomes clear when we remember that the modes travel with different phase velocities. Therefore, when the modes are in phase, the fields constructively interfere within the first waveguide and destructively interfere within the second guide. When the modes are in antiphase the opposite occurs with the maximum occurring in the second guide.

Secondly, the period of oscillation increases indefinitely with separation. This is because the even and odd modes become degenerate to each other, i.e. their propagation constants converge to the same value for increasing separation. Consequently,  $\Delta\beta_z \rightarrow 0$  as  $2D \rightarrow \infty$  and therefore the period constantly increases with increasing separation.

Finally, the energy intensity maxima in one guide are approximately equal to those in the other and, for increasing separation, become identical. This suggests that the energy will transfer back and forth between the two guides even if the separation is extremely large - say kilometres. Of course, large longitudinal lengths are required for complete transferral but, nonetheless, the energy will transfer. From a practical standpoint, however, this is impossible. Referring to Figure 5.8 and Figure 5.9 we see that for relatively small asymmetries the energy coupled into the odd mode is much smaller than that of the even. Furthermore, as the separation is increased the above effect becomes more apparent. Thus, for very large separations, any small asymmetries will result in little or no energy coupling into the odd mode. We further note that asymmetry results in the even mode of the coupled structure being

indistinguishable from that of the isolated guide. It therefore becomes pointless to consider the problem as a coupled structure. Consequently, since no two guides can ever be identical, coupling over large separations is impossible.

Figure 5.12 and Figure 5.13 show plots for structures with asymmetry in permittivity and width, respectively. Figure 5.12 follows Figure 5.11 but with  $\epsilon_b=1.9$ . Similarly, Figure 5.13 is identical to Figure 5.11 except that  $b=0.8a$ . We notice that for both plots the period of the energy transfer appears to increase with separation in the same way as the symmetrical structure. However, it was shown in Chapter 3 that the even and odd mode propagation constants on asymmetrical guides converged to different values for increasing  $2D$ . Therefore,  $\Delta\beta_z$  remains finite, and consequently the period converges to a constant value. It is further seen from Figure 5.12 and Figure 5.13 that very little energy couples into the second guide, particularly as the separation is increased. This is expected from the previous discussions.

For completeness, Figure 5.14 shows plots for an asymmetrical synchronous guide. We notice that the plot is similar to that of the symmetrical structure. The only difference, that the maximum energy intensity in the second guide is less than that of the first.

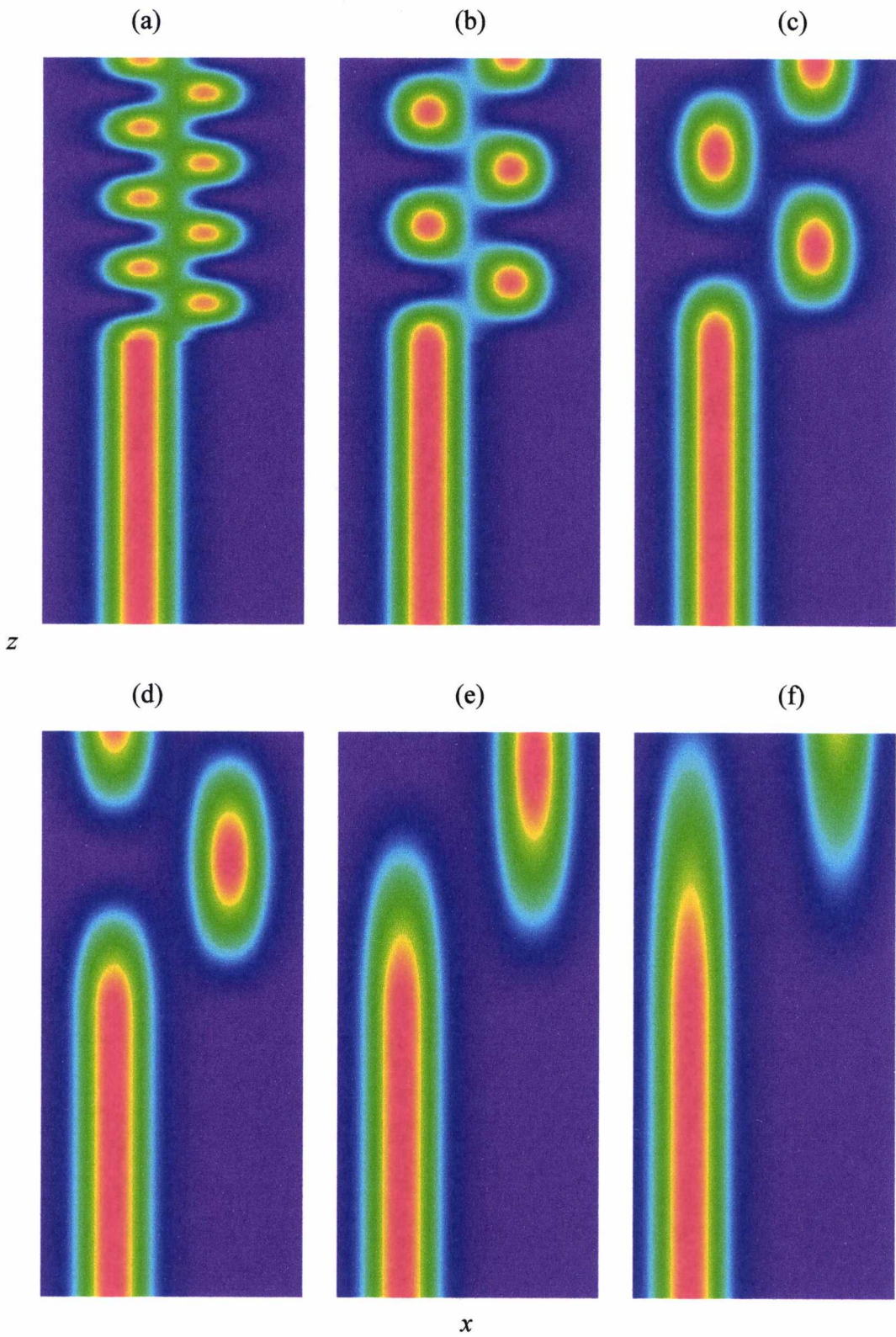


Figure 5.11. Energy distribution for symmetrical structure:  $a=b=0.2\lambda_0$ ,  $\epsilon_a=\epsilon_b=2.07$ .  
 (a)  $2D=0$ , (b)  $D=0.05\lambda_0$ , (c)  $D=0.1\lambda_0$ , (d)  $D=0.15\lambda_0$ , (e)  $D=0.2\lambda_0$  and (f)  $D=0.25\lambda_0$ .

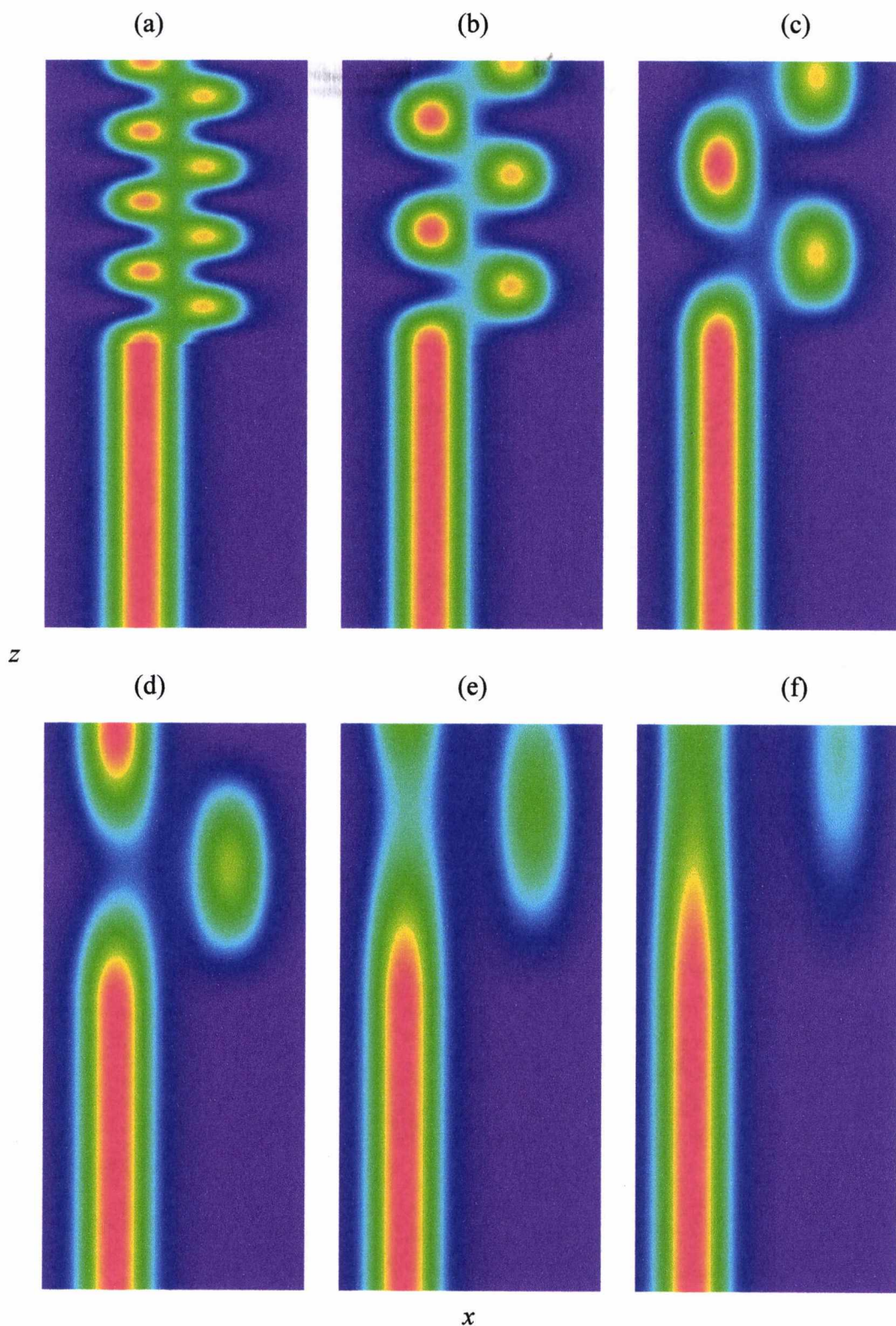


Figure 5.12. Energy distribution for permittivity asymmetry:  $\epsilon_a=2.07$ ,  $\epsilon_b=2.0$  and  $a=b=0.2\lambda_0$ . (a)  $2D=0$ , (b)  $D=0.05\lambda_0$ , (c)  $D=0.1\lambda_0$ , (d)  $D=0.15\lambda_0$ , (e)  $D=0.2\lambda_0$  and (f)  $D=0.25\lambda_0$ .

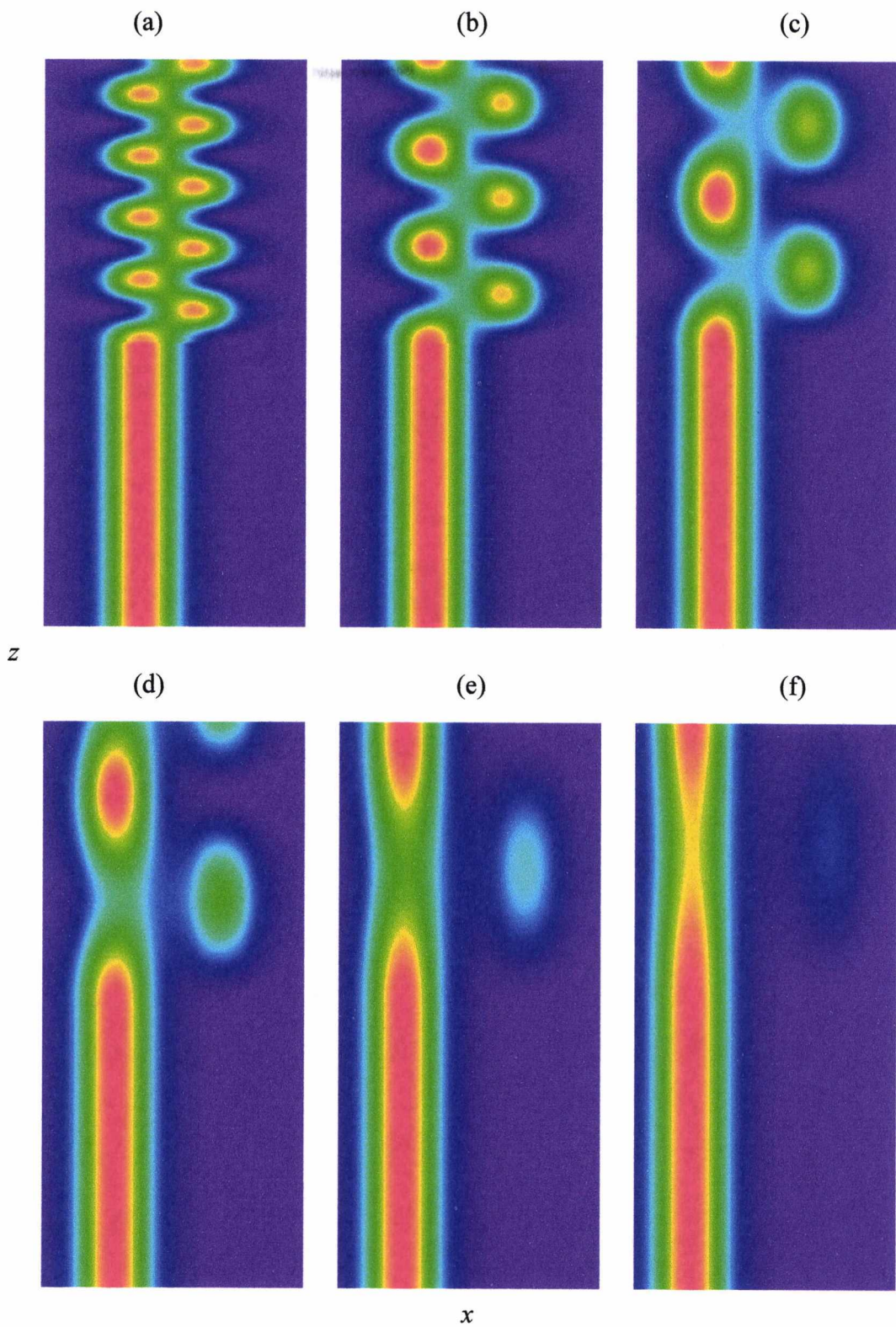


Figure 5.13. Energy distribution for width asymmetry:  $\epsilon_a = \epsilon_b = 2.07$ ,  $a = 0.2\lambda_0$  and  $b = 0.8a$ . (a)  $2D = 0$ , (b)  $D = 0.05\lambda_0$ , (c)  $D = 0.1\lambda_0$ , (d)  $D = 0.15\lambda_0$ , (e)  $D = 0.2\lambda_0$  and (f)  $D = 0.25\lambda_0$ .

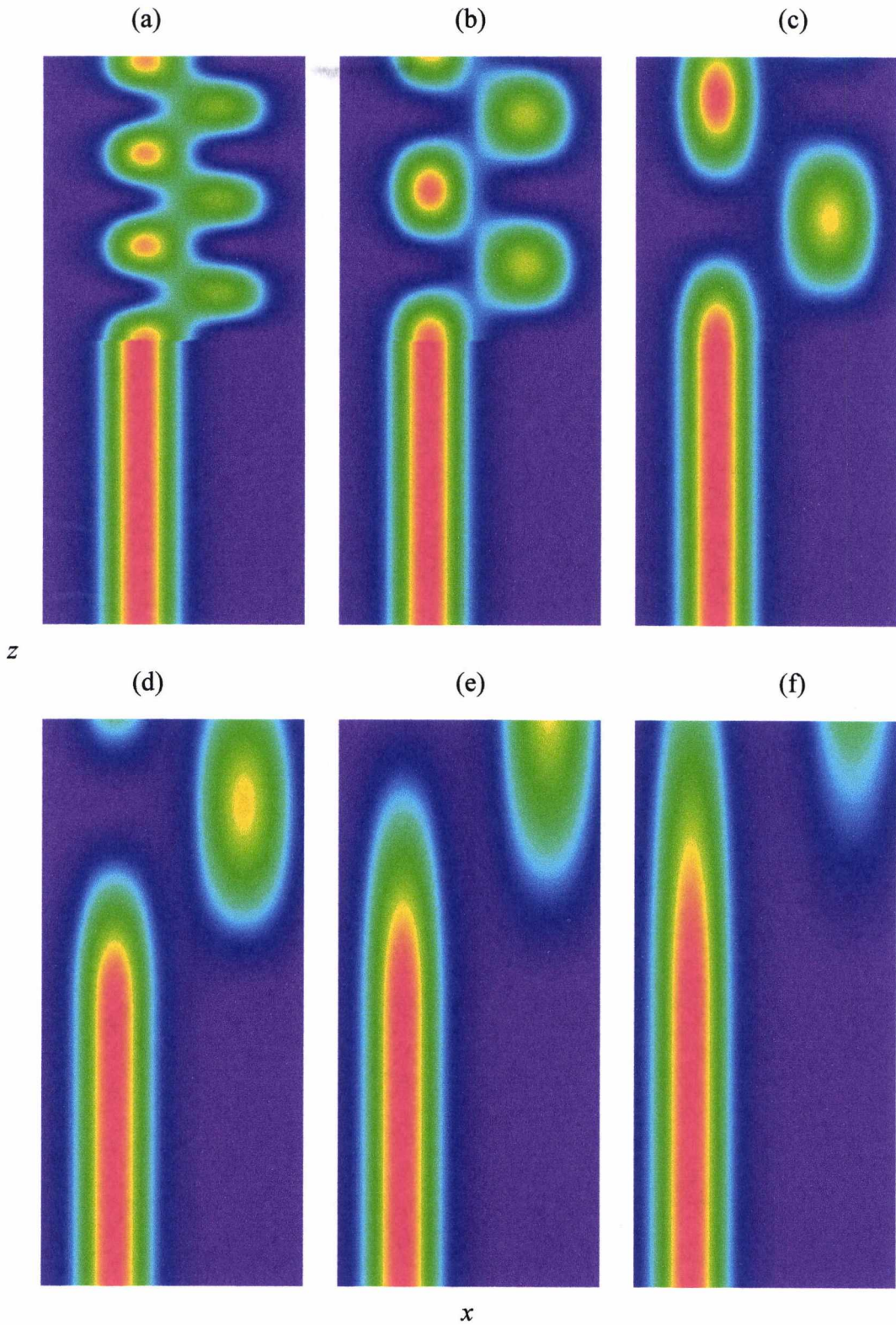


Figure 5.14. Energy distribution for asymmetrical synchronous structure:  $\epsilon_a=2.07$ ,  $\epsilon_b=1.9$ ,  $a=0.2\lambda_0$  and  $b=0.284\lambda_0$ . (a)  $2D=0$ , (b)  $D=0.05\lambda_0$ , (c)  $D=0.1\lambda_0$ , (d)  $D=0.15\lambda_0$ , (e)  $D=0.2\lambda_0$  and (f)  $D=0.25\lambda_0$ .

### 5.3 SUMMARY

In summary, exact expressions for bounded dielectric slab waveguides have been derived. It was shown that, for the cases considered here, very little energy is lost due to reflection and radiation from the discontinuities between single and coupled slab waveguides. Using this information, approximate expressions for coupled dielectric slab waveguide discontinuities were derived. Energy distribution plots around waveguide discontinuities were then displayed giving much insight into the coupling phenomena. It was shown that the energy transfers back and forth between the two guides with a beat length equal to  $\Delta\beta_z/\pi$ . Furthermore, it was shown that coupling between symmetrical (and synchronous) guides can be achieved even with large separations. However, if any asymmetries are present the coupling is greatly reduced. This has important implications for the design of dielectric waveguide components, as we shall see in the next chapter.

---

**REFERENCES**

- 1 D. Marcuse, "Theory of dielectric optical waveguides," *Academic Press*, chapter 1, 1974.
- 2 G. H. Owyang, "Foundations of optical waveguides," *Edward Arnold*, chapter 2, 1981.
- 3 S. F. Mahmoud and J. C. Beal, "Scattering of the surface waves at a dielectric discontinuity on a planar waveguide," *IEEE Trans Microwave Theory Tech.*, Vol. MTT-23, No. 2, February 1975, pp. 193-198.
- 4 K. Morishita, S. Inagaki and N. Kumagai, "Analysis of discontinuities in dielectric waveguides by means of the least squares boundary residual method," *IEEE Trans Microwave Theory Tech.*, Vol. MTT-27, No. 4, April 1979, pp. 310-315.
- 5 G. H. Brooke and M. M. Z. Kharadly, "Scattering by abrupt discontinuities on planar dielectric waveguides," *IEEE Trans Microwave Theory Tech.*, Vol. MTT-30, No. 5, May 1982, pp. 760-770.

---

## 6. DIELECTRIC WAVEGUIDE COMPONENTS

---

It is clear from the previous chapters that dielectric waveguides are superior to conventional guiding structures for interconnects between integrated circuits and test equipment at millimetre-wave frequencies above 110 GHz. For these applications, passive components such as attenuators and phase-shifters are often useful, particularly in measurement systems.

In Chapter 5 it was shown that the energy in coupled structures transfers back and forth between the two guides. If the guides are identical, large amounts of energy transfer between them. However, if any asymmetries are present, the coupling is greatly reduced. These phenomena are used in this chapter to demonstrate several dielectric waveguide components, namely an attenuator, a wavemeter and a low-loss phase-shifter. The attenuator and wavemeter exploit the coupling effects of symmetrical coupled structures to introduce large insertion losses. In contrast, for the phase-shifter, the coupling effects are prevented by introducing asymmetries. For simplicity, measurements for each component are provided at microwave frequencies, but their operation would apply equally to millimetre-wave frequencies.

### 6.1 DIELECTRIC WAVEGUIDE ATTENUATOR

The first component we consider is a dielectric waveguide attenuator. The geometry of the device is shown in Figure 6.1. A dielectric block of length  $L$  is situated parallel to the dielectric waveguide forming a short length of coupled guide. As a result, the energy transfers back and forth between the waveguide and the dielectric block with a periodicity  $\Delta\beta_z/\pi$ . If an energy maxima in the dielectric block coincides with the  $z=L$  boundary, large amounts of energy will be lost as radiation. The block can therefore be used as a useful waveguide attenuator. To ensure that maximum

attenuation is achieved, both the dielectric and the waveguide have the same cross-sectional dimensions and are made of the same material (refer to Chapter 5). Since the beat length  $\Delta\beta_z/\pi$  and therefore the amount of radiated energy is dependent on the separation, varying amounts of attenuation can be achieved by altering the distance between the dielectric and the waveguide. The device then works as a variable attenuator.

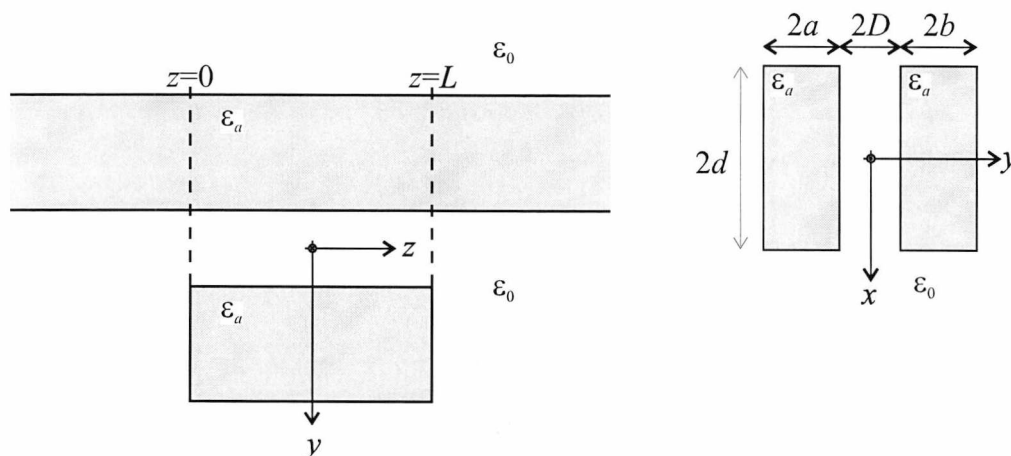


Figure 6.1. Geometry of dielectric waveguide attenuator/wavemeter.

To analyse the operation of the attenuator, we must first study the structure in Figure 6.1. Double discontinuities of this type have been described by Clarricoats and Slinn [1] for metallic waveguide. However, their method applies equally to open structures. Following the bounded approach of Chapter 5, i.e. we assume that the structure in Figure 6.1 has a metallic plane at  $-X_a$  and  $X_b$ . Then, if the isolated guide is monomode and the coupled region supports only two guided modes we find that the continuity equations for the two boundaries are given by

$$\mathbf{e}_1^a + \sum_{i=1}^{K_a} A_i' \mathbf{e}_i^a = \sum_{i=1}^{K_b} B_i \mathbf{e}_i^b + \sum_{i=1}^{K_b} B_i' \mathbf{e}_i^b \tag{6.1}$$

and

$$\mathbf{h}_1^a - \sum_{i=1}^{K_a} A_i \mathbf{h}_i^a = \sum_{i=1}^{K_b} B_i \mathbf{h}_i^b - \sum_{i=1}^{K_b} B_i' \mathbf{h}_i^b \tag{6.2}$$

at the  $z=0$  boundary and

$$\sum_{i=1}^{K_b} B_i \mathbf{e}_i^b \exp(-\gamma_i L) + \sum_{i=1}^{K_b} B'_i \mathbf{e}_i^b \exp(\gamma_i L) = \sum_{i=1}^{K_a} C_i \mathbf{e}_i^a \quad (6.3)$$

and

$$\sum_{i=1}^{K_b} B_i \mathbf{h}_i^b \exp(-\gamma_i L) - \sum_{i=1}^{K_b} B'_i \mathbf{h}_i^b \exp(\gamma_i L) = \sum_{i=1}^{K_a} C_i \mathbf{h}_i^a \quad (6.4)$$

at the  $z=L$  boundary. The orthogonality conditions can now be applied and  $K_a$  and  $K_b$  chosen to allow a solution.

However, it was shown in Chapter 4 that the reflected components are much smaller than the transmitted components. Thus, if we neglect the reflected (primed) terms in equations (6.1), (6.2), (6.3) and (6.4) we find that the continuity equations simplify to

$$\mathbf{e}_1^a = \sum_{i=1}^{K_b} B_i \mathbf{e}_i^b \quad (6.5)$$

and

$$\sum_{i=1}^{K_b} B_i \mathbf{e}_i^b \exp(-\gamma_i L) = \sum_{i=1}^{K_a} C_i \mathbf{e}_i^a. \quad (6.6)$$

Applying the orthogonality relations yields

$$B_i = \frac{P_{1i}^{ab}}{P_i^b} \quad i=1, \dots, K_b$$

and

$$C_i = \sum_{j=1}^{K_b} \frac{P_{ji}^{ba}}{P_i^a} B_j \exp(-\gamma_j L) \quad i=1, \dots, K_a \quad (6.7)$$

where the integrals  $P_i^a$ ,  $P_i^b$ ,  $P_{ij}^{ab}$  and  $P_{ij}^{ba}$  are defined in Chapter 5.

The problem can be simplified further if we assume that the radiation terms from the first boundary do not reach the second boundary, i.e. all of the energy in the forward propagating radiation modes radiates away. We then have, for the transmitted guided mode,

$$C_1 = \frac{P_{11}^{ba} P_{11}^{ab}}{P_1^a P_1^b} \exp(-\gamma_1 L) + \frac{P_{21}^{ba} P_{12}^{ab}}{P_1^a P_2^b} \exp(-\gamma_2 L) \quad (6.8)$$

The amplitude of the transmitted guided mode is now related to the power in the incident mode, and the field profiles of the guided modes in the coupled structure. Since we do not consider radiation modes in equation (6.8) the problem can be treated as an open structure. The surface integrals,  $P_i^a$ ,  $P_i^b$ ,  $P_{ij}^{ab}$  and  $P_{ij}^{ba}$  are therefore defined over an infinite cross-section.

Figure 6.2 and Figure 6.3 show the variation of the transmitted mode amplitude with separation for frequencies of 8.0 GHz and 12.0 GHz, respectively. In each case the solid line shows theoretical results, using equation (6.8), for a TE mode symmetrical coupled slab waveguide of relative permittivity  $\epsilon_a = \epsilon_b = 2.07$  and width  $2a = 2b = 10.9$  mm. The length of the dielectric block was set to  $L = 180$  mm. For comparison, experimental results for coupled PTFE dielectric waveguides of dimensions 22.86 mm by 10.9 mm are shown. The experimental results were obtained from a network analyser using the insertion loss technique, described in Chapter 4. As can be seen, the theory is in good agreement with the experimental results, except where the attenuation reaches a maximum. At this point most of the energy is in the dielectric block and it is envisaged that there will be considerable reflection from the  $z=L$  boundary. Therefore, it may not be appropriate to neglect the multiple reflections under these operating conditions. Of course, the theoretical method only considers slab waveguides with infinite  $d$  dimensions. Whereas for the experimental results the  $d$  dimension is only twice the  $a$  dimension. However, as frequency increases, the solutions of dielectric waveguides converge to those of slab waveguides [2]. This fact is demonstrated when we look at Figure 6.3. There the

experimental results are in better agreement with theoretical values than those in Figure 6.2.

A more thorough analysis would consider all the terms: radiation and reflected. In addition, the transverse field functions for rectangular rather than slab waveguides should be examined. However, here we are only concerned with the principle of operation, for which the present technique is sufficient.

Several additional points should be noted about the attenuator. Firstly, the large maximum in the insertion loss occur when the energy is predominantly in the dielectric block at the  $z=L$  boundary. This condition is satisfied when  $\Delta\beta_z L = n\pi$ , where  $n$  is an odd integer. Care must therefore be taken to ensure that  $\Delta\beta_z L < 3\pi$ , otherwise several maxima will be present in the insertion loss. Secondly, we observe that the attenuation in Figure 6.3 reaches a maximum of 7.4 dB. For many applications, this figure would be insufficient. Fortunately, further attenuation can be achieved by increasing the cross-sectional dimensions of both the waveguide and the dielectric block. Alternatively, several blocks can be placed one after each other (in the longitudinal direction). Thirdly, the structure radiates large amounts of energy from the  $z=L$  boundary. Therefore, if EMC considerations are important, radio absorbing material (RAM) should be placed at the  $z=L$  boundary to absorb any radiated energy. Finally, the dielectric block must have some movable supporting structure in order to keep it parallel to the waveguide. However, any material in contact with the block will change the propagation characteristics of the coupled guide. To minimise these effects, the dielectric block can either be housed in an expanded polystyrene jig, or small dielectric rods can be connected to the block. An alternative would be a metallic plate in place of the dielectric block. For  $E^y$  mode propagation, the method of images shows that a metallic plane situated a distance  $2D$  from the waveguide would act as a dielectric block of equal cross-section situated at  $4D$ . Unfortunately, due to the skin effect and surface roughness the metallic plane would be an imperfect mirror and consequently the structure may not be as efficient as the dielectric block.

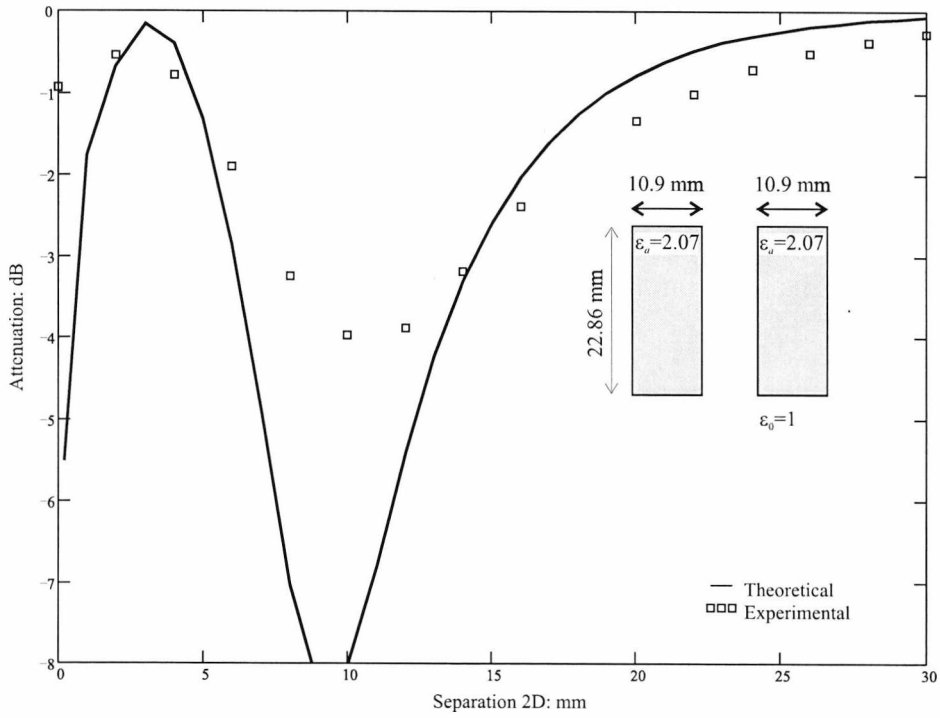


Figure 6.2. Attenuation for PTFE  $E^x$  mode dielectric waveguide attenuator with  $L=180$  mm at  $f=8.0$  GHz.

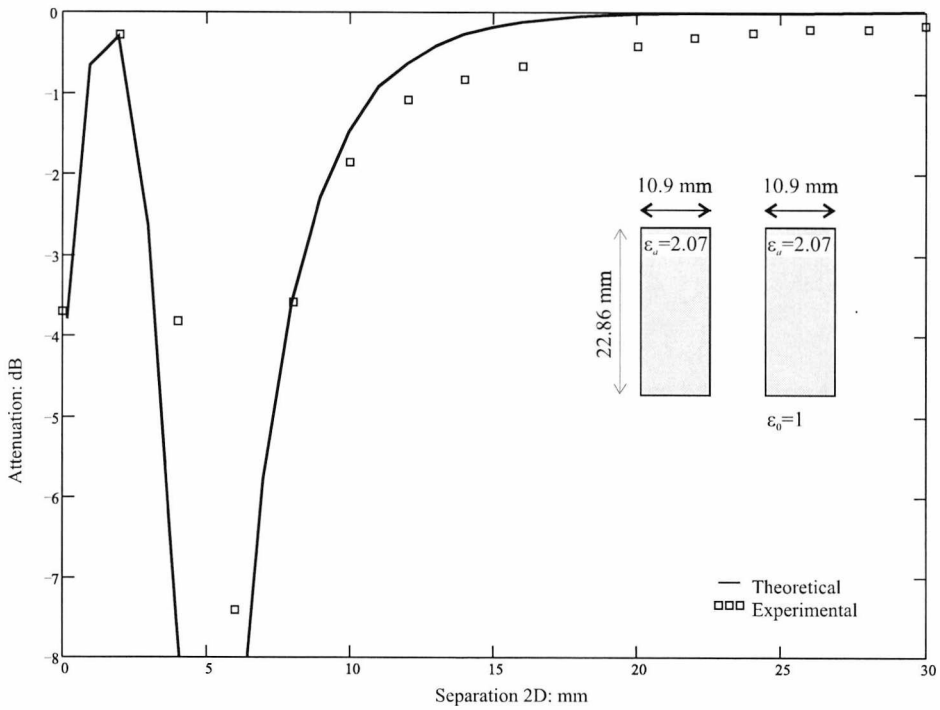


Figure 6.3. Attenuation for PTFE  $E^x$  mode dielectric waveguide attenuator with  $L=180$  mm at  $f=12.0$  GHz.

## 6.2 DIELECTRIC WAVEGUIDE WAVEMETER

We notice that the position of maximum attenuation in Figure 6.2 and Figure 6.3 varies as a function of frequency. The actual point of maximum radiation occurs when an energy maxima in the dielectric block coincides with the  $z=L$  boundary. This is satisfied when

$$\Delta\beta_z L = n\pi \text{ where } n=1, 3, 5, \dots \quad (6.9)$$

We see from Figure 6.4 that the above condition is obtained at different separations for different operating frequencies. It therefore seems plausible to measure the separation at which maximum radiation occurs and, from this value, calculate the operating frequency [3]. The structure can then be used as a simple dielectric guide wavemeter, in much the same way as variable resonant cavities are used for conventional metallic waveguide.

Figure 6.5 shows the insertion loss for a  $E_{mn}^y$  mode wavemeter. The results are for operating frequencies of 12.0, 14.0 and 16.0 GHz, with  $2a=10.9$  mm,  $2d=22.9$  mm and  $L=180$  mm. Both the waveguide and the movable dielectric are PTFE with an assumed relative permittivity  $\epsilon_a=2.07$ . It is clearly seen from Figure 6.5 that maximum insertion loss occurs at different separations for different operating frequencies. Figure 6.6 and Figure 6.7 show experimental and theoretical results for both  $E^y$  and  $E^x$  mode wavemeters, respectively. In each case, the theoretical and measured separation,  $2D$ , resulting in maximum insertion loss is plotted against frequency. The theoretical values are calculated using the slab waveguide approximation. The reason for this becomes clear when we look at Figure 6.8. We see that although the values for  $\beta_z$  calculated using the EDC method are better than the slab approximation, the difference in the two values is not. Consequently, the results in Figure 6.6 and Figure 6.7 are for slab waveguides of width  $2a=10.9$  mm and permittivity  $\epsilon_a=2.07$ .

As can be seen, the experimental results are in good agreement with theoretical values at the higher frequencies. This is because the slab guide approximation is more accurate when the modes are far from cut-off. Better theoretical results could be

achieved by using numerically intensive finite element methods. Alternatively, the wavemeter structure could be operated far from cut-off by increasing the  $2a$  dimension. This has the added advantage of sharper insertion loss, see Figure 6.5. Once more, the length  $L$  must be chosen to ensure that  $\Delta\beta_z L < 3\pi$ . Further, the coupled region should only support two guided modes, otherwise several maxima will be observed in the insertion loss.

Another useful application for the structure in Figure 6.1 would be as technique to measure the dielectric constant of an unknown material. This would again be achieved by measuring the separation of maximum radiation. However, to ensure that large amounts of energy transfer to the unknown material, the structure would need to be synchronous, or at least close to synchronism. This would require an a priori value of the unknown dielectric. Nevertheless, an approximate value for the unknown is usually given from a theoretical understanding. The above technique may therefore be worth consideration in later work.

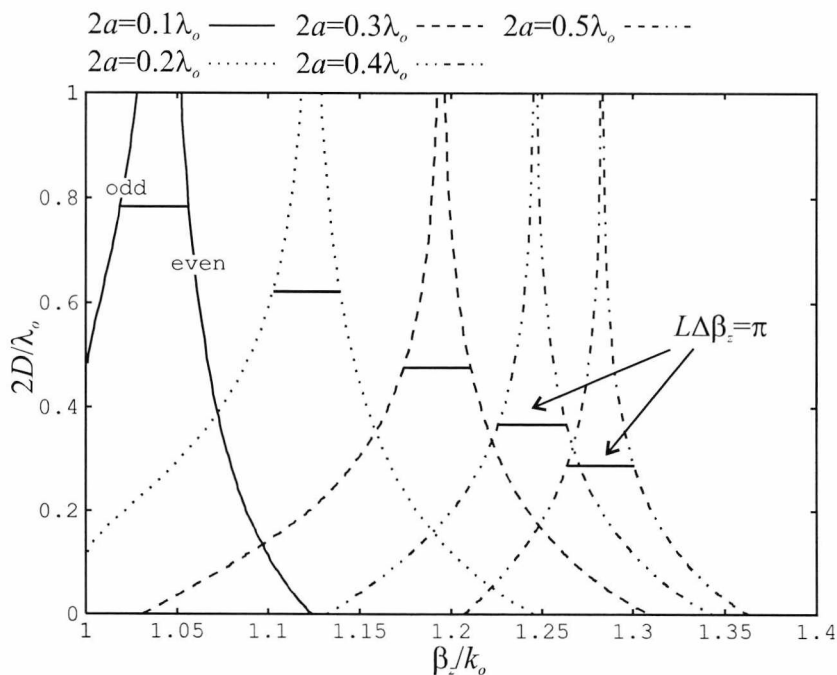


Figure 6.4. Variation of  $\Delta\beta_z$  with frequency.

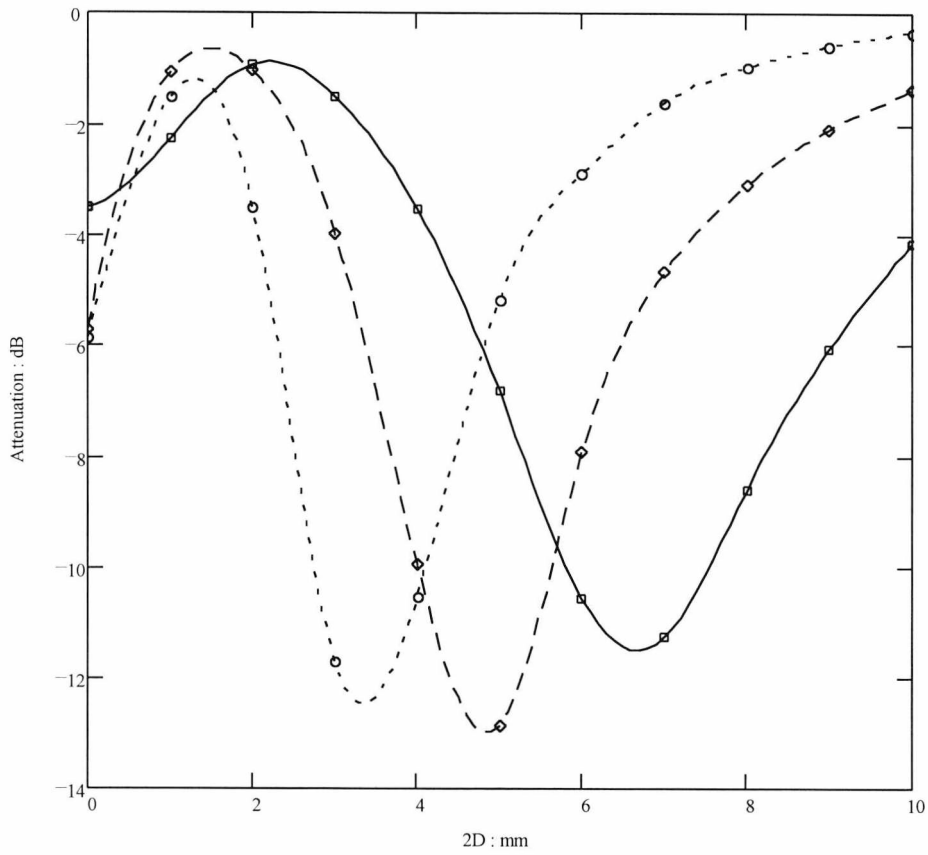


Figure 6.5. Insertion loss for  $E^y$  mode wavemeter for 12.0 GHz (solid line), 14.0 GHz (dashed line) and 16.0 GHz (dotted line). Points are experimental values, lines are interpolated values.

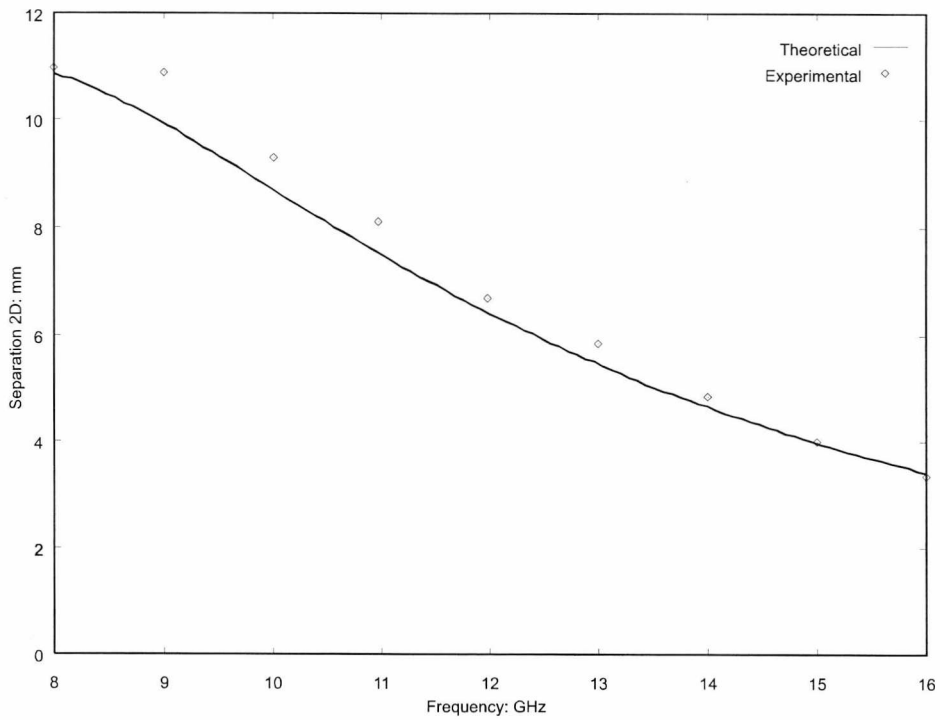


Figure 6.6. Separation of maximum attenuation against frequency for  $E^y$  modes.

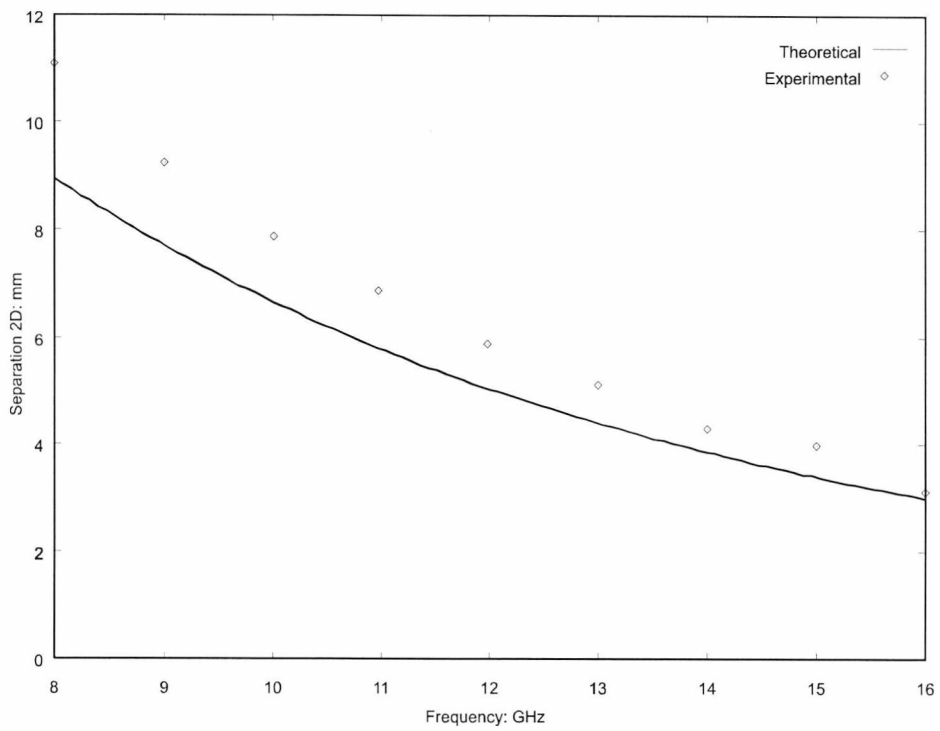


Figure 6.7. Separation of maximum attenuation against frequency for  $E^x$  modes.

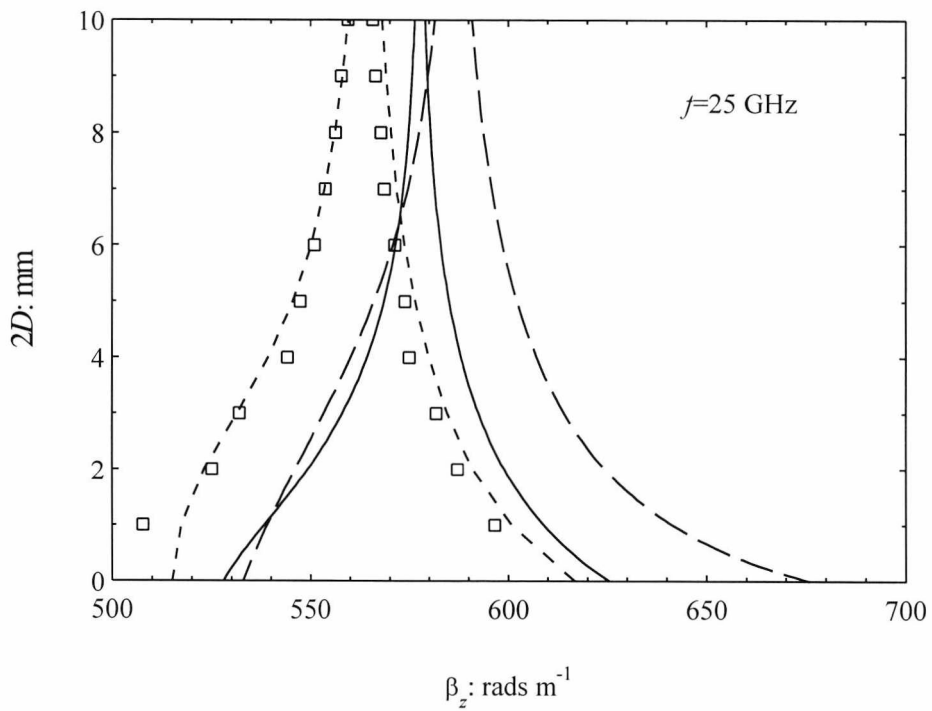


Figure 6.8.  $\beta_z$  as a function of  $2D$  for experimental (boxes), HFSS (dotted lines), slab approximation (dashed lines) and coupled EDC method (solid lines) results.

### 6.3 LOW-LOSS PHASE-SHIFTER

In Chapter 5 we saw that very little energy is coupled to the second dielectric waveguide if the guides are asymmetrical. Furthermore, in Chapter 2 it was shown that for large asymmetries the coupled guide remains monomode. Under these conditions, very little energy is lost due to radiation since the energy remains predominantly within the first guide. Therefore, the large maxima in the insertion do not exist for large asymmetries. In addition, large asymmetries reduce the radiation and reflection from the discontinuities at  $z=0$  and  $z=L$ , particularly if the dielectric block is of the same material with  $b \ll a$ . We can exploit these facts to design a low-loss phase-shifter [4].

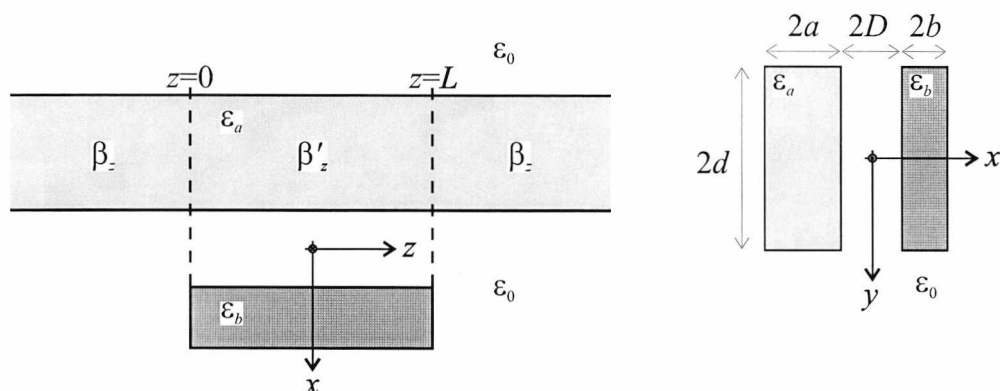


Figure 6.9. Geometry of dielectric waveguide phase-shifter.

Existing phase-shifters for millimetre-wave dielectric waveguide [5, 6, 7] use conducting planes in order to change the phase velocity of the propagating modes. By varying the distance between the dielectric waveguide and the conducting plane, a varying phase shift is achieved. However, metallic plane phase-shifters can become very lossy since they work like a symmetrical coupled dielectric waveguide. It is further envisaged that at millimetre-wave frequencies above 110 GHz the losses due to the skin effect will contribute significantly to the overall loss of metallic plane phase-shifters.

We therefore place a dielectric block, of different width and/or permittivity to the main guide, at a distance  $2D$ , refer to Figure 6.9. The phase shift of this device, if the coupled region is monomode, is given by

$$\Phi(2D) = [\beta_z - \beta'_z(2D)]L \quad (6.10)$$

where  $\beta_z$  is the longitudinal propagation constant of the isolated waveguide and  $\beta'_z$  is the propagation constant of the composite dielectric waveguide, formed by the piece of dielectric situated a distance  $2D$ .

From chapters 2 and 3 we know both  $\beta'_z(2D)$  and  $\beta_z$ ; equation (6.10) can thus be easily evaluated. Figure 6.10(a) shows experimental and theoretical results for a dielectric phase-shifter operating at 8.0 GHz and 12.0 GHz. The results show  $E_y$  mode solutions for a PTFE dielectric waveguide of relative permittivity  $\epsilon_r=2.07$  and dimensions  $2a=10.9$  mm by  $2d=22.9$  mm. The phase shifting dielectric is also PTFE with dimensions  $2b=3.4$  mm by  $2d=22.9$  mm and is of length  $L=180$  mm. As can be seen, the experimental results are in good agreement with theoretical values. We note that the theoretical results were obtained using the EDC method described in chapters 2 and 3. The experimental results were acquired in a method similar to that of the wavemeter, except that the phase delay was also considered.

Figure 6.10(b) shows plots of the attenuation. We see that the attenuation is less than 1 dB for both frequencies. If the phase-shifter is operated for  $2D > 10$  mm then the attenuation is reduced to less than 0.1 dB. This will of course reduce the maximum phase shift to less than 20 degrees. However, if the longitudinal length is increased, then from equation (6.10) we see that the phase shift is also increased. Furthermore, increasing  $L$  has no effect on the attenuation (assuming the dielectric is lossless) because the losses are only due to the discontinuities at  $z=0$  and  $z=L$ . These can be decreased further if the  $b$  dimension of the dielectric is reduced.

For the purpose of comparison, a phase-shifter using a metallic wall in place of the dielectric is given in Figure 6.11. The longitudinal length  $L$  is again 180 mm and results for both 8.0 GHz and 12.0 GHz are given. As can be seen, the attenuation for the metallic phase-shifter is far greater than that of the dielectric, especially in the low frequency case.

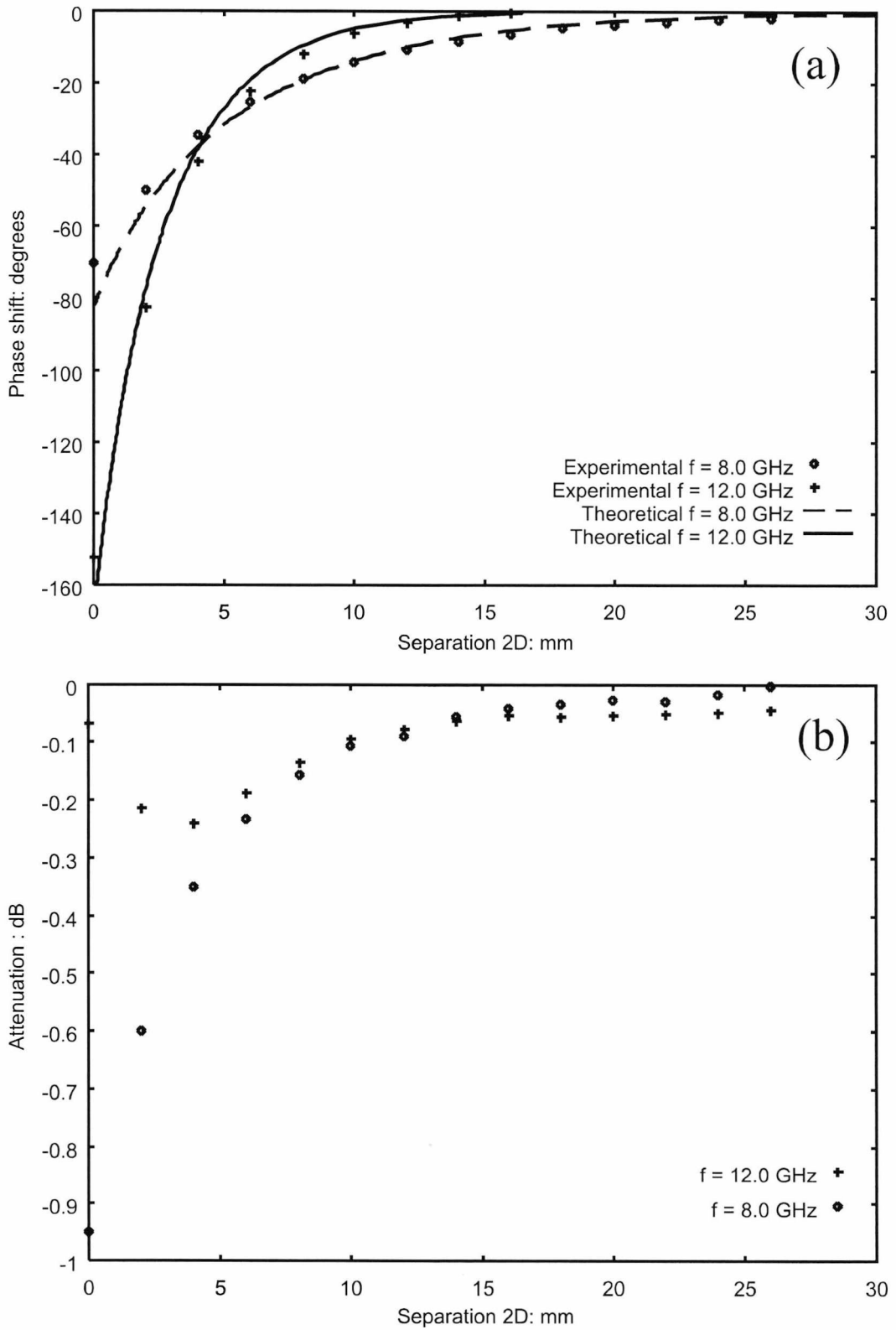


Figure 6.10. Phase shift (a) and attenuation (b) for dielectric phase-shifter.  $2a=10.9$  mm,  $2b=3.4$  mm,  $2d=22.9$  mm,  $L=180$  mm and  $\epsilon_a=\epsilon_b=2.07$ .

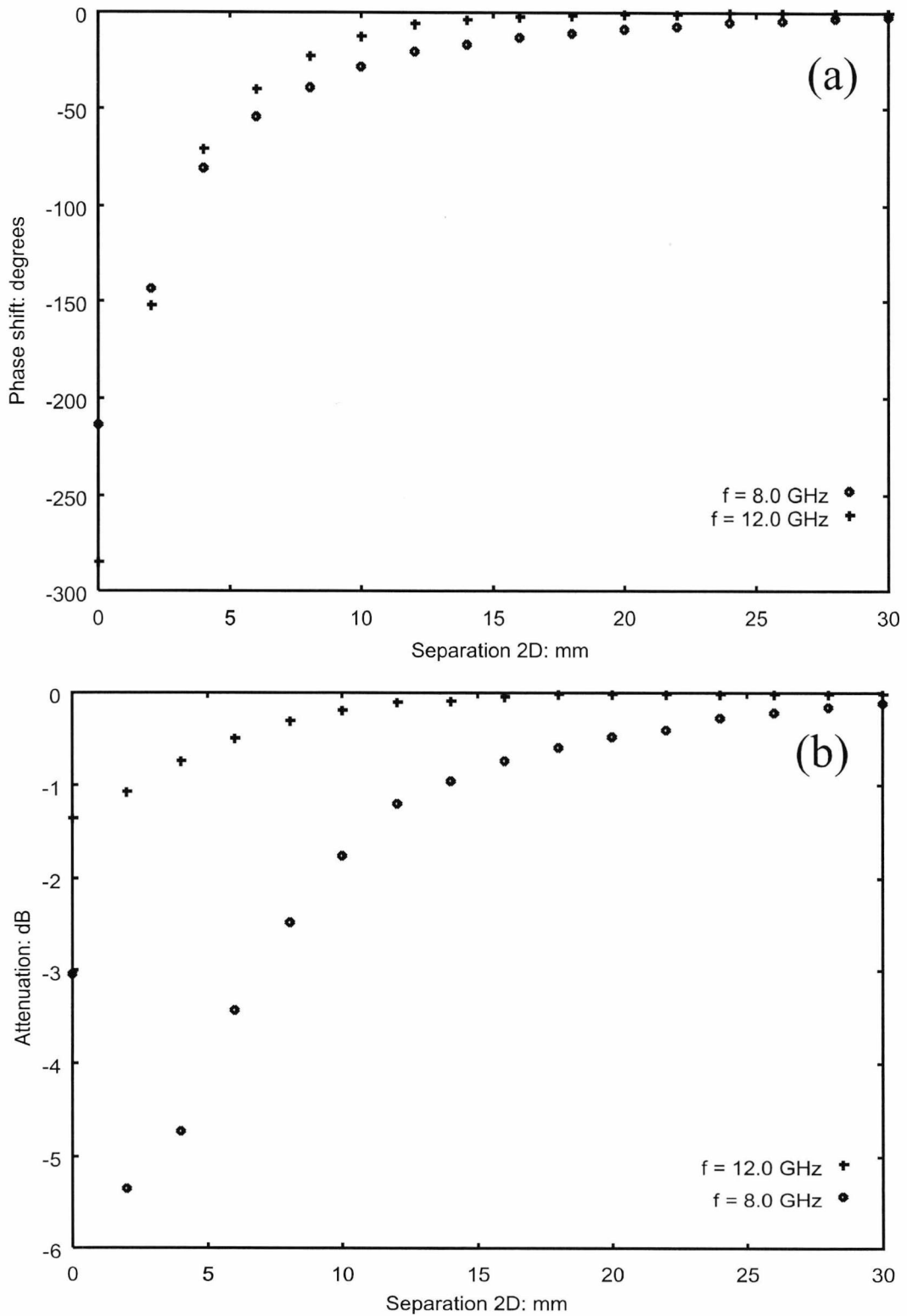


Figure 6.11. Phase shift (a) and attenuation (b) for metallic wall phase-shifter of length  $L=180$  mm.

## 6.4 SUMMARY

In Chapter 5 it was shown that the energy in coupled dielectric waveguides transfers back and forth between them with a beat length  $\Delta\beta_z/\pi$ . By exploiting this, and remembering that  $\Delta\beta_z$  changes with separation, the principle of a dielectric waveguide attenuator was presented. It was further shown that the point of maximum insertion loss was dependent on the operating frequency. Therefore, by measuring the separation at which maximum insertion occurs, a simple dielectric guide wavemeter was demonstrated. For simplicity, experimental measurements were given for low microwave frequencies, however their principle would apply equally at millimetre-wave frequencies. Components of this nature could have uses at millimetre wavelengths where conventional metallic waveguides become impractical.

In Chapter 3 it was shown that by introducing large asymmetries, a coupled dielectric waveguide structure could be made monomode. Thus, by placing a dielectric block parallel to a dielectric waveguide and varying the separation, a phase shift could be obtained without any mode beating. This has the advantage of decreasing the insertion loss since the energy does not transfer back and forth between the two guides. Instead, it remains predominantly in the main waveguide. Accordingly, by changing the distance between the waveguide and a dielectric block, a variable phase shift is achieved with minimal loss. Again, components of this type may have their use at the higher frequency ranges, particularly in multistate reflectometers realised in dielectric waveguide [8,9].

---

**REFERENCES**

- 1 P. J. B. Clarricoats and K. R. Slinn, "Numerical solution of waveguide-discontinuity problems," *Proc. IEE*, vol. 114, No. 7, July 1967, pp. 878-886.
- 2 C. Yeh, F. I. Shimabukuro and J. Chu, "Dielectric ribbon waveguide: an optimum configuration for ultra-low-loss millimeter/submillimeter dielectric waveguide," *IEEE Trans Microwave Theory Tech.*, Vol. 38, No. 6, June 1990, pp. 691-701.
- 3 P. R. Young and R. J. Collier, "A novel wavemeter for dielectric waveguide," *27<sup>th</sup> European microwave conference proceedings*, Jerusalem, 1997, vol. 2, pp. 891-896.
- 4 P. R. Young, R. J. Collier and P. G. G. Bianconi, 'A low loss phase shifter for dielectric waveguide using asymmetrical guides,' *27<sup>th</sup> European microwave conference proceedings*, Jerusalem, 1997, vol. 1, pp. 631-635.
- 5 R. J. Collier and M. F. D'Souza, "Phase shifters for dielectric guides," *IEE Proceedings-H*, Vol. 139, No. 2, pp. 202-204, April 1992.
- 6 R. J. Collier and M. F. D'Souza, "A multistate reflectometer in dielectric guide for the frequency range 75-140 GHz," *IEEE MTT-S Digest*, pp. 1027-1030, 1991.
- 7 J. W. Tao, B. Chan, H. Baudrand, J. Atechian, "Novel type of electrically-controlled phase shifter for millimeter-wave use: Theory and experiment," *IEEE MTT-S Digest*, pp. 671-674, 1991.
- 8 I. M. Boese and R. J. Collier, "Measurements at 140 GHz using a multistate reflectometer," *IEE Colloquium on Terahertz technology*, 4 December 1995.

- 
- 9 I. M. Boese, R. J. Collier, A. K. Jastrzebski, H. Ahmed, J. R. Cleaver and D. Hasko, "An on wafer probe for measurements at 140 GHz," *IEE Colloquium on Terahertz technology and its applications*, 10 April 1997.

---

## 7. CONCLUSIONS

---

We saw in Chapter 1 that dielectric waveguides have clear advantages over metallic waveguide at millimetre-wave frequencies above 110 GHz. They are easier to manufacture and therefore have cheaper production costs. They have less insertion and transition loss than metallic guides. Furthermore, they have lower dispersion and higher bandwidth making them ideal for broadband communications. It therefore seems plausible that they will replace metallic guides for above 110 GHz applications. For this to be accomplished, passive waveguide components are required such as phase-shifters, attenuators and wavemeters. Components of this type were demonstrated in Chapter 6. However, to achieve this, several additional topics were also covered. We therefore begin this chapter with a summary of the work presented in the preceding pages, followed by some suggestions on a possible future work.

### 7.1 SUMMARY

In Chapter 2, the complex propagation constants of rectangular dielectric waveguides were analysed. Firstly, for simplicity, both TE and TM mode slab waveguides with complex permittivity in the guiding and surrounding regions were considered. By making the appropriate assumptions for small loss tangents, approximate expressions were given for the attenuation and propagation constant of these guides. It was shown that for loss tangents as large as 0.1 the error in the approximate method was only of the order of a few percent. Furthermore, the expressions derived for the attenuation constant relate  $\alpha_z$  directly to the lossless propagation constant and the waveguide parameters; the attenuation constant can therefore be calculated with the minimum of effort. Secondly, by introducing the concept of an effective loss tangent, the approximate expressions were used in the effective dielectric constant (EDC) method to allow for the calculation of  $\alpha_z$  in the more useful rectangular dielectric waveguide.

Results were compared with finite element solutions and were shown to be in good agreement. Further improvements were given by using the dual effective-index method (DEIM).

Chapter 4 provided some experimental verification of the techniques. By using the open resonant cavity method, values for both the propagation and attenuation constant were obtained.  $\beta_z$  was shown to be in excellent agreement with DEIM values using published results for  $\epsilon$ . Measurement of  $\alpha_z$  proved more difficult. Nevertheless, values for  $\alpha_z$  corresponding to loss tangents within the range of published data were obtained. The work of Chapter 2 therefore provides a simple and accurate modification to the well-known effective dielectric constant method to allow for the calculation of losses in dielectric waveguides. Furthermore, since the EDC method has been applied to many different structures, such as waveguides with circular geometry or guides with nonlinearities, it is envisaged that the present modification would be applicable to a wide range of different structures.

Coupled dielectric waveguide structures form the basis of many dielectric waveguide components, from filters and couplers to, as we saw in Chapter 6, attenuators, phase-shifters and wavemeters. To analyse these components, the propagation characteristics of coupled dielectric waveguides must first be determined. In general, approximate coupled mode theories have been used for this purpose. However, due to their approximate nature, their use is not always appropriate. In Chapter 3, an alternative method for the characterisation of coupled rectangular dielectric waveguides with asymmetry in both width and permittivity was given.

Firstly, the general case of two parallel asymmetrical slab waveguides was considered. A characteristic equation for this structure was derived and shown to be far simpler than previous methods. Furthermore, unlike coupled mode theories, the technique is exact. Appendix A showed that the improved coupled mode theory gives significant errors for small separations, where either the fields are extensive in the surrounding region, or large asymmetries are present. We saw in chapters 5 and 6 that the difference in the propagation constants of the even and odd modes is often the important parameter. Consequently, the general guidance condition presented in Chapter 3 is more appropriate under these conditions since it is exact.

In coupled mode theories, the eigenmodes of the isolated structures must first be determined using the transcendental characteristic equations of Chapter 2. Secondly, the coupling terms in Appendix A are evaluated before, finally, the propagation constants are obtained. In contrast, the exact technique in Chapter 3 only requires the solution of one transcendental equation. Therefore, for coupled slab waveguides, there seems no benefit in using the approximate coupled mode theory in place of the exact technique since there is no difference in the numerical complexity of the two methods. In addition, the technique of Chapter 3 allows the evaluation of the exact field profile of the individual modes.

Since coupled mode theory uses an expansion in terms of the modes that the isolated guides support, it does not provide an ideal expansion for the fields at waveguide discontinuities. Moreover, because the coupled mode theory expands the field profile of the composite guide in terms of the isolated fields, it always predicts two or more modes. These may include modes below cut-off, i.e.  $\beta_z < \sqrt{\epsilon_2} k_0$ . Care should therefore be taken to neglect these modes. In contrast, the guidance condition in Chapter 3 can be solved over the guiding range  $\sqrt{\epsilon_2} k_0 < \beta_z < \sqrt{\epsilon_a} k_0$  and thus the physical solutions can easily be determined. Furthermore, the exact technique provided an expression for the separation at which cut-off occurs. This proved useful in Chapter 6 to ensure that the coupled structure used in the low-loss phase-shifter remained monomode and consequently did not suffer from coupling effects.

By allowing the permittivity in both the guiding and surrounding regions to become complex, approximate solutions were given for the attenuation constant  $\alpha_z$  of symmetrical coupled slab waveguides. Again, the propagation constant was given purely in terms of the lossless propagation constants and the waveguide parameters, making its evaluation straightforward. An analysis of asymmetrical structures proved too complicated and only numerical values were given for these structures. It was shown that, for certain separations, the attenuation constant of the odd mode of a symmetrical coupled guide was greater than that of the isolated structures. In contrast, the even mode attenuation constant was less. This may have implications for reducing the losses in dielectric waveguides by using coupled structures.

By using the concept of an effective loss tangent, the coupled dielectric slab waveguide solutions were used in the EDC method to solve for coupled rectangular dielectric waveguides with dielectric losses. Solutions were compared with finite

element results and were shown to be in good agreement for both the real and imaginary parts of the complex propagation constant. Furthermore, Chapter 4 gave experimental values for the propagation constant of coupled structures using the open resonant cavity technique. It was shown that the experimental results were in excellent agreement with finite element results and in good agreement with EDC values. However, the large computational times required for finite element techniques limit their use. As a result the EDC method is more suitable for practical design purposes.

The work of Chapter 3 therefore provides a technique, which is as easy to implement as coupled mode theories, but gives significantly better results. More importantly, the addition of expressions for the attenuation constant make the technique more appropriate for millimetre-wave applications where the losses can become significant.

Waveguide components based on coupled structures introduce discontinuities in the transition region from single to coupled waveguide. Transitions of this nature were analysed in Chapter 5 using the bounded mode matching approach. It was shown that very little energy was reflected or radiated from discontinuities of this type, even when the guides in the coupled region were touching. The reflected and radiation terms were therefore neglected, resulting in a simple expression for the guided mode amplitudes of the coupled structure.

It was shown that as the separation increased, equal amounts of energy couple into the even and odd modes of symmetrical or synchronous waveguides. In contrast, for asymmetrical guides, the energy couples to just one of the composite modes for increasing separation. Since the two modes travel with different velocities, the modes beat together causing the energy to transfer back and forth between the two guides with a beat length equal to the difference in the propagation constants divided by  $\pi$ . For asymmetrical guides, little energy transfers for increasing separation since the energy is only coupled to one of the guided modes. For symmetrical or synchronous guides a complete transferral is seen, for increasing separation, since each mode carries an equal amount of energy. This suggests that the energy will couple between synchronous guides whatever the separation. For large separations, very large longitudinal lengths are required for complete transferral since the modes become degenerate. However, practically, perfect symmetry or synchronism is not possible and therefore all dielectric waveguides become isolated for large asymmetries.

In Chapter 6, double waveguide discontinuities were considered. It was shown that by placing a dielectric block parallel to a dielectric waveguide to form a short length of coupled guide, an attenuation could be achieved. By varying the separation between the guide and the dielectric block, the attenuation could be varied to obtain a useful variable attenuator. The large maximum in the insertion loss of the attenuator was shown to be dependent on the operating frequency. Therefore, by measuring the separation at which this maximum attenuation occurred, the attenuator could be used as a wavemeter. By introducing large asymmetries into the coupling region, it was shown that the structure could be made to remain monomode over the composite region. This prevents the energy from transferring back and forth between the guide and the block. There is, however, a change in the phase velocity over the composite region. Accordingly, by varying the separation, the structure can be used as a low-loss variable phase-shifter. For simplicity, experimental results at microwave frequencies were given for all three components to demonstrate their operation. Nevertheless, the devices would be equally valid for millimetre-wave frequencies where dielectric waveguides are more applicable than metallic guides.

## **7.2 FUTURE WORK**

Some of the topics covered in the preceding text would benefit from additional work. A few suggestions for which are given below.

The dual effective-index method (DEIM) was used in Chapter 2 for the solution of dielectric waveguides, where it provided significantly better results than the conventional effective dielectric constant method. However, since the expressions derived by Chiang depend on the asymptotic field profiles, the technique is not applicable to coupled dielectric waveguides with asymmetry, where the fields are of a different form. It would therefore be useful, in later work, if the DEIM was modified to allow the solution of coupled structures.

The general principle of several novel waveguide components was given in Chapter 6. However, for practical applications, additional design work is required. For example, a more accurate characterisation may be required, possibly by applying a

more thorough mode matching technique. In addition, it would be useful if the components were electronically controlled, perhaps by using a stepper motor or a piezoelectric device. Furthermore, as the components main application is at millimetre-wave frequencies above 110 GHz, work is required to implement the components at these wavelengths.

It was suggested in Chapter 6 that the wavemeter could be used to measure an unknown permittivity. This would require the unknown being placed parallel to a waveguide; then, by varying the separation between the material and the waveguide a minimum would be observed in the transmitted power. The position of this minimum would be dependent on the operating frequency, the geometry and the dielectric constant of the material. Therefore, by measuring the separation at which the minimum occurs it would be possible to obtain the permittivity. This is worth additional work since it would provide a simple technique for the measurement of dielectric constant, particularly at higher frequencies.

Finally, it is hoped that as a result of this work that dielectric waveguides will be used more extensively in the millimetre-wave industry.

---

## A. COUPLED MODE THEORY

---

Coupled mode theory and the improved coupled mode theory are covered extensively in the literature [1, 2, 3]. However, for the sake of completeness, a brief outline of the method is given here. We wish to determine the field of a composite structure (Figure 3.1). Clearly a field distribution centred about one of the waveguides cannot be a good approximation of the total field since at least part of the energy will be centred about the second guide. We therefore try to express the field in terms of the field distribution on both waveguides. Thus, we let

$$\begin{Bmatrix} \mathbf{E}'(x, y, z) \\ \mathbf{H}'(x, y, z) \end{Bmatrix} \cong A(z) \begin{Bmatrix} \frac{\epsilon_A}{\epsilon'} e_{Az} + \mathbf{e}_{At} \\ \mathbf{h}_A(x, y) \end{Bmatrix} + B(z) \begin{Bmatrix} \frac{\epsilon_B}{\epsilon'} e_{Bz} + \mathbf{e}_{Bt} \\ \mathbf{h}_B(x, y) \end{Bmatrix} \quad (\text{A.1})$$

where  $\mathbf{e}_A$  and  $\mathbf{h}_A$  are the fields of waveguide A, when in isolation, and  $\mathbf{e}_B$  and  $\mathbf{h}_B$  are the fields on waveguide B, when in isolation.  $\epsilon_A$  is the permittivity profile of guide A,  $\epsilon_B$  is the permittivity profile of guide B and  $\epsilon'$  is the profile of the combined structure, i.e.  $\epsilon' = \epsilon_A + \epsilon_B$ . The  $t$  subscript denotes the transverse component of the field. Our task is to determine the amplitude functions  $A(z)$  and  $B(z)$ . This is achieved with the help of the Lorentz reciprocity theorem:

$$\iint_S \frac{\partial}{\partial z} (\mathbf{E}_t^* \times \mathbf{H}_t' + \mathbf{E}_t' \times \mathbf{H}_t^*) \cdot \hat{z} dS = -j\omega \iint_S (\epsilon' - \epsilon) \mathbf{E}^* \cdot \mathbf{E}' dS, \quad (\text{A.2})$$

where again the  $t$  subscript indicates the transverse component of the field. We let

$$\begin{Bmatrix} \mathbf{E}(x, y, z) \\ \mathbf{H}(x, y, z) \end{Bmatrix} = \begin{Bmatrix} \mathbf{e}_A(x, y) \\ \mathbf{h}_A(x, y) \end{Bmatrix} e^{-jk_z z} \quad (\text{A.3})$$

Substituting equations (A.1) and (A.3) into equation (A.2) yields

$$C_{AA} \frac{dA(z)}{dz} + jA(z)[C_{AA} k_{zA} + \kappa_{AA}] = -C_{AB} \frac{dB(z)}{dz} - jB(z)[\kappa_{BA} + C_{AB} k_{zA}], \quad (\text{A.4})$$

where

$$C_{mn} = \iint_S (\mathbf{e}_{mt}^* \times \mathbf{h}_{nt} + \mathbf{e}_{nt} \times \mathbf{h}_{mt}^*) \cdot \hat{z} dS, \quad (\text{A.5})$$

$$\kappa_{mn} = \omega \iint_S (\epsilon' - \epsilon_n) \left[ \mathbf{e}_{mt} \cdot \mathbf{e}_{nt}^* + \frac{\epsilon_m}{\epsilon'} e_{mz} e_{nz}^* \right] dS, \quad (\text{A.6})$$

$m=A, B$  and  $n=A, B$ .

We now let

$$\begin{Bmatrix} \mathbf{E}(x, y, z) \\ \mathbf{H}(x, y, z) \end{Bmatrix} = \begin{Bmatrix} \mathbf{e}_B(x, y) \\ \mathbf{h}_B(x, y) \end{Bmatrix} e^{-jk_z z}. \quad (\text{A.7})$$

Substituting equations (A.1) and (A.7) into equation (A.2) gives

$$C_{BB} \frac{dB(z)}{dz} + jB(z)[C_{BB} k_{zB} + \kappa_{BB}] = -C_{BA} \frac{dA(z)}{dz} - jA(z)[\kappa_{AB} + C_{BA} k_{zB}]. \quad (\text{A.8})$$

On eliminating  $\frac{dB(z)}{dz}$  from equations (A.4) and (A.8) we obtain

$$\frac{dA(z)}{dz} = -j\gamma_A A(z) - jK_{AB} B(z), \quad (\text{A.9})$$

where

$$\gamma_A = \frac{C_{AB}C_{BA}k_{zB} - C_{AA}C_{BB}k_{zA} + C_{AB}\kappa_{AB} - C_{BB}\kappa_{AA}}{C_{AB}C_{BA} - C_{AA}C_{BB}} \quad (\text{A.10})$$

and

$$K_{AB} = \frac{C_{AB}C_{BB}(k_{zB} - k_{zA}) + C_{AB}\kappa_{BB} - C_{BB}\kappa_{BA}}{C_{AB}C_{BA} - C_{AA}C_{BB}}. \quad (\text{A.11})$$

Similarly, eliminating  $\frac{dA(z)}{dz}$  from equations (A.4) and (A.8) gives

$$\frac{dB(z)}{dz} = -j\gamma_B B(z) - jK_{BA} A(z), \quad (\text{A.12})$$

where

$$\gamma_B = \frac{C_{AB}C_{BA}k_{zA} - C_{AA}C_{BB}k_{zB} + C_{BA}\kappa_{BA} - C_{AA}\kappa_{BB}}{C_{AB}C_{BA} - C_{AA}C_{BB}} \quad (\text{A.13})$$

and

$$K_{BA} = \frac{C_{BA}C_{AA}(k_{zA} - k_{zB}) + C_{BA}\kappa_{AA} - C_{AA}\kappa_{AB}}{C_{AB}C_{BA} - C_{AA}C_{BB}}. \quad (\text{A.14})$$

Solving equation (A.9) and (A.12) for  $A(0)=1$  and  $B(0)=0$  yields

$$A(z) = \frac{1}{2} \left[ 1 + \frac{\Delta\gamma}{\sqrt{\Delta\gamma^2 + K_{AB}K_{BA}}} \right] e^{-jk_{z1}z} + \frac{1}{2} \left[ 1 - \frac{\Delta\gamma}{\sqrt{\Delta\gamma^2 + K_{AB}K_{BA}}} \right] e^{-jk_{z2}z} \quad (\text{A.15})$$

and

$$B(z) = \frac{\sqrt{K_{AB}K_{BA}}}{2\sqrt{\Delta\gamma^2 + K_{AB}K_{BA}}} e^{-jk_{z1}z} - \frac{\sqrt{K_{AB}K_{BA}}}{2\sqrt{\Delta\gamma^2 + K_{AB}K_{BA}}} e^{-jk_{z2}z} \quad (\text{A.16})$$

where

$$\Delta\gamma = \frac{\gamma_A - \gamma_B}{2}, \quad (\text{A.17})$$

$$k_{z1} = \frac{\gamma_A + \gamma_B}{2} + \sqrt{\Delta\gamma^2 + K_{AB}K_{BA}} \quad (\text{A.18})$$

and

$$k_{z2} = \frac{\gamma_A + \gamma_B}{2} - \sqrt{\Delta\gamma^2 + K_{AB}K_{BA}}. \quad (\text{A.19})$$

For our analysis we have assumed slab waveguides. Thus, the fields in equations (A.1), (A.3) and (A.7) are known exactly, see Chapter 2. Moreover, the integrals in equations (A.5) and (A.6) are also known. Therefore all the parameters in equations (A.15) and (A.16) can be obtained, allowing us to solve for  $A(z)$  and  $B(z)$ . If we know  $A(z)$  and  $B(z)$  then the field variation in (A.1) is easily determined.

We notice that the total field is now of the form

$$\begin{aligned} \begin{Bmatrix} \mathbf{E}'(x, y, z) \\ \mathbf{H}'(x, y, z) \end{Bmatrix} &\cong \begin{Bmatrix} A_1 \mathbf{e}_A(x, y) + B_1 \mathbf{e}_B(x, y) \\ A_1 \mathbf{h}_A(x, y) + B_1 \mathbf{h}_B(x, y) \end{Bmatrix} e^{-jk_{z1}z} \\ &+ \begin{Bmatrix} A_2 \mathbf{e}_A(x, y) + B_2 \mathbf{e}_B(x, y) \\ A_2 \mathbf{h}_A(x, y) + B_2 \mathbf{h}_B(x, y) \end{Bmatrix} e^{-jk_{z2}z} \end{aligned} \quad (\text{A.20})$$

where  $A_1$ ,  $B_1$ ,  $A_2$  and  $B_2$  are constants. The first term in the above equation gives an approximate value for the even symmetry eigenmode of the composite structure; the second term gives an approximate value for the odd.  $k_{z1}$  and  $k_{z2}$  are approximate values for the propagation constants of the even and odd modes of Chapter 3, respectively.

The following Figures give an illustration of the error in the calculated propagation constant of the guided modes using the improved coupled mode theory. For comparison, the values are compared with the exact values of Chapter 3. As can be seen, the coupled mode theory gives good results for well confined structures with large separations. However, if asymmetry is present or the mode is close to cut-off, the coupled mode theory displays significant errors. Since the difference in the propagation constants is often the important parameter (Chapter 5 and 6) the exact method presented in Chapter 3 is more appropriate.

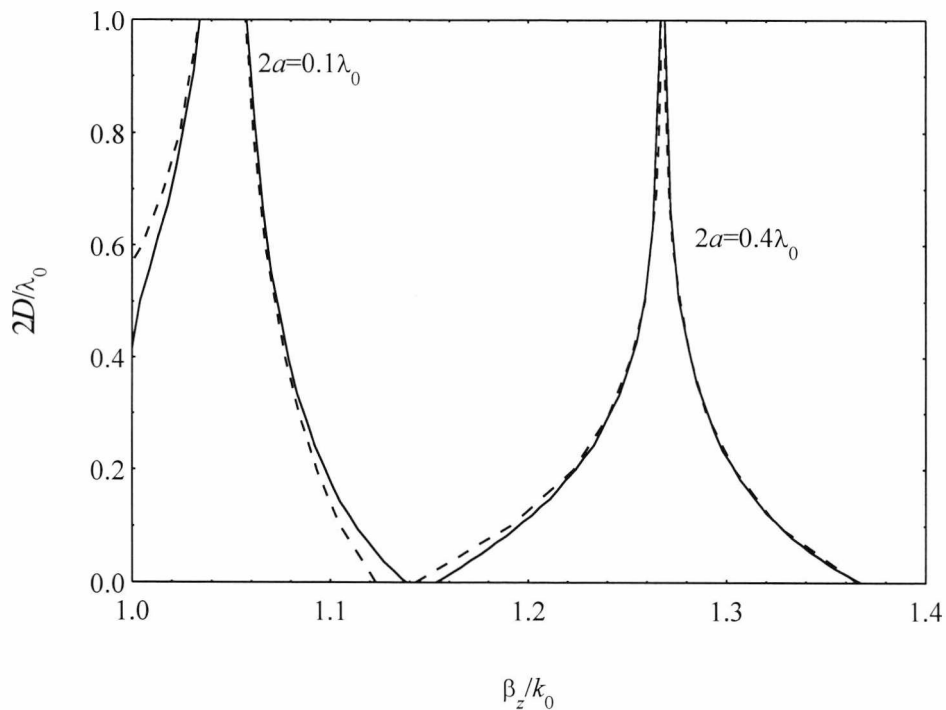


Figure A.1. Comparison of exact (solid line) and improved coupled mode theory (dashed line) for symmetrical TE coupled slab waveguide with  $2a=2b$ ,  $\epsilon_a=\epsilon_b=2.07$  and  $\epsilon_2=0$ .

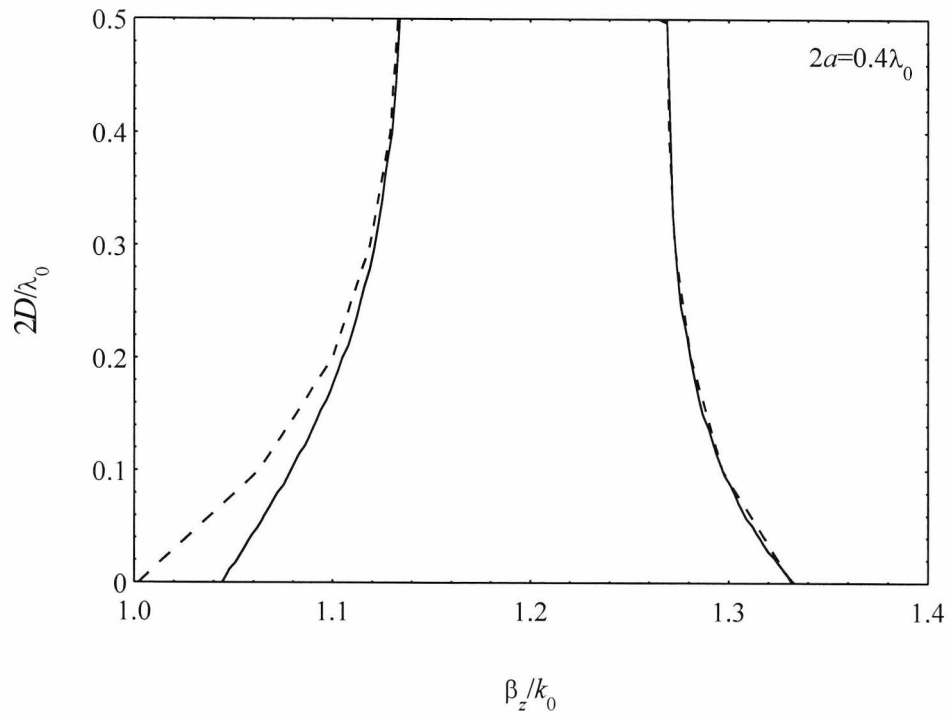


Figure A.2. Comparison of exact (solid line) and improved coupled mode theory (dashed line) for width asymmetry TE coupled slab waveguide with  $2a=0.4\lambda_0$ ,  $b=0.5a$ ,  $\epsilon_a=\epsilon_b=2.07$  and  $\epsilon_2=0$ .

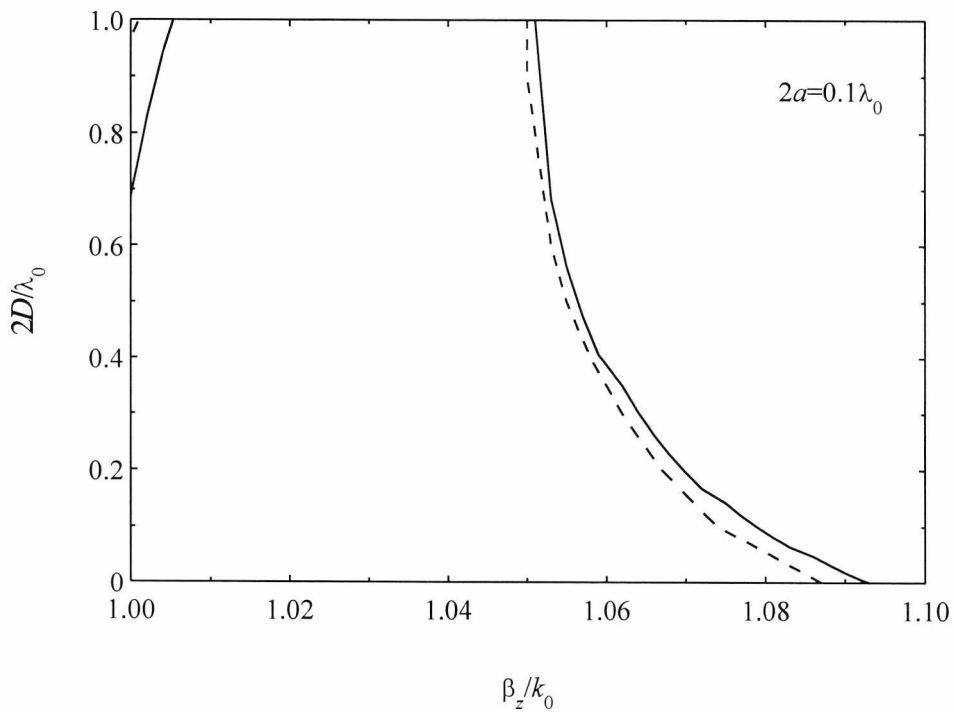


Figure A.3. Comparison of exact (solid line) and improved coupled mode theory (dashed line) for width asymmetry TE coupled slab waveguide with  $2a=0.1\lambda_0$ ,  $b=0.5a$ ,  $\epsilon_a=\epsilon_b=2.07$  and  $\epsilon_2=0$ .

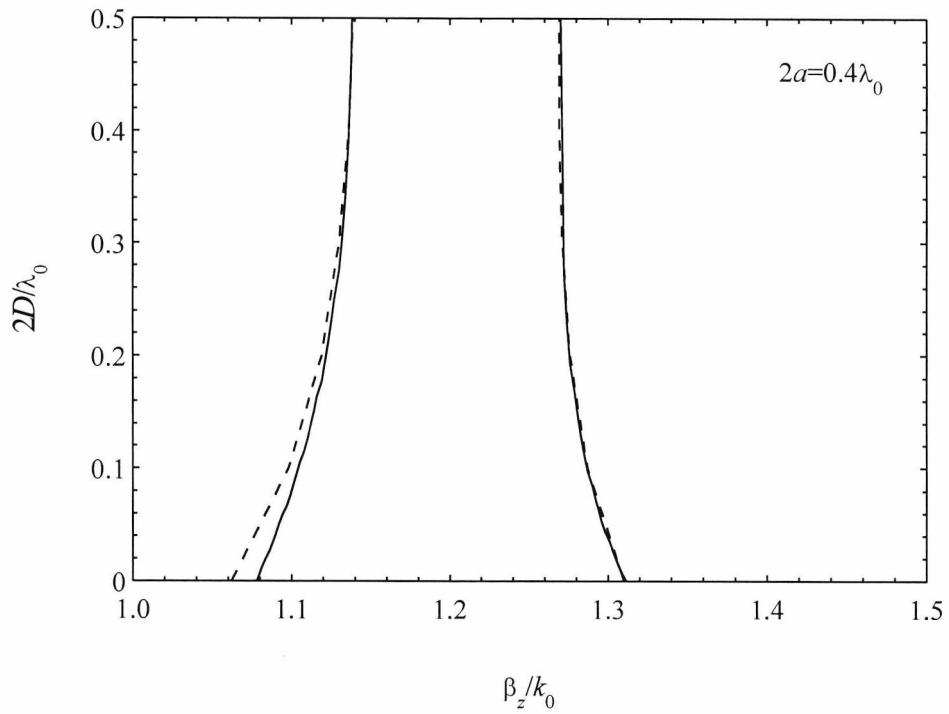


Figure A.4. Comparison of exact (solid line) and improved coupled mode theory (dashed line) for permittivity asymmetry TE coupled slab waveguide with  $2a=0.4\lambda_0$ ,  $2b=2a$ ,  $\epsilon_a=2.07$ ,  $\epsilon_b=0.8\epsilon_a$  and  $\epsilon_2=0$ .

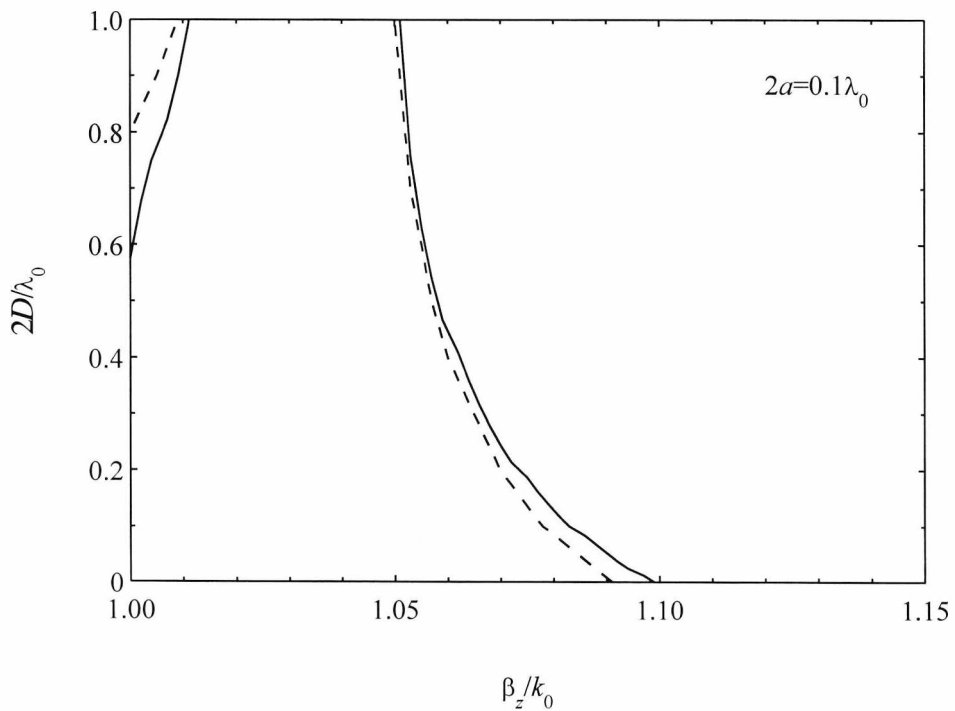


Figure A.5. Comparison of exact (solid line) and improved coupled mode theory (dashed line) for permittivity asymmetry TE coupled slab waveguide with  $2a=0.1\lambda_0$ ,  $2b=2a$ ,  $\epsilon_a=2.07$ ,  $\epsilon_b=0.8\epsilon_a$  and  $\epsilon_2=0$ .

---

## REFERENCES

- 1 H. Hung-Chia, “Coupled mode theory – As applied to microwave and optical transmission,” *VNU Science Press* (publishers), Netherlands, 1984.
- 2 H. Haus and W. Huang, “Coupled-mode theory,” *Proceedings IEEE*, vol. 79, no. 10, October 1991, pp. 1505-1518.
- 3 Wu-Pen Yuen, “On the different formulations of the coupled-mode theory for parallel dielectric waveguides,” *J. Lightwave Technol.*, vol. 12, no. 1, January 1994, pp. 82- 85.

## B. COUPLED DIELECTRIC WAVEGUIDE RESULTS

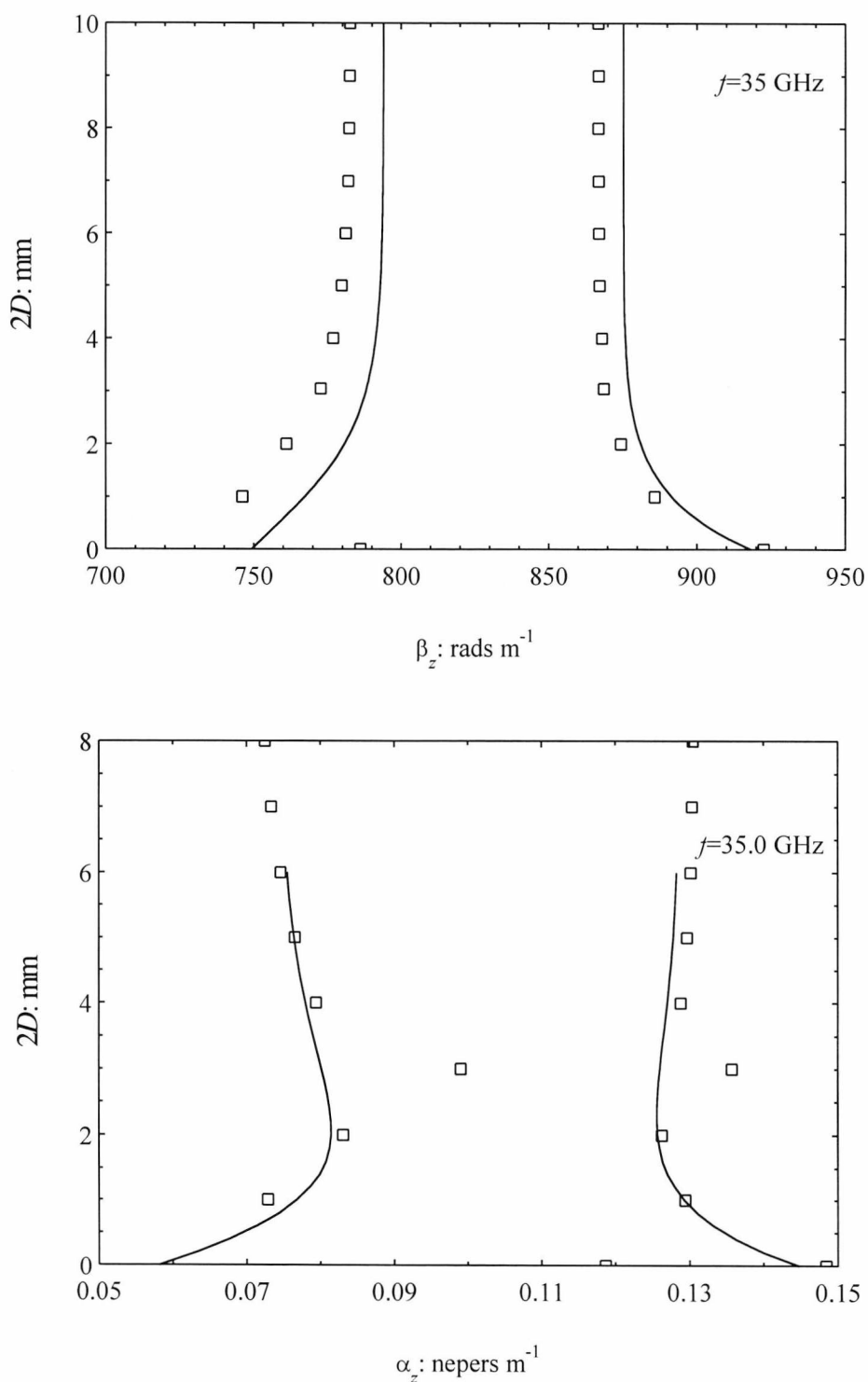


Figure B.1.  $E^x$  modes for coupled dielectric waveguide with  $f=35$  GHz,  $2a=3.556$  mm,  $2b=1.778$  mm,  $2d=7.112$  mm,  $\epsilon_a=\epsilon_b=2.07(1-j3.0\times 10^{-4})$  and  $\epsilon_2=1.0$ . Solid lines are EDC solutions boxes are HFSS solutions.

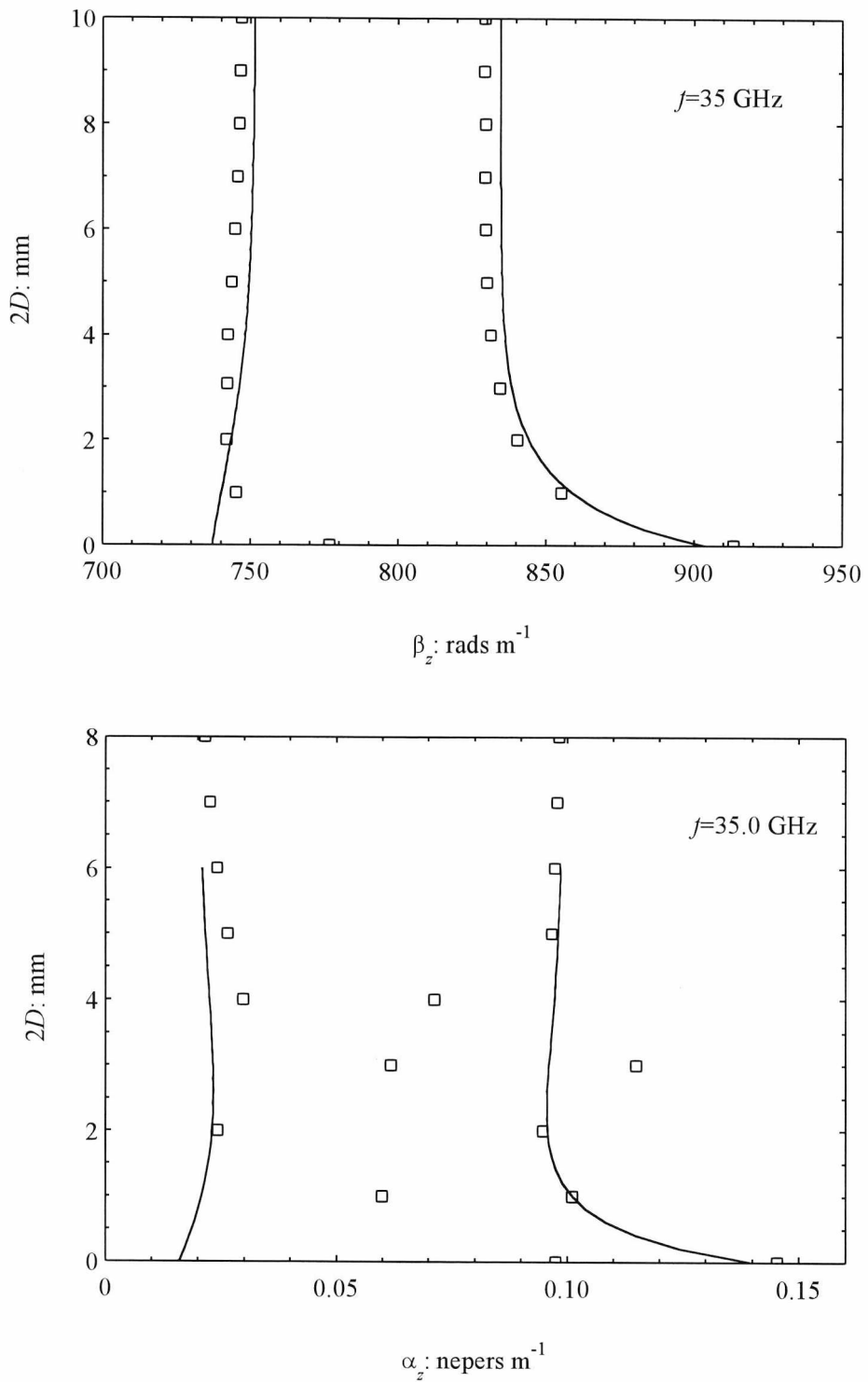


Figure B.2.  $E^y$  modes for coupled dielectric waveguide with  $f=35$  GHz,  $2a=3.556$  mm,  $2b=1.778$  mm,  $2d=7.112$  mm,  $\epsilon_a=\epsilon_b=2.07(1-j3.0\times 10^{-4})$  and  $\epsilon_2=1.0$ . Solid lines are EDC solutions boxes are HFSS solutions.

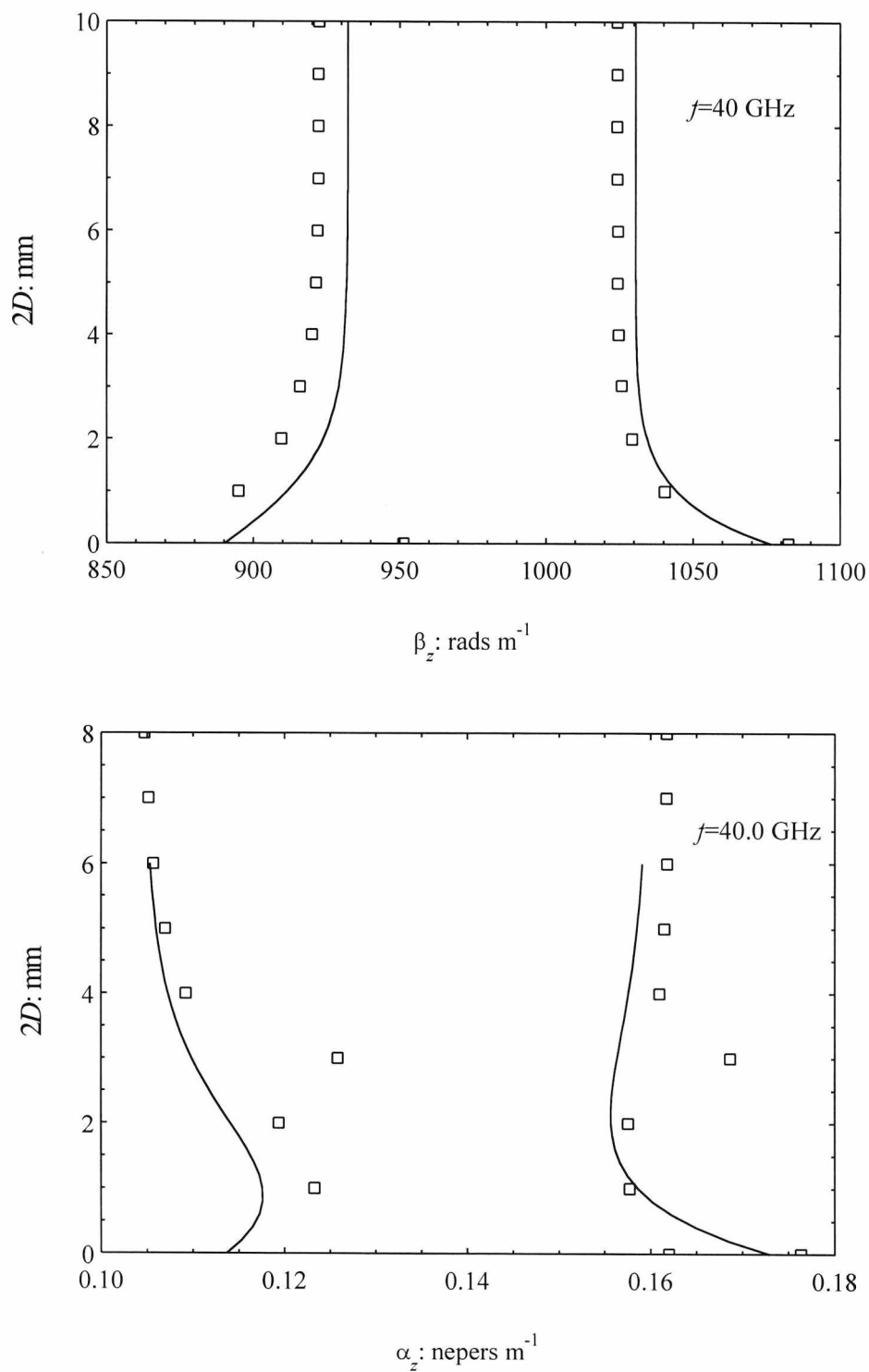


Figure B.3.  $E^x$  modes for coupled dielectric waveguide with  $f=40$  GHz,  $2a=3.556$  mm,  $2b=1.778$  mm,  $2d=7.112$  mm,  $\epsilon_a=\epsilon_b=2.07(1-j3.0\times 10^{-4})$  and  $\epsilon_2=1.0$ . Solid lines are EDC solutions boxes are HFSS solutions.

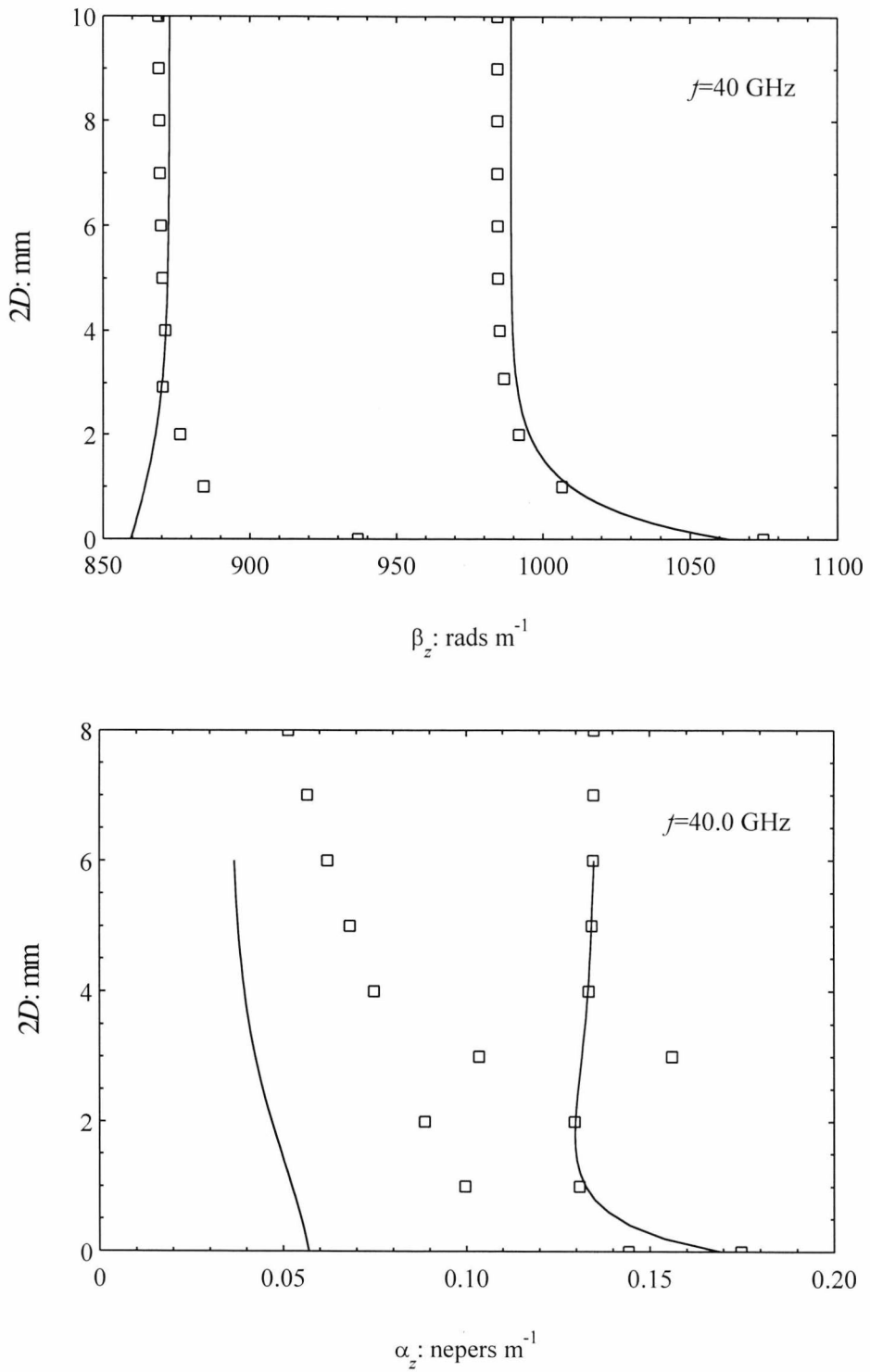


Figure B.4.  $E^y$  modes for coupled dielectric waveguide with  $f=40$  GHz,  $2a=3.556$  mm,  $2b=1.778$  mm,  $2d=7.112$  mm,  $\epsilon_a=\epsilon_b=2.07(1-j3.0\times 10^{-4})$  and  $\epsilon_2=1.0$ . Solid lines are EDC solutions boxes are HFSS solutions.

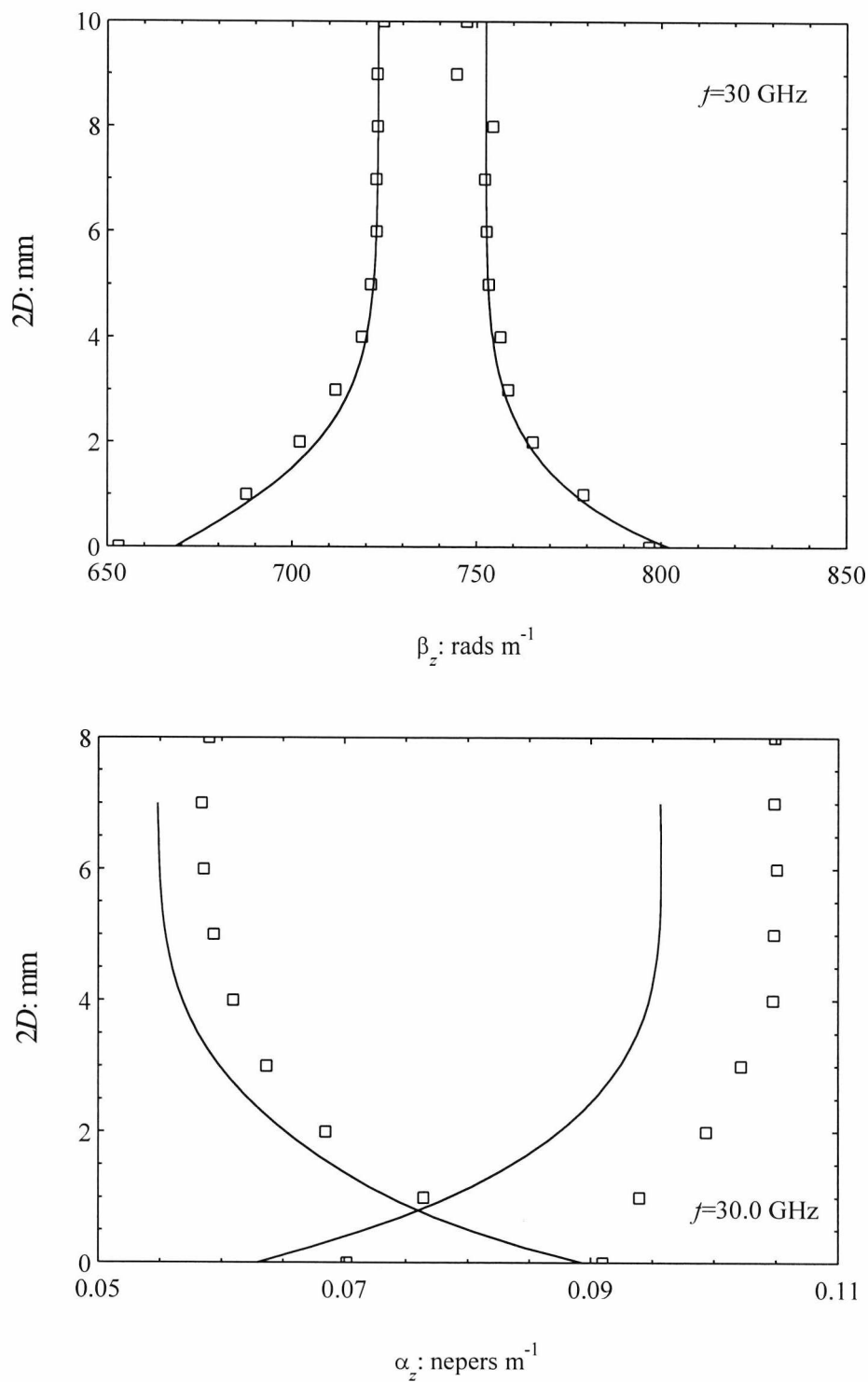


Figure B.5.  $E^x$  modes for coupled dielectric waveguide with  $f=30$  GHz,  $2a=2b=3.556$  mm,  $2d=7.112$  mm,  $\epsilon_a=2.254(1-j1.5\times 10^{-4})$ ,  $\epsilon_b=2.07(1-j3.0\times 10^{-4})$  and  $\epsilon_2=1.0$ . Solid lines are EDC solutions boxes are HFSS solutions.

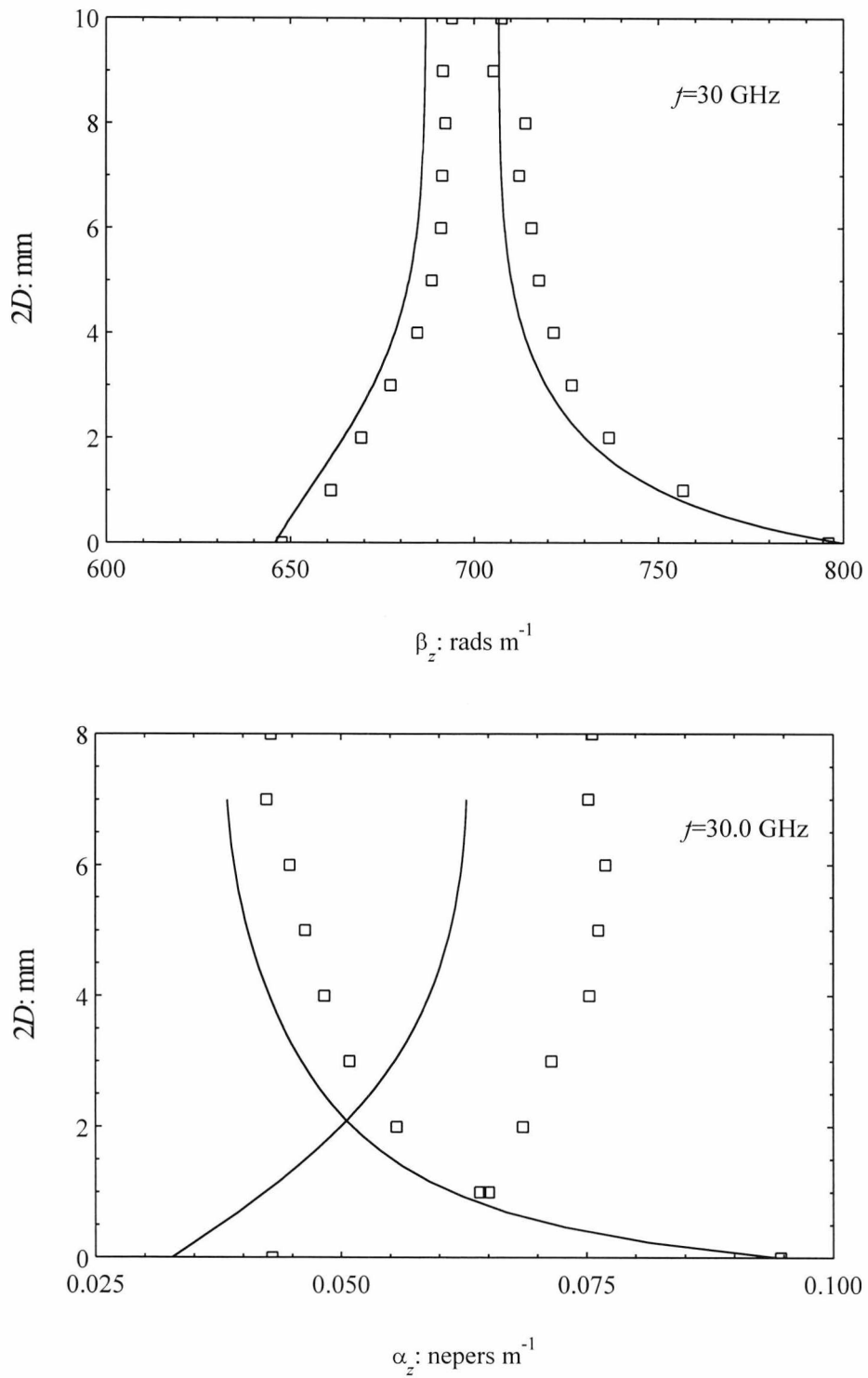


Figure B.6.  $E^y$  modes for coupled dielectric waveguide with  $f=30$  GHz,  $2a=2b=3.556$  mm,  $2d=7.112$  mm,  $\epsilon_a=2.254(1-j1.5\times 10^{-4})$ ,  $\epsilon_b=2.07(1-j3.0\times 10^{-4})$  and  $\epsilon_2=1.0$ . Solid lines are EDC solutions boxes are HFSS solutions.

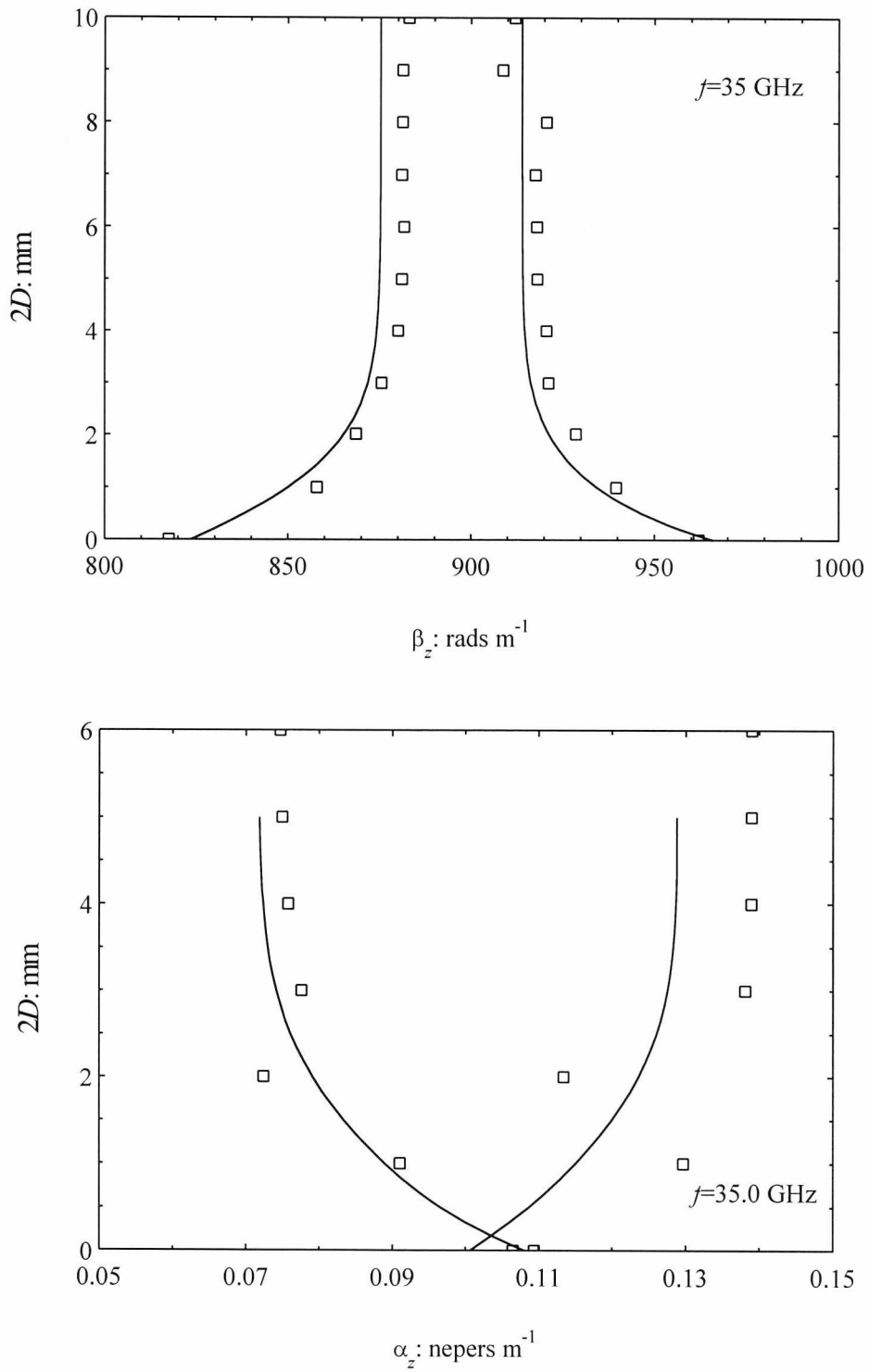


Figure B.7.  $E^x$  modes for coupled dielectric waveguide with  $f=35 \text{ GHz}$ ,  $2a=2b=3.556 \text{ mm}$ ,  $2d=7.112 \text{ mm}$ ,  $\epsilon_a=2.254(1-j1.5 \times 10^{-4})$ ,  $\epsilon_b=2.07(1-j3.0 \times 10^{-4})$  and  $\epsilon_2=1.0$ . Solid lines are EDC solutions boxes are HFSS solutions.

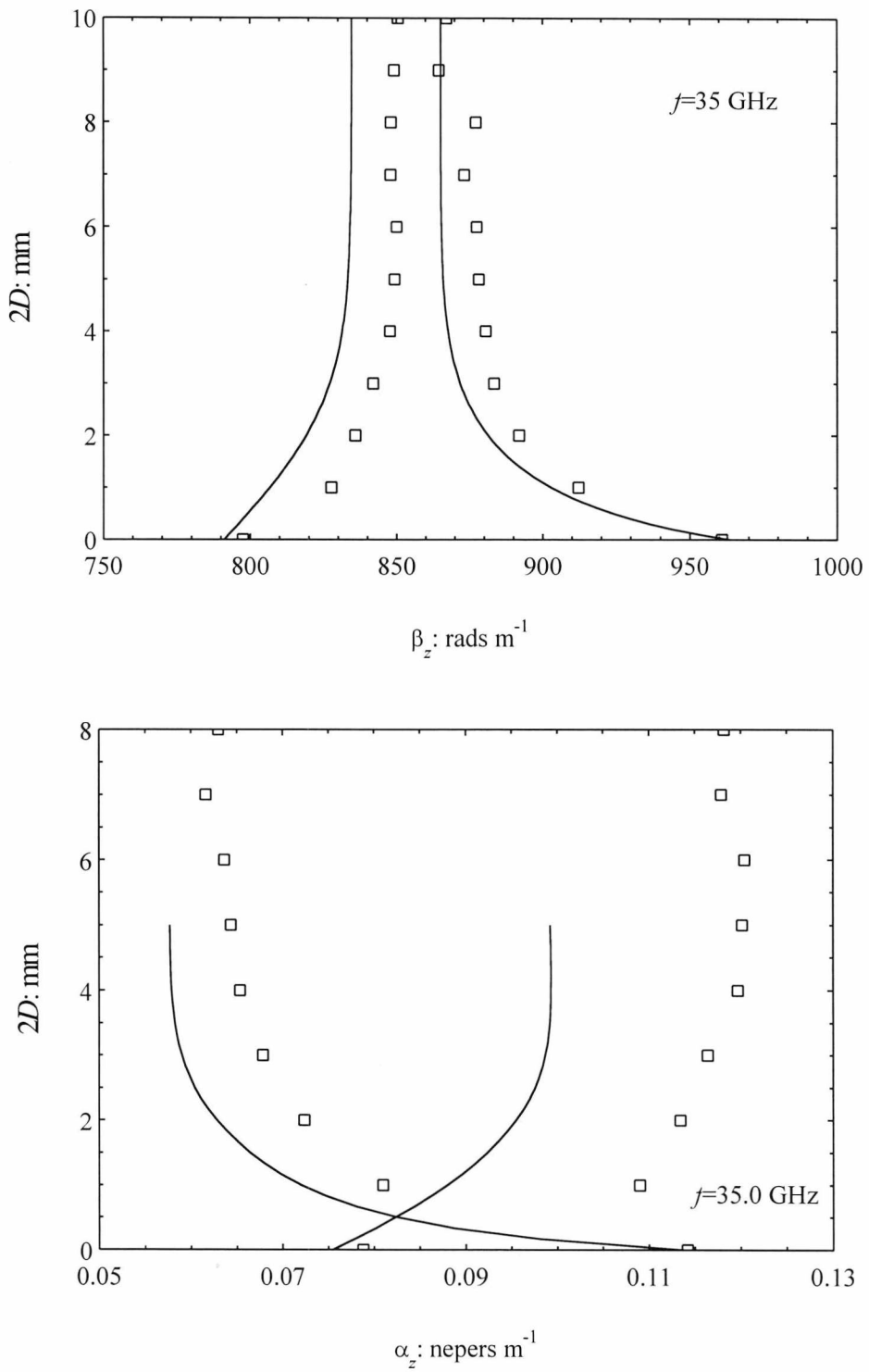


Figure B.8.  $E^y$  modes for coupled dielectric waveguide with  $f=35$  GHz,  $2a=2b=3.556$  mm,  $\epsilon_a=2.254(1-j1.5\times 10^{-4})$ ,  $\epsilon_b=2.07(1-j3.0\times 10^{-4})$ ,  $\epsilon_b=2.07$  and  $\epsilon_2=1.0$ . Solid lines are EDC solutions boxes are HFSS solutions.

---

## C. LIST OF PUBLICATIONS

---

P. R. Young and R. J. Collier, "Solution of lossy dielectric waveguides using the dual effective-index method," *Electron. Lett.*, vol. 33, No. 21, October 1997, pp. 1788-1789.

P. R. Young, R. J. Collier and P. G. G. Bianconi, "A low loss phase shifter for dielectric waveguide using asymmetrical guides," *27<sup>th</sup> European microwave conference proceedings*, vol. 1, 1997, pp. 631-635.

P. R. Young and R. J. Collier, "A novel wavemeter for dielectric waveguide," *27<sup>th</sup> European microwave conference proceedings*, vol. 2, 1997, pp. 891-896.

P. R. Young and R. J. Collier, "Extension to the effective-index method to include the calculation of losses in dielectric waveguides," *Electron. Lett.*, vol. 33, No. 13, June 1997, pp. 1151-1152.

P. R. Young and R. J. Collier, "Low loss phase shifter for dielectric waveguide" *IEEE MTT/ED/AP/LEO Societies Joint Chapter 2<sup>nd</sup> High Frequency Postgraduate Colloquium*, 1996, pp. 45-50.

P. R. Young and R. J. Collier, "The design of dielectric waveguide components using the propagation characteristics of two parallel asymmetrical slab waveguides," *M+RF 96 conference proceedings*, 1996, pp. 373-383.

P. R. Young and R. J. Collier, "Propagation characteristics of two parallel asymmetrical slab waveguides," *IEEE MTT/ED/AP/LEO Societies Joint Chapter 1<sup>st</sup> High Frequency Postgraduate Colloquium*, 1995, pp. 21-24.